Chemo-Mechanics of Lithium-Ion Battery Electrodes

by

Claudio V. Di Leo

B.S., Massachusetts Institute of Technology (2010)
M.S., Massachusetts Institute of Technology (2012)

Submitted to the Department of Mechanical Engineering
in partial fulfillment of the requirements for the degree of

Doctor of Philosophy

at the

Massachusetts Institute of Technology

June 2015

ARCHIVES
MASSACHUSETTS INSTITUTE OF TECHNOLOLGY
JUL 3 0 2015
LIBRARIES

© Massachusetts Institute of Technology 2015. All rights reserved.

Signature redacted

Author .....
Department of Mechanical Engineering
May 22, 2015

Signature redacted

Certified by .....
Lallit Anand
Rohsenow Professor of Mechanical Engineering
Thesis Supervisor

Signature redacted

Accepted by .....
David E. Hardt
Chairman, Department Committee on Graduate Students

Chemo-Mechanics of Lithium-Ion Battery Electrodes

by
Claudio V. Di Leo

Submitted to the Department of Mechanical Engineering
on May 22, 2015, in partial fulfillment of the
requirements for the degree of
Doctor of Philosophy

Abstract

Mechanical deformation plays a crucial role both in the normal operation of a Lithium-Ion battery, as well as in its degradation and ultimate failure. This thesis addresses the theoretical formulation, numerical implementation, and application of fully-coupled deformation-diffusion theories aimed at two different classes of electrode materials: (i) phase-separating electrodes, and (ii) amorphous Silicon electrodes, which are elaborated on next.

Central to the study of phase-separating electrodes is the coupling between mechanical deformation and the Cahn-Hilliard phase-field theory. We have formulated a thermodynamically consistent theory which couples Cahn-Hilliard species diffusion with large elastic deformations of a body. Through a split-method, we have numerically implemented our theory, and using our implementation we first studied the diffusion-only problem of spinodal decomposition in the absence of mechanical deformation. Second, we studied the chemo-mechanically-coupled problem of lithiation of isotropic spheroidal phase-separating electrode particles. We showed that the coupling of mechanical deformation with diffusion is crucial in determining the lithiation morphology, and hence the Li distribution, within these particles.

Amorphous silicon (a-Si), when fully lithiated, has a theoretical capacity $\approx$ 10 times larger than current-generation graphite anodes. However, the intercalation of such a large amount of Li into a-Si induces very large elastic-plastic deformations. We have formulated and numerically implemented a fully-coupled deformation-diffusion theory, which accounts for transient diffusion of lithium and accompanying large elastic-plastic deformations. We have calibrated our theory, and applied it to modeling galvanostatic charging of hollow a-Si nanotubes whose exterior walls have been oxidized to prevent outward expansion. Our predictions of the voltage vs. state-of-charge (SOC) behavior at various charging rates (C-rate) are in good agreement with experiments from the literature. Through simulation, we studied how plastic deformation affects the performance of a-Si-based anodes by reducing stress, thus enabling higher realizable capacities, and introducing dissipation.

Finally, in order to design a-Si-based anodes aimed at mitigating failure of the solid electrolyte interphase (SEI), we have formulated and studied a continuum theory for the growth of an SEI layer — a theory which accounts for the generation of growth stresses.

Thesis Supervisor: Lallit Anand
Title: Rohsenow Professor of Mechanical Engineering

Acknowledgments

First and foremost I would like to thank Professor Anand, who has mentored me from my undergraduate research through my doctoral work. Beyond imparting me with great tools for conducting research in solid mechanics, Professor Anand has taught me to always conduct research at the highest standard, and to value quality and integrity above all. His teachings will continue to inspire me throughout my career. I would also like to thank my thesis committee members, Professor David Parks, Professor Martin Bazant, and Professor Yang Shao-Horn, for their invaluable suggestions and guidance throughout my research.

A great thanks to Ray Hardin, our administrator extraordinaire, who throughout my years has provided all of the necessary support to ensured that I could focus on producing the best research possible. I would also like to thanks Pierce Hayward and Leslie Reagan for their support.

In my time at MIT I have had the pleasure of working with incredibly talented individuals. Vikas Srivastava, who was my undergraduate mentor, and continues to be a good friend. Shawn Chester and David Henann, who were teaching assistants when I first learned solid mechanics, and who continue to inspire me to this day. Kaspar Loeffel, Mary Cookson, Tony Tran, Jacques Luk-Cyr, Haowen Liu, Jafar Albinmousa, and many other students, postdocs, and faculty who have passed through the lab in my years here. Finally, Elisha Rejovitzky, who has been my closest collaborator. Our heated discussion have been invaluable to my learning.

I would like to thank my parents, Helga and Bruno, who have shown me unwavering support throughout all my years at MIT. When I was five years old, on a visit to Boston from Peru, my parents brought me to see MIT. I fell in love with the university, and I told them that one day I would study here. Since that day they have been working relentlessly to support my education, they make dreams come true.

This thesis is dedicated to my wife Lea, she inspires me to be a better person. Thank you for standing by me. Finally, to my daughter Alice, dream big, and thank you for waking me up at 5am so that I can get to work early.

Contents

List of Figures

List of Tables

Chapter 1

Introduction

1.1 Background

The development of Lithium-Ion batteries (LIBs) with improved capacity, life, safety, and cost, is of major importance for a wide range of industries — from large-scale stationary energy storage systems in renewable energy plants, to portable power systems for sustainable electric vehicles. The development of simulation-based tools for the design, life-prediction, optimization, and diagnosis of LIBs for various applications is then of crucial importance and remains at large an unsolved research question.

Lithium-ion batteries are assemblies of several cells which themselves are multilayered systems containing many anode/separator/cathode units saturated with an electrolyte. The anode and cathode layers (each $\approx 100\,\mu$m thick) are separated by a thin ($20\,\mu$m) microporous polymeric membrane which prevents physical contact between the anode and cathode while enabling ionic transport. The electrolyte consists of a lithium salt (e.g., LiPF6) in a mixed organic solvent (e.g., etheylene carbonate-dimethyl carbonate).

The electrodes themselves are composite materials of active particles embedded in a polymeric binder (e.g., PVDF) which contains a conductivity enhancer (e.g., carbon-black). At the heart of a LIB are the active particles within the electrodes. Some representative chemistries for the two electrodes are:

(i) For the negative electrode (anode): graphite in particulate form (mesocarbon microbeads); and

(ii) For the positive electrode (cathode): a lithium-metal-oxide in particulate form (e.g., $LiCoO_2$; $LiMn_2O_4$; $LiFePO_4$).

Mechanical deformation plays a crucial role both in the normal operation of a battery, as well as in its degradation, at virtually all length scales discussed above. For example, during normal operation, stress can have a significant effect on the electrochemical behavior of the

cell, while plastic deformation mechanisms can introduce unwanted dissipation. Mechanical failure, through for example fracture of the active particles or delamination of the active particles from their conductive matrix, can lead to degradation, capacity loss, and ultimately the failure of the battery.

A complete understanding of LIBs will invariably require multi-scale modeling of the various components described above, however in this thesis *the research focus is at the single active particle level.* In this thesis, we have focused on studying the coupled diffusion-deformation behavior of two different classes of electrode materials: (i) phase-separating electrodes, and (ii) amorphous Silicon electrodes, which are discussed in the following sub-sections.

1.1.1 Phase-separating electrodes

Several Li intercalation compounds of interest in battery applications exhibit phase-separation into Li-rich and Li-poor phases (cf., e.g., Bruce et al., 2008; Tang et al., 2010). Central to the study of diffusion-deformation problems in such electrode materials is understanding the coupling between mechanical deformation and the resulting phase separation behavior as modeled through the Cahn-Hilliard phase-field theory (Cahn and Hilliard, 1958, 1959). Specifically, it is important to understand how mechanical deformation can affect the distribution of Li content within the particle during charging/discharging. This distribution of Li, in turn, will affect the build up of stresses in the particle which might lead to its failure through fracture.

1.1.2 Amorphous Silicon electrodes

When fully lithiated a-Si has a theoretical gravimetric capacity $\sim$ 10 times larger than current-generation graphite anodes. However, the intercalation of such a large amount of Li into the a-Si induces very large elastic-plastic deformations — with volume changes of approximately 300% (Obrovac and Krause, 2007). Two major mechanisms by which the large deformations of the anode negatively affect its performance are:

a) *Fracture of the anode particles.* The large stresses that develop in the anode due to inhomogeneous volume changes associated with large gradients of Li-ions in the anode can lead to fracture of an anode particle. The formation and propagation of cracks in turn lead to degradation of the performance of the battery, and significantly limit its lifetime.

b) *Failure of the solid electrolyte interface (SEI).* During operation of a Li-ion battery, a passivating film, known as the solid electrolyte interface (SEI), forms on the surface of the anode. Due to the large volumetric changes associated with the lithiation of Si anodes, the SEI is placed under large tensile stresses, which in turn cause it to fail. Repeated failure and growth of the SEI leads to capacity fade of the battery.

Fracture of anode particles has been successfully mitigated through the use of nano- and micro-dimensioned particles (cf. He et al., 2011; McDowell et al., 2012; Berla et al., 2014).

In order to mitigate failure of the SEI due to the large volume changes associated with lithiating a-Si anodes, various research groups have proposed the use of novel "engineered" anodes which restrict the deformation incurred by the SEI during cyclic lithiation.

However, restriction of the expansion of a-Si during cycling leads to the generation of very large stresses, forcing the a-Si anode to deform plastically. The elastic-plastic deformation of the Si anode, resulting from the mechanical restrictions engineered into the structure, will have a significant effect on the electrochemical performance of the anode, which at present is largely unexplored, and is the focus of this part of the part of the thesis.

Finally, in order to design engineered a-Si nanostructured anodes aimed at mitigating SEI failure, we must also consider the concurrent growth and stress generation within the SEI layer. In order to understand stress generation within the SEI layer, a part of this thesis is also focused on formulating a continuum theory for the the growth of an SEI layer — a theory which accounts for the generation of the attendant growth stresses (cf. Mukhopadyay et al., 2012).

1.2 Brief summary

This thesis is comprised of three major parts:

(i) Modeling phase-separating electrode materials;

(ii) Modeling amorphous Silicon electrodes; and

(iii) Modeling growth of a solid electrolyte interphase.

Each part is discussed in more detail in the following sections, and publications in peer-reviewed journals related to each part are listed.

1.2.1 Modeling phase-separating electrode materials

We formulate a unified framework of balance laws and thermodynamically-consistent constitutive equations which couple Cahn-Hilliard-type species diffusion with large elastic deformations of a body. The traditional Cahn-Hilliard theory, which is based on the species concentration c and its spatial gradient ∇c, leads to a partial differential equation for the concentration which involves fourth-order spatial derivatives in c; this necessitates use of basis functions in finite-element solution procedures that are piecewise smooth and globally C^1-continuous. In order to use standard C^0-continuous finite-elements to implement our phase-field model, we use a split-method to reduce the fourth-order equation into two second-order partial differential equations (pdes). These two pdes, when taken together with the pde representing the balance of forces, represent the three governing pdes for chemo-mechanically-coupled problems. These equations are amenable to finite-element solution methods which employ standard C^0-continuous finite-element basis functions.

We have numerically implemented our theory by writing a user-element subroutine for the widely-used finite-element program Abaqus/Standard. We use this numerically implemented theory to first study the diffusion-only problem of spinodal decomposition in the absence of any mechanical deformation. Next, we use our fully-coupled theory and numerical-implementation to study the combined effects of diffusion and stress on the lithiation of a representative isotropic spheroidal-shaped particle of a phase-separating electrode material.

Importantly, we demonstrate that the elastic stiffness of the material can have a significant impact on the morphology of the phase front which forms inside the particle during lithiation. Specifically, we showed that increasing the elastic stiffness can change the distribution of Li from a "core-shell" type distribution, to a "planar-front" distribution. This change in Li distribution has important consequences in determining potential fracture sites, since the "planar-front" type of distribution predicts a tensile maximum principle stress on the exterior surface of the particle during lithiation, while the "core-shell" structure always predicts compressive stresses on the exterior surface during lithiation.

- Di Leo, C.V. Rejovitzky, E. Anand, L., 2014. A Cahn-Hilliard-type phase-field theory for species diffusion coupled with large elastic deformations: Application to phase-segragating Li-ion electrode materials. *Journal of the Mechanics and Physics of Solids* 70, 1-29.

1.2.2 Modeling amorphous Silicon electrodes

We have formulated a fully-coupled diffusion-deformation theory, which accounts for transient diffusion of lithium and accompanying large elastic-plastic deformations. We have numerically implemented our theory by writing a user-element subroutine for the widely-used finite-element program Abaqus/Standard. The material parameters in the theory have been calibrated to experiments of galvanostatic cycling of a half-cell composed of an a-Si thin-film anode deposited on a quartz substrate, which have been reported in the literature. We show that our calibrated theory satisfactorily reproduces the mechanical response of such an anode — as measured by the changes in curvature of the substrate, as well as the electrochemical response — as measured by the voltage versus state-of-charge (SOC) response.

We have applied our numerical simulation capability to model galvanostatic charging of hollow a-Si nanotubes whose exterior walls have been oxidized to prevent outward expansion; such anodes have been recently experimentally-realized in the literature. We show that the results from our numerical simulations are in good agreement with the the experimentally-measured voltage versus SOC behavior at various charging rates (C-rates).

Through our simulations, we have identified, and quantified, two major effects of plasticity on the electrochemical performance of a-Si anodes:

- First, for a given voltage cut-off, plasticity enables lithiation of the anode to a higher SOC. This is because plastic flow reduces the stresses generated in the material, and thus reduces the potential required to lithiate the material.

- Second, plastic deformation accounts for a significant percentage of the energy dissipated during the cycling of the anode at low C-rates.

Hence, plasticity can have either (a) a beneficial effect, that is, a higher SOC for a given voltage cut-off; or (b) a detrimental effect, that is significant energy dissipation at low C-rates.

- Di Leo, C.V. Rejovitzky, E., Anand L., 2015. Diffusion-deformation theory for amorphous silicon anodes: the role of plastic deformation on electrochemical performance. *International Journal of Solids and Structures.* In Press.

1.2.3 Modeling growth of a solid electrolyte interphase

We have formulated a continuum theory for the growth of an SEI layer — a theory which accounts for the generation of the attendant growth stresses. The theory has been numerically implemented in a finite-element program. This simulation capability for SEI growth is coupled with our previously published chemo-mechanical simulation capability for intercalation of Li in electrode particles. We have calibrated the material parameters in our theory by simulating SEI growth on graphite anodes which have been deposited on a stiff substrate. We show that our simulation tool — with suitable choices for the material parameters — can reproduce the experimentally measured substrate curvature versus state-of-charge, including reproducing the "irreversible" stresses due to SEI growth

The evolution of the stress state within the SEI layer and at the SEI/anode-particle interface for spherical- and spheroidal-shaped graphite particles is studied. This knowledge of the local interfacial stresses provides a good estimate for the propensity of potential delamination of an SEI layer from an anode particle.

- Rejovitzky, E., Di Leo, C.V., Anand, L., 2014. A theory and simulation capability for growth of a solid electrolyte interphase layer at an anode particle in a Li-ion battery. *Journal of the Mechanics and Physics of Solids* 78, 210—230.

Part I

Modeling phase-separating electrode materials

Chapter 2

Introduction

Several Li intercalation compounds of interest in battery applications exhibit phase-separation (cf., e.g., Bruce et al., 2008; Tang et al., 2010), and central to the study of coupled diffusion-deformation problems in such electrode materials is the Cahn-Hilliard phase-field theory (Cahn and Hilliard, 1958, 1959; Cahn, 1961). As background, first consider the classical Cahn-Hilliard theory for species diffusion and phase segregation which is *uncoupled* from the mechanical problem. Let $\bar{c} \in [0, 1]$ denote a normalized species concentration, $\hat{\psi}_{\mathrm{R}}(\bar{c}, \nabla\bar{c})$ the free energy per unit reference volume, and let the functional

$$\Psi(\bar{c}) = \int_{\mathrm{B}} \hat{\psi}_{\mathrm{R}}(\bar{c}, \nabla\bar{c})\, dv_{\mathrm{R}} \tag{2.1}$$

denote the total free energy of the region of space occupied by the body B. Then classically, for theories in which the free energy depends on $\nabla\bar{c}$, the chemical potential μ is defined as the *variational derivative* of the functional $\Psi(\bar{c})$:

$$\mu \stackrel{\text{def}}{=} \frac{\delta\Psi}{\delta\bar{c}} = \frac{\partial\hat{\psi}_{\mathrm{R}}(\bar{c}, \nabla\bar{c})}{\partial\bar{c}} - \mathrm{Div}\left(\frac{\partial\hat{\psi}_{\mathrm{R}}(\bar{c}, \nabla\bar{c})}{\partial\nabla\bar{c}}\right). \tag{2.2}$$

A widely-used specific form for the free energy is the following separable energy first proposed by Cahn and Hilliard

$$\hat{\psi}_{\mathrm{R}}(\bar{c}, \nabla\bar{c}) = \hat{\psi}^{c}_{\mathrm{R}}(\bar{c}) + \tfrac{1}{2}\lambda_{\mathrm{CH}}|\nabla\bar{c}|^2, \quad \lambda_{\mathrm{CH}} > 0. \tag{2.3}$$

Here, $\hat{\psi}^{c}_{\mathrm{R}}(\bar{c})$ represents the *coarse-grain* chemical free energy, a double-well potential whose wells (the "binodal points") define the phases; the second term which depends on the concentration gradient represents an *interfacial energy*, with λ_{CH} a gradient energy coefficient with units of energy per unit volume times a length squared. For the free energy (2.3), the

chemical potential, using (2.2), is

$$\mu = \frac{d\hat{\psi}_{\mathrm{R}}^{c}(\bar{c})}{d\bar{c}} - \lambda_{\mathrm{CH}}\Delta\bar{c}\,, \tag{2.4}$$

where Δ is the Laplace operator. Next, species balance requires that

$$\dot{\bar{c}} = -\mathrm{Div}\mathbf{j}_{\mathrm{R}}, \tag{2.5}$$

with the species flux $\mathbf{j}_{\mathrm{R}}$ related to the chemical potential μ through the constitutive equation

$$\mathbf{j}_{\mathrm{R}} = -\hat{m}(\bar{c})\nabla\mu, \tag{2.6}$$

where $\hat{m}(\bar{c})$, the species mobility, is a nonlinear and positive function. Using (2.4) and (2.6) in (2.5) yields the classical Cahn-Hilliard diffusion equation,

$$\dot{\bar{c}} = \mathrm{Div}\left(\hat{m}(\bar{c})\nabla\left(\frac{d\hat{\psi}_{\mathrm{R}}^{c}(\bar{c})}{d\bar{c}} - \lambda_{\mathrm{CH}}\Delta\bar{c}\right)\right). \tag{2.7}$$

Two mechanisms dominate the evolution of a solution to the Cahn-Hilliard equation: a minimization of the chemical energy $\hat{\psi}_{\mathrm{R}}^{c}(\bar{c})$ drives the solution to binodal points and separates the phases, while minimization of the interface energy $(1/2)\lambda_{\mathrm{CH}}|\nabla\bar{c}|^2$ effectively coarsens the phases.

The Cahn-Hilliard equation (2.7) involves fourth-order spatial derivatives of the concentration $\bar{c}$. For recent reviews and discussions of numerical solution techniques for the Cahn-Hilliard equation, cf., e.g., Wells et al. (2006), Kuhl and Schmidt (2007), and Gomez et al. (2008). As noted by Gomez et al. (2008), traditional numerical methods for dealing with higher-order operators *on very simple geometries* include finite differences and spectral approximations. However, for practical engineering applications, simple geometries are not very relevant, and more geometrically flexible techniques such as the finite-element method — which might allow for arbitrary two- and three-dimensional geometries — need to be utilized.

In the context of the finite element method, the fourth order equation (2.7) typically requires basis functions that are piecewise smooth and globally $\mathcal{C}^1$-continuous, but there are only a very limited number of two-dimensional finite elements possessing $\mathcal{C}^1$-continuity applicable to complex geometries, and none in three-dimensions. Instead of using $\mathcal{C}^1$-continuous functions, the most common manner to solve this equation using finite elements, has been with split-methods (also known as mixed-methods) which in addition to the primal variable $\bar{c}$, introduce an extra degree of freedom (cf., e.g., Wodo and Ganapathysubramanian, 2011). We discuss next one such method proposed by Ubachs et al. (2004).[1]

[1]Gomez et al. (2008) have developed a new numerical analysis technique for the Cahn-Hilliard diffusion problem based on an *isogeometric analysis*. In this thesis we do not discuss the isogeometric analysis proce-

In contrast to the standard derivation of the Cahn-Hilliard equation discussed above, Ubachs et al. (2004) introduced another variable $\bar{\mathfrak{c}}$, which they call a *nonlocal species concentration*, and took as the governing partial differential equation for their diffusion problem, the equation

$$\dot{\bar{c}} = \text{Div}\,(\hat{m}(\bar{c})\nabla\mu)\,, \quad \text{with} \quad \mu = \frac{d\hat{\psi}^c_{\text{R}}(\bar{c})}{d\bar{c}} + \beta(\bar{c} - \bar{\mathfrak{c}}), \qquad \beta > 0, \tag{2.8}$$

where the *nonlocal field* $\bar{\mathfrak{c}}$ is evaluated by solving another Helmholtz-type partial differential equation,

$$\bar{\mathfrak{c}} - \ell^2\Delta\bar{\mathfrak{c}} = \bar{c}, \qquad \ell > 0, \tag{2.9}$$

in which ℓ is a parameter with units of length. Note that using (2.9) we may eliminate the factor $(\bar{c} - \bar{\mathfrak{c}})$ in $(2.8)_2$ to obtain

$$\mu = \frac{d\psi^c_{\text{R}}(\bar{c})}{d\bar{c}} - \lambda\Delta\bar{\mathfrak{c}}, \quad \text{with} \quad \lambda = \beta\,\ell^2 > 0. \tag{2.10}$$

This expression for the chemical potential is similar to the Cahn-Hilliard relation (2.4), except that in (2.10) one has the Laplacian of the nonlocal field $\Delta\bar{\mathfrak{c}}$ and two parameters β and ℓ, instead of the Laplacian of the local field $\Delta\bar{c}$ and a single parameter λ_{CH}.

Equations (2.8) and (2.9), being partial differential equations, require boundary conditions. The boundary conditions for (2.8) are standard. For (2.9) Ubachs et al. (2004) introduced boundary conditions on either the value of $\bar{\mathfrak{c}}$ or its normal derivative. In their calculations they used a homogeneous Neumann-type boundary condition of the form

$$(\nabla\bar{\mathfrak{c}}) \cdot \mathbf{n}_{\text{R}} = 0 \text{ on the external boundary } \partial\text{B of the body,}$$

where $\mathbf{n}_{\text{R}}$ denotes the outward unit normal to the external boundary ∂B of the body B. *The resulting problem then consists of two coupled second-order partial differential equations* (2.8) *and* (2.9)*, which are solved using finite element methods which employ standard* C^0*-continuous finite element basis functions.*

Such a theory, which uses a nonstandard variable $\bar{\mathfrak{c}}$ in order to introduce nonlocal effects, has met with substantial operational success when modeling microstructure evolution in two-phase alloys.(cf., e.g., Ubachs et al., 2004). However, from a physical point of view the "derivation" of the important partial differential equation (2.9) for the variable $\bar{\mathfrak{c}}$ in Ubachs et al. (2004) is not entirely satisfactory.

- In particular, it is not clear whether (2.9) is a balance law, a constitutive equation, or a combination of the two. Also, it is not clear how to arrive at such an equation based on classical thermodynamic arguments.

dure, but restrict our attention to the widely-used finite-element solution methods which employ standard C^0-continuous finite-element basis functions.

On the other hand — following the formulation of micromorphic theories of continua[2] — if from the outset one introduces $\bar{c}$ as an additional kinematical variable in the theory, then it is possible to develop a thermodynamically consistent theory in a systematic fashion using the principle of virtual power, in which the important relation (2.9) represents a *microforce balance* supplemented by thermodynamically consistent constitutive equations.

Remark.

It is also possible to split the fourth-order Cahn-Hilliard equation without introducing the additional kinematical variable $\bar{c}$. In this case, the first second-order partial differential equation is still given by conservation of mass through

$$\dot{c} = \mathrm{Div}(\hat{m}(\bar{c})\nabla\mu), \tag{2.11}$$

and the second second-order partial differential is simply the equation for the chemical potential (2.4), viz.

$$\mu = \frac{d\hat{\psi}^{c}_{\mathrm{R}}(\bar{c})}{d\bar{c}} - \lambda_{\mathrm{CH}}\Delta\bar{c}. \tag{2.12}$$

Using the principle of virtual power, (2.12) may also be shown to represent a microforce balance supplemented by thermodynamically consistent constitutive equations.

These two distinct ways of deriving the Cahn-Hilliard equation using the principle of virtual power, and subsequently computing using standard finite element procedures, are studied extensively in Appendix B, where for simplicity and clarity *we neglect the mechanical deformation effects* and consider only the diffusion problem as governed by the Cahn-Hilliard equation.

The study in Appendix B also serves to determine how accurate numerical solutions to the Cahn-Hilliard equation using the nonlocal field $\bar{c}$, as governed by (2.8) and (2.9), are when compared to numerical solutions using the split method as governed by (2.11) and (2.12). □

This part of the thesis is organized as follows. In Chapter 3 we develop a thermodynamically consistent framework for coupling a Cahn-Hilliard-type phase-field theory for species diffusion with large elastic deformation. First, in Sections 3.1 through 3.8 we develop a reasonably general framework which is summarized in Section 3.9. In Section 3.10 we specialize our general framework and in Section 3.11 we summarize the governing partial differential equations and boundary conditions for our theory. Finally, in Section 3.12 we briefly discuss the numerical implementation of our theory. The theory was numerically implemented by writing a user-element subroutine for the commercial finite element program Abaqus (2010).

In Chapter 4, using our numerical capability, we study the diffusion-only problem of spinodal decomposition with the aim of determining an appropriate value for the modulus β in (2.9) for the split-method used in this work. This is also studied in detail in Appendix B.

[2]Cf., e.g., Forest (2009) and Anand et al. (2011) for recent discussions in the context of other gradient theories.

Finally, in Chapter 5, we use our fully-coupled theory and numerical implementation to study the combined effects of diffusion and stress on the lithiation of a representative spheroidal-shaped particle of a phase-separating electrode material. We finish in Chapter 6 with some concluding remarks.

Chapter 3

A Cahn-Hilliard-type phase-field theory for species diffusion coupled with large elastic deformations.

In the development of the theory in this Chapter — for clarity of the physical units of the various quantities introduced — we find it useful to formulate our theory in terms of the actual species concentration c_{R}, given in terms of moles per unit reference volume, rather than in terms of a normalized species concentration $\bar{c} \in [0, 1]$ used thus far in the introductory Chapter 2. Also, we employ a variable $\mathfrak{c}_{\mathrm{R}}$ with units of moles per unit reference volume, and its gradient $\nabla \mathfrak{c}_{\mathrm{R}}$ — with the latter being chosen to represent a measure of the inhomogeneity of the microscale species concentration. For want of a better terminology, we call $\mathfrak{c}_{\mathrm{R}}$ the "micromorphic concentration."

In this Chapter, limiting our consideration to **isothermal** conditions, we develop a reasonably general theory. An extension of this theory for *anisothermal* conditions is fairly straightforward, an example of which can be found in our previous work Di Leo (2012) and Di Leo and Anand (2013) where the theory is derived in the context of hydrogen diffusion in metals.[1]

Notation: We use standard notation of modern continuum mechanics (Gurtin et al., 2010). Specifically: ∇ and Div denote the gradient and divergence with respect to the material point $\mathbf{X}$ in the reference configuration, and $\Delta = \mathrm{Div}\nabla$ denotes the referential Laplace operator; grad div, and div grad denote these operators with respect to the point $\mathbf{x} = \boldsymbol{\chi}(\mathbf{X}, t)$ in the deformed body; a superposed dot denotes the material time-derivative. Throughout, we write $\mathbf{F}^{e-1} = (\mathbf{F}^e)^{-1}$, $\mathbf{F}^{e-\mathsf{T}} = (\mathbf{F}^e)^{-\mathsf{T}}$, etc. We write $\mathrm{tr}\,\mathbf{A}$, $\mathrm{sym}\,\mathbf{A}$, $\mathrm{skw}\,\mathbf{A}$, $\mathbf{A}_0$,

[1] Our previous work Di Leo (2012), also uses a non-local variable, similar to $\bar{\mathfrak{c}}$, however related to the equivalent plastic strain, rather than to the concentration. There the non-local variable is used to formulate a gradient plasticity theory for sole purpose of numerical regularization of shear bands.

and $\mathrm{sym}_0\mathbf{A}$ respectively, for the trace, symmetric, skew, deviatoric, and symmetric-deviatoric parts of a tensor $\mathbf{A}$. Also, the inner product of tensors $\mathbf{A}$ and $\mathbf{B}$ is denoted by $\mathbf{A}:\mathbf{B}$, and the magnitude of $\mathbf{A}$ by $|\mathbf{A}| = \sqrt{\mathbf{A}:\mathbf{A}}$.

3.1 Balance law for the diffusing species

Let $c_{\mathrm{R}}(\mathbf{X}, t)$ denote the total number of moles of the species *per unit reference volume.* Changes in c_{R} in a part P are brought about by the diffusion of the species across its boundary ∂P. The diffusion is characterized by a flux $\mathbf{j}_{\mathrm{R}}(\mathbf{X}, t)$, measured in number of moles per unit area per unit time, so that

$$-\int_{\partial \mathrm{P}} \mathbf{j}_{\mathrm{R}} \cdot \mathbf{n}_{\mathrm{R}}\, da_{\mathrm{R}}$$

represents the amount of species entering P across ∂P per unit time. Thus the rate of change of the species in P is given by

$$\dot{\int_{\mathrm{P}} c_{\mathrm{R}}\, dv_{\mathrm{R}}} = -\int_{\partial \mathrm{P}} \mathbf{j}_{\mathrm{R}} \cdot \mathbf{n}_{\mathrm{R}}\, da_{\mathrm{R}} \tag{3.1}$$

for every part P. Bringing the time derivative in (3.1) inside the integral and using the divergence theorem on the integral over ∂P, we find that

$$\int_{\mathrm{P}} \left(\dot{c}_{\mathrm{R}} + \mathrm{Div}\mathbf{j}_{\mathrm{R}}\right) dv_{\mathrm{R}} = 0. \tag{3.2}$$

Finally, since P is arbitrary, this leads to the following local balance law for c_{R},

$$\dot{c}_{\mathrm{R}} = -\mathrm{Div}\mathbf{j}_{\mathrm{R}}. \tag{3.3}$$

3.2 Basic kinematics

Consider a macroscopically-homogeneous body B with the region of space it occupies in a fixed reference configuration, and denote by $\mathbf{X}$ an arbitrary material point of B. We denote by P an arbitrary part (subbody) of the reference body B with $\mathbf{n}_{\mathrm{R}}$ the outward unit normal on the boundary ∂P of P.

A motion of B is a smooth one-to-one mapping $\mathbf{x} = \boldsymbol{\chi}(\mathbf{X}, t)$ with deformation gradient, velocity, and velocity gradient given by

$$\mathbf{F} = \nabla\boldsymbol{\chi}, \qquad \mathbf{v} = \dot{\boldsymbol{\chi}}, \qquad \mathbf{L} = \mathrm{grad}\,\mathbf{v} = \dot{\mathbf{F}}\mathbf{F}^{-1}. \tag{3.4}$$

We base the theory on a multiplicative decomposition of the deformation gradient

$$\mathbf{F} = \mathbf{F}^e\mathbf{F}^c. \tag{3.5}$$

Here, suppressing the argument t:

(i) $\mathbf{F}^c(\mathbf{X})$ represents the local distortion of the material neighborhood of $\mathbf{X}$ due to the insertion (extraction) of the chemical species; and

(ii) $\mathbf{F}^e(\mathbf{X})$ represents the subsequent stretching and rotation of this coherent chemically distorted material neighborhood, and thereby represents a corresponding elastic distortion.

We refer to $\mathbf{F}^c$ and $\mathbf{F}^e$ as the *chemical and elastic distortions*, respectively. We write

$$J \stackrel{\text{def}}{=} \det \mathbf{F} > 0, \tag{3.6}$$

and hence, using (3.5),

$$J = J^eJ^c, \qquad \text{where} \qquad J^e \stackrel{\text{def}}{=} \det \mathbf{F}^e > 0 \qquad \text{and} \qquad J^c \stackrel{\text{def}}{=} \det \mathbf{F}^c > 0, \tag{3.7}$$

so that $\mathbf{F}^e$ and $\mathbf{F}^c$ are invertible.

The right and left polar decompositions of $\mathbf{F}^e$ are given by

$$\mathbf{F}^e = \mathbf{R}^e\mathbf{U}^e = \mathbf{V}^e\mathbf{R}^e, \tag{3.8}$$

where $\mathbf{R}^e$ is a rotation, while $\mathbf{U}^e$ and $\mathbf{V}^e$ are symmetric, positive-definite right and left stretch tensors with

$$\mathbf{U}^e = \sqrt{\mathbf{F}^{e\mathsf{T}}\mathbf{F}^e} \qquad \text{and} \qquad \mathbf{V}^e = \sqrt{\mathbf{F}^e\mathbf{F}^{e\mathsf{T}}}. \tag{3.9}$$

Also, the right elastic Cauchy-Green deformation tensor is given by

$$\mathbf{C}^e = \mathbf{U}^{e2} = \mathbf{F}^{e\mathsf{T}}\mathbf{F}^e. \tag{3.10}$$

Next, by $(3.4)_3$ and (3.5)

$$\mathbf{L} = \mathbf{L}^e + \mathbf{F}^e\mathbf{L}^c\mathbf{F}^{e-1}, \tag{3.11}$$

with

$$\mathbf{L}^e = \dot{\mathbf{F}}^e\mathbf{F}^{e-1}, \qquad \mathbf{L}^c = \dot{\mathbf{F}}^c\mathbf{F}^{c-1}, \tag{3.12}$$

where $\mathbf{L}^c$ represents a distortion rate due to insertion (extraction) of the chemical species. We assume that $\mathbf{L}^c$ is given by

$$\mathbf{L}^c = \dot{c}_{\mathrm{R}}\,\mathbb{A}, \qquad \text{with} \qquad \mathbb{A} = \hat{\mathbb{A}}(c_{\mathrm{R}}). \tag{3.13}$$

Finally, using (3.4), (3.12), and (3.13), we may write (3.11), for future use, as

$$(\nabla\dot{\boldsymbol{\chi}})\mathbf{F}^{-1} = \dot{\mathbf{F}}^e\mathbf{F}^{e-1} + \dot{c}_{\mathrm{R}}\big(\mathbf{F}^e\mathbb{A}\mathbf{F}^{e-1}\big). \tag{3.14}$$

3.3 An additional variable $\mathfrak{c}_{\mathrm{R}}$

Next, we introduce another scalar $\mathfrak{c}_{\mathrm{R}}$, which we refer to as the "micromorphic concentration", measured in moles per unit volume.

- *The variable $\mathfrak{c}_R$ serves as an additional kinematical degree of freedom in developing a gradient theory for species diffusion. Specifically, in contrast to the traditional Cahn-Hilliard theory which is based on c_R and ∇c_R, here we develop a theory which depends on c_R, $\mathfrak{c}_R$, and the gradient $\nabla\mathfrak{c}_R$.*

3.4 Macroscopic and microscopic force balances derived via the principle of virtual power

Following Germain (1973) and Gurtin (2002), we formulate the macroscopic and microscopic force balances of the theory based on a nonstandard version of the principle of virtual power.

Consider an arbitrary part P of the body B. The virtual-power principle is based on a fundamental *power balance* between the *internal power* $\mathcal{W}_{\mathrm{int}}(\mathrm{P})$ expended **within** P, and the *external power* $\mathcal{W}_{\mathrm{ext}}(\mathrm{P})$ expended **on** P. Specifically, we allow for power expended *internally* by

(a) a stress $\mathbf{S}^e$ power-conjugate to $\dot{\mathbf{F}}^e$;

(b) a scalar microscopic force π power-conjugate to $\dot{c}_{\mathrm{R}}$;

(c) a scalar microscopic force $\mathfrak{p}$ power-conjugate to $\dot{\mathfrak{c}}_{\mathrm{R}}$;

(d) a vector microscopic force $\boldsymbol{\xi}$ power-conjugate to the gradient $\nabla\dot{\mathfrak{c}}_{\mathrm{R}}$;

and take $\mathcal{W}_{\mathrm{int}}(\mathrm{P})$ to be given by

$$\mathcal{W}_{\mathrm{int}}(\mathrm{P}) = \int_{\mathrm{P}} \Big(\mathbf{S}^e : \dot{\mathbf{F}}^e + \pi\,\dot{c}_{\mathrm{R}} + \mathfrak{p}\,\dot{\mathfrak{c}}_{\mathrm{R}} + \boldsymbol{\xi}\cdot\nabla\dot{\mathfrak{c}}_{\mathrm{R}}\Big)\,dv_{\mathrm{R}}, \tag{3.15}$$

where, $\mathbf{S}^e$, π, $\mathfrak{p}$ and $\boldsymbol{\xi}$ are defined over the body for all time. We also allow for power to be expended *externally* by

(a) a traction $\mathbf{t}_{\mathrm{R}}(\mathbf{n}_{\mathrm{R}})$ (for each unit vector $\mathbf{n}_{\mathrm{R}}$) that expends power over $\dot{\boldsymbol{\chi}}$ on the boundary of the part;

(b) a body-force $\mathbf{b}_{\mathrm{R}}$ that also expends power over $\dot{\chi}$; [2] and

(c) a scalar microscopic traction $\zeta(\mathbf{n}_{\mathrm{R}})$ (for each unit vector $\mathbf{n}_{\mathrm{R}}$) that expends power over $\dot{\mathfrak{c}}_{\mathrm{R}}$ on the boundary of the part;

and take $\mathcal{W}_{\mathrm{ext}}(\mathrm{P})$ to be given by

$$\mathcal{W}_{\mathrm{ext}}(\mathrm{P}) = \int_{\partial \mathrm{P}} \mathbf{t}_{\mathrm{R}}(\mathbf{n}_{\mathrm{R}}) \cdot \dot{\chi}\, da_{\mathrm{R}} + \int_{\mathrm{P}} \mathbf{b}_{\mathrm{R}} \cdot \dot{\chi}\, dv_{\mathrm{R}} + \int_{\partial \mathrm{P}} \zeta(\mathbf{n}_{\mathrm{R}})\, \dot{\mathfrak{c}}_{\mathrm{R}}\, da_{\mathrm{R}}. \tag{3.16}$$

The balance equations and traction conditions of the theory — presumed not known in advance — are derived using the *principle of virtual power*. Assume that, at some arbitrarily-chosen but *fixed time*, the fields χ, $\mathbf{F}$, $\mathbf{F}^e$, $\mathbf{F}^c$, $\mathbb{A}$, c_{R}, and $\mathfrak{c}_{\mathrm{R}}$ are known, and consider the fields $\dot{\chi}$, $\dot{\mathbf{F}}^e$, and $\dot{c}_{\mathrm{R}}$ as virtual velocities to be specified independently in a manner consistent with (3.14); that is, denoting the virtual fields by $\tilde{\chi}$, $\tilde{\mathbf{F}}^e$, and $\tilde{c}_{\mathrm{R}}$ to differentiate them from fields associated with the actual evolution of the body, we require that

$$(\nabla \tilde{\chi})\mathbf{F}^{-1} = \tilde{\mathbf{F}}^e \mathbf{F}^{e-1} + \tilde{c}_{\mathrm{R}}\big(\mathbf{F}^e \mathbb{A} \mathbf{F}^{e-1}\big). \tag{3.17}$$

Further, also considering $\dot{\mathfrak{c}}_{\mathrm{R}}$ to be a virtual velocity, and denoting the virtual counterpart of $\dot{\mathfrak{c}}_{\mathrm{R}}$ by $\tilde{\mathfrak{c}}_{\mathrm{R}}$, we define a generalized virtual velocity to be a list

$$\mathcal{V} = (\tilde{\chi}, \tilde{\mathbf{F}}^e, \tilde{c}_{\mathrm{R}}, \tilde{\mathfrak{c}}_{\mathrm{R}})$$

consistent with (3.17).

In the statement of the principle of virtual power (to be delineated below), we need the notion of *a macroscopic rigid generalized virtual velocity* $\mathcal{V}$. Recall that if the macroscopic motion of a body is rigid, then

$$\dot{\mathbf{F}} = \mathbf{\Omega}\mathbf{F}, \tag{3.18}$$

where at any time t, $\mathbf{\Omega}$ is a spatially-constant skew tensor. Accordingly, we presume that each fixed time t, for *a macroscopic rigid virtual velocity* $\mathcal{V}$, the corresponding virtual $\tilde{\mathbf{F}}$ obeys

$$\tilde{\mathbf{F}} = \mathbf{\Omega}\mathbf{F}, \tag{3.19}$$

with $\mathbf{\Omega}$ a constant skew tensor on B, *together with*

$$\tilde{c}_{\mathrm{R}} = 0 \quad \Rightarrow \quad \tilde{\mathbf{F}}^c = \mathbf{0}, \quad \text{and} \quad \tilde{\mathfrak{c}}_{\mathrm{R}} = 0, \tag{3.20}$$

so that

$$\tilde{\mathbf{F}}^e = \tilde{\mathbf{F}}\mathbf{F}^{c-1}. \tag{3.21}$$

Hence, using (3.19) we have

$$\tilde{\mathbf{F}}^e = \mathbf{\Omega}\mathbf{F}^e. \tag{3.22}$$

[2] Since time scales associated with species diffusion are usually considerably longer than those associated with wave propagation, we *neglect* all inertial effects.

Accordingly, we refer to a macroscopic virtual field $\mathcal{V}$ as *rigid* if it satisfies

$$(\nabla\tilde{\boldsymbol{\chi}}) = \tilde{\mathbf{F}} = \boldsymbol{\Omega}\mathbf{F}, \tag{3.23}$$

with $\boldsymbol{\Omega}$ a spatially constant skew tensor, together with

$$\tilde{\mathbf{F}}^e = \boldsymbol{\Omega}\mathbf{F}^e, \qquad \tilde{c}_{\mathrm{R}} = 0, \qquad \text{and} \qquad \tilde{\mathfrak{c}}_{\mathrm{R}} = 0. \tag{3.24}$$

Then, writing

$$\left.\begin{aligned} \mathcal{W}_{\mathrm{ext}}(\mathrm{P},\mathcal{V}) &= \int_{\partial\mathrm{P}} \mathbf{t}_{\mathrm{R}}(\mathbf{n}_{\mathrm{R}})\cdot\tilde{\boldsymbol{\chi}}\,da_{\mathrm{R}} + \int_{\mathrm{P}} \mathbf{b}_{\mathrm{R}}\cdot\tilde{\boldsymbol{\chi}}\,dv_{\mathrm{R}} + \int_{\partial\mathrm{P}} \zeta(\mathbf{n}_{\mathrm{R}})\,\tilde{\mathfrak{c}}_{\mathrm{R}}\,da_{\mathrm{R}},\\ \mathcal{W}_{\mathrm{int}}(\mathrm{P},\mathcal{V}) &= \int_{\mathrm{P}} \Big(\mathbf{S}^e : \tilde{\mathbf{F}}^e + \pi\tilde{c}_{\mathrm{R}} + \mathfrak{p}\,\tilde{\mathfrak{c}}_{\mathrm{R}} + \boldsymbol{\xi}\cdot\nabla\tilde{\mathfrak{c}}_{\mathrm{R}}\Big)\,dv_{\mathrm{R}}, \end{aligned}\right\} \tag{3.25}$$

respectively, for the external and internal expenditures of virtual power, the *principle of virtual power* consists of two basic requirements:

(V1) Given any part P,

$$\mathcal{W}_{\mathrm{ext}}(\mathrm{P},\mathcal{V}) = \mathcal{W}_{\mathrm{int}}(\mathrm{P},\mathcal{V}) \quad \text{for all generalized virtual velocities } \mathcal{V}. \tag{3.26}$$

(V2) Given any part P and a *rigid* virtual velocity $\mathcal{V}$,

$$\mathcal{W}_{\mathrm{int}}(\mathrm{P},\mathcal{V}) = 0 \ \text{ whenever } \mathcal{V} \text{ is a rigid macroscopic virtual velocity.} \tag{3.27}$$

To deduce the consequences of the principle of virtual power, assume that (3.26) and (3.27) are satisfied. Note that in applying the virtual balance we are at liberty to choose any $\mathcal{V}$ consistent with the constraint (3.17).

3.4.1 Macroscopic force and moment balances

Let $\tilde{c}_{\mathrm{R}} = 0$ and $\tilde{\mathfrak{c}}_{\mathrm{R}} = 0$, so that $(\nabla\tilde{\boldsymbol{\chi}})(\mathbf{F}^c)^{-1} = \tilde{\mathbf{F}}^e$. For this choice of $\mathcal{V}$, (3.26) yields

$$\int_{\partial\mathrm{P}} \mathbf{t}_{\mathrm{R}}(\mathbf{n}_{\mathrm{R}})\cdot\tilde{\boldsymbol{\chi}}\,da_{\mathrm{R}} + \int_{\mathrm{P}} \mathbf{b}_{\mathrm{R}}\cdot\tilde{\boldsymbol{\chi}}\,dv_{\mathrm{R}} = \int_{\mathrm{P}} \mathbf{S}^e : \tilde{\mathbf{F}}^e\,dv_{\mathrm{R}} = \int_{\mathrm{P}} (\mathbf{S}^e\mathbf{F}^{c-\mathsf{T}}) : \nabla\tilde{\boldsymbol{\chi}}\,dv_{\mathrm{R}}, \tag{3.28}$$

which, by defining

$$\mathbf{T}_{\mathrm{R}} \stackrel{\mathrm{def}}{=} \mathbf{S}^e\mathbf{F}^{c-\mathsf{T}}, \tag{3.29}$$

may be rewritten as

$$\int_{\partial\mathrm{P}} \mathbf{t}_{\mathrm{R}}(\mathbf{n}_{\mathrm{R}})\cdot\tilde{\boldsymbol{\chi}}\,da_{\mathrm{R}} = \int_{\mathrm{P}} \Big(\mathbf{T}_{\mathrm{R}} : \nabla\tilde{\boldsymbol{\chi}} - \mathbf{b}_{\mathrm{R}}\cdot\tilde{\boldsymbol{\chi}}\Big)\,dv_{\mathrm{R}}, \tag{3.30}$$

and using the divergence theorem we may conclude that

$$\int_{\partial \mathrm{P}} (\mathbf{t}_{\mathrm{R}}(\mathbf{n}_{\mathrm{R}}) - \mathbf{T}_{\mathrm{R}}\mathbf{n}_{\mathrm{R}}) \cdot \tilde{\boldsymbol{\chi}}\, da_{\mathrm{R}} + \int_{\mathrm{P}} (\mathrm{Div}\, \mathbf{T}_{\mathrm{R}} + \mathbf{b}_{\mathrm{R}}) \cdot \tilde{\boldsymbol{\chi}}\, dv_{\mathrm{R}} = 0.$$

Since this relation must hold for all P and all $\tilde{\boldsymbol{\chi}}$, standard variational arguments yield the traction condition

$$\mathbf{t}_{\mathrm{R}}(\mathbf{n}_{\mathrm{R}}) = \mathbf{T}_{\mathrm{R}}\mathbf{n}_{\mathrm{R}}\,, \tag{3.31}$$

and the local macroscopic force balance

$$\mathrm{Div}\, \mathbf{T}_{\mathrm{R}} + \mathbf{b}_{\mathrm{R}} = \mathbf{0}, \tag{3.32}$$

respectively.

Next, we deduce the consequences of requirement (V2) of the principle of virtual power. Using (3.24) and $(3.25)_2$, requirement (V2) of the principle of virtual power leads to the requirement that

$$\int_{\mathrm{P}} (\mathbf{S}^e\mathbf{F}^{e\top}) : \boldsymbol{\Omega}\, dv_{\mathrm{R}} = 0. \tag{3.33}$$

Since P is arbitrary, we obtain that $(\mathbf{S}^e\mathbf{F}^{e\top}) : \boldsymbol{\Omega} = 0$ for all skew tensors $\boldsymbol{\Omega}$, which implies that $\mathbf{S}^e\mathbf{F}^{e\top}$ is *symmetric*:

$$\mathbf{S}^e\mathbf{F}^{e\top} = \mathbf{F}^e\mathbf{S}^{e\top}\,. \tag{3.34}$$

Moreover, (3.34) and (3.29) imply that

$$\mathbf{T}_{\mathrm{R}}\mathbf{F}^{\top} = \mathbf{F}\mathbf{T}_{\mathrm{R}}^{\top}. \tag{3.35}$$

- *In view of* (3.32) *and* (3.35) *the stress* $\mathbf{T}_R$ *represents the classical Piola stress, with* (3.32) *and* (3.35) *representing the local macroscopic force and moment balances in the reference body.*

As is standard, the Piola stress $\mathbf{T}_{\mathrm{R}}$ is related to the symmetric Cauchy stress $\mathbf{T}$ in the deformed body by

$$\mathbf{T}_{\mathrm{R}} = J\,\mathbf{T}\,\mathbf{F}^{-\top}, \tag{3.36}$$

so that

$$\mathbf{T} = J^{-1}\mathbf{T}_{\mathrm{R}}\mathbf{F}^{\top}. \tag{3.37}$$

It is convenient to introduce two new stress measures:

- The elastic second Piola stress,

$$\mathbf{T}^e \stackrel{\mathrm{def}}{=} J^e\mathbf{F}^{e-1}\mathbf{T}\mathbf{F}^{e-\top}, \tag{3.38}$$

  which is *symmetric* on account of the symmetry of the Cauchy stress $\mathbf{T}$.

- The Mandel stress,

$$\mathbf{M}^e \stackrel{\text{def}}{=} \mathbf{C}^e\mathbf{T}^e = J^e\mathbf{F}^{e\top}\mathbf{T}\mathbf{F}^{e-\top}. \tag{3.39}$$

  which in general is *not symmetric.*

Using (3.29), (3.36) and (3.5) we find that

$$\mathbf{S}^e = J\mathbf{T}\mathbf{F}^{e-\top}. \tag{3.40}$$

Thus, using the definitions (3.38) and (3.39) we find that

$$\mathbf{F}^{e-1}\mathbf{S}^e = J^c\mathbf{T}^e \quad \text{and} \quad \mathbf{F}^{e\top}\mathbf{S}^e = J^c\mathbf{M}^e. \tag{3.41}$$

3.4.2 Microscopic force balances

To discuss the microscopic counterparts of macroscopic force balance, consider first a generalized virtual velocity with $\tilde{\boldsymbol{\chi}} = \mathbf{0}$ and $\tilde{\mathrm{c}}_{\mathrm{R}} = 0$. Choose the virtual field $\tilde{c}_{\mathrm{R}}$ arbitrarily, and let

$$\tilde{\mathbf{F}}^e = -\tilde{c}_{\mathrm{R}}\,\mathbf{F}^e\mathbb{A}.$$

Then

$$\mathbf{S}^e : \tilde{\mathbf{F}}^e = -\tilde{c}_{\mathrm{R}}\,(\mathbf{F}^{e\top}\mathbf{S}^e) : \mathbb{A} = -\big(J^c\mathbf{M}^e : \mathbb{A}\big)\tilde{c}_{\mathrm{R}}, \tag{3.42}$$

where we have used the relationship $(3.41)_2$. Using (3.42) the power balance (3.27) then yields the first microscopic virtual-power relation

$$0 = \int_{\mathrm{P}} \Big(\pi - \big(J^c\mathbf{M}^e : \mathbb{A}\big)\Big)\,\tilde{c}_{\mathrm{R}}\,dv_{\mathrm{R}} \tag{3.43}$$

to be satisfied for all $\tilde{c}_{\mathrm{R}}$ and all P. This yields the first microscopic force balance

$$\pi = J^c\mathbf{M}^e : \mathbb{A}\,. \tag{3.44}$$

Next, consider a generalized virtual velocity with $\tilde{\boldsymbol{\chi}} = \mathbf{0}$ and $\tilde{c}_{\mathrm{R}} = 0$. Choose the virtual field $\tilde{\mathrm{c}}_{\mathrm{R}}$ arbitrarily, then the power balance (3.26) yields the second microscopic virtual-power relation

$$\int_{\partial\mathrm{P}} \zeta(\mathbf{n}_{\mathrm{R}})\tilde{\mathrm{c}}_{\mathrm{R}}\,da_{\mathrm{R}} = \int_{\mathrm{P}} \Big(\mathrm{p}\,\tilde{\mathrm{c}}_{\mathrm{R}} + \boldsymbol{\xi}\cdot\nabla\tilde{\mathrm{c}}_{\mathrm{R}}\Big)\,dv_{\mathrm{R}} \tag{3.45}$$

to be satisfied for all $\tilde{\mathrm{c}}_{\mathrm{R}}$ and all P. Equivalently, using the divergence theorem,

$$\int_{\partial\mathrm{P}} \big(\zeta(\mathbf{n}) - \boldsymbol{\xi}\cdot\mathbf{n}_{\mathrm{R}}\big)\tilde{\mathrm{c}}_{\mathrm{R}}\,da_{\mathrm{R}} + \int_{\mathrm{P}} \big(\mathrm{Div}\,\boldsymbol{\xi} - \mathrm{p}\big)\tilde{\mathrm{c}}_{\mathrm{R}}\,dv_{\mathrm{R}} = 0,$$

and a standard argument yields the microscopic traction condition

$$\zeta(\mathbf{n}_{\mathrm{R}}) = \boldsymbol{\xi}\cdot\mathbf{n}_{\mathrm{R}} \tag{3.46}$$

and the second microscopic force balance

$$\mathrm{Div}\,\boldsymbol{\xi} - \mathbb{p} = 0. \tag{3.47}$$

The converse assertion — that (3.31), (3.32), (3.44), (3.46) and (3.47) imply the principle of virtual power — follows upon reversing the foregoing arguments.

Finally, using the traction conditions (3.31) and (3.46), the actual external expenditure of power (3.16) may be written as

$$\mathcal{W}_{\mathrm{ext}}(\mathrm{P}) = \int_{\partial\mathrm{P}} (\mathbf{T}_{\mathrm{R}}\mathbf{n}_{\mathrm{R}})\cdot\dot{\boldsymbol{\chi}}\, da_{\mathrm{R}} + \int_{\mathrm{P}} \mathbf{b}_{\mathrm{R}}\cdot\dot{\boldsymbol{\chi}}\, dv_{\mathrm{R}} + \int_{\partial\mathrm{P}} (\boldsymbol{\xi}\cdot\mathbf{n}_{\mathrm{R}})\,\dot{c}_{\mathrm{R}}\, da_{\mathrm{R}}. \tag{3.48}$$

Also, using $(3.41)_1$ and (3.10), the stress power $\mathbf{S}\colon\dot{\mathbf{F}}^e$ may be alternatively written as

$$\mathbf{S}\colon\dot{\mathbf{F}}^e = (J^c\mathbf{T}^e)\colon(\mathbf{F}^{e\mathsf{T}}\dot{\mathbf{F}}^e) = \tfrac{1}{2}(J^c\mathbf{T}^e)\colon\dot{\mathbf{C}}^e. \tag{3.49}$$

Thus, the corresponding internal expenditure of power (3.15) may be written as

$$\mathcal{W}_{\mathrm{int}}(\mathrm{P}) = \int_{\mathrm{P}} \left(\tfrac{1}{2}(J^c\mathbf{T}^e)\colon\dot{\mathbf{C}}^e + \pi\dot{c}_{\mathrm{R}} + \mathbb{p}\dot{c}_{\mathrm{R}} + \boldsymbol{\xi}\cdot\nabla\dot{c}_{\mathrm{R}}\right) dv_{\mathrm{R}}. \tag{3.50}$$

3.5 Free energy imbalance

Let ψ_{R} denote the Helmholtz free-energy per unit reference volume, and consider a material region P. Then, consistent with our omission of inertial effects, we neglect kinetic energy, and take the *free-energy imbalance* under *isothermal conditions* as

$$\dot{\int_{\mathrm{P}} \psi_{\mathrm{R}}\, dv_{\mathrm{R}}} \le \mathcal{W}_{\mathrm{ext}}(\mathrm{P}) - \int_{\partial\mathrm{P}} \mu\mathbf{j}_{\mathrm{R}}\cdot\mathbf{n}_{\mathrm{R}} da_{\mathrm{R}}, \tag{3.51}$$

where μ represents the chemical potential of the diffusing species. Thus, since $\mathcal{W}_{\mathrm{ext}}(\mathrm{P}) = \mathcal{W}_{\mathrm{int}}(\mathrm{P})$, upon recalling (3.50) and applying the divergence theorem to the term in (3.51) involving an integral over the boundary $\partial\mathrm{P}$ of P, we obtain

$$\int_{\mathrm{P}} \left(\dot{\psi}_{\mathrm{R}} - \frac{1}{2}(J^c\mathbf{T}^e)\colon\dot{\mathbf{C}}^e - \pi\dot{c}_{\mathrm{R}} - \mathbb{p}\dot{c}_{\mathrm{R}} - \boldsymbol{\xi}\cdot\nabla\dot{c}_{\mathrm{R}} + \mu\mathrm{Div}\,\mathbf{j}_{\mathrm{R}} + \mathbf{j}_{\mathrm{R}}\cdot\nabla\mu\right) dv_{\mathrm{R}} \le 0, \tag{3.52}$$

which upon use of the balance law (3.3), and using the fact that (3.52) must hold for all parts P, gives the local form of the free energy imbalance as

$$\dot{\psi}_{\mathrm{R}} - \frac{1}{2}(J^c\mathbf{T}^e)\colon\dot{\mathbf{C}}^e - \mu_{\mathrm{net}}\dot{c}_{\mathrm{R}} - \mathbb{p}\dot{\mathbb{c}}_{\mathrm{R}} - \boldsymbol{\xi}\cdot\nabla\dot{\mathbb{c}}_{\mathrm{R}} + \mathbf{j}_{\mathrm{R}}\cdot\nabla\mu \leq 0\,, \tag{3.53}$$

where we have written

$$\mu_{\mathrm{net}} \stackrel{\mathrm{def}}{=} \mu + \pi \tag{3.54}$$

for a *net chemical potential.*

For later use we define the dissipation density $\mathcal{D} \geq 0$ per unit volume per unit time by

$$\mathcal{D} = \frac{1}{2}(J^c\mathbf{T}^e)\colon\dot{\mathbf{C}}^e + \mu_{\mathrm{net}}\dot{c}_{\mathrm{R}} + \mathbb{p}\dot{\mathbb{c}}_{\mathrm{R}} + \boldsymbol{\xi}\cdot\nabla\dot{\mathbb{c}}_{\mathrm{R}} - \mathbf{j}_{\mathrm{R}}\cdot\nabla\mu - \dot{\psi}_{\mathrm{R}} \geq 0. \tag{3.55}$$

Remark. For brevity we have not discussed invariance properties of the various fields appearing in our theory. However, such considerations are straight-forward and extensively elaborated upon in the context of a similar diffusion-deformation theory by Anand (2012). Here, we simply note that all quantities in the free energy imbalance (3.53) and (3.55) are invariant under a change in frame. □

3.6 Constitutive theory

Guided by the free energy imbalance (3.53) we consider constitutive equations for the free energy ψ_{R}, the stress $\mathbf{T}^e$, the net chemical potential μ_{net}, the microstresses $\mathbb{p}$ and $\boldsymbol{\xi}$, and the species flux $\mathbf{j}_{\mathrm{R}}$ of the form:

$$\begin{aligned}
\psi_{\mathrm{R}} &= \check{\psi}_{\mathrm{R}}(\mathbf{C}^e, c_{\mathrm{R}}, \mathbb{c}_{\mathrm{R}}, \nabla\mathbb{c}_{\mathrm{R}}),\\
\mathbf{T}^e &= \check{\mathbf{T}}^e(\mathbf{C}^e, c_{\mathrm{R}}, \mathbb{c}_{\mathrm{R}}, \nabla\mathbb{c}_{\mathrm{R}}),\\
\mu_{\mathrm{net}} &= \check{\mu}_{\mathrm{net}}(\mathbf{C}^e, c_{\mathrm{R}}, \mathbb{c}_{\mathrm{R}}, \nabla\mathbb{c}_{\mathrm{R}}),\\
\mathbb{p} &= \check{\mathbb{p}}(\mathbf{C}^e, c_{\mathrm{R}}, \mathbb{c}_{\mathrm{R}}, \nabla\mathbb{c}_{\mathrm{R}}),\\
\boldsymbol{\xi} &= \check{\boldsymbol{\xi}}(\mathbf{C}^e, c_{\mathrm{R}}, \mathbb{c}_{\mathrm{R}}, \nabla\mathbb{c}_{\mathrm{R}}),\\
\mathbf{j}_{\mathrm{R}} &= \check{\mathbf{j}}_{\mathrm{R}}(\mathbf{C}^e, c_{\mathrm{R}}, \mathbb{c}_{\mathrm{R}}, \nabla\mathbb{c}_{\mathrm{R}}, \nabla\mu).
\end{aligned} \tag{3.56}$$

It is convenient to introduce the notation

$$\boldsymbol{\Lambda} = (\mathbf{C}^e, c_{\mathrm{R}}, \mathbb{c}_{\mathrm{R}}, \nabla\mathbb{c}_{\mathrm{R}}). \tag{3.57}$$

Substituting the constitutive equations (3.56) into the free-energy imbalance (3.53), we find that it may then be written as

$$\begin{aligned}\left[\frac{\partial\check{\psi}_{\mathrm{R}}(\mathbf{\Lambda})}{\partial\mathbf{C}^e}-\frac{1}{2}J^c\mathbf{T}^e\right]:\dot{\mathbf{C}}^e+\left[\frac{\partial\check{\psi}_{\mathrm{R}}(\mathbf{\Lambda})}{\partial c_{\mathrm{R}}}-\mu_{\mathrm{net}}\right]\dot{c}_{\mathrm{R}}+\left[\frac{\partial\check{\psi}_{\mathrm{R}}(\mathbf{\Lambda})}{\partial\mathfrak{c}_{\mathrm{R}}}-\mathbb{p}\right]\dot{\mathfrak{c}}_{\mathrm{R}}\\+\left[\frac{\partial\check{\psi}_{\mathrm{R}}(\mathbf{\Lambda})}{\partial\nabla\mathfrak{c}_{\mathrm{R}}}-\boldsymbol{\xi}\right]\cdot\nabla\dot{\mathfrak{c}}_{\mathrm{R}}+\check{\mathbf{j}}_{\mathrm{R}}(\mathbf{\Lambda},\nabla\mu)\cdot\nabla\mu\leq 0.\end{aligned}\tag{3.58}$$

This inequality is to hold hold for all values of $\mathbf{C}^e$, c_{R}, $\mathfrak{c}_{\mathrm{R}}$, and $\nabla\mathfrak{c}_{\mathrm{R}}$. Since $\dot{\mathbf{C}}^e$, $\dot{c}_{\mathrm{R}}$, $\dot{\mathfrak{c}}_{\mathrm{R}}$, and $\nabla\dot{\mathfrak{c}}_{\mathrm{R}}$ appear linearly, their "coefficients" must vanish, for otherwise $\dot{\mathbf{C}}^e$, $\dot{c}_{\mathrm{R}}$, $\dot{\mathfrak{c}}_{\mathrm{R}}$, and $\nabla\dot{\mathfrak{c}}_{\mathrm{R}}$ may be chosen to violate (3.58). We are therefore led to the thermodynamic restriction that the free energy determines the stress $\mathbf{T}^e$, the chemical potential μ, the scalar microstress $\mathbb{p}$, and the vector microstress $\boldsymbol{\xi}$ through the "state relations"

$$\left.\begin{aligned}\mathbf{T}^e&=J^{c-1}\left(2\frac{\partial\check{\psi}_{\mathrm{R}}(\mathbf{\Lambda})}{\partial\mathbf{C}^e}\right),\\ \mu&=\frac{\partial\check{\psi}_{\mathrm{R}}(\mathbf{\Lambda})}{\partial c_{\mathrm{R}}}-\pi,\\ \mathbb{p}&=\frac{\partial\check{\psi}_{\mathrm{R}}(\mathbf{\Lambda})}{\partial\mathfrak{c}_{\mathrm{R}}},\\ \boldsymbol{\xi}&=\frac{\partial\check{\psi}_{\mathrm{R}}(\mathbf{\Lambda})}{\partial\nabla\mathfrak{c}_{\mathrm{R}}},\end{aligned}\right\}\tag{3.59}$$

and we are left with the following reduced dissipation inequality

$$\mathcal{D}=-\check{\mathbf{j}}_{\mathrm{R}}(\mathbf{\Lambda})\cdot\nabla\mu\geq 0\,.\tag{3.60}$$

Remark. Combining the constitutive equations $(3.59)_2$ for μ with the first microforce balance (3.44), we obtain the following constitutive equation for the chemical potential

$$\mu=\frac{\partial\check{\psi}_{\mathrm{R}}(\mathbf{\Lambda})}{\partial c_{\mathrm{R}}}-J^c\,\mathbf{M}^e:\mathbb{A}\,.\tag{3.61}$$

□

3.7 Species flux

Henceforth we neglect the dependence of $\mathbf{j}_{\mathrm{R}}$ on the microfields $\mathfrak{c}_{\mathrm{R}}$ and $\nabla\mathfrak{c}_{\mathrm{R}}$, and assume that

$$\mathbf{j}_{\mathrm{R}}=-\check{\mathbf{M}}(\mathbf{C}^e,c_{\mathrm{R}})\,\nabla\mu,\tag{3.62}$$

where $\mathbf{M}$ is a *mobility tensor*. Using (3.62) the dissipation inequality (3.60) may be written as

$$\nabla\mu \cdot \check{\mathbf{M}}(\mathbf{C}^e, c_{\mathrm{R}})\nabla\mu \geq 0, \tag{3.63}$$

which is a requirement that the mobility tensor $\mathbf{M}$ be positive-semidefinite.

3.8 Isotropic materials

Next we restrict our attention to *isotropic materials*, an idealization that leads to several simplifications in the constitutive equations.

3.8.1 Isotropic free energy

To begin with, the free energy function $\check{\psi}_{\mathrm{R}}(\mathbf{C}^e, c_{\mathrm{R}}, \mathfrak{c}_{\mathrm{R}}, \nabla\mathfrak{c}_{\mathrm{R}})$ is then an isotropic function of its arguments. An immediate consequence is that the free energy function has the representation[3]

$$\check{\psi}_{\mathrm{R}}(\mathbf{C}^e, c_{\mathrm{R}}, \mathfrak{c}_{\mathrm{R}}, \nabla\mathfrak{c}_{\mathrm{R}}) = \check{\psi}_{\mathrm{R}}(\mathcal{I}_{\mathbf{C}^e}, c_{\mathrm{R}}, \mathfrak{c}_{\mathrm{R}}, |\nabla\mathfrak{c}_{\mathrm{R}}|), \tag{3.64}$$

with

$$\mathcal{I}_{\mathbf{C}^e} = \Big(I_1(\mathbf{C}^e), I_2(\mathbf{C}^e), I_3(\mathbf{C}^e)\Big)$$

the list of principal invariants of $\mathbf{C}^e$. Next, the spectral representation of $\mathbf{C}^e$ is

$$\mathbf{C}^e = \sum_{i=1}^{3} \omega_i^e \mathbf{r}_i^e \otimes \mathbf{r}_i^e, \qquad \text{with} \qquad \omega_i^e = \lambda_i^{e\,2}, \tag{3.65}$$

where $(\mathbf{r}_1^e, \mathbf{r}_2^e, \mathbf{r}_2^e)$ are the orthonormal eigenvectors of $\mathbf{C}^e$ and $\mathbf{U}^e$, and $(\lambda_1^e, \lambda_2^e, \lambda_3^e)$ are the positive eigenvalues of $\mathbf{U}^e$. Let

$$\mathbf{E}^e \stackrel{\text{def}}{=} \ln \mathbf{U}^e = \sum_{i=1}^{3} E_i^e \mathbf{r}_i^e \otimes \mathbf{r}_i^e, \qquad \text{with} \qquad E_i^e \stackrel{\text{def}}{=} \ln \lambda_i^e, \tag{3.66}$$

denote the logarithmic elastic strain. With the logarithmic elastic strain defined by (3.66), for isotropic materials we henceforth consider a free energy of the form

$$\psi_{\mathrm{R}} = \hat{\psi}_{\mathrm{R}}(\mathcal{I}_{\mathbf{E}^e}, c_{\mathrm{R}}, \mathfrak{c}_{\mathrm{R}}, |\nabla\mathfrak{c}_{\mathrm{R}}|), \tag{3.67}$$

with $\mathcal{I}_{\mathbf{E}^e}$ a list of principal invariants of $\mathbf{E}^e$, or equivalently a list of principal values of $\mathbf{E}^e$. Then, straightforward calculations (cf., e.g. Anand and Su, 2005) show that the Mandel

[3] In addition to a dependence of the free energy on the list $(\mathcal{I}_{\mathbf{C}^e}, c_{\mathrm{R}}, \mathfrak{c}_{\mathrm{R}}, |\nabla\mathfrak{c}_{\mathrm{R}}|)$, there is a possible dependence on the joint invariants $(\nabla\mathfrak{c}_{\mathrm{R}})\cdot\mathbf{C}^e(\nabla\mathfrak{c}_{\mathrm{R}})$ and $(\nabla\mathfrak{c}_{\mathrm{R}})\cdot\mathbf{C}^{e2}(\nabla\mathfrak{c}_{\mathrm{R}})$, but for brevity we do not include them here.

stress is *symmetric* and given by

$$\mathbf{M}^e = J^{c-1}\left(\frac{\partial\hat{\psi}_{\mathrm{R}}(\mathcal{I}_{\mathbf{E}^e}, c_{\mathrm{R}}, \mathfrak{C}_{\mathrm{R}}, |\nabla\mathfrak{C}_{\mathrm{R}}|)}{\partial\mathbf{E}^e}\right), \tag{3.68}$$

and the corresponding Cauchy stress is

$$\mathbf{T} = J^{e-1}\mathbf{R}^e\mathbf{M}^e\mathbf{R}^{e\mathsf{T}}. \tag{3.69}$$

3.8.2 Constitutive equation for the chemical distortion rate $\mathbf{L}^c$

Let Ω denote the volume of a mole of the species (partial molar volume), presumed to be constant. Then for isotropic materials we assume that the chemical distortion $\mathbf{F}^c$ is given by

$$\mathbf{F}^c = \left(J^c\right)^{1/3}\mathbf{1}, \qquad \text{with} \qquad J^c = 1 + \Omega c_{\mathrm{R}} > 0, \tag{3.70}$$

such that the total change in volume per unit reference volume when $c_{\mathrm{R}} = c_{\mathrm{R,max}}$, is given by $(\Omega \cdot c_{\mathrm{R,max}})$. Recalling the constraint (3.13), and using (3.70), we have that the chemical distortion is given by

$$\mathbf{L}^c = \dot{\mathbf{F}}^c\mathbf{F}^{c-1} = \dot{c}_{\mathrm{R}}\mathbb{A} = \dot{c}_{\mathrm{R}}\frac{1}{3}J^{c-1}\Omega\,\mathbf{1} \quad \text{and we have} \quad \mathbb{A} = \frac{1}{3}J^{c-1}\Omega\,\mathbf{1}. \tag{3.71}$$

In this case, with $\mathbb{A}$ given by $(3.71)_2$, the expression (3.61) for the chemical potential simplifies to

$$\mu = \frac{\partial\hat{\psi}_{\mathrm{R}}(\mathcal{I}_{\mathbf{E}^e}, c_{\mathrm{R}}, \mathfrak{C}_{\mathrm{R}}, \nabla\mathfrak{C}_{\mathrm{R}})}{\partial c_{\mathrm{R}}} - \Omega\left(\frac{1}{3}\mathrm{tr}\,\mathbf{M}^e\right). \tag{3.72}$$

3.8.3 Isotropic mobility

For isotropic materials the mobility tensor has the representation

$$\check{\mathbf{M}}(\mathbf{C}^e, c_{\mathrm{R}}) = \hat{m}(\mathcal{I}_{\mathbf{E}^e}, c_{\mathrm{R}})\mathbf{1}, \qquad \text{with} \qquad \hat{m}(\mathcal{I}_{\mathbf{E}^e}, c_{\mathrm{R}}) > 0 \tag{3.73}$$

a scalar mobility. The isotropic constitutive theory discussed above is summarized next.

3.9 Summary

Our theory relates the following basic fields:

$\mathbf{x} = \boldsymbol{\chi}(\mathbf{X}, t)$,	motion;
$\mathbf{F} = \nabla\boldsymbol{\chi}, \quad J = \det\mathbf{F} > 0$,	deformation gradient;
$\mathbf{F} = \mathbf{F}^e\mathbf{F}^c$,	multiplicative decomposition of $\mathbf{F}$;
$\mathbf{F}^c, \quad J^c = \det\mathbf{F}^c > 0$,	chemical distortion;
$\mathbf{F}^e, \quad J^e = \det\mathbf{F}^e > 0$,	elastic distortion;
$\mathbf{F}^e = \mathbf{R}^e\mathbf{U}^e = \mathbf{V}^e\mathbf{R}^e$,	polar decompositions of $\mathbf{F}^e$;
$\mathbf{U}^e = \sum_{\alpha=1}^{3} \lambda_\alpha^e \mathbf{r}_\alpha^e \otimes \mathbf{r}_\alpha^e$,	spectral decomposition of $\mathbf{U}^e$;
$\mathbf{V}^e = \sum_{\alpha=1}^{3} \lambda_\alpha^e \mathbf{l}_\alpha^e \otimes \mathbf{l}_\alpha^e$, where $\mathbf{l}_\alpha^e = \mathbf{R}^e\mathbf{r}_\alpha^e$,	spectral decomposition of $\mathbf{V}^e$;
$\mathbf{E}^e = \sum_{\alpha=1}^{3} (\ln\lambda_\alpha^e)\mathbf{r}_\alpha^e \otimes \mathbf{r}_\alpha^e$,	logarithmic elastic strain;
$\mathbf{E}_{\mathrm{H}}^e \overset{\mathrm{def}}{=} \mathbf{R}^e\mathbf{E}^e\mathbf{R}^{e\mathsf{T}} = \sum_{\alpha=1}^{3} (\ln\lambda_\alpha^e)\mathbf{l}_\alpha^e \otimes \mathbf{l}_\alpha^e$,	spatial logarithmic elastic strain;
$\mathbf{T} = \mathbf{T}^\mathsf{T}$,	Cauchy stress;
$\mathbf{M}^e = J^e\mathbf{R}^{e\mathsf{T}}\mathbf{T}\mathbf{R}^e$,	Mandel stress;
$\mathbf{T}_{\mathrm{R}} = J\mathbf{T}\mathbf{F}^{-\mathsf{T}}$,	Piola stress;
ψ_{R},	free energy density per unit reference volume;
ϑ = constant,	constant absolute temperature;
c_{R},	molar species concentration per unit reference volume;
$c_{\mathrm{R,max}}$,	maximum molar species concentration per unit reference volume;
$\bar{c} = c_{\mathrm{R}}/c_{\mathrm{R,max}} \in [0,1]$,	normalized species concentration;
Ω,	volume of a mole of the diffusing species;
μ,	chemical potential;
$\mathbf{j}_{\mathrm{R}}$,	referential species flux vector;
$\mathfrak{c}_{\mathrm{R}}$,	micromorphic species concentration;
$\bar{\mathfrak{c}} = \mathfrak{c}_{\mathrm{R}}/c_{\mathrm{R,max}}$,	normalized micromorphic species concentration;
$\mathfrak{p}$,	scalar microstress;
$\boldsymbol{\xi}$,	vector microstress.

3.9.1 Constitutive equations

1. **Free energy**

$$\psi_{\mathrm{R}} = \hat{\psi}_{\mathrm{R}}(\mathcal{I}_{\mathbf{E}^e}, c_{\mathrm{R}}, \mathfrak{c}_{\mathrm{R}}, |\nabla\mathfrak{c}_{\mathrm{R}}|), \tag{3.74}$$

where $\mathcal{I}_{\mathbf{E}^e}$ represents a list of the principal invariants of the logarithmic elastic strain $\mathbf{E}^e$.

2. **Mandel stress. Cauchy stress. Piola stress**

The Mandel stress is given by

$$\mathbf{M}^e = J^{c-1}\left(\frac{\partial\hat{\psi}_{\mathrm{R}}(\mathcal{I}_{\mathbf{E}^e}, c_{\mathrm{R}}, \mathbb{c}_{\mathrm{R}}, |\nabla\mathbb{c}_{\mathrm{R}}|)}{\partial\mathbf{E}^e}\right), \tag{3.75}$$

which, on account of the isotropy of $\hat{\psi}_{\mathrm{R}}$ is symmetric.

The Cauchy stress is given by

$$\mathbf{T} \overset{\text{def}}{=} J^{-1}\left(\mathbf{R}^e\frac{\partial\hat{\psi}_{\mathrm{R}}(\mathcal{I}_{\mathbf{E}^e}, c_{\mathrm{R}}, \mathbb{c}_{\mathrm{R}}, |\nabla\mathbb{c}_{\mathrm{R}}|)}{\partial\mathbf{E}^e}\,\mathbf{R}^{e\mathsf{T}}\right), \tag{3.76}$$

and the Piola stress is given by

$$\mathbf{T}_{\mathrm{R}} \overset{\text{def}}{=} \left(\mathbf{R}^e\frac{\partial\hat{\psi}_{\mathrm{R}}(\mathcal{I}_{\mathbf{E}^e}, c_{\mathrm{R}}, \mathbb{c}_{\mathrm{R}}, |\nabla\mathbb{c}_{\mathrm{R}}|)}{\partial\mathbf{E}^e}\,\mathbf{R}^{e\mathsf{T}}\right)\mathbf{F}^{-\mathsf{T}}. \tag{3.77}$$

3. Chemical potential

The quantity

$$\mu = \frac{\partial\hat{\psi}_{\mathrm{R}}(\mathcal{I}_{\mathbf{E}^e}, c_{\mathrm{R}}, \mathbb{c}_{\mathrm{R}}, |\nabla\mathbb{c}_{\mathrm{R}}|)}{\partial c_{\mathrm{R}}} - \Omega\,\frac{1}{3}\mathrm{tr}\,\mathbf{M}^e \tag{3.78}$$

represents the chemical potential, with Ω the molar volume of the species.

4. Microstress $\mathbb{p}$

The scalar microstress $\mathbb{p}$ is given by

$$\mathbb{p} = \frac{\partial\hat{\psi}_{\mathrm{R}}(\mathcal{I}_{\mathbf{E}^e}, c_{\mathrm{R}}, \mathbb{c}_{\mathrm{R}}, |\nabla\mathbb{c}_{\mathrm{R}}|)}{\partial\mathbb{c}_{\mathrm{R}}}. \tag{3.79}$$

5. Microstress $\boldsymbol{\xi}$

The vector microstress $\boldsymbol{\xi}$ is given by

$$\boldsymbol{\xi} = \frac{\partial\hat{\psi}_{\mathrm{R}}(\mathcal{I}_{\mathbf{E}^e}, c_{\mathrm{R}}, \mathbb{c}_{\mathrm{R}}, |\nabla\mathbb{c}_{\mathrm{R}}|)}{\partial\nabla\mathbb{c}_{\mathrm{R}}}. \tag{3.80}$$

6. Evolution equation for $\mathbf{F}^c$

The evolution equation for $\mathbf{F}^c$ is

$$\dot{\mathbf{F}}^c = \mathbf{L}^c\,\mathbf{F}^c, \qquad \mathbf{L}^c = \dot{c}_{\mathrm{R}}\,\mathbb{A}, \qquad \mathbb{A} = J^{c-1}\frac{1}{3}\Omega\,\mathbf{1}, \tag{3.81}$$

with

$$J^c = 1 + \Omega c_{\mathrm{R}}, \tag{3.82}$$

and with Ω a constant.

7. **Species flux**

   The species flux $\mathbf{j}_{\mathrm{R}}$ is presumed to obey the constitutive equation

$$\mathbf{j}_{\mathrm{R}} = -m\,\nabla\mu, \tag{3.83}$$

   with $m = \hat{m}(\mathcal{I}_{\mathbf{E}^e}, c_{\mathrm{R}}) > 0$ the species mobility.

3.10 Specialization of the constitutive equations

Within the limits of an isotropic idealization, the theory presented thus far is quite general. Next we introduce special constitutive equations which are useful for modeling Cahn-Hilliard-type diffusion of Li coupled to large elastic deformation of electrode materials in Li-ion batteries.

3.10.1 Free energy

We consider a separable free energy of the form

$$\hat{\psi}_{\mathrm{R}}(\mathcal{I}_{\mathbf{E}^e}, c_{\mathrm{R}}, \mathbb{c}_{\mathrm{R}}, |\nabla\mathbb{c}_{\mathrm{R}}|) = \hat{\psi}_{\mathrm{R}}^{\mathrm{chemical}}(c_{\mathrm{R}}) + \hat{\psi}_{\mathrm{R}}^{\mathrm{penalty}}(c_{\mathrm{R}}, \mathbb{c}_{\mathrm{R}}) + \hat{\psi}_{\mathrm{R}}^{\mathrm{interface}}(\nabla\mathbb{c}_{\mathrm{R}}) + \hat{\psi}_{\mathrm{R}}^{\mathrm{elastic}}(\mathcal{I}_{\mathbf{E}^e}, c_{\mathrm{R}}). \tag{3.84}$$

Here

(i) $\psi_{\mathrm{R}}^{\mathrm{chemical}}$ is the change in chemical free energy due to mixing of the species with the host material. As a simple continuum approximation to mixing, we take this to be given by a regular solution model (cf., e.g., DeHoff, 2006)

$$\psi_{\mathrm{R}}^{\mathrm{chemical}} = c_{\mathrm{R,max}}\left(\mu^0\,\bar{c} + R\vartheta\left(\bar{c}\ln\bar{c} + (1-\bar{c})\ln(1-\bar{c})\right) + \chi\,\bar{c}(1-\bar{c})\right), \tag{3.85}$$

where

$$\bar{c} = \frac{c_{\mathrm{R}}}{c_{\mathrm{R,max}}}, \qquad 0 \le \bar{c} \le 1 \tag{3.86}$$

is a *normalized species concentration*, with $c_{\mathrm{R,max}}$ the concentration of the species in moles per unit reference volume when all the accommodating sites in the host material all filled; R the universal gas constant; and ϑ the absolute temperature (assumed to be constant). Also,

- μ^0 is a reference value of the chemical potential of the diffusing species;
- the second term in (3.85), involving $R\vartheta$, represents the entropy of mixing for an ideal solution; while

– the last term in (3.85), involving χ, represents an energetic interaction between the diffusing species and the host material.

(ii) $\psi_{\mathrm{R}}^{\mathrm{penalty}}$ accounts for an energetic penalty incurred by the micromorphic concentration $\mathfrak{c}_{\mathrm{R}}$ being different from the concentration field c_{R}. Introducing

$$\bar{\mathfrak{c}} = \frac{\mathfrak{c}_{\mathrm{R}}}{c_{\mathrm{R,max}}}, \tag{3.87}$$

as a *normalized micromorphic concentration*, we take the energetic penalty to be given by the following simple quadratic form

$$\psi_{\mathrm{R}}^{\mathrm{penalty}} = c_{\mathrm{R,max}} \frac{1}{2}\beta(\bar{c} - \bar{\mathfrak{c}})^2, \tag{3.88}$$

with $\beta > 0$ a penalty energy coefficient with units of *energy per mole.*

(iii) $\psi_{\mathrm{R}}^{\mathrm{interface}}$ is an interfacial free energy which depends on the gradient of the micromorphic concentration, $\nabla\mathfrak{c}_{\mathrm{R}}$. We take it to be given by the following simple quadratic form

$$\psi_{\mathrm{R}}^{\mathrm{interface}} = c_{\mathrm{R,max}} \frac{1}{2}\lambda\,|\nabla\bar{\mathfrak{c}}|^2, \tag{3.89}$$

with $\lambda > 0$ a gradient energy coefficient with units of *energy per mole times length squared*, and it is this term which introduces an internal length scale for the width of interfaces between distinct phases.

(iv) $\psi_{\mathrm{R}}^{\mathrm{elastic}}$ is the contribution to the change in the free energy due to the elastic deformation of the host material, taken to be given by

$$\psi_{\mathrm{R}}^{\mathrm{elastic}} = J^c\left(\frac{1}{2}\mathbf{E}^e : \hat{\mathbb{C}}(\bar{c})[\mathbf{E}^e]\right), \qquad \hat{\mathbb{C}}(\bar{c}) \stackrel{\mathrm{def}}{=} 2G(\bar{c})\mathbb{I} + \left(K(\bar{c}) - \frac{2}{3}G(\bar{c})\right)\mathbf{1}\otimes\mathbf{1}, \tag{3.90}$$

where $\mathbb{C}$ is the elasticity tensor, with $\mathbb{I}$ and $\mathbf{1}$ the fourth- and second-order identity tensors, and the parameters

$$G(\bar{c}) > 0, \qquad K(\bar{c}) > 0, \tag{3.91}$$

are the concentration-dependent shear and bulk moduli, respectively.[4] The term

$$\frac{1}{2}\mathbf{E}^e : \hat{\mathbb{C}}(\bar{c})[\mathbf{E}^e]$$

[4] This is a simple generalization of the classical strain energy function of infinitesimal isotropic elasticity to finite strains using the logarithmic elastic strain (Anand, 1979, 1986), and concentration-dependent elastic moduli.

in (3.90) is a measure of the free energy per unit volume of the local structural space defined by the range of $\mathbf{F}^c(\mathbf{X})$, and multiplication of this term by $J^c = \det \mathbf{F}^c$ gives us the free energy per unit volume of the reference space.

Thus, using (3.85), (3.88), (3.89), and (3.90) in (3.84), a simple form of the free energy function which accounts for the combined effects of mixing, swelling, and finite elastic stretching is

$$\psi_{\mathrm{R}} = c_{\mathrm{R,max}} \left(\mu^0 \bar{c} + R\vartheta \left(\bar{c} \ln \bar{c} + (1-\bar{c}) \ln(1-\bar{c}) \right) + \chi \bar{c}(1-\bar{c}) + \frac{1}{2}\beta (\bar{c} - \bar{\mathbb{c}})^2 + \frac{1}{2}\lambda |\nabla \bar{\mathbb{c}}|^2 \right) + J^c \left(\frac{1}{2} \mathbf{E}^e : \mathbb{C}(\bar{c})[\mathbf{E}^e] \right). \tag{3.92}$$

3.10.2 Stress

Using (3.92) and (3.75) we find that the Mandel stress is given by

$$\mathbf{M}^e = 2G\mathbf{E}^e + (K - (2/3)G)(\mathrm{tr}\mathbf{E}^e)\mathbf{1}. \tag{3.93}$$

Then, using (3.76) we find that the Cauchy stress tensor is given by

$$\mathbf{T} = J^{e-1} \left[2G\mathbf{E}^e_{\mathrm{H}} + (K - (2/3)G)(\mathrm{tr}\mathbf{E}^e_{\mathrm{H}})\mathbf{1} \right], \tag{3.94}$$

and the Piola stress, $\mathbf{T}_{\mathrm{R}} = J\mathbf{T}\mathbf{F}^{-\mathrm{T}}$, is given by

$$\mathbf{T}_{\mathrm{R}} = J^c \left[2G\mathbf{E}^e_{\mathrm{H}} + (K - (2/3)G)(\mathrm{tr}\mathbf{E}^e_{\mathrm{H}})\mathbf{1} \right] \mathbf{F}^{-\mathrm{T}}. \tag{3.95}$$

In (3.94) and (3.95) we have used the notation $\mathbf{E}^e_{\mathrm{H}} \stackrel{\mathrm{def}}{=} \mathbf{R}^e \mathbf{E}^e \mathbf{R}^{e\mathrm{T}}$ for the spatial logarithmic elastic strain.

3.10.3 Chemical potential

Using (3.78) and (3.92), the chemical potential μ is given by

$$\mu = \mu^0 + R\vartheta \ln \left(\frac{\bar{c}}{1-\bar{c}} \right) + \chi(1-2\bar{c}) + \beta(\bar{c} - \bar{\mathbb{c}}) - \Omega \frac{1}{3} \mathrm{tr}\mathbf{M}^e + \frac{J^c}{c_{\mathrm{R,max}}} \left(\frac{1}{2} \mathbf{E}^e : \frac{\partial \hat{\mathbb{C}}(\bar{c})}{\partial \bar{c}} [\mathbf{E}^e] \right) + \Omega \left(\frac{1}{2} \mathbf{E}^e : \hat{\mathbb{C}}(\bar{c})[\mathbf{E}^e] \right). \tag{3.96}$$

3.10.4 Microforces. Governing equation for the micromorphic concentration $\bar{\mathbb{c}}$

From (3.79), (3.80), and (3.92), the microstresses $\mathbb{p}$ and $\boldsymbol{\xi}$ are given by

$$\begin{aligned} \mathbb{p} &= -\beta(\bar{c} - \bar{\mathbb{c}}), \\ \boldsymbol{\xi} &= \lambda \nabla \bar{\mathbb{c}}. \end{aligned} \tag{3.97}$$

Further, the local microforce balance (3.47), viz. $\mathrm{Div}\boldsymbol{\xi} - \mathbb{p} = 0$, together with the constitutive equations (3.97) for $\mathbb{p}$ and $\boldsymbol{\xi}$, yield

$$\lambda \Delta \bar{\mathbb{c}} + \beta(\bar{c} - \bar{\mathbb{c}}) = 0. \tag{3.98}$$

Remark. Introducing the quantity

$$\ell = \sqrt{\frac{\lambda}{\beta}} > 0, \tag{3.99}$$

which has units of length, equation (3.98) may be written as

$$\bar{\mathbb{c}} - \ell^2 \Delta \bar{\mathbb{c}} = \bar{c}. \tag{3.100}$$

The partial differential equation (3.100), together with (3.99) are identical to the Helmholtz-type equation (2.9) introduced by Ubachs et al. (2004), *but here derived in a thermodynamically consistent manner.* Further, as we shall show in Chapter 4, the parameter ℓ defined in (3.99) does not by itself control the width of the interface between phases. Once a value of β is chosen such that the micromorphic concentration $\mathbb{c}_{\mathrm{R}}$ is sufficiently close to c, then the width of the interface between phases at a given temperature depends only on the two *physical parameters* λ and χ in the free energy. □

3.10.5 Species flux

In the expression (3.83) for the species flux, we take the mobility as the following function of the species concentration,

$$\hat{m}(c_{\mathrm{R}}) = m_0\, c_{\mathrm{R}}\,(1 - \bar{c}), \quad \text{with} \quad m_0 > 0 \quad \text{a constant}, \tag{3.101}$$

which represents the physical requirement that the pure phases $\bar{c} = 0$ and $\bar{c} = 1$ have vanishing mobility. Thus, using (3.101) in (3.83) we obtain

$$\mathbf{j}_{\mathrm{R}} = -\big(m_0\, c_{\mathrm{R}}\,(1 - \bar{c})\big)\, \nabla \mu, \tag{3.102}$$

with μ given in (3.96).

Remark. In the absence of mechanical coupling, under isothermal conditions, and in the case of an ideal solution for which $\chi = 0$, and for which we neglect the gradient effects $\beta = \lambda = 0$, the gradient of the chemical potential (3.96) is given by

$$\nabla\mu = R\vartheta \left(\frac{1}{c_{\mathrm{R}}(1-\bar{c})} \right) \nabla c_{\mathrm{R}}, \tag{3.103}$$

and in this case, using (3.101) and (3.102), the species flux reduces to the classical Fick's law

$$\mathbf{j}_{\mathrm{R}} = -D_0 \, \nabla c_{\mathrm{R}}, \qquad \text{with} \qquad D_0 \stackrel{\text{def}}{=} m_0 R\vartheta > 0, \tag{3.104}$$

where D_0 represents a species diffusivity, and the partial differential equation (3.3) takes the classical form

$$\dot{c}_{\mathrm{R}} = D_0 \, \Delta c_{\mathrm{R}}. \tag{3.105}$$

□

3.11 Governing partial differential equations. Boundary conditions

3.11.1 Partial differential equations

The governing partial differential equations consist of:

1. The local macroforce balance (3.32), viz.

$$\mathrm{Div}\,\mathbf{T}_{\mathrm{R}} + \mathbf{b}_{\mathrm{R}} = \mathbf{0}, \tag{3.106}$$

   where $\mathbf{b}_{\mathrm{R}}$ is the non-inertial body force, and $\mathbf{T}_{\mathrm{R}}$ is given by (3.95).

2. The local balance equation for the species concentration (3.3), together with (3.102), gives

$$\dot{c}_{\mathrm{R}} = \mathrm{Div}\,(\hat{m}(c_{\mathrm{R}})\nabla\mu), \qquad \text{with} \qquad \hat{m}(c_{\mathrm{R}}) = m_0 \, c_{\mathrm{R}} \, (1-\bar{c}), \qquad m_0 > 0, \tag{3.107}$$

   and with the chemical potential given by (3.96).

3. The local microforce balance (3.47), together with the constitutive equations (3.97), yields the governing equation for the micromorphic concentration (3.100), viz.

$$\lambda \Delta\bar{\mathfrak{c}} + \beta(\bar{c} - \bar{\mathfrak{c}}) = 0. \tag{3.108}$$

3.11.2 Boundary and initial conditions

Let $\mathcal{S}_\chi$ and $\mathcal{S}_{\mathbf{t}_\mathrm{R}}$ denote complementary subsurfaces of the boundary $\partial\mathrm{B}$ of the body B. Then, as is standard, for a time interval $t \in [0,T]$ we consider a pair of simple boundary conditions in which the motion is specified on $\mathcal{S}_\chi$ and the surface traction on $\mathcal{S}_{\mathbf{t}_\mathrm{R}}$:

$$\left.\begin{aligned} \chi &= \breve{\chi} \quad \text{on } \mathcal{S}_\chi \times [0,T], \\ \mathbf{T}_\mathrm{R}\mathbf{n}_\mathrm{R} &= \breve{\mathbf{t}}_\mathrm{R} \quad \text{on } \mathcal{S}_{\mathbf{t}_\mathrm{R}} \times [0,T]. \end{aligned}\right\} \tag{3.109}$$

Further, letting $\mathcal{S}_{c_\mathrm{R}}$ and $\mathcal{S}_{\mathbf{j}_\mathrm{R}}$ denote complementary subsurfaces of the boundary, we consider a pair of simple boundary conditions in which the species concentration is specified on $\mathcal{S}_{c_\mathrm{R}}$ and the species flux on $\mathcal{S}_{\mathbf{j}_\mathrm{R}}$:

$$\left.\begin{aligned} c_\mathrm{R} &= \breve{c}_\mathrm{R} \quad \text{on } \mathcal{S}_{c_\mathrm{R}} \times [0,T], \\ \mathbf{j}_\mathrm{R} \cdot \mathbf{n}_\mathrm{R} &= \breve{j} \quad \text{on } \mathcal{S}_{\mathbf{j}_\mathrm{R}} \times [0,T]. \end{aligned}\right\} \tag{3.110}$$

Next, the presence of microscopic stresses results in an expenditure of power

$$\int_{\partial\mathrm{B}} (\lambda(\nabla\bar{\mathfrak{c}}) \cdot \mathbf{n}_\mathrm{R})\, \dot{\mathfrak{c}}_\mathrm{R}\, da_\mathrm{R}$$

where in writing this expenditure we have made use of the constitutive equation $(3.97)_2$. This necessitates a consideration of boundary conditions on $\partial\mathrm{B}$ involving the term $\lambda(\nabla\bar{\mathfrak{c}}) \cdot \mathbf{n}_\mathrm{R}$ and the scalar rate $\dot{\mathfrak{c}}_\mathrm{R}$.

- We restrict our attention to boundary conditions that result in a null expenditure of microscopic power in the sense that $(\lambda(\nabla\bar{\mathfrak{c}}) \cdot \mathbf{n}_\mathrm{R})\, \dot{\mathfrak{c}}_\mathrm{R} = 0$.

Consistent with our assumption of null expenditure of microscopic power, we consider a boundary condition of the form[5]

$$\lambda(\nabla\bar{\mathfrak{c}}) \cdot \mathbf{n}_\mathrm{R} = 0 \quad \text{on} \quad \partial\mathrm{B} \times [0,T]. \tag{3.111}$$

The initial data is taken as

$$\chi(\mathbf{X},0) = \chi_0(\mathbf{X}), \qquad c_\mathrm{R}(\mathbf{X},0) = c_{\mathrm{R},0}, \qquad \text{and} \quad \mathfrak{c}_\mathrm{R}(\mathbf{X},0) = \mathfrak{c}_{\mathrm{R},0} \quad \text{in} \quad \mathrm{B}. \tag{3.112}$$

The coupled set of equations (3.106), (3.107), and (3.108), together with the boundary conditions (3.109), (3.110), (3.111), and the initial conditions (3.112), yield an initial/boundary-value problem for the motion $\chi(\mathbf{X},t)$, the species concentration $c_\mathrm{R}(\mathbf{X},t)$, and the micromorphic concentration $\mathfrak{c}_\mathrm{R}(\mathbf{X},t)$.

[5] From a theoretical point of view it is clear that one may also prescribe a boundary condition of the form $\mathfrak{c}_\mathrm{R} = \breve{\mathfrak{c}}_\mathrm{R}$, where $\breve{\mathfrak{c}}_\mathrm{R}$ is a prescribed constant micromorphic concentration on a portion of $\partial\mathrm{B}$ where (3.111) is not prescribed. However, the physical nature of such a boundary condition is unclear, and we thus restrict ourselves to a boundary condition of the form (3.111).

Remark. In the standard variational derivation of the Cahn-Hilliard theory, if the functional $\Psi(\bar{c})$ in (2.1) is augmented to include a contribution from a surface energy of the body

$$\Psi(\bar{c}) = \int_{\mathrm{B}} \hat{\psi}_{\mathrm{R}}(\bar{c}, \nabla\bar{c})\, dv_{\mathrm{R}} + \int_{\partial B} \hat{\varphi}_{\mathrm{R}}(\bar{c})\, da_{\mathrm{R}}, \tag{3.113}$$

where $\hat{\varphi}_{\mathrm{R}}(\bar{c})$ is a surface free-energy per unit area of the boundary $\partial\mathrm{B}$ of the body (Cahn, 1977), then the first variation of (3.113) gives the following *natural boundary condition*,

$$(\lambda\nabla\bar{c})\cdot\mathbf{n}_{\mathrm{R}} = -\frac{d\hat{\varphi}_{\mathrm{R}}(\bar{c})}{d\bar{c}} \qquad \text{on } \partial\mathrm{B}, \tag{3.114}$$

where $\mathbf{n}_{\mathrm{R}}$ is the outward unit normal to $\partial\mathrm{B}$. Such a boundary condition has been recently considered by Cogswell and Bazant (2013) in their study of phase-separation at surfaces of nanoparticles. While surface-energy effects are clearly of substantial importance in nanometer-sized particles where the surface-to-volume ratio is large, in this study we restrict our attention to the boundary condition (3.111), and leave a study of the consequences of using a boundary conditions of the type (3.114) to future work. □

3.12 Numerical Implementation of the theory

Eq. (3.96) for the chemical potential may be written as

$$\mu = \mu^0 + R\vartheta \ln\left(\frac{\bar{c}}{1-\bar{c}}\right) + \chi(1-2\bar{c}) + \beta(\bar{c}-\bar{\mathbb{c}}) + \mu_\sigma, \tag{3.115}$$

where we have introduced a "stress potential",

$$\mu_\sigma \stackrel{\text{def}}{=} -\Omega\frac{1}{3}\mathrm{tr}\mathbf{M}^e + \frac{J^c}{c_{\mathrm{R,max}}}\left(\frac{1}{2}\mathbf{E}^e : \frac{\partial\mathbb{C}(\bar{c})}{\partial\bar{c}}[\mathbf{E}^e]\right) + \Omega\left(\frac{1}{2}\mathbf{E}^e : \mathbb{C}(\bar{c})\mathbf{E}^e\right), \tag{3.116}$$

which quantifies the effect of mechanical deformation on the chemical potential. In our numerical implementation, we restrict attention to materials for which the last two terms on the right of (3.116) are small compared to the first term, and as an approximation we take the stress chemical potential to be simply given by[6]

$$\mu_\sigma = -\Omega\frac{1}{3}\mathrm{tr}\mathbf{M}^e. \tag{3.117}$$

We have implemented our theory in the implicit finite element program Abaqus (2010) by writing a user element subroutine (UEL). We have implemented three different elements:

[6]Cf. Sethuraman et al. (2010a) for arguments leading to such an approximation even for silicon, which can absorb a large amount of lithium, and for which the values of the elastic moduli are significantly affected when it is fully lithiated.

(i) a 2D plane-strain 4-node linear isoparametric quadrilateral which we refer to as UPE4; (ii) a 2D axisymmetric 4-node linear isoparametric quadrilateral which we refer to as UAX4; and (iii) a 3D 8-node linear isoparametric brick which we refer to as U3D8. The details of our numerical procedure can be found in Appendix. A.

The degrees of freedom for these elements are the displacement components $\{u_i\}$, the normalized concentration $\bar{c}$, the normalized micromorphic concentration $\bar{\mathfrak{c}}$, and in order to resolve the stress gradients required to compute the term $\nabla\mu$ in (3.102), we treat the stress chemical potential μ_σ in (3.117) as an additional degree of freedom (cf., Bower and Guduru, 2012).

Chapter 4

Simulations for the special case of spinodal decomposition by diffusion in the absence of mechanical deformation

In this section we focus on the special case of simulating spinodal decomposition by diffusion in a body for which deformation is suppressed (a rigid body) and which is also stress free. Spinodal decomposition is a phase transformation in which an initially homogeneous binary mixture separates into distinct regions which are characterized by being either rich or poor in their concentration of a particular component. This results in the creation of interfaces with sharp concentration gradients which introduce additional energy into the system.

In the absence of any mechanical deformation, the free energy (3.92) may be written in a "normalized" manner as

$$\bar{\psi}_{\mathrm{R}} = \frac{\psi_{\mathrm{R}}}{R\vartheta c_{\mathrm{R,max}}} = \underbrace{\Big(\bar{c}\ln\bar{c} + (1-\bar{c})\ln(1-\bar{c}) + \bar{\chi}\,\bar{c}(1-\bar{c})\Big)}_{\text{chemical energy } \bar{\psi}^{\mathrm{c}}_{\mathrm{R}}} + \underbrace{\bar{\lambda}(1/2)|\nabla\bar{\mathrm{c}}|^2}_{\text{interfacial energy}} + \underbrace{\bar{\beta}(1/2)(\bar{c}-\bar{\mathrm{c}})^2}_{\text{penalty energy}} \tag{4.1}$$

where we have set the reference chemical potential $\mu^0 = 0$, and, fixing the temperature ϑ, have defined the following "normalized" quantities [1]

$$\bar{\chi} \overset{\text{def}}{=} \frac{\chi}{R\vartheta}, \quad \bar{\lambda} \overset{\text{def}}{=} \frac{\lambda}{R\vartheta}, \quad \text{and} \quad \bar{\beta} \overset{\text{def}}{=} \frac{\beta}{R\vartheta}. \tag{4.2}$$

Here,

[1] We use the term "normalized" loosely; the quantities $\bar{\chi}$ and $\bar{\beta}$ are dimensionless, however the gradient coefficient $\bar{\lambda}$ has units of length squared.

- The normalized chemical energy, $\bar{\psi}^c_{\mathrm{R}}$, the first term in (4.1), governs phase separation and depends only on the local concentration $\bar{c}$. A plot of the normalized chemical energy for $\bar{\chi} = 3$ is shown schematically in Fig. 4-1. When the initial concentration $\bar{c}$ is within the spinodal region $\bar{c} \in (\bar{c}_\gamma, \bar{c}_\delta)$ (i.e., regions where $\partial^2 \bar{\psi}_{\mathrm{R}} / \partial \bar{c}^2 < 0$), the system can spinodally decompose into multiple phases of equilibrium concentrations $\bar{c}_\alpha$ and $\bar{c}_\beta$, called the *binodal concentrations*. The system minimizes its energy by changing its initial concentration distribution and tending towards the equilibrium concentrations.

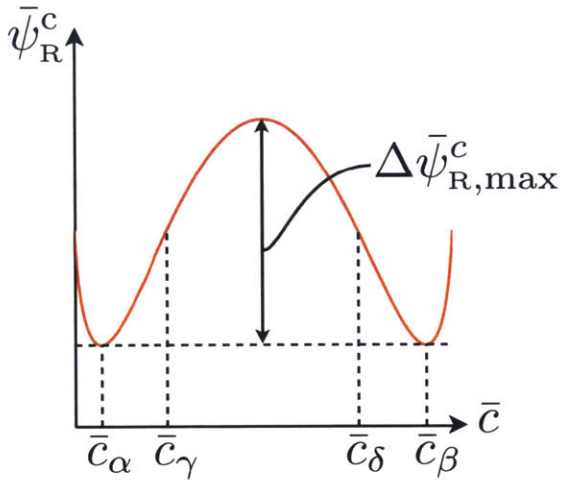

Figure 4-1: Typical double-well chemical free energy $\bar{\psi}^c_{\mathrm{R}}$ based on equation (4.1) for $\bar{\chi} = 3$.

- The second term in (4.1), the interfacial energy, depends on the gradient of the micromorphic concentration $\nabla\bar{\mathfrak{c}}$, and is scaled by an interfacial energy parameter $\bar{\lambda}$ with units of length squared. This energy can be reduced via "coarsening" of the phases, a process during which the system finds more favorable lower energy configurations by minimizing the phase interfaces.

- The third term in (4.1) represents an energetic penalty for the micromorphic concentration $\bar{\mathfrak{c}}$ being different from the actual concentration $\bar{c}$. This energy is scaled by a penalty modulus $\bar{\beta}$. As $\bar{\beta}$ is increased, the difference $|\bar{c} - \bar{\mathfrak{c}}|$ is reduced, and the solutions from the present gradient micromorphic concentration theory are expected to converge towards the solutions to the actual fourth-order Cahn-Hilliard equation (2.7).

The purpose of this section is to understand the effects of the value of the penalty modulus $\bar{\beta}$ on the solutions from our gradient micromorphic concentration theory for spinodal decomposition in two and three dimensions. Specifically, it is important to make an informed decision as to what the value of the parameter $\bar{\beta}$ should be in order to obtain solutions which are in some sense close to those which might be obtained from the actual Cahn-Hilliard theory.

Accordingly, for all simulations in this section, we fix the value of the parameters $\bar{\chi}$ and $\bar{\lambda}$ at[2]

$$\bar{\chi} = 3, \quad \bar{\lambda} = 2.5 \times 10^{-4}\,\mu\text{m}^2, \tag{4.3}$$

and study the manner in which the value of $\bar{\beta}$ affects the numerical solution of a spinodal decomposition problem. Specifically, we chose to study isolated and periodic systems in which phase separation is allowed to proceed until a "steady-state" solution for the phase morphology is attained. From the results of our numerical simulations at steady-state, we

(i) plotted the distribution of the difference $\bar{c} - \bar{\mathfrak{c}}$, from which we computed the maximum of the absolute value of the difference of the two quantities, $\max|\bar{c} - \bar{\mathfrak{c}}|$, and

(ii) also measured the phase interface width d,

and through this quantified the effect of the parameter $\bar{\beta}$ on $\max|\bar{c} - \bar{\mathfrak{c}}|$ and d.

In order to measure the width of the interface between the two phases in a consistent fashion, we chose a specific method for characterizing a phase-interface, which is shown schematically for a one-dimensional phase-separation situation in Fig. 4-2 (c.f. Wodo and Ganapathysubramanian, 2011). With respect to this figure, the interface width d is defined by the intersection of the tangent to the concentration profile at the mean concentration $\bar{c}_m = |\bar{c}_\alpha - \bar{c}_\beta|/2$ with the binodal concentrations. That is,

$$d \stackrel{\text{def}}{=} (\bar{c}_\alpha - \bar{c}_\beta)\left(\left.\frac{d\bar{c}}{dx}\right|_{\bar{c}_m}\right)^{-1}. \tag{4.4}$$

We recall from Cahn and Hilliard (1958) that an *estimate* of the concentration variation across a phase interface may be obtained as

$$\left.\frac{d\bar{c}}{dx}\right|_{\bar{c}_m} = \left(\frac{\Delta\bar{\psi}^c_{\text{R,max}}}{\bar{\lambda}}\right)^{1/2}, \tag{4.5}$$

where the quantity $\Delta\bar{\psi}^c_{\text{R,max}}$ is schematically shown in Fig. 4-1.[3] Combining (4.5) with (4.4) we have the following important estimate for the width of the interface separating the two phases,

$$d_{\text{est}} = (\bar{c}_\alpha - \bar{c}_\beta)\left(\frac{\bar{\lambda}}{\Delta\bar{\psi}^c_{\text{R,max}}}\right)^{1/2}. \tag{4.6}$$

[2]We also fix the diffusivity at $D_0 = 1.0 \times 10^{-14}\,\text{m}^2/\text{sec}$. For the purpose of the study reported in this section, the value of the diffusivity D_0 acts only to change the time-scale within which a nominal steady-state in the morphology of phase separation is reached — it has no effect on the actual morphology of the phase separation. Thus, any reasonable value of D_0 would suffice, and is not crucial for the conclusions that we shall draw from our simulations regarding the value of $\bar{\beta}$.

[3] Here, Δ does not represent the Laplace operator. For the specific free-energy considered here, $\Delta\bar{\psi}^c_{\text{R,max}}$ is the difference in the value of the chemical free energy at the mean concentration $\bar{c}_m$, and value of the chemical free energy at either of the binodal points $\bar{c}_\alpha$ or $\bar{c}_\beta$.

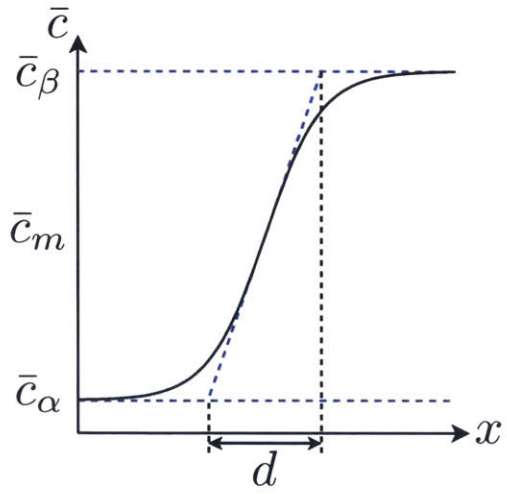

Figure 4-2: Schematic of a phase front between binodal concentrations $\bar{c}_\alpha$ and $\bar{c}_\beta$, and the definition of the interface width d.

Using the values (4.3) for the material parameters $\bar{\chi}$ and $\bar{\lambda}$, we obtain the estimate

$$d_{\text{est}} = 40\,\text{nm}. \tag{4.7}$$

We use this estimate (4.7) for the interface width to choose an appropriately fine finite-element mesh so as to get a good resolution of the phase interfaces in our numerical simulations.

4.1 Two-dimensional simulations of phase-separation

The results in the form of contours of $\bar{c}$ shown in Fig. 4-3, are from a simulation which was performed on a square domain with an edge length $L = 800\,\text{nm}$ and meshed with 100×100 two-dimensional square elements. Each element is of an edge length of 8 nm, which gave a mesh resolution of $d_{\text{est}}/8\,\text{nm} = 5$ elements across a potential phase interface. The initial concentration in the domain was given as a random uniform distribution with a mean of $\bar{c}_0 = 0.63$ and a maximum fluctuation of 0.05. The initial distribution $\bar{\mathfrak{c}}_0$ of the micromorphic concentration $\bar{\mathfrak{c}}$ was taken to be identical to that of the actual concentration $\bar{c}$. Periodic boundary conditions on $\bar{c}$ and $\bar{\mathfrak{c}}$ were applied on all the boundaries. For the particular simulation shown in this figure, the penalty modulus is taken as $\bar{\beta} = 1000$. Fig. 4-3 illustrates the evolution of phases during spinodal decomposition — from the early stages of the spinodal decomposition, when the components are well-mixed and the concentration is nearly homogenous, until a steady-state is reached, at which time two distinct phases are observed. In this particular simulation, the steady-state morphology consists of a circular concentration-poor region surrounded by a concentration-rich domain.

In order to maximize the accuracy of our numerical measurement of the interface width d, we performed additional simulations with an improved mesh resolution. Specifically, we considered a square domain with an edge length $L = 200\,\text{nm}$ which was again meshed with 100×100 two-dimensional square elements, so that each element is now of an edge length $2\,\text{nm}$. This gives an improved mesh resolution of $d_{\text{est}}/2\,\text{nm} = 20$ elements across a potential phase interface. In these simulations, keeping all other parameters constant, we varied

$$\bar{\beta} \in [5, 10, 25, 50, 100, 250, 500, 750, 1000].$$

In Fig. 4-4 we show contours of the difference $\bar{c} - \bar{\mathfrak{c}}$ at steady-state for various values of $\bar{\beta}$, using the simulations with refined mesh. In this figure one can clearly observe that as the value of $\bar{\beta}$ increases from 5 towards 1000, the difference $\bar{c} - \bar{\mathfrak{c}}$ decreases to a low value of $|\bar{c} - \bar{\mathfrak{c}}| \lessapprox 5 \times 10^{-4}$ for $\bar{\beta} = 1000$. In Fig. 4-5 we plot the maximum of the absolute value of the difference, $\max|\bar{c} - \bar{\mathfrak{c}}|$, for increasing values of $\bar{\beta}$ on a log-log scale. From this figure we observe that $\max|\bar{c} - \bar{\mathfrak{c}}|$ tends to zero as the penalty modulus $\bar{\beta}$ is increased. Thus, as $\bar{\beta}$ is increased the solutions from our theory approach those that would be obtained by using the standard Cahn-Hilliard theory.

As an alternative measure of convergence we measured the interface widths d from the same simulations shown in Fig. 4-4 for different values of $\bar{\beta}$. The result is shown in Fig. 4-6 (a); note that the x-scale in this figure is logarithmic. This figure clearly shows that as the value of $\bar{\beta}$ is increased to a value greater than about $\bar{\beta} \approx 100$, the interface-width converges to a finite value of $d \approx 30\,\text{nm}$. To emphasize this result, in Fig. 4-6 (b) we plot the variation of $|(d_{\bar{\beta}} - d_{\bar{\beta}=1000})/d_{\text{est}}|$ as a function $\bar{\beta}$, on a log-log scale. This plot clearly shows that for values $\bar{\beta} > 100$ the difference $|(d_{\bar{\beta}} - d_{\bar{\beta}=1000})/d_{\text{est}}|$ is approximately 1%.

These results show that using a value of $\bar{\beta} = 1000$ the solutions from our theory should approach the solutions that might be obtained from the standard Cahn-Hilliard theory.

4.2 Three-dimensional simulations of phase-separation

For completeness, we repeat the calculations shown in the previous section, but this time in three dimensions. The simulation shown in Fig. 4-7 was performed in a cubic domain with an edge length $L = 400$ nm and meshed with $50 \times 50 \times 50$ three-dimensional cubic elements, so that each element is of edge length 8 nm, which gives a mesh resolution of $d_{\text{est}}/8\,\text{nm} = 5$ elements across a potential phase interface. The initial concentration in the domain is given as a random uniform distribution with a mean of $\bar{c}_0 = 0.75$ and a maximum fluctuation of 0.05. The initial distribution $\bar{\mathfrak{c}}_0$ of the micromorphic concentration $\bar{\mathfrak{c}}$ is taken to be identical to that of the actual concentration $\bar{c}$. As before, periodic boundary conditions on $\bar{c}$ and $\bar{\mathfrak{c}}$ are applied on all the boundaries. For the particular simulation shown in Fig. 4-7 the penalty modulus is taken as $\bar{\beta} = 1000$.

In order to illustrate the evolution of phases during spinodal decomposition in three dimensions, Fig. 4-7 shows iso-surfaces of the normalized concentration $\bar{c}$ as they evolve

in time. In this particular simulation, the steady-state morphology consists of a spherical concentration-poor region surrounded by a concentration-rich domain.

As in the two-dimensional calculations, in order to maximize the accuracy of our numerical measurement of d, we performed additional simulations with an improved mesh resolution. Specifically we considered a cubic domain with a smaller edge length of $L = 200\,\text{nm}$, which was again meshed with the same number of $50 \times 50 \times 50$ three-dimensional cubic elements, so that each element is now of edge length $4\,\text{nm}$. This gives an improved mesh resolution of $d_{\text{est}}/4\,\text{nm} = 10$ elements across a potential phase interface. As before, keeping all other parameters constant, we varied $\bar{\beta} \in [5, 1000]$.

Fig. 4-8 shows iso-surfaces of the difference $\bar{c} - \bar{\mathfrak{c}}$ for various values of $\bar{\beta}$, using the simulations with refined mesh. As before, in Fig. 4-5 we also show the convergence of $\max|\bar{c} - \bar{\mathfrak{c}}|$ for the 3D simulations. Again, as $\bar{\beta}$ increases to $\bar{\beta} = 1000$, the $\max|\bar{c} - \bar{\mathfrak{c}}|$ decreases to a value less than approximately 5×10^{-4}. The variation of the interface width d with varying $\bar{\beta}$ for the 3D simulations is also shown in Fig. 4-6 and follows the same trend as the two-dimensional simulations described above.

To conclude this brief study on spinodal decomposition in the absence of mechanical deformation we note that:

- Our simulations show that as we increase the value of the penalty modulus $\bar{\beta}$ the value of $\max|\bar{c} - \bar{\mathfrak{c}}|$ tends to zero. This indicates that the solutions from our theory based on the gradient of the microconcentration $\mathfrak{c}_{\text{R}}$ will approach those that might be obtained using the classical Cahn-Hilliard theory which is based on the gradient of c_{R}.[4]

- The convergence of the values of the interface-width d as the penalty modulus $\bar{\beta}$ increases gives us a methodology for choosing an appropriately high value of $\bar{\beta}$. For a sufficiently large value of $\bar{\beta}$, the interface width d is controlled solely by the physical parameters $\bar{\lambda}$ and $\bar{\chi}$.

- The results from our two- and three-dimensional numerical study show that for the material parameters chosen, a value of $\bar{\beta} = 1000$ is sufficiently large to provide an accurately converged solution to the problem of phase-separation.

Having determined an appropriate value for the penalty modulus $\bar{\beta}$, we next study the important chemo-mechanically-coupled problem of lithiation of a spheroidal-shaped electrode particle.

An additional analysis of the convergence of the split-method discussed in this chapter to the solutions of the classical Cahn-Hilliard theory is given in Appendix A, where we compare to solutions of the classical Cahn-Hilliard theory obtained using a different split-method, not involving $\mathfrak{c}_{\text{R}}$. See also the remark at the end of Chapter 2.

[4] We also note that the two- and three-dimensional simulations shown here closely resemble those of Wodo and Ganapathysubramanian (2011) who used an operator-split method to solve the Cahn-Hilliard equation which does not include the introduction of the micrmorphic concentration $\bar{\mathfrak{c}}$.

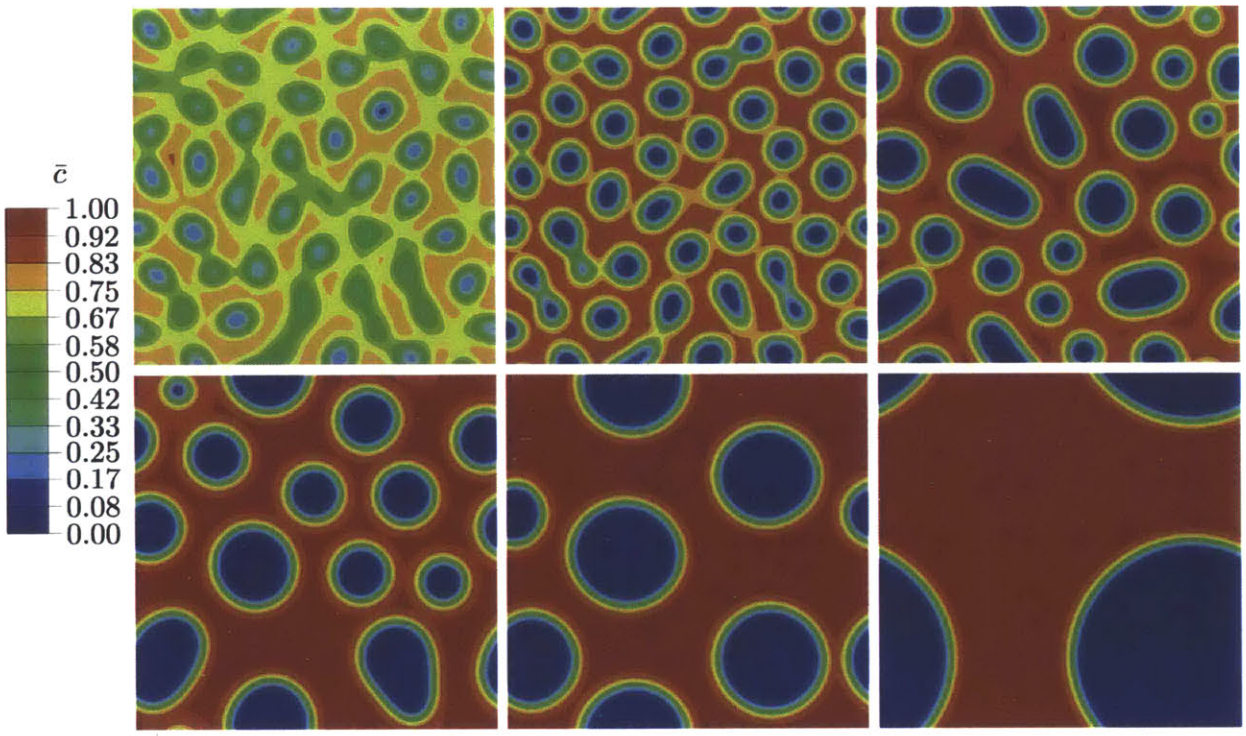

Figure 4-3: Contours of normalized concentration $\bar{c}$ showing the evolution of phase-separation morphology in two dimensions for $\bar{c}_0 = 0.63$, at different times $t \approx [0.4, 0.8, 6.5, 20, 100, 10^5]$ seconds.

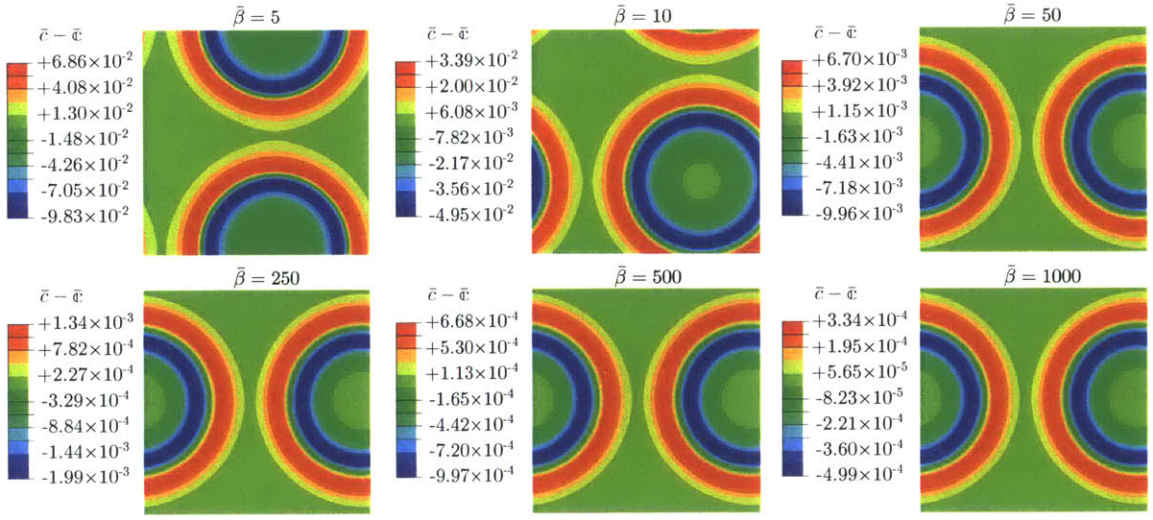

Figure 4-4: Contours of the difference $\bar{c} - \bar{\bar{c}}$ at steady-state for various values of $\bar{\beta}$ in two dimensions.

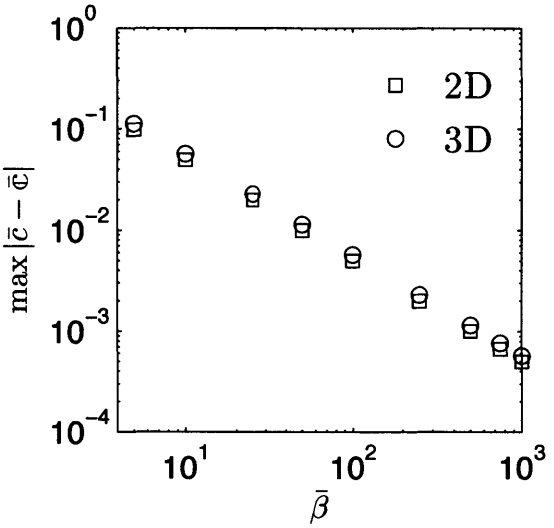

Figure 4-5: Convergence of the maximum of the absolute difference $|\bar{c} - \bar{\mathfrak{c}}|$ as a function of the normalized penalty modulus $\bar{\beta}$ in both two and three dimensions.

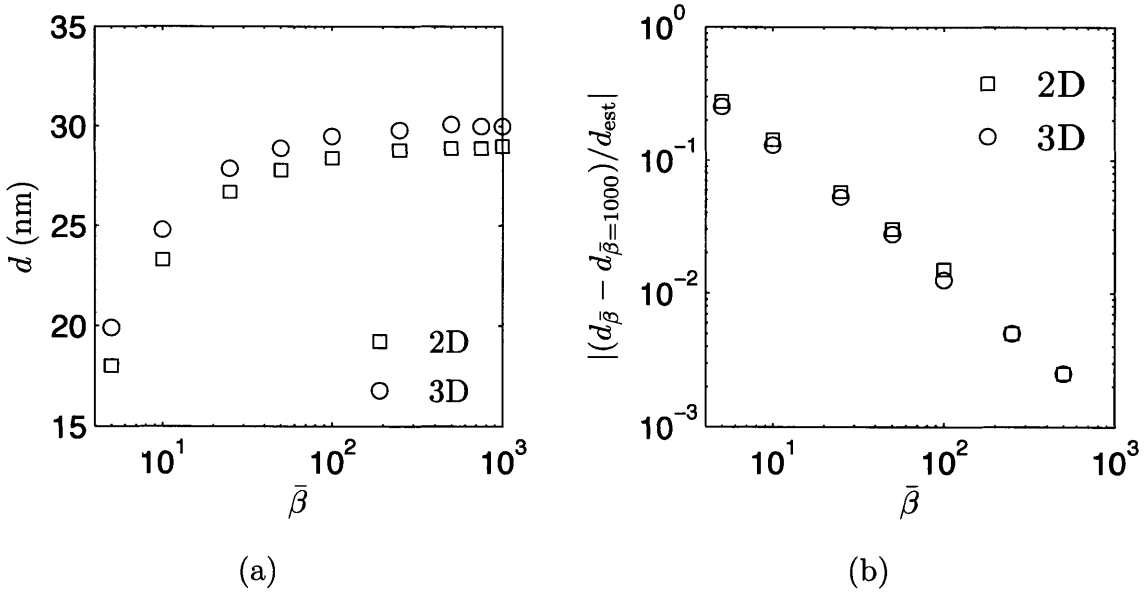

Figure 4-6: (a) Interface-width d as a function of the normalized penalty modulus $\bar{\beta}$. (b) Convergence of the front-width d as a function of the normalized penalty modulus $\bar{\beta}$. In both two and three dimensions.

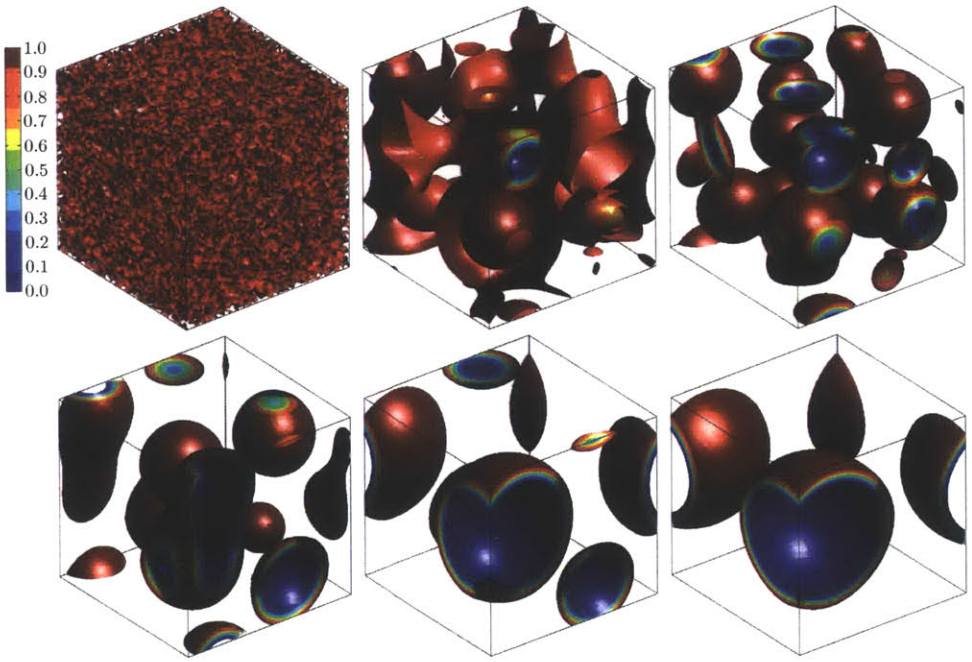

Figure 4-7: Iso-surfaces of normalized concentration $\bar{c}$ showing the evolution of phase-separation morphology in three dimensions for $\bar{c}_0 = 0.75$, at different times $t \approx [0, 3.5, 4.8, 17, 36, 10^5]$ seconds.

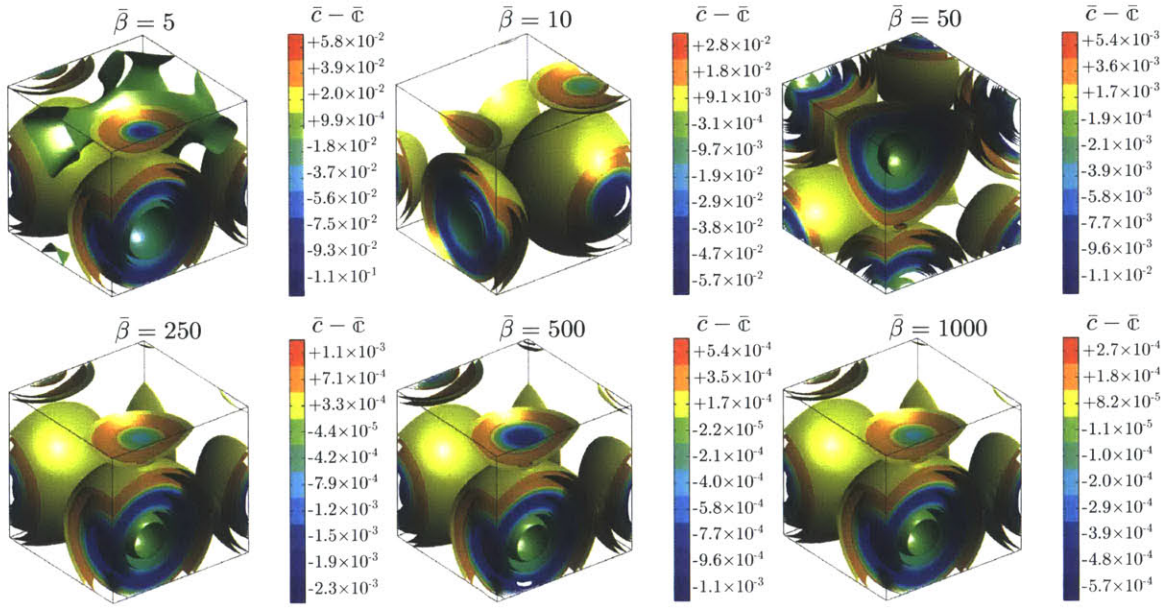

Figure 4-8: Iso-surfaces of the difference $\bar{c} - \bar{\mathbb{c}}$ at steady-state for various values of $\bar{\beta}$ in three dimensions.

Chapter 5

Coupled chemo-mechanical simulations of lithiation of a spheroidal electrode particle

We consider lithiation of a spheroidal particle whose semi-major axis (axis of radial symmetry) is 0.5 μm, and semi-minor axis is 0.3 μm, see Fig. 5-1. The illustrative material properties used in our simulations are shown in Table 5.1. They represent values for a particle made from "isotropic" $LiFePO_4$. Using (4.6) and the values of $\bar{\chi}$ and $\bar{\lambda}$ chosen in Table 5.1, we estimate a potential phase-interface-width of $d_{\text{est}} = 0.04\,\mu$m (in the absence of stress), which is much smaller than the particular particle size chosen for study.[1]

Our interest in this section is to study the effect of stress through the stress potential μ_σ on lithiation. To vary the magnitude of μ_σ which depends on $\mathrm{tr}\mathbf{M}^e$ (cf., eq. 3.117), we shall — keeping the Poisson's ratio ν fixed — vary the value of the Young's modulus of the particle, which will in turn change the magnitude of the Mandel stress $\mathbf{M}^e$ (cf., eq. 3.93). Thus, introducing a normalized elastic modulus

$$\bar{E} = \frac{E}{E_0}, \tag{5.1}$$

where E_0 is the value of the Young's modulus given in Table 5.1, we shall vary the value of $\bar{E}$ in the range

$$\bar{E} \in [0.1, 0.2, 1],$$

and study the effect of stress in the particle on lithiation.

[1] $LiFePO_4$ is an important olivine-type material which is widely-used for the positive electrode in modern Li-ion batteries. We recognize that actual $LiFePO_4$ particles currently used in practice are highly anisotropic nanoparticles, and not isotropic and micron-dimensioned. We leave a study of the important effects of crystallographic anisotropy and the nano-size of $LiFePO_4$ to future work.

Parameter	Value	Source	Parameter	Value
E_0	124.5 (GPa)	a	$\bar{\chi}$	3
ν	0.25	a	$\bar{\lambda}$	2.5×10^{-4} (μm^2)
$c_{\max}$	2.29×10^4(mol/m^3)	b	$\bar{\kappa}$	10^3
Ω	4.05×10^{-6}(m^3/mol)	c	ϑ	300 (K)
D_0	1×10^{-14}(m^2/sec)	d		

Table 5.1: Material properties used in the simulations. Values for the Young's modulus E and the Poisson's ratio ν are the average of the values for $FePO_4$ and $LiFePO_4$, estimated by Maxisch and Ceder (2006) for isotropic polycrystalline materials from the anisotropic single-crystal constants. Sources: a — Maxisch and Ceder (2006), b — Zeng and Bazant (2014), c — Rousse et al. (2003), d — Malik et al. (2010).

Due to the symmetry of the geometry, we mesh only one quarter of the cross-section of the spheroidal particle with 3675 four-noded fully-integrated axi-symmetric elements; cf. Fig. 5-1. The boundary conditions used in our simulations are as follows:

- **Mechanical boundary conditions**: The nodes along edge AB (radial symmetry) are constrained to have zero radial displacement, while the nodes along edge BC (mirror symmetry) are constrained to have zero vertical displacement. Further, the exterior boundary AC is taken to be traction-free. Also, no body forces are applied.

- **Chemical boundary conditions**: The edges AB and BC are prescribed zero flux conditions, $\mathbf{j}_{\mathrm{R}} \cdot \mathbf{n}_{\mathrm{R}} = 0$, while on the exterior boundary AC the species flux is controlled by the boundary condition

$$\mathbf{j}_{\mathrm{R}} \cdot \mathbf{n}_{\mathrm{R}} = k(\mu_{\mathrm{Li}}^{(\text{electrode surf.})} - \tilde{\mu}_{\mathrm{ext}}), \tag{5.2}$$

  where $\mu_{\mathrm{Li}}^{(\text{electrode surf.})}$ is the chemical potential at the boundary of the electrode particle — which depends on both the concentration and the stress at the boundary through (3.96) — and $\tilde{\mu}_{\mathrm{ext}}$ is the externally "applied" electrochemical potential. The quantity $\tilde{\mu}_{\mathrm{ext}}$ is controlled in our simulations to model *lithium insertion* ($\mu_{\mathrm{Li}}^{(\text{electrode surf.})} < \tilde{\mu}_{\mathrm{ext}}$) and *lithium extraction* ($\mu_{\mathrm{Li}}^{(\text{electrode surf.})} > \tilde{\mu}_{\mathrm{ext}}$). The parameter $k > 0$ is a factor which characterizes the apparent conductance of the electrode/electrolyte interface to a flux of Li ions.[2]

  In our simulations we use a value of $k = 1$. This value was chosen so that the lithiation of the particles is limited by the diffusion of Li in the bulk of the electrode particle, and

[2]This boundary condition can also be derived by considering linear electrochemical reaction kinetics at this boundary, see Sect. 8.13, in which the boundary condition would stem from a suitable linearization of (8.167).

not by the conductance of Li across the electrode/electrolyte interface, cf. the remark below.

- **Boundary condition for the micromorphic concentration $\mathfrak{c}_R$**: We set

$$\nabla \mathfrak{c}_R \cdot \mathbf{n}_R = 0$$

on all boundaries AB, BC, and AC; cf., eq. $(3.111)_2$.

Remark. The flux of Li through the surface is controlled by the conductance parameter k defined in (5.2) above, while the flux of the lithium within the bulk of the electrode particle is controlled by the mobility parameter m (cf. 3.83). The ratio k/m has units of inverse length, and with L denoting a characteristic length dimension of the particle, we may — using the analogy with standard ideas in heat-transfer — define a dimensionless "Biot"-number

$$\mathrm{Bi} \stackrel{\mathrm{def}}{=} \frac{kL}{m}. \tag{5.3}$$

As in heat-transfer, if $\mathrm{Bi} \gg 1$ then the surface reaction processes offers little resistance to species transfer, while if $\mathrm{Bi} \ll 1$ then the surface reaction processes offer substantial resistance to species transfer while the species concentration within the particle is almost constant.

In this part of our work we are concerned with circumstances in which $\mathrm{Bi} \gg 1$, such that that the surface reaction processes offer little resistance to species transfer. Accordingly, for our simulations of the lithiation of a spheroidal particle, with $m \approx m_0 c_{R,\max} = D_0 c_{R,\max}/R\vartheta$, we find that for the values of D_0, $c_{R,\max}$, and ϑ given in Table 5.1, and a characteristic length of the particle $L = 0.3\,\mu\mathrm{m}$, that a value $k = 1\,\mathrm{mol}^2/(\mathrm{m}^2\ \mathrm{J\ s})$ gives $B = 3.3 \times 10^5$ — a value which is very much larger than 1. Accordingly, in the simulations reported in Chapter 5 we use a value of surface conductance $k = 1\,\mathrm{mol}^2/(\mathrm{m}^2\ \mathrm{J\ s})$. □

We have conducted simulations for two different chemical loading conditions:

(a) **Slow ramp of $\tilde{\mu}_{\mathrm{ext}}$**: First we consider the case in which $\tilde{\mu}_{\mathrm{ext}}$ is ramped linearly from an initial value $\tilde{\mu}_i$ to a final value $\tilde{\mu}_f$,

$$\tilde{\mu}_{\mathrm{ext}} = \tilde{\mu}_i + (\tilde{\mu}_f - \tilde{\mu}_i)(t/T), \tag{5.4}$$

over a time $T = 30\,\mathrm{min}$. We consider this ramp to be *slow*, since the ramp-time of $T = 30\,\mathrm{min}$ is much larger than the characteristic time scale for diffusion $\tau = (0.5\,\mu\mathrm{m})^2/D_0 = 25\,\mathrm{s}$ of Li in the particle. The initial and final electrochemical potentials are chosen based on the chemical potential of the Li in the stress-free electrode at normalized concentrations of $\bar{c} = 0.005$ and $\bar{c} = 0.995$:[3]

$$\mu_i(\bar{c} = 0.005) = -5.8\,\mathrm{kJ/mol}, \quad \text{and} \quad \mu_f(\bar{c} = 0.995) = 5.8\,\mathrm{kJ/mol}. \tag{5.5}$$

[3]These values where simply computed using eq. (3.115) with $\bar{c} - \bar{\mathfrak{c}} = 0$, and $\mu_\sigma = 0$.

(b) **Step change in $\tilde{\mu}_{\text{ext}}$**: In this case $\tilde{\mu}_{\text{ext}}$ is ramped from $\tilde{\mu}_i$ to $\tilde{\mu}_f$ nearly instantaneously, and then held constant. Numerically, this was realized by ramping $\tilde{\mu}_{\text{ext}}$ to its final value in $T = 1\,\text{sec}$,[4] and then maintaining it constant until full lithiation was achieved.

5.1 Lithiation under a slow ramp of $\tilde{\mu}_{\text{ext}}$

When the electrochemical potential $\tilde{\mu}_{\text{ext}}$ is ramped slowly from $\tilde{\mu}_i$ to $\tilde{\mu}_f$, bulk diffusion of Li in the particle is much faster than the rate of increase of the concentration of Li on the boundary. This leads to a concentration profile inside the particle which is essentially homogeneous up until the point at which phase-separation initiates at the boundary of the particle.

A commonly used quantity in the Li-ion battery literature is the *state-of-charge* (SOC),

$$\text{SOC} \stackrel{\text{def}}{=} \frac{\left(\int_{\text{B}} \bar{c}\, dv_{\text{R}}\right)}{\left(\int_{\text{B}} dv_{\text{R}}\right)}, \tag{5.6}$$

which represents the volume average of the net species concentration in the particle. We use this average quantity as a measure of the extent of lithiation of the particle.

Fig. 5-2(a) shows the sate-of-charge (SOC) of the particle as a function of time for the entire simulation span from 0 to 1800 s, while Fig. 5-2(b) focuses-in on the time period $1060 \leq t \leq 1120\,\text{s}$ in which a Li-rich and a Li-poor phase co-exist within the particle. The effect of varying $\bar{E} \in [0.1, 0.2, 1]$ on the state-of-charge versus time curves is not very distinguishable in Fig. 5-2(a), but is clearly visible in the time-window shown in Fig. 5-2(b), when the particle exhibits phase-separation. As $\bar{E}$ increases, Fig. 5-2(b) shows that the time taken to lithiate the particle decreases. That is, the increased level of stresses, and hence μ_σ, act to enable faster lithiation of the particle under the particular chemical-boundary conditions considered here.

The different values of $\bar{E}$ also result in different distributions of the normalized Li concentration $\bar{c}$, and the maximum principal Cauchy stress σ_1 in the particle. The contour plots of these quantities at $t = 1080\text{s}$, indicated by a dashed line in Fig. 5-2(b), are shown in Fig. 5-2(c).

Fig. 5-2(c) (top) shows that at the smallest value of $\bar{E} = 0.1$, one obtains a "core-shell" type of Li distribution in the particle. However, as the value of $\bar{E}$ increases from 0.1 to 1.0, one no longer obtains a core-shell type of lithium distribution — instead, because of the spheroidal geometry, a mildly curved "planar front" separates a high-Li concentration region from the low-Li concentration region. This is an important result because it indicates that the widely-presumed "core-shell" type of lithiation is not the most energetically favorable lithium concentration distribution under the conditions of the problem under study. The contours in Fig. 5-2(c) (top) also show a widening of the interface separating the two phases

[4] As opposed to $T = 30\text{mins}$ in case (a).

as the value of $\bar{E}$ increases — this is another manifestation of the effect of stress in coupled diffusion-deformation problems.

The change in the distribution of the lithium concentration with increasing values of $\bar{E}$ also has an important effect on the resulting stress distribution in the particle. Fig. 5-2(c) (bottom) shows contours of the maximum principal stress σ_1. Note that unlike the situation for $\bar{E} = 0.1$, where the maximum principal stress on the periphery of the particle is compressive, $\sigma_1 \lessapprox -100$ MPa, — which is what one expects from a core-shell-like distribution of the Li-concentration — for the case $\bar{E} = 1.0$ there are regions on the periphery of the particle with values of $\sigma_1 \gtrapprox 700$ MPa. Since fracture of brittle electrode particles is usually dictated by large positive values of the maximum principal stress, this result predicts substantially different potential sites for fracture than are predicted by a theory in which the coupling of the diffusion and phase-separation with the attendant mechanical swelling is not properly accounted for.

In Fig. 5-3(a) we plot the externally-applied electrochemical potential $\tilde{\mu}_{\text{ext}}$ as a function of SOC, for both Li-insertion and Li-extraction, where the Li-extraction step is simulated by simply reversing the $\tilde{\mu}_{\text{ext}}$ ramp to vary from $\tilde{\mu}_f$ to $\tilde{\mu}_i$. To make contact with the manner in which these results are typically presented in the literature, in Fig. 5-3(b) we plot the interfacial voltage V versus SOC, where

$$V \stackrel{\text{def}}{=} V^0 - \frac{\tilde{\mu}_{\text{ext}}}{F}. \tag{5.7}$$

Here, $V^0 = 3.42$ volts denotes the reference open-circuit voltage of an $LiFePO_4$-electrode versus a reference Li-metal electrode (c.f. Bai et al., 2011), F is the Faraday constant, and V is the potential difference between the $LiFePO_4$-electrode and the electrolyte. This figure clearly shows the *signature plateau in the experimentally-observed voltage versus SOC curves for Li-ion batteries with $LiFePO_4$ cathodes* (cf. Fig. 7 in Tarascon and Armand, 2001b).

The barely discernible multiple lines in the plateau regions of Fig. 5-3 correspond to different values of $\bar{E}$; there is essentially no effect of varying $\bar{E}$ on the curves shown in this figure. This is a result of the fact that we have prescribed the externally-applied electrochemical potential $\tilde{\mu}_{\text{ext}}$, and thus can not discern the effects of stress by simply looking at plots of $\tilde{\mu}_{\text{ext}}$ versus SOC.

5.2 Lithiation under a step change in $\tilde{\mu}_{\text{ext}}$

Next we consider the case in which $\tilde{\mu}_{\text{ext}}$ is quickly ramped from $\tilde{\mu}_i$ to $\tilde{\mu}_f$ in 1 second, and then held constant until full lithiation of the particle has been achieved. Fig. 5-4(a) shows the SOC of the particle as a function of time for different values of $\bar{E}$. Note first that in contrast to the results in the previous subsection for the slow ramp, for the step change boundary condition phase-separations occur nearly instantaneously for all values of $\bar{E}$. The SOC versus time curves show different rise-times for different values of $\bar{E}$. Consistent with

the results of the simulations in the previous subsection, we observe that an increase $\bar{E}$ results in *faster lithiation of the particle.*

Fig. 5-4 (b) shows contours of the normalized concentration $\bar{c}$ (top), and of the maximum principal stress σ_1 (bottom). These contours correspond to a time of $t = 3\,\mathrm{s}$, which is indicated by a dashed line in Fig. 5-4(b). In contrast to the previous simulations, the contours of $\bar{c}$ show that in all of the simulations, regardless of the magnitude of $\bar{E}$, the particles lithiate with a "core-shell" type of phase distribution. Such a phase distribution is a direct result of the fast "step"-change of the electrochemical potential on the boundary. Since $\tilde{\mu}_{\mathrm{ext}}$ is ramped to $\tilde{\mu}_f$ in 1s, this amount of time is much shorter than the time for diffusion of $\tau = 25\,\mathrm{s}$ of Li in the particle; there is not enough time for two phases to form and stably co-exist on the surface of the particle, and the result is a core-shell type of phase distribution in the particle. Consistent with the simulations shown previously in Fig. 5-2, an increase in $\bar{E}$ for the present boundary condition also results in a widening of the interface separating the two phases. The maximum tensile values of the maximum principal Cauchy stress occur in the interior of the particle during lithiation — it reaches a high value of $\sigma_1 = 1.2\mathrm{GPa}$ for $\bar{E} = 1$.

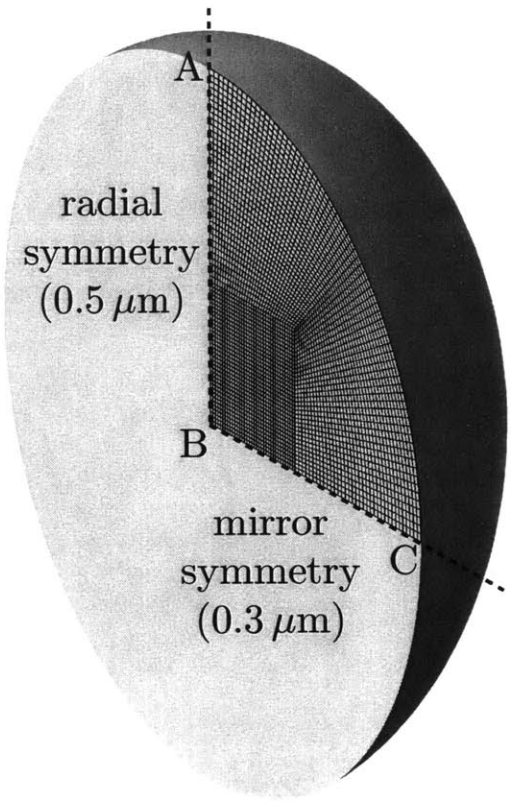

Figure 5-1: Spheroid geometry and finite-element mesh used in computation. Due to the symmetry of the problem, only a quarter of the cross-section of the spheroid is meshed with axisymmetric elements.

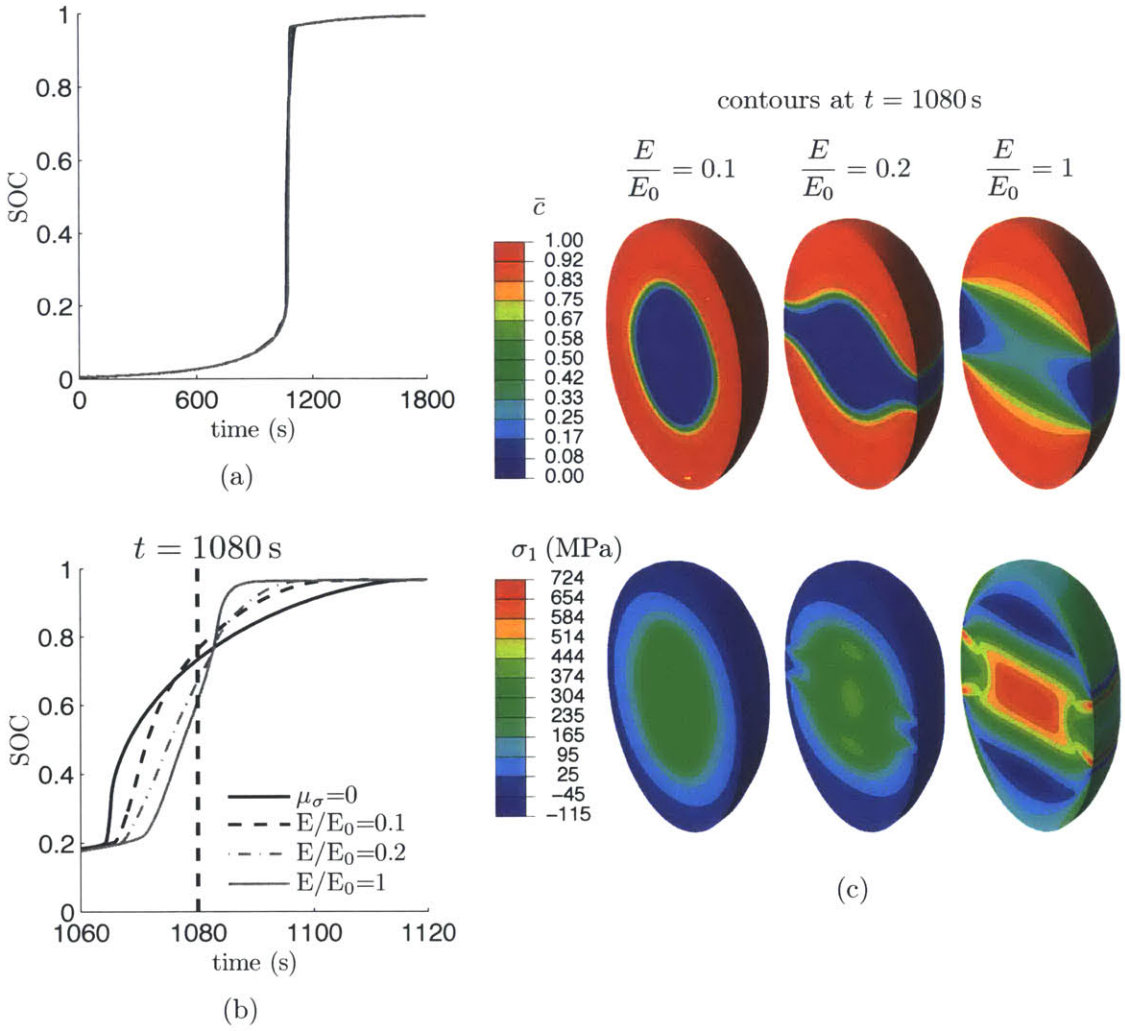

Figure 5-2: Simulations with varying Young's modulus under an applied **slow ramp** of the external electrochemical potential. (a) State of charge (SOC) vs. time for the entire lithiation simulation. (b) SOC vs. time focused around the time at which phase-separation occurs. (c) Contours at $t = 1080\,\mathrm{sec}$ of normalized concentration $\bar{c}$ (top), and of the maximum principal stress σ_1 (bottom), for three varying values of the normalized modulus $\bar{E} = E/E_0$.

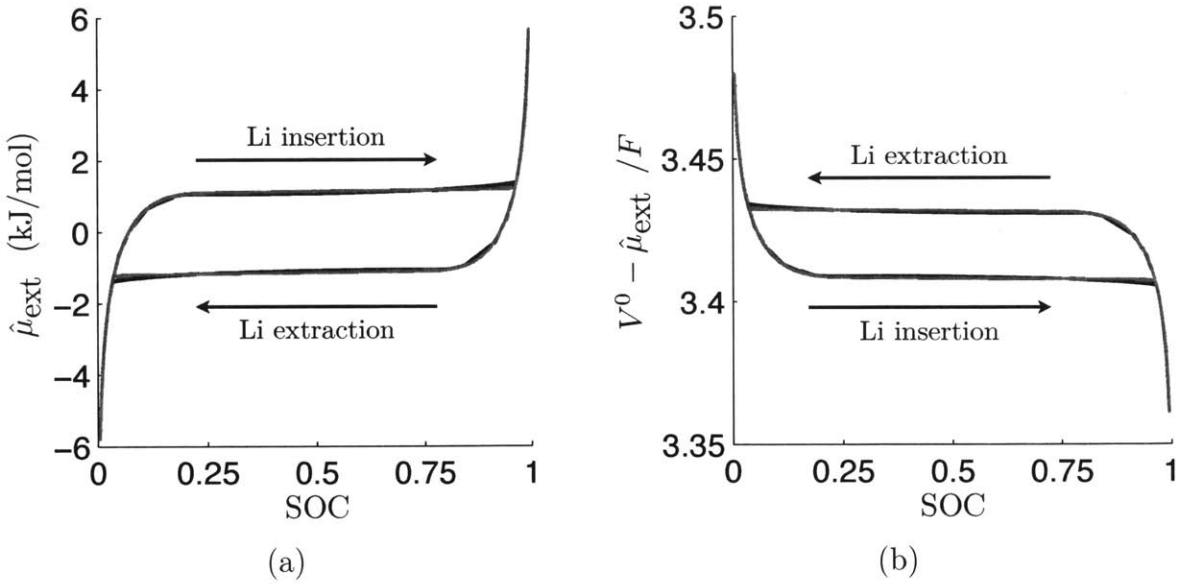

Figure 5-3: (a) Applied electrochemical potential vs. state of charge. (b) Applied voltage vs. state of charge. ($V^0 = 3.42\,\text{V}$ is the standard potential against Li metal, and F is Faraday's constant)

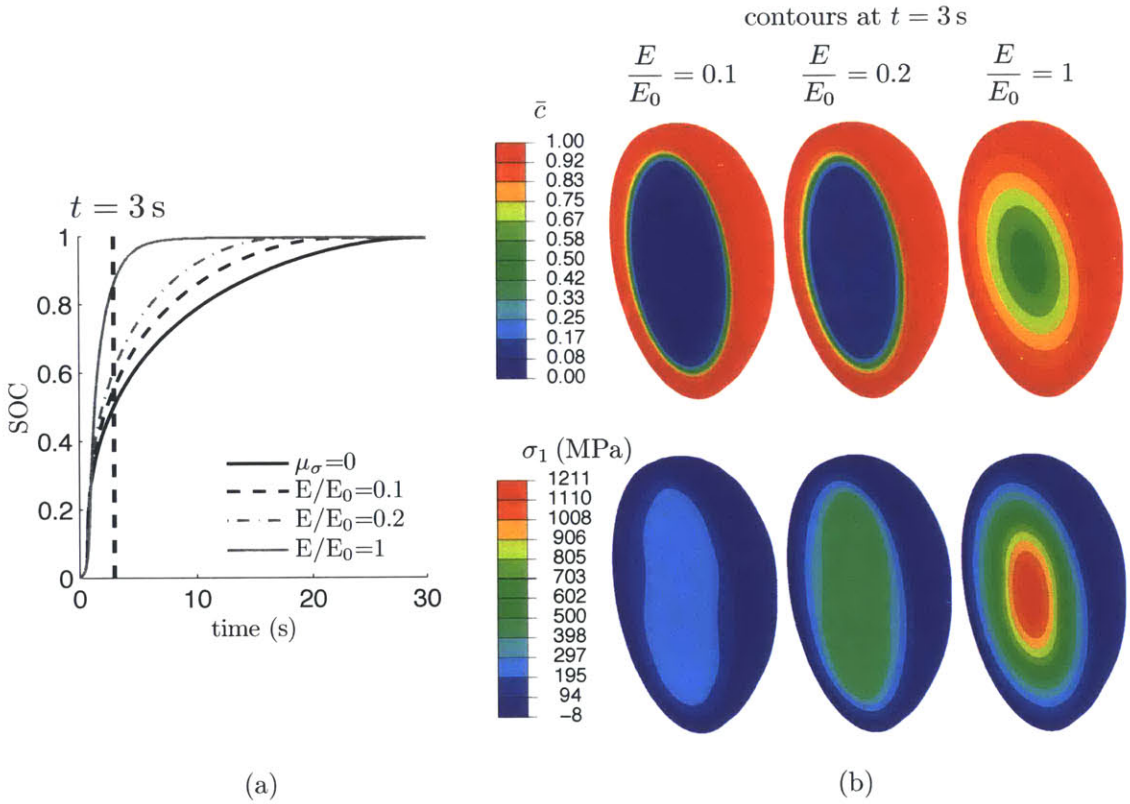

(a) (b)

Figure 5-4: Simulations with varying Young's modulus under an applied **step** of the external electrochemical potential. (a) State of charge vs. time. (b) Contours at $t = 3\,\text{sec}$ of normalized concentration $\bar{c}$ (top), and of maximum principal stress σ_1 (bottom), for three varying values of the normalized modulus $\bar{E} = E/E_0$.

Chapter 6

Concluding remarks

We have formulated a thermodynamically-consistent theory which couples Cahn-Hilliard-type species diffusion with large elastic deformations of a body. In contrast to the traditional Cahn-Hilliard theory which is based on c_{R} and ∇c_{R}, our theory is based on c_{R}, another scalar $\mathfrak{c}_{\mathrm{R}}$, and its gradient $\nabla \mathfrak{c}_{\mathrm{R}}$. For the diffusion-only problem which is uncoupled from mechanics, instead of a partial differential equation (pde) for the concentration c_{R} which involves fourth-order spatial derivatives, one then obtains two coupled second-order pdes for c_{R} and $\mathfrak{c}_{\mathrm{R}}$. These two pdes, when taken together with the pde representing the balance of forces, represent the three governing pdes for the chemo-mechanically-coupled problem. These equations are amenable to finite element solution methods, which employ standard C^0-continuous finite element basis functions.

The general constitutive theory is specialized for isotropic materials, and within the isotropic idealization the constitutive equations are further specialized to model the chemo-mechanically-coupled problem of diffusion of Li in phase-separating electrode materials for Li-ion batteries.

The specialized theory has been implemented in the widely-used finite-element package Abaqus (2010) by writing custom user-element subroutines (UELs). This numerical simulation capability is used to study aspects of (a) the diffusion-only problem of spinodal decomposition, and (b) the chemo-mechanically-coupled problem of lithiation of a spheroidal-shaped particle of a representative cathode material.

Much remains to be done to extend the theory and the numerical simulation capability to model actual electrode materials. Many cathode and anode materials currently used in Li-ion batteries are highly anisotropic and used as particles with nano-metric dimensions — they are not isotropic and micron-dimensioned. Our general chemo-mechanically-coupled phase-field theory is amenable to be specialized to account for such anisotropies, but we leave such specializations and a study of the important effects of crystallographic anisotropy and the nanometric size of modern electrode particles to future work. Also of major importance for future study is the role of the many different types of boundary conditions which are

encountered in the operation of actual Li-ion batteries. For nanometer-sized particles in which the surface-to-volume ratio is large, there is also a need to properly formulate and study the effects of boundary conditions which account for possibly-important surface energy effects.

Part II

Modeling amorphous Silicon electrodes

Chapter 7

Introduction

The development of Li-ion batteries with improved capacity, life, safety, and cost, is of major importance for a wide range of industries — from large-scale stationary energy storage systems in renewable energy plants, to portable power systems for sustainable electric vehicles. In an attempt to increase capacity, researchers have proposed the use of lithium-metal alloys, e.g. lithium-silicon and lithium-tin alloys, or a combination of lithium-metal alloys and graphite, as potential anode materials since they possess a higher capacity for Li than the current-generation graphite anodes (cf., e.g., Li et al., 1999; Tarascon and Armand, 2001a; Scrosati and Garche, 2010). For example, when fully lithiated to $Li_{15}Si_4$, a silicon anode can theoretically achieve a specific capacity of $\sim 3.5\,\mathrm{Ah/g}$, which compares with only $0.37\,\mathrm{Ah/g}$ for the current-generation graphite anodes. However, the intercalation of such a large amount of Li into the silicon induces very large elastic-plastic deformations — with volume changes of approximately of $\sim 300\%$ (Obrovac and Krause, 2007). The two major mechanisms by which the large deformations of the anode negatively affect its performance are:

- *Fracture of the anode particles.* The large stresses that develop in the anode due to inhomogeneous volume changes associated with large gradients of Li-ions in the anode can lead to fracture of an anode particle. The formation and propagation of cracks in turn lead to degradation of the performance of the battery, and significantly limit its lifetime.

- *Failure of the solid electrolyte interface (SEI).* During operation of a Li-ion battery, a passivating film, known as the solid electrolyte interface (SEI), forms on the surface of the anode. Due to the large volumetric changes associated with the lithiation of Si anodes, the SEI is placed under large tensile stresses, which in turn cause it to fail. Repeated failure and growth of the SEI leads to capacity fade of the battery.

In order to develop a successful Si-based anode, both the problems mentioned above need to be addressed. Fracture of anode particles has been successfully mitigated through the

use of nano- and micro-dimensioned particles. When the anode is composed of crystalline silicon (c-Si), nano-dimensioned materials have been successfully lithiated without fracture, even though lithiation in these materials occurs by a two-phase mechanism where pure c-Si reacts with Li, forming a heavily lithiated amorphous Li_xSi phase (often $Li_{15}Si_4$) behind a propagating phase front (cf., e.g., Ryu et al., 2011; Liu et al., 2012b). More recently, it has been found that the lithiation behavior of *amorphous Si* (a-Si) is substantially different from that of c-Si. Indeed, a-Si nanoparticles have been observed to be quite robust to fracture during cycling (He et al., 2011; McDowell et al., 2012), and Berla et al. (2014) have recently shown that a-Si is resistant to fracture even at the micron scale ($\sim 2\mu$m). *In this thesis, we focus on modeling the response of amorphous Silicon (a-Si) as an anode material.* For brevity, henceforth we often simply write Si rather than a-Si.

In order to mitigate failure of the SEI due to the large volume changes associated with lithiating Si anodes, various research groups have proposed the use of novel "engineered" anodes which restrict the deformation incurred by the SEI during cyclic lithiation. One such engineered anode, developed by Wu et al. (2012), consists of an ensemble of hollow Si nanotubes whose exterior surfaces have been oxidized to form silicon-dioxide. The electrolyte contacts the anode only at the silicon-dioxide surface, and thus the SEI grows only on the exterior of the nanotube and is not in contact with the Si. The relatively stiff silicon-dioxide shell acts as a mechanical constraint layer which prevents the outward expansion of the nanotube, and thus effectively restricts the deformation which is incurred by the SEI. However, the presence of the silicon-dioxide constraining layer leads to the generation of very large stresses during cyclic lithiation, forcing the Si anode to deform plastically towards the inside of the hollow nanotube. The elastic-plastic deformation of the Si anode, resulting from the mechanical constraint imposed by the silicon-dioxide layer, will have a significant effect on the electrochemical performance of the anode, which at present is largely unexplored, and is the focus of this thesis. We expect, as noted by Sethuraman et al. (2010b), that plasticity will play a role both in determining the energy dissipated during cycling of the anode as well as in determining the realizable capacity of the anode.

Recently, Zhao et al. (2011), Bower et al. (2011), and Anand (2012) have proposed theories which couple large elastic-plastic deformations with large volumetric swelling due to diffusion of lithium. Further, substantial progress has been made recently by Bucci et al. (2014) to calibrate the theory of Bower et al. (2011) to results from their experiments in which a half-cell based on an a-Si thin film deposited on a quartz substrate is electrochemically cycled while the curvature of the substrate is simultaneously measured; cf. also Pharr et al. (2014). However, to the best of our knowledge, such theories have not been used to determine how the elastic-plastic deformation of a-Si affects the electrochemical performance of anodes with more complex geometries such as those of the oxidized hollow a-Si nanotubes of Wu et al. (2012).[1]

[1]We note that Zhao et al. (2012) have previously studied the generation of stresses in spherical and cylindrical hollow core-shell nanostructures. However, in their study they used various simplifying assumptions — e.g., rigid-perfectly-plastic material, no effect of concentration on the material properties, plane-strain condi-

Accordingly, the purpose of this thesis is to report on our theory and finite-element-based numerical simulation method for modeling geometrically complex a-Si anodes of the type studied by Wu et al. (2012). We have applied our simulation capability to quantifying how the elastic-plastic deformation deformation of engineered silicon anodes affects their electrochemical performance.

This Part of the thesis is structured as follows. In Chapter 8 we develop a thermodynamically consistent framework for coupling species diffusion with large elastic-plastic deformations. First, in Sections 8.1 through 8.8 we develop a reasonably general theoretical framework. In Section 8.10 we specialize our general framework, which is summarized in Section 8.11, and in Section 8.12 we further summarize the governing partial differential equations and the boundary conditions for our theory. Finally, in Section 8.14 we briefly discuss the numerical implementation of our theory. The theory was numerically implemented by writing user-element subroutines for the commercial finite element program Abaqus (2010).

In Chapter 9, in order to estimate the material parameters in our theory which are not directly available in the literature, we calibrate the material parameters of our theory to results from substrate curvature experiments available in the recent literature (Pharr et al., 2014; Bucci et al., 2014).

In Chapter 10 we apply our fully calibrated theory to modeling the hollow double-walled amorphous Silicon nanotube anodes of Wu et al. (2012). Beyond comparing our simulation predictions to the results from their experiments, we investigate the importance of plasticity on the electrochemical behavior of such anodes. We finish in Chapter 11 with some concluding remarks.

tions, uniform concentration, etc. Further, they made no attempt to model the voltage versus state-of-charge response of the system, and compare model predictions against experimental results.

Chapter 8

Diffusion-deformation theory for amorphous silicon anodes

In order to model the experimentally-observed chemo-mechanical response of a-Si (e.g., Pharr et al., 2014; Bucci et al., 2014), the theory summarized below accounts for:

(i) large elastic-plastic deformations using finite deformation kinematics;

(ii) variation of the elastic moduli with varying lithium content;

(iii) dependence of the yield strength on lithium content; and

(iv) rate-sensitive plastic response.

We are interested in studying *amorphous* Si. Hence, from the onset, we will assume that the deformation incurred by the body due to intercalation is isotropic, this will be made mathematically precise in the sections to follow. Further, we note that we restrict ourselves to *isothermal* conditions.

Notation: We use standard notation of modern continuum mechanics (Gurtin et al., 2010). Specifically: ∇ and Div denote the gradient and divergence with respect to the material point $\mathbf{X}$ in the reference configuration; grad and div denote these operators with respect to the point $\mathbf{x} = \boldsymbol{\chi}(\mathbf{X}, t)$ in the deformed body; a superposed dot denotes the material time-derivative. Throughout, we write $\mathbf{F}^{e-1} = (\mathbf{F}^e)^{-1}$, $\mathbf{F}^{e-\mathsf{T}} = (\mathbf{F}^e)^{-\mathsf{T}}$, etc. We write $\operatorname{tr}\mathbf{A}$, $\operatorname{sym}\mathbf{A}$, $\operatorname{skw}\mathbf{A}$, $\mathbf{A}_0$, and $\operatorname{sym}_0\mathbf{A}$ respectively, for the trace, symmetric, skew, deviatoric, and symmetric-deviatoric parts of a tensor $\mathbf{A}$. Also, the inner product of tensors $\mathbf{A}$ and $\mathbf{B}$ is denoted by $\mathbf{A}:\mathbf{B}$, and the magnitude of $\mathbf{A}$ by $|\mathbf{A}| = \sqrt{\mathbf{A}:\mathbf{A}}$.

8.1 Kinematics

Consider a macroscopically-homogeneous body B with the region of space it occupies in a fixed reference configuration, and denote by $\mathbf{X}$ an arbitrary material point of B. A motion of B is then a smooth one-to-one mapping $\mathbf{x} = \boldsymbol{\chi}(\mathbf{X}, t)$ with deformation gradient, velocity, and velocity gradient given by

$$\mathbf{F} = \nabla\boldsymbol{\chi}, \qquad \mathbf{v} = \dot{\boldsymbol{\chi}}, \qquad \mathbf{L} = \operatorname{grad}\mathbf{v} = \dot{\mathbf{F}}\mathbf{F}^{-1}. \tag{8.1}$$

We base the theory on a multiplicative decomposition of the deformation gradient

$$\mathbf{F} = \mathbf{F}^e\mathbf{F}^p\mathbf{F}^s, \qquad \text{with} \qquad \mathbf{F}^s = \lambda^s\mathbf{1}, \qquad \lambda^s > 0. \tag{8.2}$$

Here, suppressing the argument t:

(i) $\mathbf{F}^s(\mathbf{X})$ represents the local distortion of the material neighborhood of $\mathbf{X}$ due to a volumetric swelling (de-swelling) due to insertion (extraction) of lithium, with λ^s the swelling stretch;

(ii) $\mathbf{F}^p(\mathbf{X})$ represents the local irreversible plastic deformation of the swollen neighborhood of $\mathbf{X}$ caused by inelastic mechanisms such as the motion of dislocations in crystalline materials or shear transformations of atomic clusters in amorphous materials; and

(iii) $\mathbf{F}^e(\mathbf{X})$ represents the subsequent stretching and rotation of this coherent swollen and plastically deformed material neighborhood, and thereby represents a corresponding elastic distortion.

We refer to $\mathbf{F}^s$, $\mathbf{F}^p$, and $\mathbf{F}^e$ as the *swelling, plastic, and elastic distortions*, respectively. We write

$$J \stackrel{\text{def}}{=} \det\mathbf{F} > 0, \tag{8.3}$$

and hence, using (8.2),

$$J = J^eJ^pJ^s, \qquad \text{where} \qquad J^e \stackrel{\text{def}}{=} \det\mathbf{F}^e > 0 \qquad J^p \stackrel{\text{def}}{=} \det\mathbf{F}^p > 0, \qquad \text{and} \qquad J^s \stackrel{\text{def}}{=} \det\mathbf{F}^s > 0, \tag{8.4}$$

so that $\mathbf{F}^e$, $\mathbf{F}^p$ and $\mathbf{F}^s$ are invertible. Note that from $(8.2)_2$,

$$J^s = (\lambda^s)^3. \tag{8.5}$$

The right and left polar decompositions of $\mathbf{F}^e$ are given by

$$\mathbf{F}^e = \mathbf{R}^e\mathbf{U}^e = \mathbf{V}^e\mathbf{R}^e, \tag{8.6}$$

where $\mathbf{R}^e$ is a rotation, while $\mathbf{U}^e$ and $\mathbf{V}^e$ are symmetric, positive-definite right and left stretch tensors with

$$\mathbf{U}^e = \sqrt{\mathbf{F}^{e\mathsf{T}}\mathbf{F}^e} \qquad \text{and} \qquad \mathbf{V}^e = \sqrt{\mathbf{F}^e\mathbf{F}^{e\mathsf{T}}}. \tag{8.7}$$

Also, the right elastic Cauchy-Green deformation tensor is given by

$$\mathbf{C}^e = \mathbf{U}^{e2} = \mathbf{F}^{e\mathsf{T}}\mathbf{F}^e. \tag{8.8}$$

Next, by $(8.1)_3$ and (8.2), and noting that $\mathbf{F}^s$ is spherical in form,

$$\mathbf{L} = \mathbf{L}^e + \mathbf{F}^e\Big(\mathbf{L}^p + \mathbf{L}^s\Big)\mathbf{F}^{e-1}, \tag{8.9}$$

with

$$\mathbf{L}^e = \dot{\mathbf{F}}^e\mathbf{F}^{e-1}, \qquad \mathbf{L}^p = \dot{\mathbf{F}}^p\mathbf{F}^{p-1}, \qquad \mathbf{L}^s = \dot{\mathbf{F}}^s\mathbf{F}^{s-1}. \tag{8.10}$$

As is standard, we define the elastic, plastic and swelling stretching and spin tensors through

$$\left.\begin{aligned} \mathbf{D}^e &= \mathrm{sym}\mathbf{L}^e, \qquad \mathbf{W}^e = \mathrm{skw}\,\mathbf{L}^e,\\ \mathbf{D}^p &= \mathrm{sym}\mathbf{L}^p, \qquad \mathbf{W}^p = \mathrm{skw}\,\mathbf{L}^p,\\ \mathbf{D}^s &= \mathrm{sym}\mathbf{L}^s, \qquad \mathbf{W}^s = \mathrm{skw}\,\mathbf{L}^s, \end{aligned}\right\} \tag{8.11}$$

so that $\mathbf{L}^e = \mathbf{D}^e + \mathbf{W}^e$, $\mathbf{L}^p = \mathbf{D}^p + \mathbf{W}^p$, and $\mathbf{L}^s = \mathbf{D}^s + \mathbf{W}^s$.

Further from (8.2), $(8.10)_3$, and $(8.11)_3$

$$\mathbf{D}^s = \big(\dot{\lambda}^s\lambda^{s-1}\big)\mathbf{1} \qquad \text{and} \qquad \mathbf{W}^s = \mathbf{0}. \tag{8.12}$$

Also, since

$$\dot{J}^s = J^s\,\mathrm{tr}\mathbf{D}^s, \tag{8.13}$$

we have

$$\mathbf{D}^s = \frac{1}{3}\big(\dot{J}^sJ^{s-1}\big)\mathbf{1}, \tag{8.14}$$

and, since $\mathbf{L}^s \equiv \mathbf{D}^s$, we have

$$\dot{\mathbf{F}}^s = \mathbf{D}^s\mathbf{F}^s. \tag{8.15}$$

Next, we make two basic kinematical assumptions concerning plastic flow:

(i) First, we make the standard assumption that *plastic flow is incompressible*, so that

$$J^p = \det\mathbf{F}^p = 1 \qquad \text{and} \qquad \mathrm{tr}\mathbf{L}^p = \mathrm{tr}\mathbf{D}^p = 0. \tag{8.16}$$

Hence, using (8.4)

$$J = J^eJ^s. \tag{8.17}$$

(ii) Second, from the outset we constrain the theory by limiting our discussion to circumstances under which the material may be idealized as isotropic. For isotropic elastic-viscoplastic theories utilizing the multiplicative decomposition of $\mathbf{F}$, it is widely assumed that the plastic flow is *irrotational*, in the sense that

$$\mathbf{W}^p = \mathbf{0}. \tag{8.18}$$

Then, $\mathbf{L}^p \equiv \mathbf{D}^p$ and

$$\dot{\mathbf{F}}^p = \mathbf{D}^p \mathbf{F}^p. \tag{8.19}$$

Further, on account of (8.12) and (8.18), (8.9) reduces to

$$\mathbf{L} = \mathbf{L}^e + \mathbf{F}^e\Big(\mathbf{D}^p + \mathbf{D}^s\Big)\mathbf{F}^{e-1}. \tag{8.20}$$

For later use we introduce a positive-valued variable $\bar{\epsilon}^p$ called the equivalent tensile plastic strain, which we assume evolves according to the differential equation[1]

$$\dot{\bar{\epsilon}}^p = \sqrt{2/3}|\mathbf{D}^p| \quad \text{subject to the initial condition} \quad \bar{\epsilon}^p(\mathbf{X}, 0) = 0. \tag{8.21}$$

Then, whenever $|\mathbf{D}^p| \neq 0$,

$$\mathbf{N}^p = \frac{\mathbf{D}^p}{|\mathbf{D}^p|}, \qquad \text{with} \qquad \operatorname{tr}\mathbf{N}^p = 0, \tag{8.22}$$

defines the plastic flow direction, and therefore

$$\mathbf{D}^p = \sqrt{3/2}\,\dot{\bar{\epsilon}}^p \mathbf{N}^p. \tag{8.23}$$

8.2 Frame-indifference

A change in frame, at each fixed time t, is a transformation — defined by a rotation $\mathbf{Q}(t)$ and a spatial point $\mathbf{y}(t)$ — which transforms spatial points $\mathbf{x}$ to spatial points

$$\mathbf{x}^* = \boldsymbol{\mathcal{F}}(\mathbf{x}), \tag{8.24}$$

$$= \mathbf{y}(t) + \mathbf{Q}(t)(\mathbf{x} - \mathbf{o}), \tag{8.25}$$

with $\mathbf{o}$ a fixed spatial origin. The function $\boldsymbol{\mathcal{F}}$ represents a rigid mapping of the *observed space into itself.*

By (8.25) the transformation law for the motion $\mathbf{x} = \boldsymbol{\chi}(\mathbf{X}, t)$ has the form

$$\boldsymbol{\chi}^*(\mathbf{X}, t) = \mathbf{y}(t) + \mathbf{Q}(t)(\boldsymbol{\chi}(\mathbf{X}, t) - \mathbf{o}). \tag{8.26}$$

Hence the deformation gradient $\mathbf{F}$ transforms according to

$$\mathbf{F}^* = \mathbf{Q}\mathbf{F}. \tag{8.27}$$

Since *frame changes only involve the observed space*, the reference space and the local intermediate spaces (which are the ranges of $\mathbf{F}^s(\mathbf{X})$ and $\mathbf{F}^p\mathbf{F}^s(\mathbf{X})$) are independent of the

[1]This is a slight abuse in notation in the sense that $\dot{\bar{\epsilon}}^p$ is *not the material time derivative* of $\bar{\epsilon}^p$, but is defined to be $\sqrt{2/3}$ times the norm of $\mathbf{D}^p$.

choice of a change in frame. Thus

$$\mathbf{F}^s \quad \text{and} \quad \mathbf{F}^p \quad \text{are invariant under a change in frame.} \tag{8.28}$$

This observation, (8.2), and (8.27) yield the transformation law

$$\mathbf{F}^{e*} = \mathbf{Q}\mathbf{F}^e. \tag{8.29}$$

Also, using (8.10) and (8.28),

$$\mathbf{D}^p \quad \text{and} \quad \mathbf{D}^s \quad \text{are invariant,} \tag{8.30}$$

and, by $(8.10)_1$, $\mathbf{L}^{e*} = \mathbf{Q}\mathbf{L}^e\mathbf{Q}^\top + \dot{\mathbf{Q}}\mathbf{Q}^\top$, and hence

$$\mathbf{D}^{e*} = \mathbf{Q}\mathbf{D}^e\mathbf{Q}^\top, \qquad \mathbf{W}^{e*} = \mathbf{Q}\mathbf{W}^e\mathbf{Q}^\top + \dot{\mathbf{Q}}\mathbf{Q}^\top. \tag{8.31}$$

Further, by (8.6),

$$\mathbf{Q}\mathbf{F}^e = \mathbf{Q}\mathbf{R}^e\mathbf{U}^e = \mathbf{Q}\mathbf{V}^e\mathbf{Q}^\top\mathbf{Q}\mathbf{R}^e,$$

and we may conclude from the uniqueness of the polar decomposition that

$$\mathbf{R}^{e*} = \mathbf{Q}\mathbf{R}^e, \qquad \mathbf{V}^{e*} = \mathbf{Q}\mathbf{V}^e\mathbf{Q}^\top, \qquad \mathbf{U}^e \text{ is invariant.} \tag{8.32}$$

In addition, on account of the definition (8.8) and $(8.32)_3$,

$$\mathbf{C}^e \text{ is also invariant.} \tag{8.33}$$

8.3 Balance of forces and moments

Throughout, we denote by P an arbitrary part (subregion) of the reference body B, with $\mathbf{n}_\mathrm{R}$ the outward unit normal on the boundary ∂P of P.

Since time scales associated with species diffusion are usually considerably longer than those associated with wave propagation, we neglect all inertial effects. Then, standard considerations of balance of forces and moments, when expressed referentially, give:

(a) There exists a stress tensor $\mathbf{T}_\mathrm{R}$, called the Piola stress, such that the surface traction on an element of the surface ∂P of P, is given by

$$\mathbf{t}_\mathrm{R}(\mathbf{n}_\mathrm{R}) = \mathbf{T}_\mathrm{R}\mathbf{n}_\mathrm{R}. \tag{8.34}$$

(b) $\mathbf{T}_\mathrm{R}$ satisfies the macroscopic force balance

$$\mathrm{Div}\,\mathbf{T}_\mathrm{R} + \mathbf{b}_\mathrm{R} = \mathbf{0}, \tag{8.35}$$

where $\mathbf{b}_{\mathrm{R}}$ is an external body force per unit reference volume, which, consistent with neglect of inertial effects, is taken to be time-independent.

(c) $\mathbf{T}_{\mathrm{R}}$ obeys the the symmetry condition

$$\mathbf{T}_{\mathrm{R}}\mathbf{F}^{\mathsf{T}} = \mathbf{F}\mathbf{T}_{\mathrm{R}}^{\mathsf{T}}, \tag{8.36}$$

which represents a balance of moments.

Further, under a change in frame, $\mathbf{T}_{\mathrm{R}}$ transforms as

$$\mathbf{T}_{\mathrm{R}}^{*} = \mathbf{Q}\mathbf{T}_{\mathrm{R}}. \tag{8.37}$$

Finally, as is standard, the Piola stress $\mathbf{T}_{\mathrm{R}}$ is related to the standard symmetric Cauchy stress $\mathbf{T}$ in the deformed body by

$$\mathbf{T}_{\mathrm{R}} = J\,\mathbf{T}\,\mathbf{F}^{-\mathsf{T}}, \tag{8.38}$$

so that

$$\mathbf{T} = J^{-1}\mathbf{T}_{\mathrm{R}}\mathbf{F}^{\mathsf{T}}. \tag{8.39}$$

On account of (8.27) and (8.37) the transformation rule for the Cauchy stress $\mathbf{T}$ under a change in frame is

$$\mathbf{T}^{*} = \mathbf{Q}\mathbf{T}\mathbf{Q}^{\mathsf{T}}. \tag{8.40}$$

8.4 Balance law for the diffusing species

Let $c_{\mathrm{R}}(\mathbf{X}, t)$ denote the *molar concentration of lithium per unit reference volume*, and let $c(\mathbf{X}, t) = J^{-1}c_{\mathrm{R}}$ denote the *molar concentration of lithium per unit deformed volume*. Changes in c in a part $\mathcal{P}_t$ are brought about by the diffusion of lithium across its boundary $\partial\mathcal{P}_t$. The diffusion is characterized by a flux $\mathbf{j}(\mathbf{X}, t)$, the number of moles of lithium measured per unit area per unit time of the deformed body. Thus the rate of change of lithium in $\mathcal{P}_t$ is given by

$$\overline{\int_{\mathcal{P}_t} c\,dv}^{\cdot} = -\int_{\partial\mathcal{P}_t} \mathbf{j}\cdot\mathbf{n}\,da \tag{8.41}$$

for every part $\mathcal{P}_t$. In bringing the time derivative in (8.41) inside the integral, we must account for the fact that the intergal is taken over the deformed body, which may be changing with time. Using the fact that $dv = J\,dv_{\mathrm{R}}$, and $c = Jc_{\mathrm{R}}$, we may manipulate the left hand side of (8.41) to bring the time derivative inside the integral as follows

$$\overline{\int_{\mathcal{P}_t} c\,dv}^{\cdot} = \overline{\int_{\mathrm{P}} (cJ)\,dv_{\mathrm{R}}}^{\cdot} = \int_{\mathrm{P}} \overline{(cJ)}^{\cdot}\,dv_{\mathrm{R}} = \int_{\mathcal{P}_t} \overline{(cJ)}^{\cdot}\,J^{-1}\,dv = \int_{\mathcal{P}_t} \dot{c}_{\mathrm{R}}\,J^{-1}\,dv. \tag{8.42}$$

and hence (8.41), using (8.42) may be written as

$$\int_{\mathcal{P}_t} \dot{c}_{\mathrm{R}}\, J^{-1}\, dv = -\int_{\partial\mathcal{P}_t} \mathbf{j}\cdot\mathbf{n}\, da. \tag{8.43}$$

Using the divergence theorem on the integral over $\partial\mathcal{P}_t$, we find that

$$\int_{\mathcal{P}_t} (\dot{c}_{\mathrm{R}} J^{-1} + \mathrm{div}\mathbf{j})\, dv = 0. \tag{8.44}$$

Since P is arbitrary, this leads to the following local balance law for c_{R},

$$\dot{c}_{\mathrm{R}} = -J\mathrm{div}\mathbf{j}. \tag{8.45}$$

For later use, we define a flux $\mathbf{j}_{\mathrm{R}}$ per unit are per unit time in the reference body. Mass balance (8.45) may then also be expressed in terms of the referential divergence of the referential flux as

$$\dot{c}_{\mathrm{R}} = -\mathrm{Div}\mathbf{j}_{\mathrm{R}}. \tag{8.46}$$

8.5 Balance of energy. Entropy imbalance. Free energy imbalance

Our discussion of thermodynamics involves the following fields:

ε_{R}	the internal energy density per unit reference volume,
η_{R}	the entropy density per unit reference volume,
$\mathbf{q}_{\mathrm{R}}$	the heat flux per unit reference area,
q_{R}	the external heat supply per unit reference volume,
ϑ	the absolute temperature ($\vartheta > 0$),
μ	the chemical potential,

and follows the discussion of (Gurtin et al., 2010, § 64). Consider a material region P. Then, consistent with our omission of inertial effects, we neglect kinetic energy, and take the balance law for energy as

$$\overline{\int_{\mathrm{P}} \varepsilon_{\mathrm{R}}\, dv_{\mathrm{R}}} = -\int_{\partial\mathrm{P}} \mathbf{q}_{\mathrm{R}}\cdot\mathbf{n}_{\mathrm{R}}\, da_{\mathrm{R}} + \int_{\mathrm{P}} q_{\mathrm{R}}\, dv_{\mathrm{R}} + \int_{\partial\mathrm{P}} (\mathbf{T}_{\mathrm{R}}\mathbf{n}_{\mathrm{R}})\cdot\dot{\boldsymbol{\chi}}\, da_{\mathrm{R}} + \int_{\mathrm{P}} \mathbf{b}_{\mathrm{R}}\cdot\dot{\boldsymbol{\chi}}\, dv_{\mathrm{R}} - \int_{\partial\mathrm{P}} \mu\mathbf{j}_{\mathrm{R}}\cdot\mathbf{n}_{\mathrm{R}} da_{\mathrm{R}}, \tag{8.47}$$

where the last term in (8.47) represents the flux of energy carried into P by the flux $\mathbf{j}_{\mathrm{R}}$ of lithium.

Also, the second law takes the form of an entropy imbalance

$$\overline{\int_{\mathrm{P}} \eta_{\mathrm{R}}\, dv_{\mathrm{R}}}^{\cdot} \geq -\int_{\partial \mathrm{P}} \frac{\mathbf{q}_{\mathrm{R}} \cdot \mathbf{n}_{\mathrm{R}}}{\vartheta}\, da_{\mathrm{R}} + \int_{\mathrm{P}} \frac{q_{\mathrm{R}}}{\vartheta}\, dv_{\mathrm{R}}. \tag{8.48}$$

Assume now that *isothermal conditions* prevail, so that

$$\vartheta \equiv \text{constant},$$

and introduce the Helmholtz free energy per unit reference volume defined by

$$\psi_{\mathrm{R}} = \varepsilon_{\mathrm{R}} - \vartheta \eta_{\mathrm{R}}. \tag{8.49}$$

Then, upon multiplying the entropy imbalance (8.48) by ϑ and subtracting the result from the energy balance (8.47) yields the free energy imbalance

$$\overline{\int_{\mathrm{P}} \psi_{\mathrm{R}}\, dv_{\mathrm{R}}}^{\cdot} \leq \int_{\partial \mathrm{P}} (\mathbf{T}_{\mathrm{R}} \mathbf{n}_{\mathrm{R}}) \cdot \dot{\boldsymbol{\chi}}\, da_{\mathrm{R}} + \int_{\mathrm{P}} \mathbf{b}_{\mathrm{R}} \cdot \dot{\boldsymbol{\chi}}\, dv_{\mathrm{R}} - \int_{\partial \mathrm{P}} \mu \mathbf{j}_{\mathrm{R}} \cdot \mathbf{n}_{\mathrm{R}} da_{\mathrm{R}}. \tag{8.50}$$

We henceforth restrict attention to *isothermal processes* and for that reason base the theory on the free energy imbalance (8.50).

Applying the divergence theorem to the terms in (8.50) involving integrals over the boundary $\partial \mathrm{P}$ of P, we obtain

$$\int_{\mathrm{P}} \Big(\dot{\psi}_{\mathrm{R}} - (\mathrm{Div} \mathbf{T}_{\mathrm{R}} + \mathbf{b}_{\mathrm{R}}) \cdot \dot{\boldsymbol{\chi}} - \mathbf{T}_{\mathrm{R}} : \dot{\mathbf{F}} + \mu \mathrm{Div} \mathbf{j}_{\mathrm{R}} + \mathbf{j}_{\mathrm{R}} \cdot \nabla \mu \Big)\, dv_{\mathrm{R}} \leq 0, \tag{8.51}$$

which upon use of the balance laws (8.35) and (8.46), and using the fact that (8.51) must hold for all parts P, gives the local form of the free energy imbalance as

$$\dot{\psi}_{\mathrm{R}} - \mathbf{T}_{\mathrm{R}} : \dot{\mathbf{F}} - \mu \dot{c}_{\mathrm{R}} + \mathbf{j}_{\mathrm{R}} \cdot \nabla \mu \leq 0\,. \tag{8.52}$$

Next, using (8.2), $(8.10)_{2,3}$, (8.17) and (8.38), we find that the stress-power $\mathbf{T}_{\mathrm{R}} : \dot{\mathbf{F}}$ admits the decomposition

$$\mathbf{T}_{\mathrm{R}} : \dot{\mathbf{F}} = J^s \Big[(J^e \mathbf{F}^{e-1} \mathbf{T} \mathbf{F}^{e-\top}) : (\mathbf{F}^{e\top} \dot{\mathbf{F}}^e) + (\mathbf{C}^e J^e \mathbf{F}^{e-1} \mathbf{T} \mathbf{F}^{e-\top}) : \mathbf{L}^p + (\mathbf{C}^e J^e \mathbf{F}^{e-1} \mathbf{T} \mathbf{F}^{e-\top}) : \mathbf{L}^s \Big]. \tag{8.53}$$

In view of (8.53), we introduce two new stress measures:

- The elastic second Piola stress,

$$\mathbf{T}^e \stackrel{\mathrm{def}}{=} J^e \mathbf{F}^{e-1} \mathbf{T} \mathbf{F}^{e-\top}, \tag{8.54}$$

which is *symmetric* on account of the symmetry of the Cauchy stress $\mathbf{T}$.

- The Mandel stress,

$$\mathbf{M}^e \stackrel{\text{def}}{=} \mathbf{C}^e\mathbf{T}^e, \tag{8.55}$$

which in general is *not symmetric.*

Note that on account of the transformation rule (8.29) for $\mathbf{F}^e$, and the transformation rule (8.40), the elastic second Piola stress and the Mandel stress are invariant under a change in frame,

$$\mathbf{T}^{e*} = \mathbf{T}^e \qquad \text{and} \qquad \mathbf{M}^{e*} = \mathbf{M}^e. \tag{8.56}$$

Further, since the rate of change of elastic right Cauchy-Green tensor $\mathbf{C}^e$ is

$$\dot{\mathbf{C}}^e = \mathbf{F}^{e\mathsf{T}}\dot{\mathbf{F}}^e + \dot{\mathbf{F}}^{e\mathsf{T}}\mathbf{F}^e, \tag{8.57}$$

the stress-power (8.53) may be written as

$$\mathbf{T}_{\mathrm{R}} : \dot{\mathbf{F}} = \frac{1}{2}(J^s\mathbf{T}^e) : \dot{\mathbf{C}}^e + J^s\mathbf{M}^e : \mathbf{L}^p + J^s\mathbf{M}^e : \mathbf{L}^s. \tag{8.58}$$

Next, recalling $(8.12)_2$, (8.14), (8.16) and (8.18), we may write the stress-power (8.58) as

$$\mathbf{T}_{\mathrm{R}} : \dot{\mathbf{F}} = \frac{1}{2}(J^s\mathbf{T}^e) : \dot{\mathbf{C}}^e + J^s\mathbf{M}_0^e : \mathbf{D}^p + \frac{1}{3}(\mathrm{tr}\,\mathbf{M}^e)\dot{J}^s. \tag{8.59}$$

Hence, using (8.59) in (8.52), the local free energy imbalance may be written as

$$\dot{\psi}_{\mathrm{R}} - \frac{1}{2}(J^s\mathbf{T}^e) : \dot{\mathbf{C}}^e - \frac{1}{3}(\mathrm{tr}\,\mathbf{M}^e)\dot{J}^s - \mu\dot{c}_{\mathrm{R}} - J^s\mathbf{M}_0^e : \mathbf{D}^p + \mathbf{j}_{\mathrm{R}} \cdot \nabla\mu \leq 0. \tag{8.60}$$

8.6 Constitutive constraint between J^s and c_{R}

We assume that

$$J^s = \breve{J}^s(c_{\mathrm{R}}), \tag{8.61}$$

with

$$\Omega(c_{\mathrm{R}}) \stackrel{\text{def}}{=} \frac{d\breve{J}^s(c_{\mathrm{R}})}{dc_{\mathrm{R}}} > 0, \tag{8.62}$$

so that changes in J^s arise entirely due to the change in species content. The quantity $\Omega(c_{\mathrm{R}}) > 0$ represents a *partial molar volume.* We may then also write

$$\dot{J}^s = \Omega\dot{c}_{\mathrm{R}}. \tag{8.63}$$

Using (8.63) we can rewrite the swell stretching (8.14) as

$$\mathbf{D}^s = \frac{1}{3}\Omega J^{s-1}\dot{c}_{\mathrm{R}}\,\mathbf{1}. \tag{8.64}$$

Using (8.63), the free energy imbalance (8.60) becomes

$$\dot{\psi}_{\mathrm{R}} - \frac{1}{2}(J^s\mathbf{T}^e)\colon\dot{\mathbf{C}}^e - \mu_{\mathrm{net}}\,\dot{c}_{\mathrm{R}} - J^s\mathbf{M}_0^e\colon\mathbf{D}^p + \mathbf{j}_{\mathrm{R}}\cdot\nabla\mu \leq 0, \tag{8.65}$$

where we have written

$$\mu_{\mathrm{net}} \stackrel{\mathrm{def}}{=} \mu + \Omega\,\frac{1}{3}(\mathrm{tr}\mathbf{M}^e) \tag{8.66}$$

for an *net chemical potential.*

We note that under a change in frame

$$\psi_{\mathrm{R}},\ c_{\mathrm{R}},\ \mu,\ \mathbf{j}_{\mathrm{R}},\ \text{and}\ \nabla\mu\ \text{are invariant,} \tag{8.67}$$

ψ_{R}, c_{R}, and μ because they are scalars, and $\mathbf{j}_{\mathrm{R}}$ and $\nabla\mu$ since they are referential vector fields. Also, recalling (8.33) and (8.56), we have that

$$\mathbf{C}^e,\ \mathbf{T}^e,\ \text{and}\ \mathbf{M}^e\ \text{are invariant under a change in frame.} \tag{8.68}$$

Thus with the invariance properties discussed above, all quantities in the free energy imbalance (8.65) are invariant under a change in frame.

8.7 Constitutive theory

8.7.1 Energetic constitutive equations

Guided by the free-energy imbalance (8.65) we first consider the following set of constitutive equations for the free energy ψ_{R}, the stress $\mathbf{T}^e$, and the net chemical potential μ_{net}:

$$\left.\begin{aligned}\psi_{\mathrm{R}} &= \breve{\psi}_{\mathrm{R}}(\mathbf{C}^e, c_{\mathrm{R}}),\\ \mathbf{T}^e &= \breve{\mathbf{T}}^e(\mathbf{C}^e, c_{\mathrm{R}}),\\ \mu_{\mathrm{net}} &= \breve{\mu}_{\mathrm{net}}(\mathbf{C}^e, c_{\mathrm{R}}).\end{aligned}\right\} \tag{8.69}$$

Substituting the constitutive equations (8.69) into the free-energy imbalance (8.65), we find that it may then be written as

$$\Big(\frac{\partial\breve{\psi}_{\mathrm{R}}(\mathbf{C}^e, c_{\mathrm{R}})}{\partial\mathbf{C}^e} - \tfrac{1}{2}(J^s\bar{\mathbf{T}}^e)\Big)\colon\dot{\mathbf{C}}^e + \Big(\frac{\partial\breve{\psi}_{\mathrm{R}}(\mathbf{C}^e, c_{\mathrm{R}})}{\partial c_{\mathrm{R}}} - \bar{\mu}_{\mathrm{net}}\Big)\dot{c}_{\mathrm{R}} - J^s\,\mathbf{M}_0^e\colon\mathbf{D}^p + \mathbf{j}_{\mathrm{R}}\cdot\nabla\mu \leq 0\,. \tag{8.70}$$

This inequality is to hold for all values of $\mathbf{C}^e$ and c_{R}. Since $\dot{\mathbf{C}}^e$ and $\dot{c}_{\mathrm{R}}$ appear linearly, their "coefficients" must vanish, for otherwise $\dot{\mathbf{C}}^e$ and $\dot{c}_{\mathrm{R}}$ may be chosen to violate (8.70). We are therefore led to the thermodynamic restriction that the free energy determines the stress $\mathbf{T}^e$

and the chemical potential μ through the "state relations"

$$\left.\begin{aligned} \mathbf{T}^e &= J^{s-1}\Big(2\frac{\partial \breve{\psi}_{\mathrm{R}}(\mathbf{C}^e, c_{\mathrm{R}})}{\partial \mathbf{C}^e}\Big), \\ \mu &= \frac{\partial \breve{\psi}_{\mathrm{R}}(\mathbf{C}^e, c_{\mathrm{R}})}{\partial c_{\mathrm{R}}} - \Omega\,\frac{1}{3}(\mathrm{tr}\mathbf{M}^e), \end{aligned}\right\} \tag{8.71}$$

and we are left with the following reduced dissipation inequality

$$J^s\,\mathbf{M}_0^e\colon\mathbf{D}^p - \mathbf{j}_{\mathrm{R}}\cdot\nabla\mu \geq 0\,. \tag{8.72}$$

8.7.2 Dissipative constitutive equations

Recall the quantity $\bar{\epsilon}^p$ defined in (8.21). We use it as a scalar *hardening variable* to account for the strain-hardening characteristics typically observed during plastic deformation. Since $\bar{\epsilon}^p$ is a scalar field it is invariant under a change in frame.

It is important to note that in the dissipation inequality (8.72) the quantity $\mathbf{M}_0^e\colon\mathbf{D}^p$ is the plastic dissipation per unit volume of the local intermediate space mapped by $\mathbf{F}^s\mathbf{F}^p$, and multiplying this term by J^s gives the plastic dissipation per unit volume of the reference space. Thus, guided by (8.72), and experience with existing plasticity theories, we assume that the plastic stretching is given in terms of the stress deviator $\mathbf{M}_0^e$, as well as the equivalent tensile plastic strain $\bar{\epsilon}^p$ and the species content c_{R}:

$$\mathbf{D}^p = \breve{\mathbf{D}}^p(\mathbf{M}_0^e, \bar{\epsilon}^p, c_{\mathrm{R}}). \tag{8.73}$$

To the constitutive equation (8.73), we append a Fick-type relation for the flux of the diffusing species,

$$\mathbf{j} = -\mathbf{M}\,\mathrm{grad}\,\mu, \quad \text{where} \quad \mathbf{M} = \breve{\mathbf{M}}(\mathbf{C}^e, c_{\mathrm{R}}, \bar{\epsilon}^p) \tag{8.74}$$

is a *mobility tensor*. The constitutive equation (8.74) may be expressed in the reference body as

$$\mathbf{j}_{\mathrm{R}} = -(J\mathbf{C}^{-1})\mathbf{M}\nabla\mu. \tag{8.75}$$

Remark. The constitutive equation (8.74) for the species flux differs from (3.62) used in Part I. In Part I, it was the referential species flux, $\mathbf{j}_{\mathrm{R}}$, which was taken to be given by a mobility times the negative of the referential gradient of the chemical potential $(-\nabla\mu)$. We believe that (8.74) is the more appropriate form for the species flux for large deformations of continually isotropic materials. However, we note that (3.62) in Part I is more appropriate for instances in which the microstructure affects the manner in which diffusion occurs within a body. In such instances, a referential description of the species flux is important in accounting for how the transport and rotation of the microstructure will affect diffusion. □

Using (8.73), (8.75), (8.21) and (8.22), the dissipation inequality (8.72) may be written as

$$J^s \sqrt{3/2}(\mathbf{M}_0^e\colon\ \mathbf{N}^p)\dot{\bar{\epsilon}}^p + \nabla\mu \cdot (J\mathbf{C}^{-1}\mathbf{M})\nabla\mu \geq 0. \tag{8.76}$$

Henceforth, we define

$$\bar{\sigma} \stackrel{\text{def}}{=} \sqrt{3/2}(\mathbf{M}_0^e : \mathbf{N}^p) \tag{8.77}$$

as the *equivalent tensile stress*, so that (8.76) may be written as

$$J^s\, \bar{\sigma}\dot{\bar{\epsilon}}^p + \nabla\mu \cdot (J\mathbf{C}^{-1}\mathbf{M})\nabla\mu \geq 0. \tag{8.78}$$

Recalling that $J^s > 0$ and $J > 0$, we assume that each of the two terms in (8.78) individually satisfy

$$\bar{\sigma}\, \dot{\bar{\epsilon}}^p > 0 \quad \text{for} \quad \dot{\bar{\epsilon}}^p > 0, \tag{8.79}$$

$$\nabla\mu \cdot (\mathbf{C}^{-1}\mathbf{M})\nabla\mu \geq 0. \tag{8.80}$$

In this case, we note from (8.80) that the tensor $\mathbf{C}^{-1}\mathbf{M}$ is positive semi-definite.

Finally, note that on account of the transformation rules listed in the paragraph containing (8.67) and (8.68), the constitutive equations (8.69), (8.73), and (8.74) are frame-indifferent.

8.8 Isotropy

As mentioned previously, *we have restricted our attention to isotropic materials.* In this case,

(†) the response functions $\breve{\psi}_{\mathrm{R}}$, $\breve{\mathbf{T}}^e$, $\breve{\mu}_{\mathrm{net}}$, and $\breve{\mathbf{D}}^p$ must also each be *isotropic.*

(‡) the mobility tensor has the representation

$$\breve{\mathbf{M}}(\mathbf{C}^e, c_{\mathrm{R}}, \bar{\epsilon}^p) = \tilde{m}(\mathcal{I}_{\mathbf{C}^e}, c_{\mathrm{R}}, \bar{\epsilon}^p)\mathbf{1}, \quad \text{with} \quad \tilde{m}(\mathcal{I}_{\mathbf{C}^e}, c_{\mathrm{R}}, \bar{\epsilon}^p) > 0 \tag{8.81}$$

a scalar mobility, and with

$$\mathcal{I}_{\mathbf{C}^e} = \Big(I_1(\mathbf{C}^e), I_2(\mathbf{C}^e), I_3(\mathbf{C}^e)\Big)$$

the list of principal invariants of $\mathbf{C}^e$.

8.8.1 Isotropic free energy

An immediate consequence of the isotropy of the free energy is that the free energy function has the representation

$$\breve{\psi}_{\mathrm{R}}(\mathbf{C}^e, c_{\mathrm{R}}) = \tilde{\psi}_{\mathrm{R}}(\mathcal{I}_{\mathbf{C}^e}, c_{\mathrm{R}}). \tag{8.82}$$

Thus, from $(8.71)_1$, it follows that

$$\mathbf{T}^e = J^{s-1}\Big(2\,\frac{\partial\tilde{\psi}(\mathcal{I}_{\mathbf{C}^e}, c_{\mathrm{R}})}{\partial\mathbf{C}^e}\Big), \tag{8.83}$$

and that $\mathbf{T}^e$ is an *isotropic function of* $\mathbf{C}^e$. Then since the Mandel stress is defined by (cf. (8.55))

$$\mathbf{M}^e = \mathbf{C}^e\mathbf{T}^e,$$

we find that $\mathbf{T}^e$ and $\mathbf{C}^e$ commute,

$$\mathbf{C}^e\mathbf{T}^e = \mathbf{T}^e\mathbf{C}^e, \tag{8.84}$$

and hence that *the Mandel stress* $\mathbf{M}^e$ *is symmetric.*

Next, the spectral representation of $\mathbf{C}^e$ is

$$\mathbf{C}^e = \sum_{i=1}^{3} \omega_i^e \mathbf{r}_i^e \otimes \mathbf{r}_i^e, \qquad \text{with} \qquad \omega_i^e = \lambda_i^{e\,2}, \tag{8.85}$$

where $(\mathbf{r}_1^e, \mathbf{r}_2^e, \mathbf{r}_2^e)$ are the orthonormal eigenvectors of $\mathbf{C}^e$ and $\mathbf{U}^e$, and $(\lambda_1^e, \lambda_2^e, \lambda_3^e)$ are the positive eigenvalues of $\mathbf{U}^e$.

Let

$$\mathbf{E}^e \stackrel{\text{def}}{=} \ln \mathbf{U}^e = \sum_{i=1}^{3} E_i^e\, \mathbf{r}_i^e \otimes \mathbf{r}_i^e, \tag{8.86}$$

denote the logarithmic elastic strain with principal values

$$E_i^e \stackrel{\text{def}}{=} \ln \lambda_i^e\,, \tag{8.87}$$

and consider an elastic free energy function of the form

$$\tilde{\psi}_{\mathrm{R}}(\mathcal{I}_{\mathbf{C}^e}, c_{\mathrm{R}}) = \check{\psi}_{\mathrm{R}}(E_1^e, E_2^e, E_3^e, c_{\mathrm{R}}). \tag{8.88}$$

Then, straightforward calculations show that the Mandel stress is given by

$$\mathbf{M}^e = J^{s-1} \sum_{i=1}^{3} \frac{\partial\check{\psi}(E_1^e, E_2^e, E_3^e, c_{\mathrm{R}})}{\partial E_i^e}\, \mathbf{r}_i^e \otimes \mathbf{r}_i^e. \tag{8.89}$$

With the logarithmic elastic strain defined by (8.86), and bearing (8.88) and (8.89), for isotropic elastic materials we henceforth consider a free energy of the form

$$\check{\psi}_{\mathrm{R}}(E_1^e, E_2^e, E_3^e, c_{\mathrm{R}}) = \hat{\psi}_{\mathrm{R}}(\mathcal{I}_{\mathbf{E}^e}, c_{\mathrm{R}}) \tag{8.90}$$

with $\mathcal{I}_{\mathbf{E}^e}$ a list of principal invariants of $\mathbf{E}^e$, or equivalently a list of principal values of $\mathbf{E}^e$. The Mandel stress is then given by

$$\mathbf{M}^e = J^{s-1}\left(\frac{\partial\hat{\psi}_{\mathrm{R}}(\mathcal{I}_{\mathbf{E}^e}, c_{\mathrm{R}})}{\partial\mathbf{E}^e}\right), \tag{8.91}$$

and the corresponding Cauchy stress is

$$\mathbf{T} = J^{e-1}\mathbf{R}^e\mathbf{M}^e\mathbf{R}^{e\mathsf{T}}. \tag{8.92}$$

8.8.2 Plastic flow rule for isotropic materials

Recall the constitutive equation (8.73) along with (8.23) for the plastic stretching $\mathbf{D}^p$,

$$\mathbf{D}^p = \breve{\mathbf{D}}^p(\mathbf{M}_0^e, \bar{\epsilon}^p, c_{\mathrm{R}}) = \sqrt{3/2}\,\breve{\dot{\epsilon}}^p(\mathbf{M}_0^e, \bar{\epsilon}^p, c_{\mathrm{R}})\,\breve{\mathbf{N}}^p(\mathbf{M}_0^e, \bar{\epsilon}^p, c_{\mathrm{R}}). \tag{8.93}$$

Guided by (8.76), we henceforth adopt the classical codirectionality hypothesis, which asserts that the direction of plastic flow $\breve{\mathbf{N}}^p$ is parallel to and points in the same direction as $\mathbf{M}_0^e$,

$$\breve{\mathbf{N}}^p = \frac{\mathbf{M}_0^e}{|\mathbf{M}_0^e|}. \tag{8.94}$$

Further, note that on account of the isotropy of $\breve{\mathbf{D}}^p$, the equivalent tensile plastic strain rate function $\breve{\dot{\epsilon}}^p(\mathbf{M}^e, \bar{\epsilon}^p, c_{\mathrm{R}})$ is also isotropic, and has the representation

$$\dot{\bar{\epsilon}}^p = \breve{\dot{\epsilon}}^p(\mathcal{I}_{\mathbf{M}_0^e}, \bar{\epsilon}^p, c_{\mathrm{R}}) \geq 0, \tag{8.95}$$

where $\mathcal{I}_{\mathbf{M}_0^e}$ is the list of principal invariants of $\mathbf{M}_0^e$.

A further consequence of (8.94) is that from the definition (8.77) for the equivalent tensile stress we have

$$\bar{\sigma} = \sqrt{3/2}(\mathbf{M}_0^e : \mathbf{N}^p) = \sqrt{3/2}\,|\mathbf{M}_0^e|. \tag{8.96}$$

Further, in accordance with prior experience, we henceforth neglect any dependence on $\det\mathbf{M}_0^e$ in the expression (8.95) for viscoplastic flow. Then, using (8.77) and (8.94), the plastic stretching $\mathbf{D}^p$ in (8.93) may be written as

$$\mathbf{D}^p = \frac{3}{2}\dot{\bar{\epsilon}}^p\frac{\mathbf{M}^e}{\bar{\sigma}} \qquad \text{with} \qquad \dot{\bar{\epsilon}}^p = \hat{\dot{\epsilon}}^p(\bar{\sigma}, \bar{\epsilon}^p, c_{\mathrm{R}}) \geq 0. \tag{8.97}$$

8.9 Summary of the constitutive theory

Our theory relates the following basic fields:

$\mathbf{x} = \boldsymbol{\chi}(\mathbf{X}, t)$,	motion;
$\mathbf{F} = \nabla\boldsymbol{\chi}, \quad J = \det \mathbf{F} > 0$,	deformation gradient;
$\mathbf{F} = \mathbf{F}^e\mathbf{F}^p\mathbf{F}^s$,	multiplicative decomposition of $\mathbf{F}$;
$\mathbf{F}^s = \lambda^s\mathbf{1}, \quad J^s = (\lambda^s)^3 > 0$,	swelling distortion;
$\mathbf{F}^p, \quad J^p = \det \mathbf{F}^p = 1$,	plastic distortion;
$\mathbf{F}^e, \quad J^e = \det \mathbf{F}^e > 0$,	elastic distortion;
$\mathbf{F}^e = \mathbf{R}^e\mathbf{U}^e = \mathbf{V}^e\mathbf{R}^e$,	polar decompositions of $\mathbf{F}^e$;
$\mathbf{C}^e = \mathbf{F}^{e\mathsf{T}}\mathbf{F}^e = \mathbf{U}^{e\,2}$,	elastic right Cauchy-Green tensor;
$\mathbf{U}^e = \sum_{\alpha=1}^{3} \lambda_\alpha^e \mathbf{r}_\alpha^e \otimes \mathbf{r}_\alpha^e$,	spectral decomposition of $\mathbf{U}^e$;
$\mathbf{V}^e = \sum_{\alpha=1}^{3} \lambda_\alpha^e \mathbf{l}_\alpha^e \otimes \mathbf{l}_\alpha^e$, where $\mathbf{l}_\alpha^e = \mathbf{R}^e\mathbf{r}_\alpha^e$,	spectral decomposition of $\mathbf{V}^e$;
$\mathbf{E}^e = \sum_{\alpha=1}^{3} (\ln \lambda_\alpha^e)\mathbf{r}_\alpha^e \otimes \mathbf{r}_\alpha^e$,	logarithmic elastic strain;
$\mathbf{E}_{\mathrm{H}}^e \stackrel{\text{def}}{=} \mathbf{R}^e\mathbf{E}^e\mathbf{R}^{e\mathsf{T}} = \sum_{\alpha=1}^{3} (\ln \lambda_\alpha^e)\mathbf{l}_\alpha^e \otimes \mathbf{l}_\alpha^e$,	spatial logarithmic elastic strain;
$\mathbf{T} = \mathbf{T}^\mathsf{T}$,	Cauchy stress;
$\mathbf{M}^e = J^e\mathbf{R}^{e\mathsf{T}}\mathbf{T}\mathbf{R}^e$,	Mandel stress;
$\mathbf{T}_{\mathrm{R}} = J\mathbf{T}\mathbf{F}^{-\mathsf{T}}$,	Piola stress;
ψ_{R},	free energy density per unit reference volume;
c_{R},	molar concentration per unit reference volume;
c,	molar concentration per unit volume in the deformed body;
μ,	chemical potential;
$\mathbf{j}_{\mathrm{R}}$,	referential species flux vector;
$\mathbf{j}$,	spatial species flux vector.

8.9.1 Constitutive equations

1. Swelling ratio J^s

The swelling ratio J^s is related to the species concentration through a constitutive relation

$$J^s = \hat{J}^s(c_{\mathrm{R}}), \tag{8.98}$$

where

$$\hat{\Omega}(c_{\mathrm{R}}) \stackrel{\text{def}}{=} \frac{d\hat{J}^s(c_{\mathrm{R}})}{dc_{\mathrm{R}}} > 0, \tag{8.99}$$

represents a *partial molar volume.*

2. Free energy

$$\psi_{\mathrm{R}} = \hat{\psi}_{\mathrm{R}}(\mathcal{I}_{\mathbf{E}^e}, c_{\mathrm{R}}), \tag{8.100}$$

where $\mathcal{I}_{\mathbf{E}^e}$ represents a list of the principal invariants of the elastic strain $\mathbf{E}^e$.

3. Mandel stress. Cauchy stress

The Mandel stress is given by

$$\mathbf{M}^e = J^{s-1}\left(\frac{\partial\hat{\psi}_{\mathrm{R}}(\mathcal{I}_{\mathbf{E}^e}, c_{\mathrm{R}})}{\partial\mathbf{E}^e}\right), \tag{8.101}$$

which, on account of the isotropy of $\bar{\psi}_{\mathrm{R}}$ is *symmetric*. The *equivalent tensile stress* is defined by

$$\bar{\sigma} \stackrel{\text{def}}{=} \sqrt{(3/2)}\,|\mathbf{M}_0^e|. \tag{8.102}$$

The Cauchy stress is related to the Mandel stress by

$$\mathbf{T} \stackrel{\text{def}}{=} J^{e-1}\,(\mathbf{R}^e\mathbf{M}^e\mathbf{R}^{e\mathsf{T}}). \tag{8.103}$$

4. Chemical potential

The quantity

$$\mu = \frac{\partial\hat{\psi}_{\mathrm{R}}(\mathcal{I}_{\mathbf{E}^e}, c_{\mathrm{R}})}{\partial c_{\mathrm{R}}} - \hat{\Omega}(c_{\mathrm{R}})\frac{1}{3}(\mathrm{tr}\,\mathbf{M}^e), \tag{8.104}$$

represents the chemical potential, with Ω he partial molar volume of lithium.

5. Evolution equation for $\mathbf{F}^s$

The evolution equation for $\mathbf{F}^s$ is

$$\dot{\mathbf{F}}^s = \mathbf{D}^s\,\mathbf{F}^s, \tag{8.105}$$

with $\mathbf{D}^s$ given by

$$\mathbf{D}^s = \frac{1}{3}\Omega J^{s-1}\dot{c}_{\mathrm{R}}\mathbf{1}. \tag{8.106}$$

6. Evolution equation for $\mathbf{F}^p$

The evolution equation for $\mathbf{F}^p$ is

$$\dot{\mathbf{F}}^p = \mathbf{D}^p\,\mathbf{F}^p, \tag{8.107}$$

where $\mathbf{D}^p$ is given by

$$\mathbf{D}^p = \dot{\bar{\epsilon}}^p(3\mathbf{M}_0^e/2\bar{\sigma}), \tag{8.108}$$

and $\dot{\bar{\epsilon}}^p$ is given by a constitutive equation

$$\dot{\bar{\epsilon}}^p = \hat{\dot{\bar{\epsilon}}}^p(\bar{\sigma}, \bar{\epsilon}^p, c_{\mathrm{R}}) \geq 0. \tag{8.109}$$

Here

$$\bar{\epsilon}^p(\mathbf{X},t) = \int_0^t \dot{\bar{\epsilon}}^p(\mathbf{X},\zeta)\, d\zeta \qquad \text{with} \qquad \bar{\epsilon}^p(\mathbf{X},0) = 0, \tag{8.110}$$

is the *equivalent tensile plastic strain.*

7. Species flux

The spatial species flux $\mathbf{j}$ is presumed to obey

$$\mathbf{j} = -m \operatorname{grad} \mu, \tag{8.111}$$

which yields a referential species flux

$$\mathbf{j}_{\mathrm{R}} = -m(J\mathbf{C}^{-1})\, \nabla\mu, \tag{8.112}$$

with $\hat{m}(\mathcal{I}_{\mathbf{E}^e}, c_{\mathrm{R}}, \bar{\epsilon}^p) \geq 0$ the mobility of the diffusing species.

The evolution equations for $\mathbf{F}^s$ and $\mathbf{F}^p$ need to be accompanied by initial conditions. Typical initial conditions presume that the body is initially (at time $t = 0$, say) in a *pristine state* in the sense that

$$\mathbf{F}(\mathbf{X},0) = \mathbf{F}^s(\mathbf{X},0) = \mathbf{F}^p(\mathbf{X},0) = \mathbf{1}, \tag{8.113}$$

so that by $\mathbf{F} = \mathbf{F}^e\mathbf{F}^p\mathbf{F}^s$ we also have $\mathbf{F}^e(\mathbf{X},0) = \mathbf{1}$.

8.10 Specialization of the constitutive equations

The theory presented thus far is quite general. We now introduce special constitutive equations aimed at modeling a-Si anodes. The specialized choices are based largely on the experimental observations of Pharr et al. (2014) and Bucci et al. (2014), which will be discussed in detail in Chapter 9, when the theory is calibrated.

8.10.1 Swelling ratio J^s

For the constitutive equation (8.98) we assume that J^s varies linearly with c_{R},

$$J^s = 1 + \Omega(c_{\mathrm{R}} - c_{\mathrm{R},0}), \tag{8.114}$$

with a *constant* partial molar volume $\Omega > 0$, and with $c_{\mathrm{R},0}$ the concentration of Li when $J^s = 1$. $c_{\mathrm{R},0}$ is often taken as the initial concentration with the assumption that $J^s = 1$ is the initial condition for the volume ratio swelling distortion.

8.10.2 Free energy

We consider a separable free energy of the form

$$\hat{\psi}_{\mathrm{R}}(\mathcal{I}_{\mathbf{E}^e}, c_{\mathrm{R}}) = \hat{\psi}^c_{\mathrm{R}}(c_{\mathrm{R}}) + \hat{\psi}^e_{\mathrm{R}}(\mathcal{I}_{\mathbf{E}^e}, c_{\mathrm{R}}). \tag{8.115}$$

Here:

(i) ψ^c_{R} is the change in chemical free energy due to mixing/intercalation of the lithium ions with the host electrode. It is taken to be given by

$$\psi^c_{\mathrm{R}} = R\vartheta\, c_{\mathrm{R,max}} \Big(\bar{c}\ln\bar{c} + (1-\bar{c})\ln(1-\bar{c})\Big) + c_{\mathrm{R,max}} \sum_{n=2}^{7} a_n \cdot \bar{c}^{(n)} \tag{8.116}$$

where

$$\bar{c} \stackrel{\text{def}}{=} \frac{c_{\mathrm{R}}}{c_{\mathrm{R,max}}}, \qquad 0 \leq \bar{c} \leq 1, \tag{8.117}$$

is a normalized lithium ion concentration, with $c_{\mathrm{R,max}}$ the concentration of lithium in moles per unit reference volume when all the intercalation sites are filled. In (8.116), R is the gas constant, ϑ is the absolute temperature, and the polynomial dependence $\sum_{n=2}^{7} a_n \cdot \bar{c}^{(n)}$, in which a_n are fitting coefficients, is motivated by the recent paper by Bucci et al. (2014).

(ii) ψ^e_{R} is the contribution to the change in the free energy due to the elastic deformation of the host electrode material, taken to be given by

$$\psi^e_{\mathrm{R}} = J^s \left(\frac{1}{2}\mathbf{E}^e : \hat{\mathbb{C}}(\bar{c})[\mathbf{E}^e]\right), \qquad \hat{\mathbb{C}}(\bar{c}) \stackrel{\text{def}}{=} 2\hat{G}(\bar{c})\mathbb{I} + \left(\hat{K}(\bar{c}) - \frac{2}{3}\hat{G}(\bar{c})\right)\mathbf{1}\otimes\mathbf{1}, \tag{8.118}$$

where $\hat{\mathbb{C}}(\bar{c})$ is a *concentration dependent* elasticity tensor, with $\mathbb{I}$ and $\mathbf{1}$ the fourth- and second-order identity tensors, and the parameters

$$\hat{G}(\bar{c}) > 0, \qquad \hat{K}(\bar{c}) > 0, \tag{8.119}$$

are the concentration-dependent shear modulus and bulk modulus, respectively. The term[2]

$$\frac{1}{2}\mathbf{E}^e : \hat{\mathbb{C}}(\bar{c})[\mathbf{E}^e]$$

in (8.118) is a measure of the free energy per unit volume of the local intermediate space defined by the range of $\mathbf{F}^p\mathbf{F}^s(\mathbf{X})$, and multiplication of this term by J^s gives us the free energy per unit volume of the reference space.

[2] This is a simple generalization of the classical strain energy function of infinitesimal isotropic elasticity to finite strains using the logarithmic elastic strain (Anand, 1979, 1986), and concentration-dependent elastic moduli.

Thus, using (8.116) and (8.118) in (8.115), a simple form of the free energy function which accounts for the combined effects of mixing, swelling, and finite elastic stretching is

$$\psi_{\mathrm{R}} = \mu^0 c_{\mathrm{R}} + R\vartheta c_{\mathrm{R,max}} \Big(\bar{c}\ln\bar{c} + (1-\bar{c})\ln(1-\bar{c})\Big) + c_{\mathrm{R,max}} \sum_{n=2}^{7} a_n \cdot \bar{c}^{(n)} + J^s \left(\frac{1}{2}\mathbf{E}^e : \hat{\mathbb{C}}(\bar{c})[\mathbf{E}^e]\right), \tag{8.120}$$

with

$$\hat{\mathbb{C}}(\bar{c}) \stackrel{\text{def}}{=} 2\hat{G}(\bar{c})\mathbb{I} + \left(\hat{K}(\bar{c}) - \frac{2}{3}\hat{G}(\bar{c})\right)\mathbf{1}\otimes\mathbf{1} \tag{8.121}$$

the elasticity tensor, and $J^s = 1 + \Omega(c_{\mathrm{R}} - c_{\mathrm{R},0})$.

8.10.3 Stress. Chemical potential

Using (8.120) and (8.101) we find that the Mandel stress is given by

$$\mathbf{M}^e = 2\hat{G}(\bar{c})\mathbf{E}^e + (\hat{K}(\bar{c}) - (2/3)\hat{G}(\bar{c}))(\mathrm{tr}\,\mathbf{E}^e)\mathbf{1}. \tag{8.122}$$

Then, using (8.103) we find that the Cauchy stress tensor is given by[3]

$$\mathbf{T} = J^{e-1}\Big(2\hat{G}(\bar{c})\mathbf{E}^e_{\mathrm{H}} + (K(c_{\mathrm{R}}) - (2/3)\hat{G}(\bar{c}))(\mathrm{tr}\,\mathbf{E}^e_{\mathrm{H}})\mathbf{1}\Big). \tag{8.123}$$

Hence the Piola stress, $\mathbf{T}_{\mathrm{R}} = J\mathbf{T}\mathbf{F}^{-\mathsf{T}}$, is given by

$$\mathbf{T}_{\mathrm{R}} = J^s\Big(2\hat{G}(\bar{c})\mathbf{E}^e_{\mathrm{H}} + (\hat{K}(\bar{c}) - (2/3)\hat{G}(\bar{c}))(\mathrm{tr}\,\mathbf{E}^e_{\mathrm{H}})\mathbf{1}\Big)\mathbf{F}^{-\mathsf{T}}. \tag{8.124}$$

In (8.123) and (8.124) we have used the notation

$$\mathbf{E}^e_{\mathrm{H}} = \ln\mathbf{V}^e \tag{8.125}$$

for the logarithmic elastic strain in the deformed body.

[3]Cf. Qi et al. (2010) and Shenoy et al. (2010) for a first-principles calculation of the variation of elastic constants of silicon and graphite with increasing Li content. Their calculations show that graphite is substantially stiffened by lithium, while silicon is substantially *softened*.

Also, using (8.104) and (8.120), the chemical potential μ is given by

$$\begin{aligned}\mu &= R\vartheta \ln\left(\gamma\frac{\bar{c}}{1-\bar{c}}\right)\\ &- \left(\Omega\frac{1}{3}(\mathrm{tr}\,\mathbf{M}^e) - \frac{J^s}{c_{\mathrm{R,max}}}\left(\tfrac{1}{2}\mathbf{E}^e : \frac{\partial\hat{\mathbb{C}}(\bar{c})}{\partial\bar{c}}[\mathbf{E}^e]\right) - \Omega\left(\tfrac{1}{2}\mathbf{E}^e : \hat{\mathbb{C}}(c_{\mathrm{R}})[\mathbf{E}^e]\right)\right).\end{aligned} \tag{8.126}$$

where in writing (8.126) we have defined an "activity coefficient" γ by

$$R\vartheta\ln(\gamma) = \sum_{n=2}^{7} a_n \cdot n \cdot \bar{c}^{(n-1)}. \tag{8.127}$$

8.10.4 Species flux

In the expression (8.111) for the species flux, we take mobility as the following function of the species concentration

$$\hat{m}(c_{\mathrm{R}}) = m_0 c\,(1-\bar{c}), \qquad \text{with} \qquad m_0 > 0, \tag{8.128}$$

which represents the physical requirement that the pure phases $c = 0$ and $\bar{c} = 1$ have vanishing mobility. Further,

$$D_0 \overset{\text{def}}{=} m_0 R\vartheta > 0 \tag{8.129}$$

denotes the *diffusivity* of the chemical species.

Then, using (8.128) in (8.111) we obtain

$$\mathbf{j} = -m_0 c(1-\bar{c})\mathrm{grad}\,\mu \tag{8.130}$$

with μ given in (8.126).

8.10.5 Plastic flow rate $\dot{\bar{\epsilon}}^p$

Next, we consider the flow function (8.109) which specifies the equivalent tensile plastic strain rate. We introduce two positive-valued scalar resistances Y and Y_* with dimensions of stress. We assume that Y_* is a *constant*, while

$$Y = \hat{Y}(\bar{c})$$

depends on the species concentration $\bar{c}$. The resistance Y accounts for strain hardening/softening characteristics of the material. Then, as a simple specific expression for $\dot{\bar{\epsilon}}^p$, we choose

a the following power-law form

$$\dot{\bar{\epsilon}}^p = \begin{cases} 0 & \text{if} \quad \bar{\sigma} \leq Y, \\ \dot{\epsilon}_0 \left(\dfrac{\bar{\sigma} - Y}{Y_*} \right)^m & \text{if} \quad \bar{\sigma} > Y. \end{cases} \tag{8.131}$$

For non-zero plastic strain rate, (8.131) may be inverted to give the following strength relation,

$$\bar{\sigma} = \hat{Y}(\bar{c}) + Y_* \left(\frac{\dot{\bar{\epsilon}}^p}{\dot{\epsilon}_0} \right)^{1/m} \quad \text{when} \quad \dot{\bar{\epsilon}}^p > 0. \tag{8.132}$$

Here $\dot{\epsilon}_0$ is reference tensile plastic strain rate, and m is a measure of the strain-rate sensitivity of the material.

In order to model the experimentally-observed concentration-dependent change in the yield strength of a-Si, we adopt the following specific form for $\hat{Y}(\bar{c})$,

$$\hat{Y}(\bar{c}) = Y_{\text{sat}} + (Y_0 - Y_{\text{sat}}) \exp\left(-\frac{\bar{c}}{\bar{c}_*} \right), \tag{8.133}$$

with $\{Y_0, Y_{\text{sat}}, \bar{c}_*\}$ three positive-valued material parameters. This function produces a simple exponential softening response from an initial value Y_0 to a lower saturation value $Y_{\text{sat}} < Y_0$, with $\bar{c}_*$ controlling the rate of decay. Further, as a special value for Y_* in the rate-dependent response (8.146), we take

$$Y_* = Y_{\text{sat}}. \tag{8.134}$$

8.11 Summary of the specialized constitutive theory

Our specialized theory relates the following basic fields:

$\mathbf{x} = \boldsymbol{\chi}(\mathbf{X}, t)$	motion;
$\mathbf{F} = \nabla\boldsymbol{\chi}$	deformation gradient;
$\mathbf{F} = \mathbf{F}^e\mathbf{F}^p\mathbf{F}^s$	multiplicative decomposition of $\mathbf{F}$;
$\mathbf{F}^s, \mathbf{F}^p, \mathbf{F}^e$	swelling, plastic, and elastic distortions;
$\mathbf{F}^e = \mathbf{R}^e\mathbf{U}^e$	polar decompositions of $\mathbf{F}^e$;
$\mathbf{U}^e = \sum_{\alpha=1}^{3} \lambda_\alpha^e \mathbf{r}_\alpha^e \otimes \mathbf{r}_\alpha^e$	spectral decomposition of $\mathbf{U}^e$;
$\mathbf{E}^e = \sum_{\alpha=1}^{3} (\ln \lambda_\alpha^e)\mathbf{r}_\alpha^e \otimes \mathbf{r}_\alpha^e$	logarithmic elastic strain;
$\mathbf{E}_{\mathrm{H}}^e = \mathbf{R}^e\mathbf{E}^e\mathbf{R}^{e\mathsf{T}}$	spatial logarithmic elastic strain;
$\mathbf{T} = \mathbf{T}^{\mathsf{T}}$	Cauchy stress;
$\mathbf{M}^e = J^e\mathbf{R}^{e\mathsf{T}}\mathbf{T}\mathbf{R}^e$	Mandel stress;
c_{R}	molar concentration per unit reference volume;
$c_{\mathrm{R,max}}$	maximum molar concentration per unit reference volume;
$\bar{c} = c_{\mathrm{R}}/c_{\mathrm{R,max}} \in [0, 1]$	normalized concentration;
$c = J^{-1}c_{\mathrm{R}}$	molar concentration per unit volume in the deformed body;
μ	chemical potential;
$\mathbf{j}$	spatial species flux vector.

8.11.1 Constitutive equations

1. **Kinematics.** Multiplicative decomposition of the deformation gradient,

$$\mathbf{F} = \mathbf{F}^e\mathbf{F}^p\mathbf{F}^s, \tag{8.135}$$

with

$$J = \det\mathbf{F} > 0, \qquad J^e = \det\mathbf{F}^e > 0, \qquad J^p = \det\mathbf{F}^p = 1, \qquad J^s = \det\mathbf{F}^s > 0. \tag{8.136}$$

2. **Swelling distortion.** Based on the isotropy of a-Si, we take the swelling distortion $\mathbf{F}^s$ to be spherical and to depend on the Li concentration,

$$\mathbf{F}^s = (J^s)^{1/3}\mathbf{1}, \quad \text{with} \quad J^s = 1 + \Omega(c_{\mathrm{R}} - c_{\mathrm{R},0}), \tag{8.137}$$

where Ω is a constant *partial molar volume* of the intercalating Li in the body, and $c_{\mathrm{R},0}$ is the initial concentration of Li.

3. **Free energy.** The free energy per unit reference volume is taken as

$$\psi_{\mathrm{R}} = \underbrace{R\vartheta c_{\mathrm{R,max}}\Big(\bar{c}\ln\bar{c} + (1-\bar{c})\ln(1-\bar{c})\Big) + c_{\mathrm{R,max}}\sum_{n=2}^{7} a_n \cdot \bar{c}^{(n)}}_{\text{chemical energy}} + \underbrace{J^s\left(\frac{1}{2}\mathbf{E}^e : \hat{\mathbb{C}}(\bar{c})[\mathbf{E}^e]\right)}_{\text{elastic energy}}. \tag{8.138}$$

Here, R is the gas constant, ϑ is the constant absolute temperature, and the polynomial dependence $\sum_{n=2}^{7} a_n \cdot \bar{c}^{(n)}$ in the chemical free energy, in which a_n are fitting coefficients, is motivated by the recent paper Bucci et al. (2014). Further,

$$\hat{\mathbb{C}}(\bar{c}) = 2\hat{G}(\bar{c})\mathbb{I} + (\hat{K}(\bar{c}) - (2/3)\hat{G}(\bar{c}))\mathbf{1}\otimes\mathbf{1}, \tag{8.139}$$

is a *concentration-dependent* elasticity tensor, with $\hat{G}(\bar{c})$ and $\hat{K}(\bar{c})$ concentration-dependent shear and bulk moduli, respectively.

4. **Stress.** The Mandel and Cauchy stress tensors are respectively given by,

$$\begin{aligned} \mathbf{M}^e &= J^{s-1}\frac{\partial\psi_{\mathrm{R}}}{\partial\mathbf{E}^e} = 2\hat{G}(\bar{c})\mathbf{E}^e + \left(\hat{K}(\bar{c}) - \frac{2}{3}\hat{G}(\bar{c})\right)(\mathrm{tr}\,\mathbf{E}^e)\mathbf{1}, \qquad \text{and} \\ \mathbf{T} &= J^{e-1}\mathbf{R}^e\mathbf{M}^e\mathbf{R}^{e\mathsf{T}} = J^{e-1}\left(2\hat{G}(\bar{c})\mathbf{E}^e_{\mathrm{H}} + \left(\hat{K}(\bar{c}) - \frac{2}{3}\hat{G}(\bar{c})\right)(\mathrm{tr}\,\mathbf{E}^e_{\mathrm{H}})\mathbf{1}\right). \end{aligned} \tag{8.140}$$

5. **Chemical Potential.** The chemical potential of the Li in the anode is given by,

$$\begin{aligned} \mu &= \frac{\partial\psi_{\mathrm{R}}}{\partial c_{\mathrm{R}}} - \Omega\frac{1}{3}\mathrm{tr}\,\mathbf{M}^e \\ &= R\vartheta\ln\left(\gamma\frac{\bar{c}}{1-\bar{c}}\right) - \Omega\frac{1}{3}\mathrm{tr}\,\mathbf{M}^e + \frac{J^s}{c_{\mathrm{R,max}}}\left(\frac{1}{2}\mathbf{E}^e : \frac{d\hat{\mathbb{C}}(\bar{c})}{d\bar{c}}[\mathbf{E}^e]\right) + \Omega\left(\frac{1}{2}\mathbf{E}^e : \hat{\mathbb{C}}(\bar{c})[\mathbf{E}^e]\right) \end{aligned} \tag{8.141}$$

where, following Bucci et al. (2014), we have defined an "activity coefficient" γ by

$$R\vartheta\ln(\gamma) = \sum_{n=2}^{7} a_n \cdot n \cdot \bar{c}^{(n-1)}. \tag{8.142}$$

The polynomial coefficients a_n are determined by fitting to experimental or numerical simulations of the open-circuit potential of Si during lithiation. Such a fit was performed by Bucci et al. (2014) for a-Si; we use their fitting coefficients in this paper.

6. **Evolution equation for $\mathbf{F}^p$.** The plastic distortion evolves according to

$$\dot{\mathbf{F}}^p = \mathbf{D}^p\mathbf{F}^p, \qquad \text{with} \qquad \mathbf{D}^p = \dot{\bar{\epsilon}}^p \left(\frac{3\mathbf{M}_0^e}{2\bar{\sigma}}\right), \qquad \dot{\bar{\epsilon}}^p \geq 0, \qquad \mathbf{F}^p(\mathbf{X},0) = \mathbf{1}, \tag{8.143}$$

where

$$\bar{\sigma} \stackrel{\text{def}}{=} \sqrt{3/2}|\mathbf{M}_0^e| \tag{8.144}$$

defines an *equivalent tensile stress*, and $\dot{\bar{\epsilon}}^p$ denotes an *equivalent tensile plastic strain rate.* We introduce a positive-valued, stress-dimensioned, and concentration-dependent *yield strength* $Y(\bar{c}) > 0$, and assume that a no-flow condition,

$$\dot{\bar{\epsilon}}^p = 0 \quad \text{if} \quad \bar{\sigma} \leq \hat{Y}(\bar{c}), \tag{8.145}$$

holds. During plastic flow, $\dot{\bar{\epsilon}}^p > 0$, the equivalent tensile stress is taken to be equal to a *rate-dependent flow strength,*

$$\bar{\sigma} = \hat{Y}(\bar{c}) + Y_* \left(\frac{\dot{\bar{\epsilon}}^p}{\dot{\epsilon}_0}\right)^{1/m}, \tag{8.146}$$

where $Y_* > 0$ is a positive-valued, stress-dimensioned constant, $\dot{\epsilon}_0$ is a reference tensile plastic strain rate, and m is a measure of the strain-rate sensititivy of the material. Equations (8.145) and (8.146) may be combined to give the equivalent tensile plastic strain rate as,

$$\dot{\bar{\epsilon}}^p = \begin{cases} 0 & \text{if} \quad \bar{\sigma} \leq Y(\bar{c}), \\ \dot{\epsilon}_0 \left(\dfrac{\bar{\sigma} - \hat{Y}(\bar{c})}{Y_*}\right)^m & \text{if} \quad \bar{\sigma} > Y(\bar{c}). \end{cases} \tag{8.147}$$

In order to model the experimentally-observed concentration-dependent change in the yield strength of a-Si, we adopt the following specific form for $Y(\bar{c})$,

$$\hat{Y}(\bar{c}) = Y_{\text{sat}} + (Y_0 - Y_{\text{sat}}) \exp\left(-\frac{\bar{c}}{\bar{c}_*}\right), \tag{8.148}$$

with $\{Y_0, Y_{\text{sat}}, \bar{c}_*\}$ three positive-valued material parameters. This function produces a simple exponential softening response from an initial value Y_0 to a lower saturation value $Y_{\text{sat}} < Y_0$, with $\bar{c}_*$ controlling the rate of decay. Further, as a special value for Y_* in the rate-dependent response (8.146), we take

$$Y_* = Y_{\text{sat}}. \tag{8.149}$$

7. **Species flux.** The *spatial flux* $\mathbf{j}$, of the intercalating Li is taken to depend on the *spatial gradient* $\operatorname{grad}\mu$, of the chemical potential:

$$\mathbf{j} = -m \operatorname{grad}\mu, \quad \text{with} \quad m = \frac{D_0}{R\vartheta} c(1-\bar{c}) \geq 0 \quad \text{the mobility.} \tag{8.150}$$

Here, D_0 is a constant diffusion coefficient.

8.12 Governing partial differential equations. Boundary and initial conditions

The governing partial differential equations consist of:

1. The local force balance

$$\operatorname{div}\mathbf{T} + \mathbf{b} = \mathbf{0}, \tag{8.151}$$

where the Cauchy stress $\mathbf{T}$ is given by (8.140), and $\mathbf{b}$ is the non-inertial body force.

2. The local balance for the species concentration

$$\dot{c}_{\mathrm{R}} = -J \operatorname{div}\mathbf{j}, \tag{8.152}$$

with the flux $\mathbf{j}$ given by (8.150).

With $\mathcal{S}_{\mathbf{u}}$ and $\mathcal{S}_{\mathbf{t}}$ denoting complementary subsurfaces of the boundary $\partial\mathcal{B}_t$ of the deformed body $\mathcal{B}_t$, as boundary conditions we consider a pair of simple boundary conditions in which the displacement $\mathbf{u} = \mathbf{x} - \mathbf{X}$ is specified on $\mathcal{S}_{\mathbf{u}}$ and the surface traction on $\mathcal{S}_{\mathbf{t}}$:

$$\left.\begin{aligned} \mathbf{u} &= \breve{\mathbf{u}} \quad \text{on} \quad \mathcal{S}_{\mathbf{u}} \times (0,T), \\ \mathbf{T}\mathbf{n} &= \breve{\mathbf{t}} \quad \text{on} \quad \mathcal{S}_{\mathbf{t}} \times (0,T). \end{aligned}\right\} \tag{8.153}$$

With $\mathcal{S}_\mu$ and $\mathcal{S}_{\mathbf{j}}$ another pair of complementary subsurfaces of the boundary $\partial\mathcal{B}_t$, we also consider boundary conditions in which the chemical potential is specified on $\mathcal{S}_\mu$ and the spatial species flux on $\mathcal{S}_{\mathbf{j}}$

$$\left.\begin{aligned} \mu &= \breve{\mu} \quad \text{on } \mathcal{S}_\mu \times (0,T), \\ \mathbf{j}\cdot\mathbf{n} &= \breve{j} \quad \text{on } \mathcal{S}_{\mathbf{j}} \times (0,T). \end{aligned}\right\} \tag{8.154}$$

The initial data is taken as

$$\mathbf{u}(\mathbf{X},0) = \mathbf{0}, \quad \text{and} \quad \mu(\mathbf{X},0) = \mu_0(\mathbf{X}) \quad \text{in} \quad \mathrm{B}. \tag{8.155}$$

The coupled set of equations (8.151) and (8.152), together with (8.153), (8.154) and (8.155) yield an initial/boundary-value problem for the displacement $\mathbf{u}(\mathbf{X},t)$ and the chemical potential $\mu(\mathbf{X},t)$.

8.13 Electrode/electrolyte interfacial reaction kinetics. Butler-Volmer equation

ELECTROCHEMICAL POTENTIAL: The **electrochemical potential** of the ith charged species in a chemical reaction is defined as

$$\tilde{\mu}_i \stackrel{\text{def}}{=} \mu_i + z_i F \phi_I, \tag{8.156}$$

where μ_i is its **chemical potential**, z_i is its valence, F is Faraday's constant,[4] and ϕ_I is the electric potential in phase I in which the charged species is found.[5]

Consider an electrode containing some Li submerged in a bath of an electrolyte containing Li^+ ions. We make the following assumptions regarding this system:

- The electrode material is considered insoluble in the electrolyte.
- We assume that within the electrode there are more than enough electrons to combine with the Li ions, so that lithium in the electrode exists as a *neutral species.*
- We consider the electrical conductivity of the electrode to be large, and the diffusion of Li^+ through the electrolyte to be fast.
- We denote the electric potential in the electrode by ϕ^e, and the electric potential in the electrolyte by ϕ. Further, we assume that both of these electric potentials are uniform, and variations in the electric potential occur only at the electrode/electrolyte interface.

Consider now the following electrochemical reaction at the surface of the electrode,

$$\mathrm{Li}^{(\text{electrode surf.})} \rightleftarrows \mathrm{Li}^{+(\text{electrolyte})} + \mathrm{e}^{-(\text{electrode surf.})}, \tag{8.157}$$

and let

$$\tilde{\mu}_{\mathrm{Li}}^{(\text{electrode surf.})}, \quad \tilde{\mu}_{\mathrm{Li}^+}^{(\text{electrolyte})}, \quad \text{and} \quad \tilde{\mu}_{\mathrm{e}^-}^{(\text{electrode surf.})}, \tag{8.158}$$

respectively, denote the the electrochemical potentials of the Li atoms on the surface of the electrode, Li ions in the electrolyte, and the electrons on the surface of the electrode.

Remark. Henceforth, for brevity, we will omit the superscripts used in (8.157) and (8.158) to denote the location of each species. Thus, for the ensuing discussion, the neutral Li as well as the electrons should always be considered as being on the the surface of the electrode, while the Li^+ ions should always be considered as being in the electrolyte. Hence, the subscript denoting the species type is also an indicator of its location. □

[4]The Faraday constant is the magnitude of electric charge per mole of electrons. It has a value $9.64853399(24) \times 10^4$ C mol^{-1}.

[5]Henceforth we distinguish the electrochemical potential with an overset tilde, $\tilde{\mu}$, while the chemical potential, μ, will not have an overset tilde.

Let the difference between the electrochemical potentials of the reactant and products in (8.157) divided by Faraday's constant be denoted by

$$\eta \stackrel{\text{def}}{=} \frac{1}{F}\Big(\tilde{\mu}_{\text{Li}} - (\tilde{\mu}_{\text{Li}^+} + \tilde{\mu}_{\text{e}^-})\Big). \tag{8.159}$$

This represents a "driving force" for the chemical reaction (8.157) in the sense that:

- If $\eta > 0$, then lithium is favored to be expelled form the electrode into the electrolyte — Li is oxidized to form Li^+.
- If $\eta < 0$, then lithium is favored to be intercalated form the electrolyte into the electrode — Li^+ is reduced to form Li.
- And, the condition $\eta = 0$ represents the condition for **equilibrium** of the reaction in equation (8.157).

The electrochemical potentials in (8.159) may be further expressed in terms of their chemical potentials and electric potentials as

$$\begin{aligned} \tilde{\mu}_{\text{Li}} &= \mu_{\text{Li}}, \\ \tilde{\mu}_{\text{Li}^+} &= \mu_{\text{Li}^+} + F\phi, \\ \tilde{\mu}_{\text{e}^-} &= \mu_{\text{e}^-} - F\phi^{\text{e}}, \end{aligned} \tag{8.160}$$

where in writing (8.160) we have made use of the fact that Li atoms in the electrode are a *neutral species*, that the Li ions are positively charged (valance of $+1$), and that the electrons are negatively charged (valance of -1). Further note that the electric potential acting on the Li ions is that of the electrolyte, ϕ, and the electric potential acting on the electrons is that of the electrode, ϕ^{e}.

Next, consistent with our earlier assumptions, we assume further that the activities of the Li^+ ions in the electrolyte and the electrons e^- in the electrode have a value of unity[6] — that is the electrolyte and the electrode may be treated as infinite reservoirs which supply Li^+ ions and electrons e^- to the chemical reaction at the surface of the electrode particle. Then, the electrochemical potentials (8.160) may be written as

$$\begin{aligned} \tilde{\mu}_{\text{Li}} &= \mu^0_{\text{Li}} + \hat{\mu}_{\text{Li}}(\bar{c}, \mathbf{M}^e, \vartheta), \\ \tilde{\mu}_{\text{Li}^+} &= \mu^0_{\text{Li}^+} + F\phi, \\ \tilde{\mu}_{\text{e}^-} &= \mu^0_{\text{e}^-} - F\phi^{\text{e}}, \end{aligned} \tag{8.161}$$

[6]The chemical potential of a species is usually written as

$$\mu_i = \mu_i^0 + R\vartheta \ln(a_i),$$

where a_i represents the *activity* of the species, and μ_i^0 represents the reference value when $a_i = 1$.

where the reference potentials μ^0_{Li}, $\mu^0_{\text{Li}^+}$ and $\mu^0_{\text{e}^-}$ are constants, and where we have recalled that the chemical potential of the Li at the surface of the electrode is a function of the concentration, the Mandel stress, and the temperature, (c.f. eq. 8.141). Using (8.161) we may write the quantity η defined (8.159) as

$$\eta = \frac{\hat{\mu}_{\text{Li}}(\bar{c}, \mathbf{M}^e, \vartheta)}{F} - \frac{(\mu^0_{\text{Li}^+} + \mu^0_{\text{e}^-} - \mu^0_{\text{Li}})}{F} + \Delta\phi, \tag{8.162}$$

where

$$\Delta\phi \stackrel{\text{def}}{=} (\phi^{\text{e}} - \phi), \tag{8.163}$$

represents the *voltage drop* across the electrode/electroyte interface.

Equilibrium: At equilibrium $\eta = 0$. Thus, using (8.162), we may define an *equilibrium interfacial voltage* as

$$\Delta\phi_{\text{eq}} = V_0^* - \frac{\hat{\mu}_{\text{Li}}(\bar{c}, \mathbf{M}^e, \vartheta)}{F}, \tag{8.164}$$

where

$$V_0^* \stackrel{\text{def}}{=} \frac{(\mu^0_{\text{Li}^+} + \mu^0_{\text{e}^-} - \mu^0_{\text{Li}})}{F} \equiv \text{constant}. \tag{8.165}$$

In the absence of stresses, (8.164) represents the standard Nernst equation for the system under consideration.

Using (8.164), we may rewrite (8.162) as

$$\eta = \Delta\phi - \Delta\phi_{\text{eq}}. \tag{8.166}$$

The quantity η is commonly referred to as the **overpotential**, since — as is clear from (8.166) — it represents the electric potential above (or below) an equilibrium value required to drive the chemical reaction.

Deviation from equilibrium: When the overpotential $\eta \neq 0$, the chemical reaction (8.157) takes place, and there is a resulting current I. The current I *per unit area* is a function of the overpotential η, and is widely taken to be given by the phenomenological Butler-Volmer equation (cf., e.g., Newman and Thomas-Alyea, 2010; Bazant, 2013),

$$I = I_0 \left(\exp\left(-\alpha \frac{F\eta}{R\vartheta} \right) - \exp\left((1-\alpha) \frac{F\eta}{R\vartheta} \right) \right). \tag{8.167}$$

Here, I_0 is a concentration-dependent *exchange current*, given by

$$I_0 = F k_0 (1-\bar{c})^{\alpha} \bar{c}^{(1-\alpha)}, \tag{8.168}$$

$0 < \alpha < 1$ is a symmetry factor which biases the reaction, and k_0 is a rate constant which is typically determined experimentally. In our simulations we assume $\alpha = 0.5$, in which case

(8.167) may be inverted to yield

$$\eta = 2\frac{R\vartheta}{F}\sinh^{-1}\left(-\frac{1}{2}\frac{I}{I_0}\right), \quad \text{with} \quad I_0 = Fk_0(1-\bar{c})^{1/2}(\bar{c})^{1/2}. \tag{8.169}$$

Remark. In writing the (8.168), we have made an assumption that the exchange current I_0 depend only on the concentration in a fashion that is consistent with an ideal solid solution (cf. Bazant, 2013). Due to the fact that the chemical potential μ_{Li} depends also on the mechanical deformation through the Mandel stress, we expect that I_0 should also depend on the mechanical deformation through the Mandel stress. We neglect any such dependence here. Hence, our interfacial reaction kinetics, as given by the Butler-Volmer equation (8.167), depend on the Mandel stress only through the overpotential η. We leave a detailed investigation of the effect of stress on the exchange current I_0 for a future work. □

Equilibrium potential. Cell voltage: Let

$$\Delta\phi_{\text{cnt}} \stackrel{\text{def}}{=} \phi^{\text{cnt}} - \phi,$$

define the voltage drop at the counter-electrode/electrolyte interface in the cell, where ϕ^{cnt} is the electric potential of the counter-electrode which is a constant. Then, we define an **equilibrium potential** for the cell through

$$U \stackrel{\text{def}}{=} \Delta\phi_{\text{eq}} - \Delta\phi_{\text{cnt}}. \tag{8.170}$$

Then, using (8.170) and (8.164), we obtain that

$$U = V_0 - \frac{\hat{\mu}_{\text{Li}}(\bar{c}, \mathbf{M}^e, \vartheta)}{F}, \qquad \text{where} \qquad V_0 \stackrel{\text{def}}{=} V_0^* - \Delta\phi_{\text{cnt}} \equiv \text{constant}. \tag{8.171}$$

Thus, the parameter V_0 depends on the counter-electrode used. It is a Li foil in all the experiments considered in this part of the thesis.

Finally, the **cell voltage** is defined as the voltage drop between the electrode and the counter electrode

$$\begin{aligned} V &\stackrel{\text{def}}{=} \phi^e - \phi^{\text{cnt}} \\ &= (\phi^{\text{e}} - \phi) - (\phi^{\text{cnt}} - \phi) = \Delta\phi - \Delta\phi_{\text{cnt}}, \end{aligned} \tag{8.172}$$

where in writting (8.172) we have made use of the assumption that the electrolyte electric potential ϕ is constant through the electrolyte. Using (8.166), (8.169), and (8.171) the cell

voltage may be written as

$$\begin{aligned} V &= U + \eta \\ &= V_0 - \frac{\hat{\mu}_{\mathrm{Li}}(\bar{c}, \mathbf{M}^e, \vartheta)}{F} + 2\frac{R\vartheta}{F}\sinh^{-1}\left(-\frac{1}{2}\frac{I}{I_0}\right). \end{aligned} \tag{8.173}$$

Flux boundary condition: As discussed in $(8.154)_2$, at a point on the surface of the deformed body we may prescribe a flux boundary condition, $\mathbf{j}\cdot\mathbf{n} = \breve{j}$. The prescribed flux $\breve{j}$ is related to an applied current I per unit area at that point by

$$\breve{j} = -I/F. \tag{8.174}$$

For such an applied flux boundary condition, we may then use (8.173) to compute the voltage V corresponding the applied current per unit area I.

Remark. When a battery is cycled under constant current conditions, that is galvanostatic conditions, it is the *total* current

$$I_{\mathrm{total}} = \int_{\partial\mathcal{B}_t} I\, da,$$

which is constant across the electrode, while the current density I may not be uniform across the electrode even though the Voltage V might be. In a finite-element simulation of an arbitrary shaped-electrode which has been discretized to have m elements on the exterior boundary of the body, one must prescribe an *integral* constraint of the form

$$I_{\mathrm{total}} = \sum_{k=1}^{m}\int_{\partial\mathcal{B}_t^e} I_k\, da = \sum_{k=1}^{m}\int_{\partial\mathcal{B}_t^e} -F\,\breve{j}_k\, da \tag{8.175}$$

where $\breve{j}_k$ represents the flux to be prescribed on the desired surface of the k-th element. However, in the simulations considered in this part of the thesis the diffusion is essentially one-dimensional in nature, there is a single element on the surface of our simulation domains, and the simple eq. (8.174) applies. □

8.14 Numerical implementation of the theory

We have implemented our coupled diffusion-deformation theory described in Sect. 8.11 by writing a user-element subroutine (UEL) for Abaqus (2010), for a 2D axisymmetric 4-node linear isoparametric quadrilateral element. The details of our numerical procedure can be found in Appendix. C.

We note that in our numerical implementation we have ignored the last two terms in (8.141) for the chemical potential. These terms are quadratic in the elastic strains, and

expected to be smaller in magnitude than the other terms in (8.141). Cf. Sethuraman et al. (2010b) for arguments leading to such an approximation even for silicon, which can absorb a large amount of lithium, and for which the values of the elastic moduli are significantly affected when it is fully lithiated.

Chapter 9

Calibration of the material parameters in the theory

The purpose of this Chapter is to report on the calibration of the material parameters in our theory. The calibrated values are summarized in Table 9.1 at the end of this Section. A majority of the material properties necessary to characterize our constitutive theory are available in the literature. For the rest, we discuss in detail the procedures that we have used to estimate the values from published experimental data, primarily from the substrate-curvature experiments reported by Pharr et al. (2014).

9.1 Chemical properties

- The x in $\mathrm{Li}_x\mathrm{Si}$ represents the stoichiometric amount of Li in the compound $\mathrm{Li}_x\mathrm{Si}$. We assume here that Si may be fully lithiated to the compound $\mathrm{Li}_{15}\mathrm{Si}_4$, so that $x_{\max} = 3.75$. Note that x is related to the normalized concentration $\bar{c}$ by $x = x_{\max}\bar{c}$.

- With $\rho_{\mathrm{Si}} = 7.874 \cdot 10^4\,\mathrm{mol/m^3}$ the molar density of Si (Mohr et al., 2008), the maximum molar concentration of Li in Si is then given by $c_{\mathrm{R,max}} = 3.75 \cdot \rho_{\mathrm{Si}} = 0.295 \cdot 10^6\,\mathrm{mol/m^3}$.

- The maximum volumetric swelling of Si has been measured by Obrovac and Krause (2007) as $\Omega c_{\mathrm{R,max}} = 2.625$, and hence the partial molar volume of Li in Si is $\Omega = 8.89 \cdot 10^{-6}\,\mathrm{m^3/mol}$.

- The diffusivity D_0 of Li in Si has been measured by Ding et al. (2009) to be $D_0 = 10^{-16}\,\mathrm{m^2/sec}$.

- Finally, the coefficients used by Bucci et al. (2014) to fit the activity coefficient (8.142) are $a_2/F = 0.8735\,\mathrm{V}$, $a_3/F = 0.7185\,\mathrm{V}$, $a_4/F = -4.504\,\mathrm{V}$, $a_5/F = 6.876\,\mathrm{V}$, $a_6/F =$

$-4.6272\,\mathrm{V}$, and $a_7/F = 1.1744\,\mathrm{V}$, where $F = 9.6485{\cdot}10^4\,\mathrm{C/mol}$ is the Faraday constant. The reference potential is $V_0 = 0.88\,\mathrm{V}$

9.2 Elastic properties

With

$$a = \frac{x}{x+1} = \frac{x_{\max}\bar{c}}{x_{\max}\bar{c}+1} \tag{9.1}$$

denoting the atomic fraction of Li atoms, the variation of the Young's modulus E, and the Poisson's ratio ν, with Li concentration is taken to obey a simple rule-of-mixtures proposed by Sethuraman et al. (2012),

$$E = a\,E_{\mathrm{Li}} + (1-a)\,E_{\mathrm{Si}}, \quad \text{and} \quad \nu = a\,\nu_{\mathrm{Li}} + (1-a)\,\nu_{\mathrm{Si}}, \tag{9.2}$$

where $(E_{\mathrm{Li}}, \nu_{\mathrm{Li}})$ are the elastic properties of pure Li, and $(E_{\mathrm{Si}}, \nu_{\mathrm{Si}})$ are the elastic properties of pure Si. Although the mixture rule (9.2) is linear with respect to the atom fraction a, see Fig. 9-1(a), it produces a non-linear result with respect to either the stoichiometric coefficient x or the normalized concentration $\bar{c} = x/x_{\max}$, as shown in Fig. 9-1(b). The elastic moduli (E, ν) are converted to (G, K) by using the standard relations $G = E/(2(1+\nu))$ and $K = E/(3(1-2\nu))$.

9.3 Plastic Properties. Reaction Constant

The remaining material properties that need to be calibrated are the plastic properties $\{Y_0, Y_{\mathrm{sat}}, \bar{c}_*, \dot{\epsilon}_0, m\}$ in equations (8.147) and (8.148), as well as the reaction constant k_0 in the expression $(8.169)_2$ for the exchange current I_0. Pharr et al. (2014) and Bucci et al. (2014) have recently reported on their novel experiments in which a half-cell based on an a-Si thin-film anode deposited on a quartz substrate is galvanostatically cycled against a Li electrode, while the curvature of the substrate is simultaneously monitored. We have calibrated the plastic properties and the reaction constant by conducting finite-element simulations of the substrate curvature experiments and adjusting these material parameters so that pertinent numerical results match those which were measured experimentally by Pharr et al. (2014).

In the experiments of Pharr et al. (2014), a 100nm amorphous silicon film was deposited on a quartz substrate and first lithiated/delithiated galvanostatically against a Li-electrode in a half cell at a C-rate of 1/8 for one cycle. During the second cycle the lithiation rate was varied in order to induce different strain rates in the silicon film to probe the rate sensitivity of plastic flow of a-Si. During their experiment a substrate-curvature measuring technique was used to estimate the nominal stress in the a-Si film by using the classical Stoney formula (Stoney, 1909)

$$\sigma_n = \frac{1}{6}\frac{E_s}{1-\nu_s}\frac{h_s^2}{h_f}\kappa, \tag{9.3}$$

where κ is the experimentally-measured curvature of the substrate, E_s and ν_s are the Young's modulus and Poisson's ratio of the substrate, and h_s and h_f are the thicknesses of the substrate and the film layers, respectively.

As noted by Pharr et al. (2014), in their experiments there is loss of Li to the formation of SEI on the silicon anode. Thus, what is experimentally controlled during their galvanostatic experiments is the *total flux of lithium into the system*, j_{tot}, and not the flux of lithium, j_{Si} into the silicon anode; a portion j_{SEI} of the total flux in the system is consumed in the formation of the SEI. Thus,

$$j_{\text{Si}} = j_{\text{tot}} - j_{\text{SEI}}. \tag{9.4}$$

In our simulations we prescribe the flux of lithium into the silicon j_{Si}. Thus, in order to compare our simulations to the experimental results of Pharr et al. (2014), we need to estimate j_{SEI}. Following recent models of SEI formation (cf. e.g. Smith et al., 2011b; Pinson and Bazant, 2013), and based on our previous paper on modeling SEI growth, Rejovitzky et al. (2014), we assume that the rate of loss of Lithium is inversely proportional to the square-root of time[1]

$$j_{\text{SEI}} = B/\sqrt{t}, \tag{9.5}$$

where B is a proportionality constant. Thus, combining (9.5) with (9.4), we obtain

$$j_{\text{Si}} = j_{\text{tot}} - B/\sqrt{t}. \tag{9.6}$$

The total flux j_{tot} depends on the charging rate and is determined by the experimental conditions. From the experiment results of Pharr et al. (2014) we have estimated that[2]

$$B = 1.3364 \cdot 10^{-5}\,\text{mol}/(\text{m}^2\text{sec}^{1/2}).$$

For later use we introduce the quantity

$$x_{\text{tot}} = \frac{A}{V}\frac{3.75}{c_{\text{R,max}}}\int_0^t j_{\text{tot}}\,d\tau, \tag{9.7}$$

which represents a normalized measure of the total amount of Li going into the system; here A and V are the initial area and volume of the a-Si anode respectively.

The simulation domain used to numerically represent the substrate curvature experiments of Pharr et al. (2014) is shown in Fig. 9-2. In order to minimize computational effort, we have only considered a small section of an axisymmetric plate adjacent to the axis of radial

[1]Bucci et al. (2014) have accounted for Li lost to SEI formation in a similar manner; however, they accounted for the flux of Li lost to SEI formation using a model which also depends on the applied voltage. Here, for simplicity, and since modeling SEI formation is not the main objective of this paper, we simply model loss of Li to SEI formation through (9.6).

[2]Specifically, from their voltage versus SOC plot, we estimate the difference in concentration at 1 V before and after the first cycle, and based on the experimental C-rate, determine how much Li was lost in one full cycle.

symmetry as the simulation domain, and meshed it with a single column of elements.[3] The silicon layer was meshed with 20 user-elements whose constitutive behavior is described by the coupled diffusion-deformation theory summarized in Sect. 8.11. The glass layer is meshed with 20 built-in Abaqus elements whose constitute behavior is taken to be linear elastic with a Young's modulus of $E_s = 72\,\text{GPa}$ and Poissons ratio $\nu_s = 0.165$.

The boundary/initial conditions used for the substrate-curvature simulations are as follows:

- **Mechanical boundary conditions:** With respect to Fig. 9-2(b), consistent with radial symmetry, the nodes along edge AB are constrained to have zero radial displacement. All nodes along the edge CD are constrained to remain on a straight line as defined by the nodes at points C and D. The line formed by these nodes is free to move and rotate, and it is from the rotation of this line with respect to its initial vertical position that we compute the simulated curvature of the plate. Finally, the node at point B is constrained to have zero vertical displacement to prevent any rigid body motions.

- **Flux boundary conditions:** With respect to Fig. 9-2(b), on the nodes along edge AC we prescribe the flux of lithium according to (9.6). As in the experiment of Pharr et al. (2014), the total flux j_{tot} is set to correspond to a C-rate of 1/8 for the first full cycle. During the second cycle, the C-Rate was set to 1/8 for 1 h followed by a number of segments with different C-rates. The time of each segment was chosen such that the total flux into the system during each segment was equal. Specifically, C-rate jumps from 1/8 to

$$\text{C-rate} \in [1/2, 1/4, 1/16, 1/32, 1/64, 1/128], \tag{9.8}$$

  were considered.

The results from our material parameter calibration procedure are shown in Figs. 9-3 and 9-4. Fig. 9-3(a) compares the simulated nominal stress (solid line) as a function of the total lithium content x_{tot}, against the corresponding experimental measurement (dashed line) (Pharr et al., 2014). The simulation captures the experimentally-observed behavior relatively well. In obtaining this fit the material parameters

$$\dot{\epsilon}_0 = 2.3 \cdot 10^{-3}\,1/\text{sec} \quad \text{and} \quad m = 2.94,$$

for the material rate-sensitivity were taken directly from Pharr et al. (2014), and only the the parameters

$$\{Y_0, Y_{\text{sat}}, \bar{c}_*\}$$

in (8.148) were adjusted to fit the data.

[3] In the experiments of Pharr et al. (2014), there is also a 15 nm layer of Ti and a 300 nm layer of Cu between the glass substrate and the silicon film. Since these layers are relatively stiff, and much thinner than the glass substrate, we do not include them in our finite element model.

Fig. 9-3(b) shows the simulated voltage V (solid line) versus the total lithium content x_{tot}, against the corresponding experimental measurement (dashed line) (Pharr et al., 2014). Note that in the simulation shown in Fig. 9-3(b) we maintained a C-rate equal to 1/8; accordingly we have cropped the experimental data before the start of the C-rate jumps. The simulated voltage was computed using equation (8.173) by appropriately adjusting the parameter k_0 in the expression $(8.169)_2$ for the exchange current I_0. We adjusted k_0 so that the total dissipation of energy in one full cycle (i.e. the area inside the curves encompassed by the second and third half-cycles) in the simulation was approximately equal to that in the experiment.

With respect to the comparisons shown in Fig. 9-3, we make the following observations:

- In Fig. 9-3(a), the onset of plasticity, followed by plastic softening, occurs earlier in the simulation than in the experiment. This is likely due to the fact that we have *underestimated* the amount of Li lost to SEI formation in the early stages of lithiation.

- The functional form (8.148) for the variation of the yield strength with species concentration in the simulation captures the experimentally-observed plastic softening with increasing concentration, relatively well. During delithiation, the model as well as the experiments predict an increase in flow resistance due to a decrease in the concentration of lithium.

- The simulated elastic unloading after the first half-cycle matches well with the corresponding experimental results. This suggests that the mixing rule (9.2), combined with the elastic constants listed in Table 9.1, are well suited to characterizing the variation in elastic properties with changing Li concentration.

- As shown in Fig. 9-3(b), the simulation, using the reaction kinetics described in Sect. 8.13, gives a fairly good approximation of the experimentally-measured voltage versus x_{tot} response.

Finally, Figs. 9-4(b) and (c) compare the simulated and experimentally-measured stress-jumps due to changes in C-rate. Note that the axes in the two figures are identical in order to provide an accurate visual comparison of the stress increments and decrements with changes in C-rate. The simple power-law strain-rate-sensitivity for the a-Si in the theory produces stress-jumps which are comparable to those measured experimentally by Pharr et al. (2014).

The final list of calibrated values for a-Si is summarized in Table 9.1. Note that only the three material parameters $\{Y_0, Y_{\text{sat}}, \bar{c}_*\}$ for the rate-independent part of the plastic deformation resistance, and the reaction kinetics parameter k_0 for the exchange current have been fitted in this work; all the other parameters have been obtained from values published in the literature. With all the material parameters in the theory fixed to the values shown in this Table, in the next Section we apply our numerical simulation capability to model the hollow double-walled Silicon anodes developed by Wu et al. (2012).

Table 9.1: Material properties for our fully-coupled elastic-plastic deformation-diffusion model for amorphous Silicon anodes

	Parameter	Value	Source
Chemical	D_0	$10^{-16}\,\mathrm{m}^2/\mathrm{sec}$	Ding et al. (2009)
	$\Omega c_{\mathrm{R,max}}$	2.625	Obrovac and Krause (2007)
	$c_{\mathrm{R,max}} = 3.75 \cdot \rho_{\mathrm{Si}}$	$0.295 \cdot 10^6\,\mathrm{mol}/\mathrm{m}^3$	$\rho_{\mathrm{Si}} = 7.874 \cdot 10^4\,\mathrm{mol}/\mathrm{m}^3$ from Mohr et al. (2008)
	$[a_2, a_3, a_4, a_5, a_6, a_7]/F$	$[0.8735, 0.7185, -4.504, 6.876, -4.6272, 1.1744]\,\mathrm{V}$	Bucci et al. (2014)
Elastic	$E_{\text{a-Si}}$	80 GPa	Sethuraman et al. (2012)
	$\nu_{\text{a-Si}}$	0.22	
	E_{Li}	4.91 GPa	
	ν_{Li}	0.36	
Plastic Rate-Dependent	$\dot{\epsilon}_0$	$2.3 \cdot 10^{-3}\,1/\mathrm{sec}$	Pharr et al. (2014)
	m	2.94	
Plastic Rate-Independent	Y_0	1.6 GPa	Fitted to Pharr et al. (2014)
	Y_{sat}	0.4 GPa	
	$\bar{c}_*$	0.04	
Reaction Kinetics	k_0	$3.25 \cdot 10^{-7}\,\mathrm{mol/sec}$	Fitted to Pharr et al. (2014)

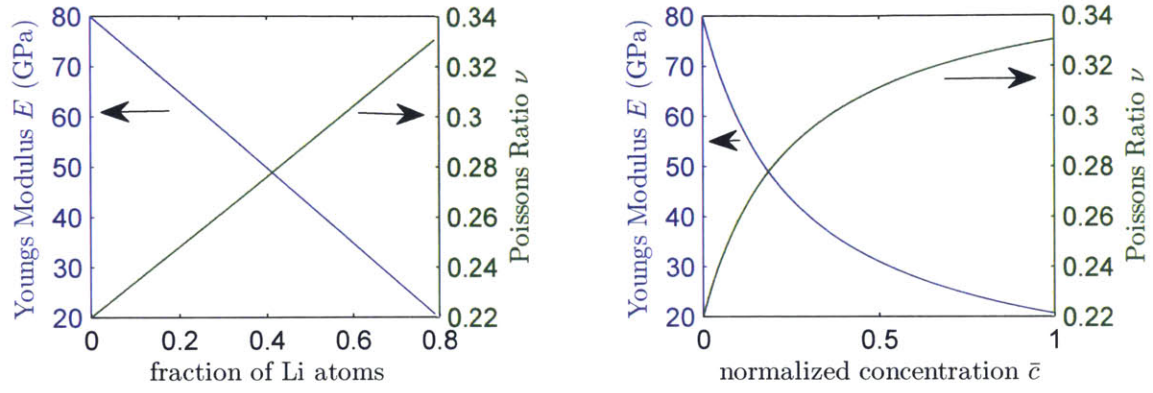

Figure 9-1: Variation of the elastic constants in Li_xSi as a function of (a) the fraction of Li atoms (number of Li atoms/total number of atoms), and (b) as a function of the normalized Li concentration $\bar{c}$.

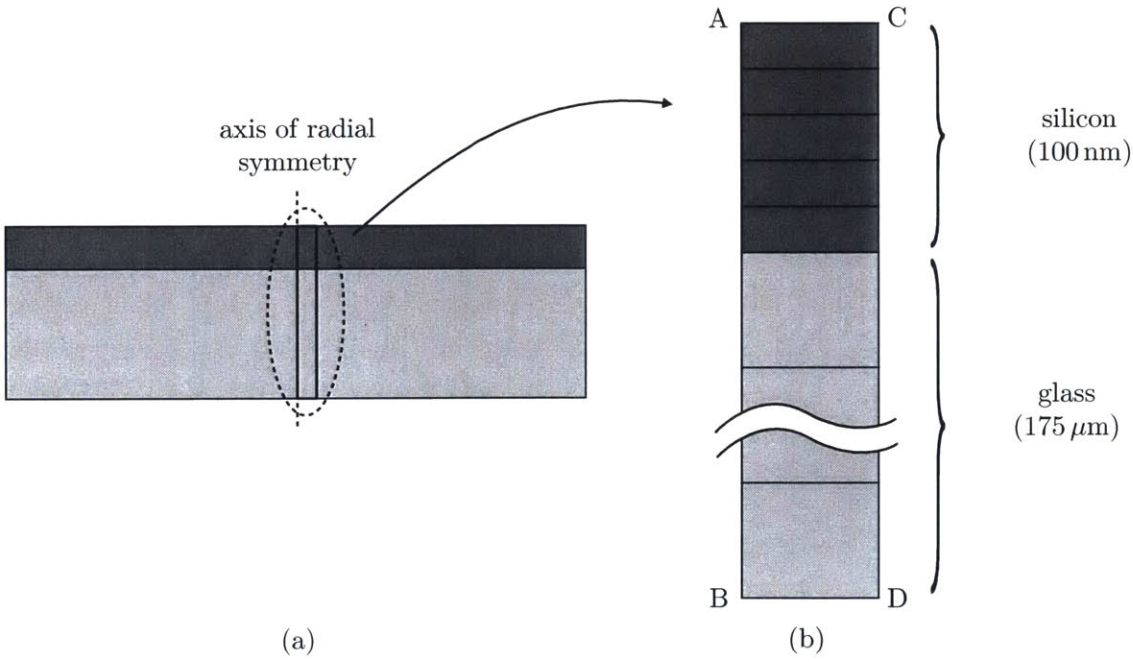

Figure 9-2: (a) Plate geometry showing simulation domain at the axis of radial symmetry, and (b) schematic of the single-column finite-element mesh used in the substrate curvature simulations.

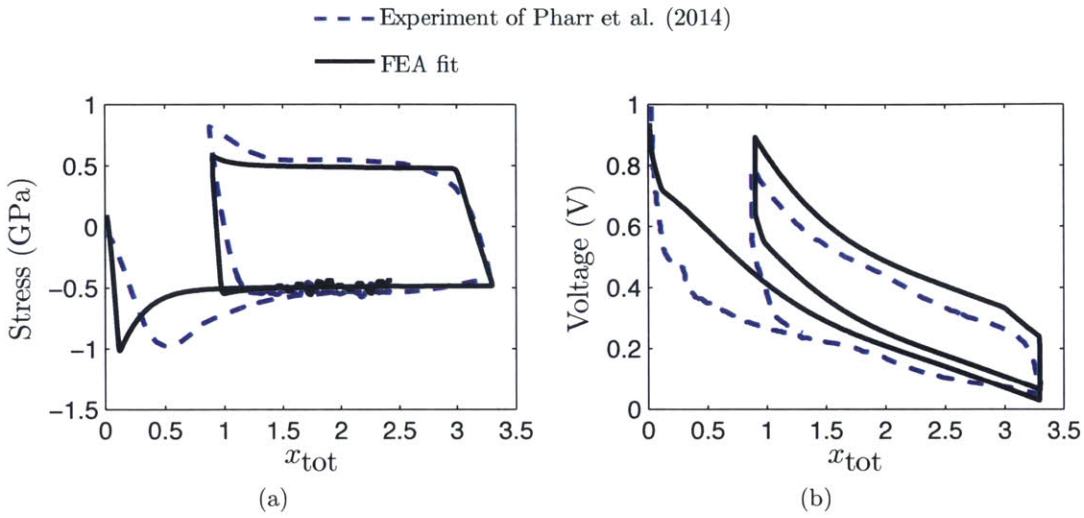

Figure 9-3: Fit of our substrate curvature simulation to the experiments of Pharr et al. (2014) showing (a) the nominal stress in the Si film, and (b) the voltage, both as functions of the total lithium content.

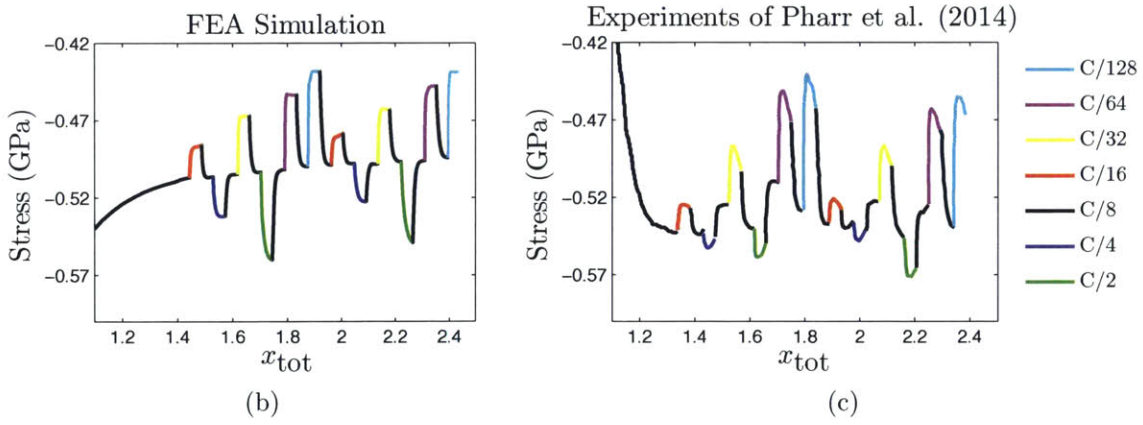

Figure 9-4: Nominal stress jumps produced by varying the C-rate from (a) our finite-element simulation, and (b) the experiments of Pharr et al. (2014).

Chapter 10

Modeling a hollow double-walled a-Si nanotube anode

As discussed in the introduction, in order to mitigate failure of the SEI, various research groups have proposed the use of novel Si anode designs which restrict the deformation incurred by the SEI during cyclic lithiation. One such design, experimentally-realized by Wu et al. (2012), involves fabricating an anode which consists of an ensemble of hollow a-Si nanotubes whose outside has been oxidized; see Fig. 10-1(a) for a TEM image. These structures are referred by the authors as double-walled nanotubes, where the two walls refer to an interior Si core and an exterior silicon-dioxide shell; see schematic Fig. 10-1(b). Since the electrolyte contacts the anode only on its exterior surface — the exposed surface of silicon-dioxide, the SEI will also grow only on the exterior of the nanotube. During cycling, the relatively stiff silicon-dioxide shell acts as a mechanical constraint layer which prevents the outward expansion of the nanotube, effectively restricting the deformation incurred by the SEI.

In this Section we apply our calibrated fully-coupled theory for a-Si to model such a geometrically-complex anode design. We do so with *all material properties for a-Si fixed at the values shown in Table 9.1, which were calibrated from independent experiments.* In our simulations, the mechanical properties of the SiO_2 layer are simply taken to be linear elastic with a Young's modulus of $E = 90\,\text{GPa}$, and a Poisson's ratio of $\nu = 0.17$.

In modeling the hollow nanotubes of Wu et al. (2012), we assume that they are axisymmetric and have a length much larger than their diameter, so that diffusion of Li occurs entirely in the radial direction. In accordance with these assumptions, and in order to save computational effort, we take a sliver of the hollow tube, cf. Fig. 10-1(b), as our simulation domain, and mesh it with a single row of elements; cf. Fig. 10-1(c). With respect to Fig. 10-1(c) we apply the following boundary:

- **Mechanical boundary conditions:** The nodes along the edge AC are constrained to have zero-displacement in the vertical z-direction. Consistent with our assumption

of a long thin tube, the nodes along edge DF are constrained to remain flat but are allowed to displace in the z-direction. The edges AF and CD are traction-free.

- **Chemical potential boundary conditions:** Consistent with our assumption of radial diffusion only, we constrain the chemical potential of the nodes on edge AC to equal the chemical potential of the nodes on edge DF.

- **Flux boundary conditions:** In these simulations we neglect the transport of Li through the SiO_2 layer. Then, consistent with the experiments which were done at a constant current, we prescribe a flux of Li into the Si directly on the nodes on edge BE. The magnitude of the flux is computed based on a desired C-rate through

$$\breve{j} = -(V/A)(\text{C-rate}/3600)c_{\text{R,max}},$$

where V and A are the initial volume and area of the Si anode respectively, and $c_{\text{R,max}}$ is the maximum molar concentration given in Table 9.1. In these simulations, for simplicity, we do not consider any loss of Li to SEI formation. As in the experiments of Wu et al. (2012), the simulated anode is cycled between voltage limits of 0.01 V and 1 V, where the simulated voltage is computed during the simulation using (8.173).

For later use, we define the state-of-charge (SOC) of the a-Si anode at a given time by

$$\text{SOC} = \int_{\text{B}} \bar{c}\, dV / \int_{B} dV. \tag{10.1}$$

Remark. As reported by Wu et al. (2012), and recently studied in detail by Zhang et al. (2014), it is expected that during cycling the SiO_2 film will react with Li to form a silicon-oxygen-lithium compound. This reaction, which is believed to be non-reversible, will consume lithium and also lead to an expansion of the SiO_2 film. In our simulations we do not attempt to model the uptake of Li, and the consequent expansion of the SiO_2 film during cycling. We make this purposeful choice for two reasons: (i) We would like to maintain our focus on the theory for a-Si and its response in the geometrically-complex anode under study; and (ii) It is unclear at present what the product of the reaction involving SiO_2 and Li is; and as such, attempting to model this would result in a number of additional fitting parameters which cannot — at this stage of available experimental data — be independently determined. □

10.1 Typical simulation output

A typical result of our simulations is shown in Fig. 10-2, where we cycled a hollow double-walled nanotube anode at a C-rate of 1 for three half-cycles between voltage limits of 0.01 and 1V. On the left in Fig. 10-2 we show contours of the normalized concentration $\bar{c}$ (top),

and contours of equivalent plastic strain $\bar{\epsilon}^p$ (bottom) in the a-Si. These contours are plotted at states (A) and (B), which respectively represent the states at the beginning and end of *the last half-cycle*; see the figure on the right, where these states are marked by dashed lines. From the contours of equivalent plastic strain we note that at the end of 3 half-cycles, the anode has accumulated a very large amount of plastic deformation — up to 210% plastic strain.

On the right of Fig. 10-2 we show plots of the equilibrium U (blue), and the voltage V (red), both as functions of the SOC. The difference between these two curves is the overpotential, $\eta = V - U$, which arises entirely due to the surface reaction kinetics described in Sect. 8.13. The equilibrium potential represents the intrinsic response of the Si anode, and visualizing it together with the voltage allows us to discern the contribution from the mechanical deformation of the Si anode to the overall voltage versus SOC behavior. The dissipation due to plastic deformation is evident in the hysteretic behavior of the equilibrium potential versus SOC curve. In this particular simulation, *plasticity accounts for* $\approx 15\%$ *of the total dissipation during one cycle.*

10.2 Comparison between our simulation results and the experiments of Wu et al. (2012)

Next, we compare our simulation results to the experimentally-measured voltage versus capacity curves of Wu et al. (2012). To convert the capacity data reported by these authors to SOC, we assume, as reported by the authors, that Si comprises 60% of the total mass of the active material, and that the maximum capacity of Si is 3.579 Ah/g. In order to compare the results from our simulations to those obtained experimentally, we ignore the results from the first half-cycle in our simulations, and shift the minimum SOC achieved in subsequent cycles to be zero. Fig. 10-3 (a) compares our simulated results (solid lines) for voltage versus SOC, against the experimental results (dashed lines) of Wu et al. (2012) at two C-rates — a C-rate of 1 (red) and a C-rate of 20 (blue). Although there are some discrepancies between the simulated and experimental results, our theory is capable of qualitatively reproducing the overall experimentally-measured response reasonably well.[1]

In order to get a more quantitative comparison between simulations and experiments, we may calculate two additional quantities from the voltage versus SOC curves at different C-rates:

- First, the *total dissipation* in one full cycle at a given C-rate is given by the corresponding area inside the voltage versus SOC curve.

[1] In our simulations we have considered only a single nanotube, while the experimental results of Wu et al. (2012) were obtained from an anode which was made up of an *ensemble* of nanotubes of various dimensions. Some of the differences between the simulated and experimental results shown in Fig. 10-3 are clearly due to the fact that we are considering only a single nanotube. In future work we aim to simulate an anode composed of many nanotubes of various dimensions.

- Second, the *maximum capacity* at a given C-rate corresponds to the capacity when the voltage hits the lower cutoff limit of 0.01 V.

We have carried out such calculations for several different C-rates. Fig. 10-3(b) shows the total dissipation as a function of C-rate — the simulations are shown as red circles, and the corresponding experiments are shown as black squares; note that the abscissa for the C-rates is logarithmic. It is clear from Fig. 10-3(b) that our simulations overestimate the total dissipation; however, our simulations correctly predict the experimentally-observed trend that the total dissipation is the largest at a C-rate ≈ 1, and decreases as the C-rate increases. The maximum capacity as a function of C-rate is shown in Fig. 10-3(c) — again the simulations are shown as red circles, and the corresponding experiments are shown as black squares. We obtain a good *quantitative prediction* of the experimentally-measured maximum capacity as a function of C-rate.

We emphasize again that the results shown in Fig. 10-3 were obtained by using material properties for a-Si which were were calbrated from *independent experiments*. This shows that the theory and simulation capability presented in this part of the thesis is capable, with reasonable accuracy, of modeling the electrochemical response of a geometrically-complex Si anode.

10.3 Role of plastic deformation on the electrochemical response of the a-Si anode

The simulation capability developed here allows us to explore the role of plastic deformation on the voltage versus SOC behavior of the anode during cycling. We expect, as noted by Sethuraman et al. (2010b), that plasticity will play a role both in determining the energy dissipated during cycling of the anode as well as in determining the realizable capacity of the anode.

First, we estimate the contribution of plasticity to the overall dissipation during cyclic lithiation/delithiation. Fig. 10-4(a) shows the plastic dissipation per cycle as a function of the C-rate. The dissipation due to plasticity is larger at low C-rates than at high C-rates. There are two factors that contribute to this behavior: First, since the plastic response of a-Si is rate-dependent, it exhibits a lower flow resistance at lower C-rates. Second, at low C-rates the voltage cutoff of 0.01 V is reached at higher values of SOC, and therefore the anode is deformed to a greater extent than at high C-rates.

Fig. 10-4 (b) shows the plastic dissipation normalized by the total dissipation (in percent) as a function of the C-rate. This figure clearly shows that at low C-rates plasticity plays a major role in the total dissipation of the anode over one cycle; *it accounts for over 30% of the total dissipation at a C-rate of 1/10.*

Although plasticity can contribute significantly to the total dissipation of energy of the anode per cycle, it also has the beneficial effect of relieving the build-up of elastic stresses in the material. This in turn reduces the voltage required to lithiate the anode to a particular SOC.

To illustrate this important effect we have performed simulations *suppressing plastic deformation*, while maintaining all other parameters constant. The results are shown in Fig. 10-5, where we compare a simulation with plasticity (red lines) to a simulation without plasticity (blue lines), both at a C-rate of 1. Fig. 10-5(a) compares the voltage V versus SOC for the two simulations. This figure clearly shows that the simulation without plasticity reaches the cutoff voltage of 0.01 V at a SOC of ≈ 0.3, whereas the simulation with plasticity reaches the cutoff at a much higher SOC of ≈ 0.7. The point in the first half-cycle where the two curves deviate indicates the onset of plasticity in the simulations with plasticity. Fig. 10-5(b) compares the equilibrium potential U versus SOC from the two simulations. Note that there is no discernible hysteretic behavior in the simulation without plasticity, since there is almost no dissipation of energy in the intrinsic behavior of the Si anode when plasticity is suppressed.[2]

We have carried out such calculations for several different C-rates. Figs. 10-5(c) and (d), respectively, show the total dissipation per cycle as a function of C-rate, and the maximum capacity (SOC at $V = 0.01\,\text{V}$) as a function of C-rate. Clearly, the simulations without plasticity produce significantly different results than those with plasticity.

[2] There are two possible dissipation mechanism in the electrode, one due to plastic deformation, and one due to gradients in the chemical potential (c.f. eq. (8.11) in Anand, 2012). In our simulations, due to the nano-metric size of the anodes considered, the gradients of the chemical potential are very small and consequently the dissipation due to gradients in the chemical potential is very small.

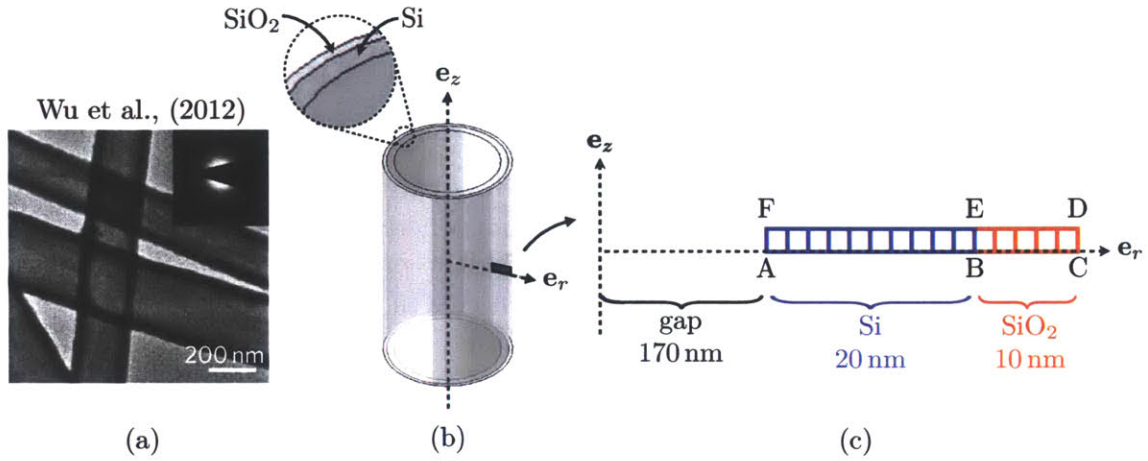

Figure 10-1: Modeling hollow double-walled nanotubes. (a) Shows a TEM of the experimentally-realized nanotubes reproduced from Wu et al. (2012). (b) Shows a representative hollow double-walled nanotube where, consistent with our assumptions of axisymmetry and radial diffusion, we take a sliver of the tube on the $\mathbf{e}_z$-$\mathbf{e}_r$ plane as our simulation domain. (c) Shows a schematic of the simulation domain (not to scale) and a representative finite-element mesh.

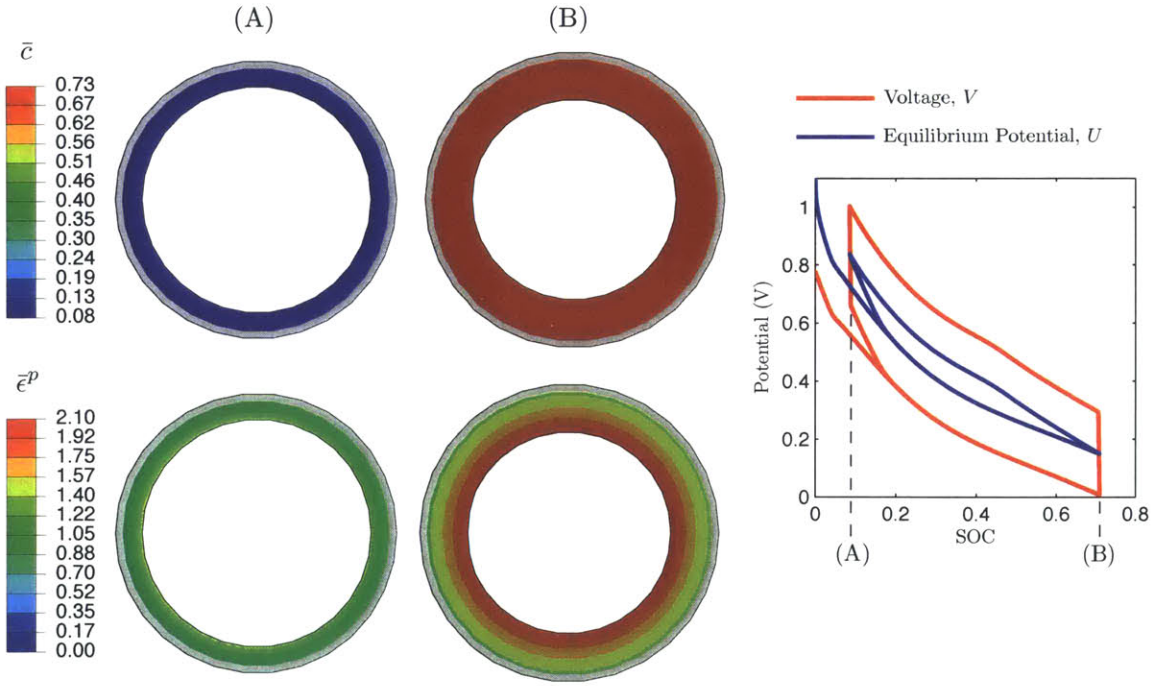

Figure 10-2: Simulation of a hollow double-walled nanotube anode cycled at a C-rate of 1 between voltage limits of 0.01 and 1 V for 3 half-cycles. Contours of normalized concentration $\bar{c}$ (top) and equivalent plastic strain $\bar{\epsilon}^p$ (bottom), in the a-Si anode, at (A) the start, and (B) the end of the last half-cycle. On the right we plot the voltage V, and equilibrium potential U, as functions of SOC, for the same simulation.

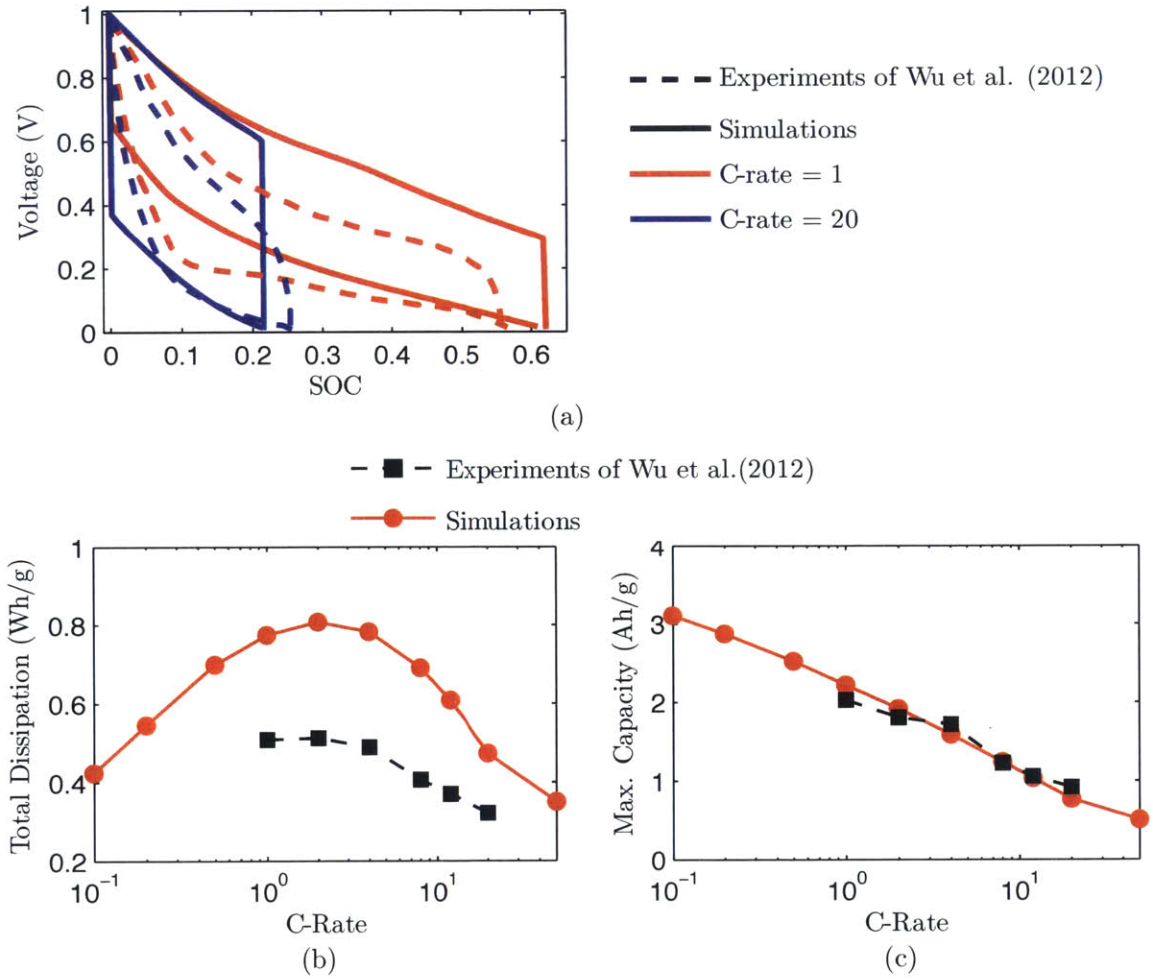

Figure 10-3: Comparison between simulated hollow double-walled nanotubes and the experiments of Wu et al. (2012). (a) Voltage versus SOC at C-rates of 1 and 20, (b) total dissipation over one full cycle as a function of C-rate, and (c) maximum capacity (i.e. SOC at cutoff of $V = 0.01\,\mathrm{V}$) as a function of C-rate.

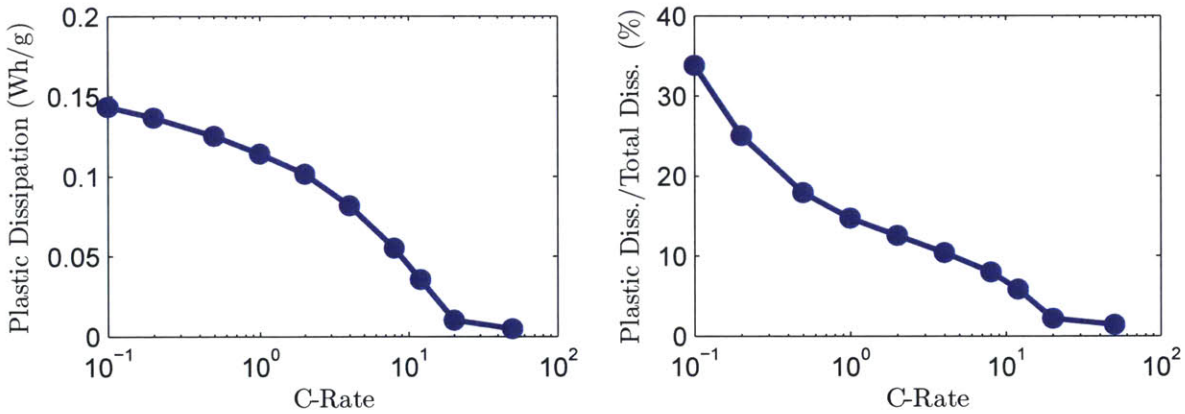

Figure 10-4: Simulations of hollow double-walled nanotubes. (a) Plastic dissipation over one full cycle as a function of C-rate. (b) Plastic dissipation normalized by total dissipation, in percent, as a function of C-rate. Note the logarithmic x-axis.

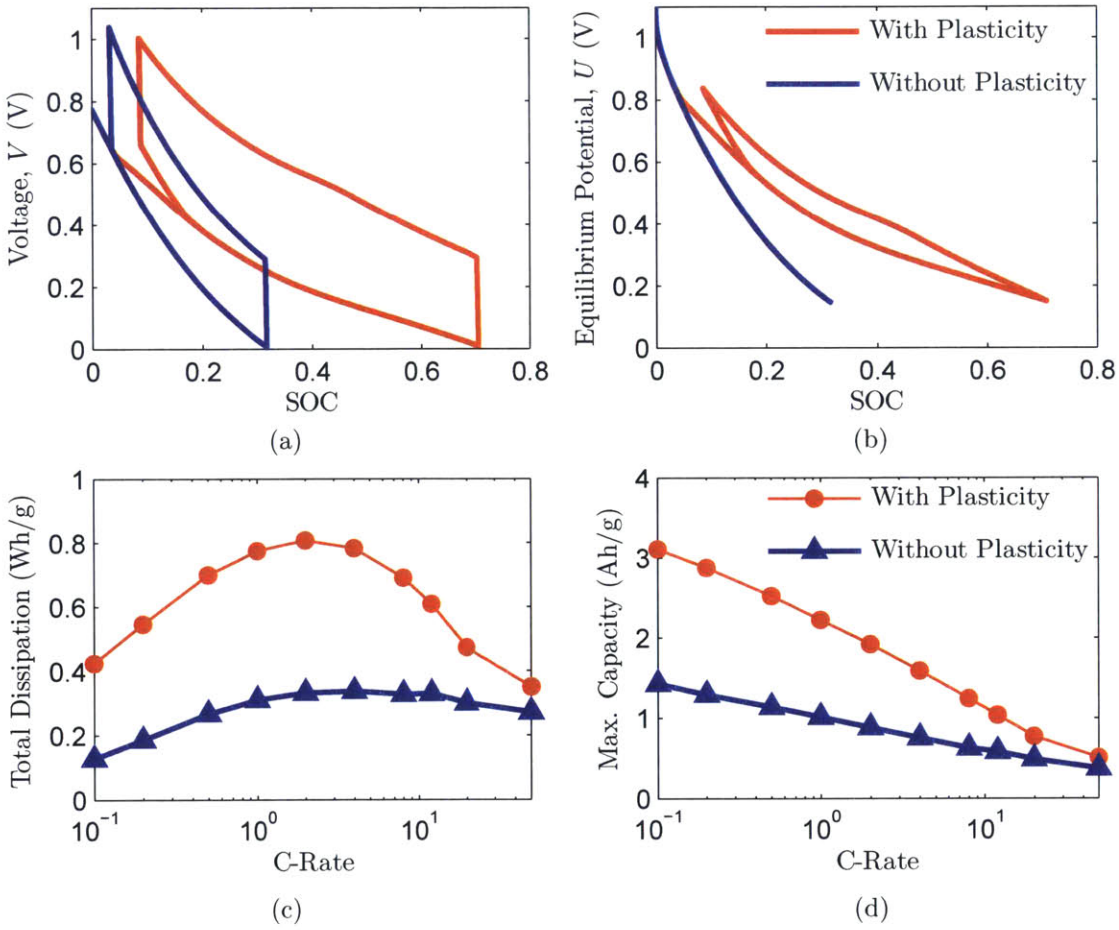

Figure 10-5: Simulations of hollow double-walled nanotubes with and without plasticity. (a) Voltage versus SOC, (b) equilibrium potential versus SOC, (c) total dissipation over one cycle versus C-rate, and (d) maximum capacity (i.e. SOC at cutoff of $V = 0.01$ V) versus C-rate. Note the logarithmic x-axis.

Chapter 11

Concluding remarks

We have formulated and numerically implemented a fully-coupled diffusion-deformation theory, which accounts for transient diffusion of lithium and accompanying large elastic-plastic deformations of a-Si. The material parameters in the theory have been calibrated to results from experiments reported in the literature. We have applied our numerical simulation capability to model galvanostatic charging of hollow a-Si nanotubes whose exterior walls have been oxidized to prevent outward expansion (Wu et al., 2012). We have shown that the results from our numerical simulations are in good agreement with the experimentally-measured voltage versus SOC behavior at various charging rates (C-rates). Through our simulations, we have identified two major effects of plasticity on the performance of a-Si-based anodes:

- First, plasticity enables lithiation of the anode to a higher SOC for a given voltage cut-off. This is because plastic flow reduces the stresses generated in the material, and thus reduces the potential required to lithiate the material.

- Second, plastic deformation accounts for a significant amount of the energy dissipated during the cycling of the anode at low C-rates. For the particular geometry of the anode considered in Chapter 10, plasticity accounts for over 30% of the total dissipation per cycle at a low C-rate of 1/10.

Hence, plasticity can have either a beneficial effect — that is, a higher SOC for a given voltage cut-off, or a detrimental effect — that is, significant energy dissipation at low C-rates, on the electrochemical performance of a-Si-based anodes.

The design of a-Si-based anodes for optimal performance is non-trivial. The fully-coupled diffusion-deformation theory and simulation capability reported in this thesis should be useful in developing a detailed understanding of the electro-chemo-mechanical operation of a-Si-based anodes, and optimizing their design for future applications. Furthermore, the favorable comparison between the predictions from our continuum theory and the experimental results shown in this work, demonstrates the applicability and importance of continuum-

level models in making meaningful predictions of the electrochemical response of a-Si based nanostructured anodes.

Finally, the theory and numerical simulation tools developed in this work will help one to formulate models at the porous-electrode-scale, where one must consider the interactions between anode particles and binder and between anode particles themselves. Using the foundations developed here, such a (non-trivial) extension of this work will allow one to study how the stresses generated within an anode particle affects its interaction with other particles, as well as study how the stresses generated in the microstructure might affect loss of conductivity due to failure of the anode-particle/binder interfaces.

Part III

Modeling growth of a solid electrolyte interphase

Chapter 12

Introduction

12.1 Introduction

One of the major concerns in Li-Ion batteries is the mitigation of "aging" of the battery — which refers to electro-chemo-mechanical degradation, capacity fade, and power loss of the system.

Amongst the many mechanisms which cause aging in Li-ion batteries, a major mechanism is the formation, due to decomposition of the electrolyte, of a thin *solid electrolyte interphase* (SEI) layer on the surface of anode particles. The SEI layer is electronically insulating which prevents further decomposition of the electrolyte, but it is ionically conductive and allows the diffusion of Li ions through it. However, the formation of SEI consumes Li-ions, which competes with the desired amount of Li for intercalation in the active anode material, and this causes capacity fade. In addition, since Li-ions must diffuse through the SEI layer, the formation of a SEI layer is accompanied by an increase of cell resistance. Often, the cyclic volume changes of an anode particle during Li-ion intercalation and deintercalation can cause the SEI layer to crack, delaminate, and spall from the surface of the anode particle. New SEI is then formed on the freshly exposed particle surface, which consumes more Li-ions and causes additional capacity fade. Both the chemical and mechanical integrity of the SEI are critical to the safety and performance of Li-ion batteries (cf., e.g., Lee et al., 2007; Verma et al., 2010; Barré et al., 2013).

The purpose of this work is develop a new theory and finite-element-based capability for the simulation of growth of a solid electrolyte interphase layer at an anode particle in a Li-ion battery. The theory attempts to account for the generation of stress due to the growth of a SEI layer, as well as the stress that arises due to the lithiation and delithiation of the anode particle. In the literature, the stress generated due to the growth of the SEI layer is often called "irreversible" while the stress related to the swelling/de-swelling of the anode particles during lithiation/delithiation is called "reversible."

12.2 Substrate curvature experiments of Mukhopadyay et al. (2012)

In a recent novel paper, Mukhopadyay et al. (2012) presented experimental measurements of the reversible and irreversible stresses during SEI formation on a thin-film graphite anode. In their experiments they used a 250 μm thick, 1 in diameter quartz substrate on which, using chemical vapor deposition (CVD) techniques, they deposited (i) a 15 nm thick Ti layer; (ii) a 200 nm thick Ni layer; and finally (iii) a 200 nm layer of c-axis oriented graphite. The Ti and Ni were deposited to act as a catalyst for graphitization and as a current collector. This multilayered plate was then assembled into an electrochemical cell which was charged and discharged under galvanostatic conditions against a Li-metal cathode to develop a SEI layer on the graphite anode. The TEM micrograph in Fig. 12-1, reproduced from Mukhopadyay et al. (2012), shows a $\approx$ 100nm-thick SEI layer which has formed on the graphite (CVD C) anode after 50 cycles of charging and discharging. After the initial deposition of the graphite layer, as well as during electrochemical cycling during which the SEI layer was formed, Mukhopadyay et al. measured the curvature of the plate using an array of parallel laser beams focused on the back side of the quartz substrate. The results from their experiments are schematically shown in Fig. 12-2:

- Fig. 12-2 (a) shows the undeformed quartz substrate.
- After CVD deposition of the graphite layer at 1000°C and cool-down to room temperature, the graphite contracts more than the substrate and this results in a positive curvature, Fig. 12-2 (b).
- At the end of the first half-cycle of charging the authors observed a reduction in the positive curvature of the plate; cf. Fig. 12-2 (c) relative to Fig. 12-2 (b). This reduction in curvature occurs due to the expansion of the graphite upon lithiation, and also due to the growth of the SEI layer.
- After the first complete lithiation/delithiation cycle, the graphite contracts to its initial delithiated state. However, the authors observed a reduction in the curvature of the plate with respect to the curvature at the beginning of the first lithiation, cf. Fig. 12-2 (d) relative to Fig. 12-2 (b). This reduction in curvature is an important indicator of the expansion strain during the growth of the SEI layer.
- At the end of the second charging half-cycle the authors observed a further decrease of curvature due to expansion of the graphite and the SEI, cf. Fig. 12-2 (e) relative to Fig. 12-2 (d).
- After the second complete lithiation/delithiation cycle, they observed an increase in curvature, cf. Fig. 12-2 (f) relative to Fig. 12-2 (e). This slight increase in curvature is driven by the contraction of the graphite, while the continued formation and expansion of the SEI layer counteracts the graphite contraction. Note that due to the growth

strain in the SEI, the observed curvature at the end of the second cycle was lower than the curvature at the end of the first cycle, cf. Fig. 12-2 (f) relative to Fig. 12-2 (d).

In subsequent cycles the authors observed a steady decrease in curvature due to the formation of SEI, superimposed by cyclic curvature changes due to the lithiation/delithiation of the graphite.

From their experimental measurements of the curvature changes of their multi-layered plate, Mukhopadyay et al. calculated the changes in *a nominal equi-biaxial stress, σ_n, in the combined graphite/SEI "film" on the quartz substrate* using the classical Stoney formula (Stoney, 1909),

$$\sigma_n = \left(\frac{1}{6} \frac{E_Q}{(1-\nu_Q)} \frac{h_Q^2}{h_G} \right) \kappa; \tag{12.1}$$

here, κ is the curvature of the plate, E_Q and ν_Q are the Young's modulus and the Poisson's ratio of the quartz substrate, and h_Q and h_G are the thicknesses of the quartz and graphite layers. Fig. 12-3 from their paper shows the cyclic electrical potential which was imposed in their battery for the first 20 cycles of charging/discharging, together with the results for the nominal stress that they inferred from their curvature measurements. The stress levels corresponding to the peaks of the cyclic stress profile represent the "irreversible" stress generation due to the growth of the SEI layer, while the stress levels during cycling represent the "reversible" stress due to lithiation and delithiation. Fig. 12-3 shows that in the course of 20 charge/discharge cycles the initially high $\sim 0.9\,\text{GPa}$ tensile nominal-stress, which is introduced due to the deposition of the graphite on the quartz, reduces by a factor of two to $\sim 0.4\,\text{GPa}$ due to the growth of the SEI and the attendant generation of compressive stresses in this layer. Reversible stresses in anodes due to lithiation/delithiation have been extensively addressed in the literature — however, to the best of our knowledge, Mukhopadyay et al. are the first group to report on experimental measurements of "irreversible" stresses due to growth of SEI on an anode.

As mentioned above, the purpose of this work is to report on our new continuum-mechanical theory and finite-element-based capability for the simulation of growth of a solid electrolyte interphase layer at an anode particle in a Li-ion battery. In formulating our theory we attempt to account for (i) the stress generation due to the lithiation and delithiation of anode particles, and (ii) the stress-generation due to the growth of an SEI layer. We have applied our theory and simulation capability for:

1. A study of the problem of SEI formation on the surface of a flat anode undergoing cyclic lithiation and delithiation, as in the study of Mukhopadyay et al. (2012). We demonstrate that we can reproduce their experimental results with reasonable *quantitative* accuracy.

2. A study of the problem of SEI formation on the surface of spherical and spheroidal graphite particles undergoing cyclic lithiation and delithiation. The stress state in the SEI layer and at the SEI-particle interface are calculated and the propensity of potential delamination of the SEI layer from the particle is identified. We show that the interplay

between reversible particle swelling/deswelling and irreversible SEI growth has a crucial effect on the magnitude of the stress levels that are generated, and consequently on the mechanical integrity of the SEI layer.

12.3 Modeling of lithiation/delithiation of anode particles

In order to properly simulate the growth of an SEI layer on the surface of an anode particle of a Li-ion battery, we must of course account for the chemo-mechanical deformation during charging and discharging of the anode itself — a process during which commonly used anode materials undergo substantial volume changes. As we shall show, such volumetric changes of an anode particle can have a significant effect on the stress distribution that is developed within the SEI layer. In order to model the intercalation of Li in an anode we will use our recently published theory for species diffusion coupled with large elastic deformations (Di Leo et al., 2014), discussed in detail in Chapter 3. Since this Li intercalation theory is not the main subject of this part of the thesis, we defer a brief summary of this theory to Section 13.3, and in the next section we turn our attention to the main subject, viz., modeling the growth of an SEI layer.

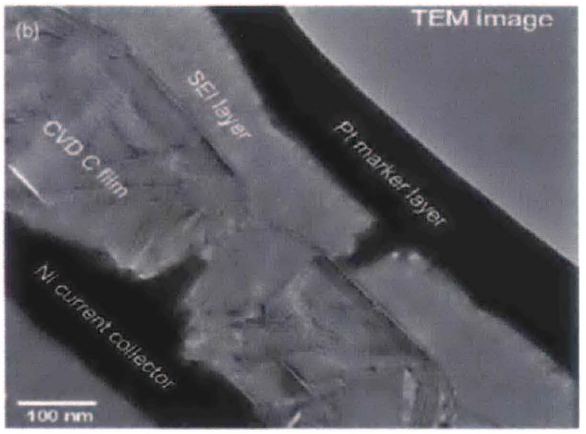

Figure 12-1: TEM micrograph of a SEI layer on a graphite anode. From Mukhopadyay et al. (2012).

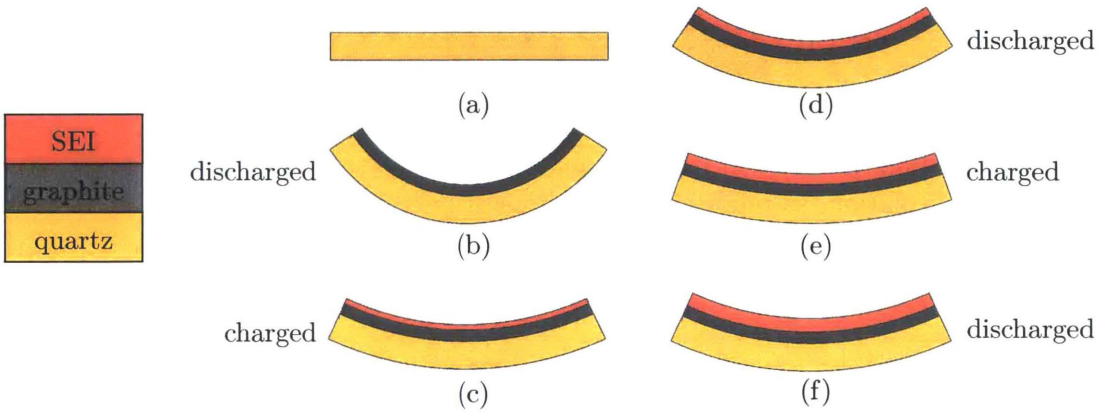

Figure 12-2: A schematic of the observed plate-curvature changes in the experiments of Mukhopadyay et al. (2012): (a) the initially straight plate; (b) the curved plate after carbon deposition; (c) the curved plate, with the charged graphite at the end of the first half-cycle; (d) the curved plate at the end of the first charging/discharging cycle; (e) the curved plate, charged graphite after one and a half cycles; and (f) the curved plate, discharged at the end of two cycles.

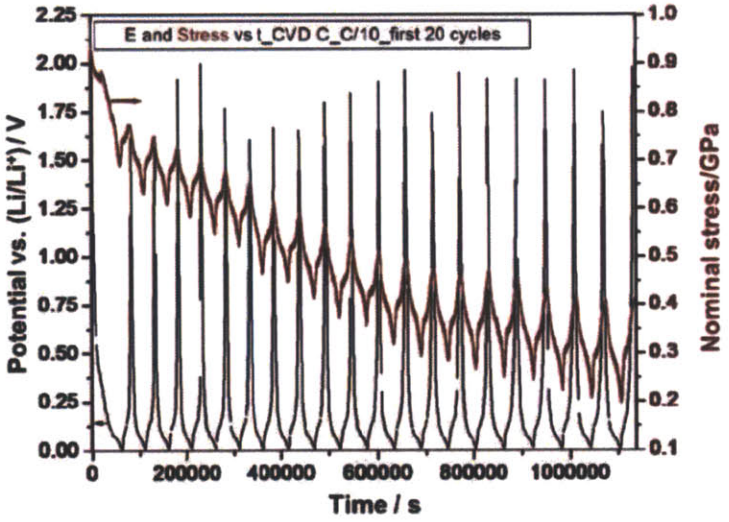

Figure 12-3: Variation of electrical potential and nominal stress with time for the first 20 cycles of lithiation and delithiation, as reported by Mukhopadyay et al. (2012).

Chapter 13

Theory and simulation capability for the growth of a solid electrolyte interphase

The process of growth of an SEI layer involves the addition of new mass onto the surface of an anode particle which is accompanied by a growth strain in the SEI — as a result, the newly-deposited SEI layer and the anode contain balanced residual stresses. Although the deposition of the layer and the associated strain generation occur simultaneously, we conceptually *idealize* the growth of an SEI layer on a surface of interest as a *two-step process* shown schematically in Fig. 13-1:

- The first step, which we refer to as **deposition**, results in the formation of a **strain-free** layer of SEI on the surface of interest, cf. Fig. 13-1 (a) to (b). This process controls the rate of increase of the thickness of the SEI layer perpendicular to the surface of interest.

- The second step, which we refer to as **in-plane expansion**, models the evolution of strain mismatch between the SEI layer and the substrate, cf. Fig. 13-1 (b) to (c). *Note that the reference configuration for the start of the expansion process is the "strain-free" layer created during the deposition step.*

Taken together, this idealized two-step process serves to model the experimentally observed growth of a SEI layer on a substrate.

In the next two sections we detail the theory and the numerical modeling of each of these two conceptually-separated sub-processes.

Remark. The intrinsic mechanism for the growth strains in the SEI and the attendant large growth stresses (of the order of -1 GPa) is not completely clear. Based on their recent

experimental study on the chemical and morphological changes, and stress generation during SEI formation on c-axis oriented graphitic carbon electrodes, A. et al. (2014) have suggested that it is the disruption of the surface of the graphite caused by solvated ions during the initial stages of formation of the SEI which is the dominant cause of stress at high potentials (above 0.5 V).

Our continuum model for SEI growth does not explicitly account for any specific mechanism for the formation and growth of the SEI. Rather, it assumes only that SEI formation occurs and is accompanied by growth strains which can results in stress generation at the SEI/anode interface. □

13.1 Numerical modeling of SEI deposition

Fig. 13-2 shows a schematic of our numerical simulation scheme for modeling the deposition of an SEI layer by the sequential conversion of multiple layers of finite elements — from elements with properties representing the electrolyte, to elements with properties representing the SEI. Fig. 13-2(a) shows three rows of elements representing the electrolyte (colored blue) adjacent to three rows of elements representing the graphite (colored gray); the electrolyte elements are sequentially converted to strain-free SEI elements (colored pink) at three prescribed times $(t_{\text{dep}}^{(1)}, t_{\text{dep}}^{(2)}, t_{\text{dep}}^{(3)})$. Fig. 13-2 (b) shows the resulting profile of the total SEI layer thickness h versus time t. In our numerical simulations we will choose the conversion times $t \in [t_{\text{dep}}^{(1)}, t_{\text{dep}}^{(2)}, t_{\text{dep}}^{(3)}, \ldots, t_{\text{dep}}^{(N)}]$ for the different electrolyte layers so that the resulting thickness $h(t)$ of the total SEI layer approximates the experimentally-observed square-root growth profile (Smith et al., 2011a). That is, we will choose the times when the electrolyte layers convert to SEI such that SEI total thickness growth approximates

$$h(t) \propto \sqrt{t}. \tag{13.1}$$

We emphasize that this square-root growth profile is something that we shall prescribe — it is not an outcome of a diffusion-controlled chemical reaction model.

The electrolyte is modeled as a linear elastic material with a very low Young's modulus of $E = 0.5\,\text{MPa}$, and a zero-valued Poisson's ratio, $\nu = 0$. Thus, any deformation of the graphite/electrolyte system produces stresses in the graphite which are essentially unaffected by the presence of the electrolyte elements. The specific constitutive behavior of the newly-formed strain-free SEI layer for times $t > t_{\text{dep}}$ is described in the next section.

Prior to the conversion of an electrolyte element to an SEI element, that is for $t < t_{\text{dep}}$, the standard deformation gradient $\mathbf{F}(t)$ is used for the constitutive calculations for an electrolyte element. The stress-free reference configuration for an SEI element of interest is its configuration at the time $t = t_{\text{dep}}$, when it is first converted from an element representing electrolyte to an element representing SEI. Thus, to model the subsequent in-plane expansion of a newly-deposited SEI element, the appropriate deformation gradient that is to be used

for constitutive calculations is the *relative deformation gradient*,

$$\mathbf{F}_{\text{SEI}}(\tau) \stackrel{\text{def}}{=} \mathbf{F}_{t_{\text{dep}}}(\tau) = \mathbf{F}(\tau)\mathbf{F}(t_{\text{dep}})^{-1} \qquad \text{for } \tau > t_{\text{dep}}. \tag{13.2}$$

13.2 Modeling of in-plane expansion of SEI

In this section we detail our constitutive theory for modeling the in-plane expansion of the SEI layer once it has been deposited on the surface of an anode. This theory is based — in major part — on the theory of "growing matter in living systems" (cf., e.g., Kuhl, 2014, for a recent review of the substantial literature on this topic), which employs the widely-used Kröner (1960)-Lee (1969) multiplicative decomposition of the deformation gradient,

$$\mathbf{F} = \mathbf{F}^e\mathbf{F}^g. \tag{13.3}$$

Here, for modeling the in-plane expansion of the SEI,

- The deformation gradient in (13.3) is to be interpreted as the deformation gradient $\mathbf{F}_{\text{SEI}}$ defined in (13.2),
$$\mathbf{F} \equiv \mathbf{F}_{\text{SEI}}. \tag{13.4}$$
- Also, we shall take $\mathbf{F}^g$ to be of the specific form given in eq. (13.14), which restricts the "growth" to an in-plane expansion (more on this below).

For economy of notation we shall continue to use the standard notation in (13.3), with the understanding that the deformation gradient $\mathbf{F}$ in what follows in this section is $\mathbf{F}_{\text{SEI}}$, and that $\mathbf{F}^g$ will have the form (13.14), so that the "growth" represented by $\mathbf{F}^g$ refers only to in-plane expansion of the SEI.

13.2.1 Kinematics

We denote by B the reference configuration for the SEI. An arbitrary material point of B is denoted by $\mathbf{X}$, and a *motion* of B is a smooth one-to-one mapping $\mathbf{x} = \boldsymbol{\chi}(\mathbf{X}, t)$ with *deformation gradient*, *velocity*, and *velocity gradient* given by[1]

$$\mathbf{F} = \nabla\boldsymbol{\chi}, \qquad \mathbf{v} = \dot{\boldsymbol{\chi}}, \qquad \mathbf{L} = \operatorname{grad}\mathbf{v} = \dot{\mathbf{F}}\mathbf{F}^{-1}. \tag{13.5}$$

[1]Notation: We use standard notation of modern continuum mechanics Gurtin et al. (2010). Specifically: ∇ and Div denote the gradient and divergence with respect to the material point $\mathbf{X}$ in the reference configuration; grad and div denote these operators with respect to the point $\mathbf{x} = \boldsymbol{\chi}(\mathbf{X}, t)$ in the deformed body; a superposed dot denotes the material time-derivative. Throughout, we write $\mathbf{F}^{e-1} = (\mathbf{F}^e)^{-1}$, $\mathbf{F}^{e-\mathsf{T}} = (\mathbf{F}^e)^{-\mathsf{T}}$, etc. We write $\operatorname{tr}\mathbf{A}$, $\operatorname{sym}\mathbf{A}$, $\operatorname{skw}\mathbf{A}$, $\mathbf{A}_0$, and $\operatorname{sym}_0\mathbf{A}$ respectively, for the trace, symmetric, skew, deviatoric, and symmetric-deviatoric parts of a tensor $\mathbf{A}$. Also, the inner product of tensors $\mathbf{A}$ and $\mathbf{B}$ is denoted by $\mathbf{A}:\mathbf{B}$, and the magnitude of $\mathbf{A}$ by $|\mathbf{A}| = \sqrt{\mathbf{A}:\mathbf{A}}$.

Following modern developments of large-deformation plasticity theory (cf., e.g., Gurtin et al., 2010) and growth theory (cf., e.g., Kuhl, 2014), we base our theory on the multiplicative decomposition (13.3) of the deformation gradient. Where, suppressing the argument t:

(i) $\mathbf{F}^g(\mathbf{X})$ represents the local distortion of the material neighborhood of $\mathbf{X}$ due to growth; and

(ii) $\mathbf{F}^e(\mathbf{X})$ represents the subsequent stretching and rotation of this coherent but distorted material neighborhood, and thereby represents a corresponding elastic distortion.

We refer to $\mathbf{F}^g$ and $\mathbf{F}^e$ as the *growth and elastic distortions*, respectively, and we refer to the local space at $\mathbf{X}$ represented by the range of $\mathbf{F}^g(\mathbf{X})$, as the *intermediate space* at $\mathbf{X}$.

As is standard, we assume that

$$J \stackrel{\text{def}}{=} \det \mathbf{F} > 0, \tag{13.6}$$

and hence, using (13.3),

$$J = J^e J^g, \qquad \text{where} \qquad J^e \stackrel{\text{def}}{=} \det \mathbf{F}^e > 0 \qquad \text{and} \qquad J^g \stackrel{\text{def}}{=} \det \mathbf{F}^g > 0, \tag{13.7}$$

so that $\mathbf{F}^e$ and $\mathbf{F}^g$ are invertible.

The right polar decomposition of $\mathbf{F}^e$ is given by

$$\mathbf{F}^e = \mathbf{R}^e \mathbf{U}^e, \tag{13.8}$$

where $\mathbf{R}^e$ is a rotation, while $\mathbf{U}^e$ is a symmetric, positive-definite tensor with

$$\mathbf{U}^e = \sqrt{\mathbf{F}^{e\mathsf{T}} \mathbf{F}^e}. \tag{13.9}$$

As is standard, we define the elastic right Cauchy-Green tensor by

$$\mathbf{C}^e = \mathbf{U}^{e2} = \mathbf{F}^{e\mathsf{T}} \mathbf{F}^e. \tag{13.10}$$

By $(13.5)_3$ and (13.3),

$$\mathbf{L} = \mathbf{L}^e + \mathbf{F}^e \mathbf{L}^g \mathbf{F}^{e-1}, \tag{13.11}$$

with

$$\mathbf{L}^e = \dot{\mathbf{F}}^e \mathbf{F}^{e-1}, \qquad \mathbf{L}^g = \dot{\mathbf{F}}^g \mathbf{F}^{g-1}. \tag{13.12}$$

We define the elastic and growth stretching and spin tensors through

$$\left.\begin{aligned} \mathbf{D}^e &= \operatorname{sym} \mathbf{L}^e, \qquad \mathbf{W}^e = \operatorname{skw} \mathbf{L}^e, \\ \mathbf{D}^g &= \operatorname{sym} \mathbf{L}^g, \qquad \mathbf{W}^g = \operatorname{skw} \mathbf{L}^g, \end{aligned}\right\} \tag{13.13}$$

so that $\mathbf{L}^e = \mathbf{D}^e + \mathbf{W}^e$ and $\mathbf{L}^g = \mathbf{D}^g + \mathbf{W}^g$.

Since an increase in thickness of the SEI layer in a direction perpendicular to the anode surface does not result in generation of "growth stresses", we have modeled SEI growth as two separate processes (cf. Section 3): (a) deposition, which results in a stress-free increase in thickness, and (b) area growth which gives rise to growth stresses because of the constraint of the substrate. Accordingly, we make the following additional kinematical assumptions concerning SEI growth. Let $\Pi_{\mathrm{R}}(\mathbf{X})$ denote a plane through an infinitesimal neighborhood of $\mathbf{X}$ on the surface of the anode oriented by a unit normal vector $\mathbf{m}_{\mathrm{R}}(\mathbf{X})$. Then, as a specific model for $\mathbf{F}^g$ we consider *isotropic area growth*, described by

$$\mathbf{F}^g = \mathbf{m}_{\mathrm{R}} \otimes \mathbf{m}_{\mathrm{R}} + \lambda_{\perp}^g \, (\mathbf{1} - \mathbf{m}_{\mathrm{R}} \otimes \mathbf{m}_{\mathrm{R}}), \tag{13.14}$$

where $\lambda_{\perp}^g$ represents the *growth stretch* in the plane Π_{R} perpendicular to $\mathbf{m}_{\mathrm{R}}$. Futher, we define

$$\epsilon_{\perp}^g \stackrel{\text{def}}{=} \ln \lambda_{\perp}^g, \tag{13.15}$$

as a corresponding *growth strain*, and introduce an

$$\textit{area growth ratio } \Theta^g,$$

which represents the ratio of the area normal to $\mathbf{m}_{\mathrm{R}}$ in the intermediate configuration to the area normal to $\mathbf{m}_{\mathrm{R}}$ in the reference configuration. Due to our assumption of pure in-plane growth, Θ^g is identically equal to J^g and related to $\lambda_{\perp}^g$ as follows:

$$\Theta^g \equiv J^g = (\lambda_{\perp}^g)^2. \tag{13.16}$$

Thus, note that

$$\dot{\Theta}^g = 2\Theta^g \dot{\epsilon}_{\perp}^g. \tag{13.17}$$

Since,

$$\dot{\mathbf{F}}^g = \dot{\lambda}_{\perp}^g \, (\mathbf{1} - \mathbf{m}_{\mathrm{R}} \otimes \mathbf{m}_{\mathrm{R}}), \tag{13.18}$$

and

$$\mathbf{F}^{g-1} = \mathbf{m}_{\mathrm{R}} \otimes \mathbf{m}_{\mathrm{R}} + \frac{1}{\lambda_{\perp}^g}(\mathbf{1} - \mathbf{m}_{\mathrm{R}} \otimes \mathbf{m}_{\mathrm{R}}), \tag{13.19}$$

using $(13.12)_2$, (13.19), and (13.15) we obtain

$$\mathbf{L}^g = \dot{\epsilon}_{\perp}^g \, (\mathbf{1} - \mathbf{m}_{\mathrm{R}} \otimes \mathbf{m}_{\mathrm{R}}). \tag{13.20}$$

Upon using (13.17) in (13.20) gives

$$\mathbf{L}^g = (\dot{\Theta}^g \Theta^{g-1}) \, \mathbb{S}, \tag{13.21}$$

where

$$\mathbb{S} \stackrel{\text{def}}{=} \frac{1}{2}(\mathbf{1} - \mathbf{m}_{\mathrm{R}} \otimes \mathbf{m}_{\mathrm{R}}). \tag{13.22}$$

We restrict attention to circumstances in which

$$\dot{\Theta}^g \geq 0, \tag{13.23}$$

so that in-plane growth is *irreversible.* Note that $\mathbf{L}^g$ is symmetric, so that

$$\mathbf{L}^g \equiv \mathbf{D}^g, \tag{13.24}$$

and

$$\mathbf{W}^g = \mathbf{0}. \tag{13.25}$$

13.2.2 Free energy imbalance

Introducing the Helmholtz free energy ψ_{R} per unit reference volume, the classical local free-energy imbalance under isothermal conditions is (Gurtin et al., 2010),

$$\dot{\psi}_{\mathrm{R}} - \mathbf{T}_{\mathrm{R}} : \dot{\mathbf{F}} \leq 0\,, \tag{13.26}$$

where, with $\mathbf{T}_{\mathrm{R}}$ denoting the standard Piola stress, the term $\mathbf{T}_{\mathrm{R}} : \dot{\mathbf{F}}$ in (13.26) represents the stress-power per unit reference volume.

Recall that the Piola stress $\mathbf{T}_{\mathrm{R}}$ is related to the symmetric Cauchy stress $\mathbf{T}$ by

$$\mathbf{T}_{\mathrm{R}} = J\,\mathbf{T}\,\mathbf{F}^{-\mathsf{T}}. \tag{13.27}$$

Thus, using (13.3), $(13.12)_2$, (13.16), and (13.27), the stress-power may be written as

$$\begin{aligned}
\mathbf{T}_{\mathrm{R}} : \dot{\mathbf{F}} &= \mathbf{T}_{\mathrm{R}} : (\dot{\mathbf{F}}^e \mathbf{F}^g + \mathbf{F}^e \dot{\mathbf{F}}^g), \\
&= (\mathbf{T}_{\mathrm{R}} \mathbf{F}^{g\mathsf{T}}) : \dot{\mathbf{F}}^e + (\mathbf{F}^{e\mathsf{T}} \mathbf{T}_{\mathrm{R}}) : \dot{\mathbf{F}}^g, \\
&= \Theta^g \left((J^e \mathbf{F}^{e-1} \mathbf{T} \mathbf{F}^{e-\mathsf{T}}) : (\mathbf{F}^{e\mathsf{T}} \dot{\mathbf{F}}^e) + (\mathbf{C}^e J^e \mathbf{F}^{e-1} \mathbf{T} \mathbf{F}^{e-\mathsf{T}}) : \mathbf{L}^g \right).
\end{aligned} \tag{13.28}$$

In view of (13.28), we introduce two new stress measures:

- The elastic second Piola stress,

$$\mathbf{T}^e \stackrel{\text{def}}{=} J^e \mathbf{F}^{e-1} \mathbf{T} \mathbf{F}^{e-\mathsf{T}}, \tag{13.29}$$

  which is *symmetric* on account of the symmetry of the Cauchy stress $\mathbf{T}$.

- The Mandel stress,

$$\mathbf{M}^e \stackrel{\text{def}}{=} \mathbf{C}^e \mathbf{T}^e, \tag{13.30}$$

  which in general is *not symmetric.*

Further, from (13.10)

$$\dot{\mathbf{C}}^e = \dot{\mathbf{F}}^{e\mathsf{T}} \mathbf{F}^e + \mathbf{F}^{e\mathsf{T}} \dot{\mathbf{F}}^e\,. \tag{13.31}$$

Thus, using the definitions (13.29), (13.30) and the relation (13.31), the stress-power (13.28) may be written as

$$\mathbf{T}_{\mathrm{R}} : \dot{\mathbf{F}} = \Theta^g \left(\tfrac{1}{2} \mathbf{T}^e : \dot{\mathbf{C}}^e + \mathbf{M}^e : \mathbf{L}^g \right). \tag{13.32}$$

Using (13.32) in (13.26), and using (13.21) allows us to write the free energy imbalance as

$$\dot{\psi}_{\mathrm{R}} - \Theta^g \left(\tfrac{1}{2} \mathbf{T}^e : \dot{\mathbf{C}}^e \right) - \dot{\Theta}^g \mathbf{M}^e : \mathbb{S} \leq 0 . \tag{13.33}$$

Remark. For brevity we have not discussed invariance properties of the various fields appearing in our theory. However, such considerations are straight-forward and extensively elaborated upon in the context of plasticity theories, which have a similar structure, by Gurtin et al. (2010). Here, we simply note that all quantities in the free energy imbalance (13.33) are invariant under a change in frame. □

13.2.3 Energetic constitutive equations

Guided by the free-energy imbalance (13.33), we first consider the following set of constitutive equations for the free energy ψ_{R} and the stress $\mathbf{T}^e$:

$$\left.\begin{aligned} \psi_{\mathrm{R}} &= \bar{\psi}_{\mathrm{R}}(\mathbf{C}^e, \Theta^g), \\ \mathbf{T}^e &= \bar{\mathbf{T}}^e(\mathbf{C}^e, \Theta^g). \end{aligned}\right\} \tag{13.34}$$

Substituting the constitutive equations (13.34) into the dissipation inequality, we find that the free-energy imbalance (13.33) may then be written as

$$\left(\frac{\partial \bar{\psi}_{\mathrm{R}}(\mathbf{C}^e, \Theta^g)}{\partial \mathbf{C}^e} - \Theta^g \left(\tfrac{1}{2} \bar{\mathbf{T}}^e(\mathbf{C}^e, \Theta^g) \right) \right) : \dot{\mathbf{C}}^e - \left(- \frac{\partial \bar{\psi}_{\mathrm{R}}(\mathbf{C}^e, \Theta^g)}{\partial \Theta^g} + \mathbf{M}^e : \mathbb{S} \right) \dot{\Theta}^g \leq 0 . \tag{13.35}$$

This inequality is satisfied provided that the free energy determines the stress $\mathbf{T}^e$ through the "state relation"

$$\mathbf{T}^e = \Theta^{g-1} \left(2 \frac{\partial \bar{\psi}_{\mathrm{R}}(\mathbf{C}^e, \Theta^g)}{\partial \mathbf{C}^e} \right), \tag{13.36}$$

together with the dissipation inequality

$$\mathcal{F} \dot{\Theta}^g \geq 0, \tag{13.37}$$

where

$$\mathcal{F} \stackrel{\text{def}}{=} \mathcal{A} + \mathbf{M}^e : \mathbb{S} \tag{13.38}$$

represents a thermodynamic force conjugate to $\dot{\Theta}^g$, with

$$\mathcal{A}(\mathbf{C}^e, \Theta^g) \stackrel{\text{def}}{=} -\frac{\partial \bar{\psi}_{\text{R}}(\mathbf{C}^e, \Theta^g)}{\partial \Theta^g}, \tag{13.39}$$

representing an energetic constitutive contribution to $\mathcal{F}$ — called the *affinity* (cf., e.g., Loeffel and Anand, 2011).

13.2.4 Dissipative constitutive equation

Guided by (13.37), we presume that the area expansion rate $\dot{\Theta}^g$ is given by a constitutive equation

$$\dot{\Theta}^g = \hat{\dot{\Theta}}^g(\Theta^g, \mathcal{F}) \geq 0, \tag{13.40}$$

such that $\mathcal{F}\dot{\Theta}^g > 0$ holds whenever $\dot{\Theta}^g > 0$.

13.2.5 Specialization of the constitutive equations

Free energy

Next, restricting ourselves to an isotropic elastic response for the SEI, the free energy function $\bar{\psi}_{\text{R}}(\mathbf{C}^e, \Theta^g)$ is taken as an isotropic function of its arguments. An immediate consequence is that the free energy function has the representation

$$\bar{\psi}_{\text{R}}(\mathbf{C}^e, \Theta^g) = \breve{\psi}_{\text{R}}(\mathcal{I}_{\mathbf{C}^e}, \Theta^g), \tag{13.41}$$

with

$$\mathcal{I}_{\mathbf{C}^e} = \Big(I_1(\mathbf{C}^e), I_2(\mathbf{C}^e), I_3(\mathbf{C}^e)\Big)$$

the list of principal invariants of $\mathbf{C}^e$. Next, the spectral representation of $\mathbf{C}^e$ is

$$\mathbf{C}^e = \sum_{i=1}^{3} \omega_i^e \mathbf{r}_i^e \otimes \mathbf{r}_i^e, \qquad \text{with} \qquad \omega_i^e = \lambda_i^{e\,2}, \tag{13.42}$$

where $(\mathbf{r}_1^e, \mathbf{r}_2^e, \mathbf{r}_2^e)$ are the orthonormal eigenvectors of $\mathbf{C}^e$ and $\mathbf{U}^e$, and $(\lambda_1^e, \lambda_2^e, \lambda_3^e)$ are the positive eigenvalues of $\mathbf{U}^e$. Let

$$\mathbf{E}^e \stackrel{\text{def}}{=} \ln \mathbf{U}^e = \sum_{i=1}^{3} E_i^e \, \mathbf{r}_i^e \otimes \mathbf{r}_i^e, \qquad \text{with} \qquad E_i^e \stackrel{\text{def}}{=} \ln \lambda_i^e, \tag{13.43}$$

denote the logarithmic elastic strain. With the logarithmic elastic strain defined by (13.43), for isotropic materials we henceforth consider a free energy of the form

$$\psi_{\text{R}} = \hat{\psi}_{\text{R}}(\mathcal{I}_{\mathbf{E}^e}, \Theta^g), \tag{13.44}$$

with $\mathcal{I}_{\mathbf{E}^e}$ a list of principal invariants of $\mathbf{E}^e$, or equivalently a list of principal values of $\mathbf{E}^e$. Then, straightforward calculations (cf., e.g., Anand and Su, 2005, Section 7.2) show that the Mandel stress is *symmetric* and given by

$$\mathbf{M}^e = \Theta^{g-1}\left(\frac{\partial\hat{\psi}_{\mathrm{R}}(\mathcal{I}_{\mathbf{E}^e},\Theta^g)}{\partial\mathbf{E}^e}\right), \tag{13.45}$$

and the corresponding Cauchy stress is given by

$$\mathbf{T} = J^{e-1}\mathbf{R}^e\mathbf{M}^e\mathbf{R}^{e\top}. \tag{13.46}$$

Next, we consider the free energy to be a separable function of the form

$$\hat{\psi}_{\mathrm{R}}(\mathcal{I}_{\mathbf{E}^e},\Theta^g) = \psi^e(\mathcal{I}_{\mathbf{E}^e},\Theta^g) + \psi_{\mathrm{R}}^{\mathrm{chem}}(\Theta^g). \tag{13.47}$$

Here:

(i) ψ^e is an elastic energy given by

$$\psi^e(\mathcal{I}_{\mathbf{E}^e},\Theta^g) = \Theta^g\underbrace{\left(\tfrac{1}{2}\mathbf{E}^e:\mathbb{C}\mathbf{E}^e\right)}_{\psi_0^e}, \qquad \mathbb{C} \overset{\text{def}}{=} 2G\mathbb{I} + \left(K - \frac{2}{3}G\right)\mathbf{1}\otimes\mathbf{1}, \tag{13.48}$$

where $\mathbb{C}$ is the elasticity tensor, with $\mathbb{I}$ and $\mathbf{1}$ the fourth- and second-order identity tensors, and the parameters

$$G > 0, \qquad K > 0, \tag{13.49}$$

are the shear modulus and bulk modulus, respectively. The term ψ_0^e in (13.48) is an elastic energy measured per unit volume of the intermediate space; multiplication by Θ^g converts it to an energy measured per unit volume of the reference space. This is a simple generalization of the classical strain energy function of infinitesimal isotropic elasticity to moderately large elastic strains (Anand, 1979, 1986).

(ii) $\psi_{\mathrm{R}}^{\mathrm{chem}}$ is a chemical energy related to the SEI reaction. We assume the following simple linear relation (cf., e.g., Loeffel and Anand, 2011)

$$\psi_{\mathrm{R}}^{\mathrm{chem}} = H(1-\Theta^g), \tag{13.50}$$

where the parameter $H > 0$ represents a *chemistry modulus*. Thus, as Θ^g increases from unity the free-energy decreases, which implies that area growth is energetically favorable.

Thus

$$\psi_{\mathrm{R}} = \Theta^g\left[\tfrac{1}{2}\mathbf{E}^e:\mathbb{C}\mathbf{E}^e\right] + H(1-\Theta^g). \tag{13.51}$$

Then, by (13.45), (13.39), and (13.48), the Mandel stress and the affinity are given by

$$\begin{aligned} \mathbf{M}^e &= \mathbb{C}\mathbf{E}^e = 2G\mathbf{E}^e_0 + K(\mathrm{tr}\,\mathbf{E}^e)\mathbf{1}, \\ \mathcal{A} &= H - \left[\tfrac{1}{2}\mathbf{E}^e : \mathbb{C}\mathbf{E}^e\right]. \end{aligned} \tag{13.52}$$

Using $(13.52)_1$, (13.46), and (13.43) the Cauchy stress $\mathbf{T}$ is given by

$$\mathbf{T} = J^{e-1}\left(2G\mathbf{E}^e_{\mathrm{H}} + (K - (2/3)G)(\mathrm{tr}\ \mathbf{E}^e_{\mathrm{H}})\mathbf{1}\right) \qquad \text{with} \qquad \mathbf{E}^e_{\mathrm{H}} \stackrel{\mathrm{def}}{=} \mathbf{R}^e\mathbf{E}^e\mathbf{R}^{e\mathsf{T}}, \tag{13.53}$$

where $\mathbf{E}^e_{\mathrm{H}}$ is Hencky's spatial logarithmic strain.

Also, from $(13.52)_2$ and (13.38) the "driving force" $\mathcal{F}$ for $\dot{\Theta}^g$ is

$$\mathcal{F} = H + \mathbf{M}^e : \mathbb{S} - \tfrac{1}{2}\mathbf{E}^e : \mathbb{C}\mathbf{E}^e. \tag{13.54}$$

Evolution equation for Θ^g

Guided by Kuhl (2014), we choose a simple special form for (13.40),

$$\dot{\Theta}^g = \begin{cases} k\left(1 - \dfrac{\Theta^g}{\Theta^g_{\max}}\right)\mathcal{F} & \text{if } \mathcal{F} > 0, \\ 0 & \text{otherwise,} \end{cases} \tag{13.55}$$

where, $k > 0$ is a positive-valued (possibly temperature-dependent) parameter with units of $\mathrm{m}^3/(\mathrm{J}\cdot\mathrm{sec})$, and $\Theta^g_{\max}$ is the maximum area growth.

This completes the constitutive theory for modeling the in-plane expansion of the SEI.

13.3 Summary of a theory for lithium intercalation coupled with large elastic deformation

In order to model the diffusion of Li in the anode, and the resulting volumetric expansion/-contraction of the anode due to Li intercalation, we make use of our recently published theory for species diffusion coupled with large elastic deformations (Di Leo et al., 2014), which is discussed in detail in Chapter 3. The theory of Di Leo et al. (2014) was formulated to also account for phase separation. Here we restrict our attention to a simplified version of the theory which neglects phase separation. The simplified version of the theory, using notation and terminology essentially identical to that of the previous section, is summarized below:

13.3.1 Constitutive equations

1. **Kinematics.** The deformation gradient is multiplicatively decomposed into an elastic distortion $\mathbf{F}^e$, and a chemical distortion $\mathbf{F}^c$ through

$$\mathbf{F} = \mathbf{F}^e\mathbf{F}^c, \quad J = J^eJ^c. \tag{13.56}$$

2. **Chemical distortion.** We take the chemical distortion to be spherical and to depend on the Li concentration,

$$\mathbf{F}^c = (J^c)^{1/3}\mathbf{1} \quad \text{with} \quad J^c = 1 + \Omega(c_{\text{R}} - c_0) > 0, \tag{13.57}$$

where Ω is a constant partial molar volume of the intercalating Li in the body, with c_0 the initial concentration.

3. **Stress.** The Mandel and Cauchy stress tensors are given by

$$\begin{aligned} &\mathbf{M}^e = 2G\mathbf{E}^e + (K - (2/3)G)(\text{tr}\mathbf{E}^e)\mathbf{1}, \\ &\mathbf{T} = J^{e-1}\left(2G\mathbf{E}^e_{\text{H}} + (K - (2/3)G)(\text{tr}\mathbf{E}^e_{\text{H}})\mathbf{1}\right), \qquad \text{with} \qquad \mathbf{E}^e_{\text{H}} \stackrel{\text{def}}{=} \mathbf{R}^e\mathbf{E}^e\mathbf{R}^{e\text{T}}. \end{aligned} \tag{13.58}$$

4. **Chemical Potential.** The chemical potential of the Li in the anode is given by

$$\mu = \mu^0 + R\vartheta \ln\left(\frac{\bar{c}}{1-\bar{c}}\right) - \Omega\frac{1}{3}\text{tr}\mathbf{M}^e, \tag{13.59}$$

where $\bar{c} \stackrel{\text{def}}{=} c_{\text{R}}/c_{\text{R,max}}$ is the normalized Li concentration, with $c_{\text{R,max}}$ the maximum Li concentration, R is the gas constant, ϑ is the temperature, and μ^0 is a constant reference chemical potential. In our calculations we consider only isothermal conditions at $\vartheta = 300\text{K}$.

5. **Species flux.** The flux $\mathbf{j}_{\text{R}}$ of the intercalating Li is taken to be linear in the gradient of the chemical potential,

$$\mathbf{j}_{\text{R}} = -m\nabla\mu, \tag{13.60}$$

where the mobility m of the Li is a function of the concentration given by

$$m = \frac{D_0}{R\vartheta}c_{\text{R}}(1-\bar{c}), \tag{13.61}$$

with D_0 a constant diffusion coefficient.

13.4 Governing partial differential equations. Boundary conditions

In the absence of non-inertial body forces and neglect of inertial forces, standard considerations of balance of forces, when expressed spatially in the deformed body $\mathcal{B} = \chi(\mathrm{B})$, give that the symmetric Cauchy stress tensor $\mathbf{T}$ satisfies the force balance

$$\operatorname{div}\mathbf{T} = \mathbf{0}. \tag{13.62}$$

With $\mathcal{S}_{\mathbf{u}}$ and $\mathcal{S}_{\mathbf{t}}$ denoting complementary subsurfaces of the boundary $\partial\mathcal{B}$ of the deformed body, we consider a pair of boundary conditions in which the displacement $\mathbf{u} = \mathbf{x} - \mathbf{X}$ is specified on $\mathcal{S}_{\mathbf{u}}$ and the surface traction on $\mathcal{S}_{\mathbf{t}}$ for a time interval $t \in [0, T]$:

$$\left.\begin{aligned} \mathbf{u} &= \breve{\mathbf{u}} \quad \text{on } \mathcal{S}_{\mathbf{u}} \times [0,T], \\ \mathbf{T}\mathbf{n} &= \breve{\mathbf{t}} \quad \text{on } \mathcal{S}_{\mathbf{t}} \times [0,T]. \end{aligned}\right\} \tag{13.63}$$

Then (13.62), the constitutive equations for $\mathbf{T}$ expressed in terms of the deformation, together with (13.63) yields a boundary value problem for the displacement field $\mathbf{u}(\mathbf{x}, t)$. The field equation (13.62) and boundary conditions (13.63) are taken to hold for the anode, the electrolyte, and the SEI, with the stress $\mathbf{T}$ given by their respective constitutive equations.

We neglect diffusion of Li in the SEI. Mass balance for diffusion of Li in the anode requires that the balance equation

$$\dot{c}_{\mathrm{R}} = -\operatorname{Div}(\mathbf{j}_{\mathrm{R}}) \tag{13.64}$$

hold in the anode, with the flux given by (13.60). The initial condition for c_{R} is taken as

$$c_{\mathrm{R}}(\mathbf{X}, 0) = c_{\mathrm{R},0}. \tag{13.65}$$

Letting $\mathcal{S}_{\mu}$ and $\mathcal{S}_{\mathbf{j}_{\mathrm{R}}}$ denote complementary subsurfaces of the boundary $\partial\mathrm{B}$ of the reference body B describing the anode material, we consider a pair of simple boundary conditions in which the chemical potential is specified on $\mathcal{S}_{\mu}$ and the species flux on $\mathcal{S}_{\mathbf{j}_{\mathrm{R}}}$:

$$\left.\begin{aligned} \mu &= \breve{\mu} \quad \text{on } \mathcal{S}_{\mu} \times [0,T], \\ \mathbf{j}_{\mathrm{R}} \cdot \mathbf{n}_{\mathrm{R}} &= \breve{j} \quad \text{on } \mathcal{S}_{\mathbf{j}_{\mathrm{R}}} \times [0,T]. \end{aligned}\right\} \tag{13.66}$$

13.4.1 Numerical implementation of the theory

We have implemented our SEI growth theory, described above in Sections 13.1 and 13.2, in the implicit finite element program Abaqus (2010) by writing a a 2D axisymmetric 4-node linear isoparametric quadrilateral user element subroutine (UEL).[2] We have coupled

[2]We have also implemented a 2D plane-strain 4-node linear isoparametric quadrilateral element, and a 3D 8-node linear isoparametric brick; however, we do not show any simulations using these elements in this paper.

this numerical capability for SEI growth with our previously developed user element subroutine(UEL) for simulation of lithiation and delithiation of electrode particles, Section 13.3. For brevity, we omit all details of our numerical implementation.

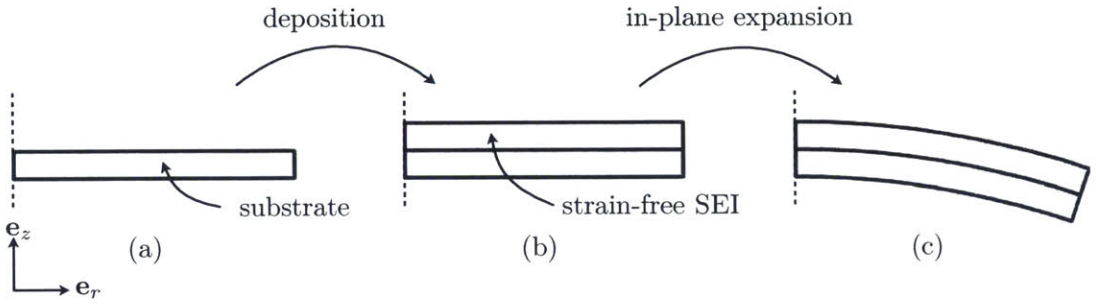

Figure 13-1: Idealization of SEI growth as a two-step process: (i) A "deposition" process in the direction normal to the substrate, from (a) to (b), which involves the addition of mass to the system to create a "strain-free" SEI layer. (ii) The "in-plane expansion" of the newly-deposited SEI layer, from (b) to (c).

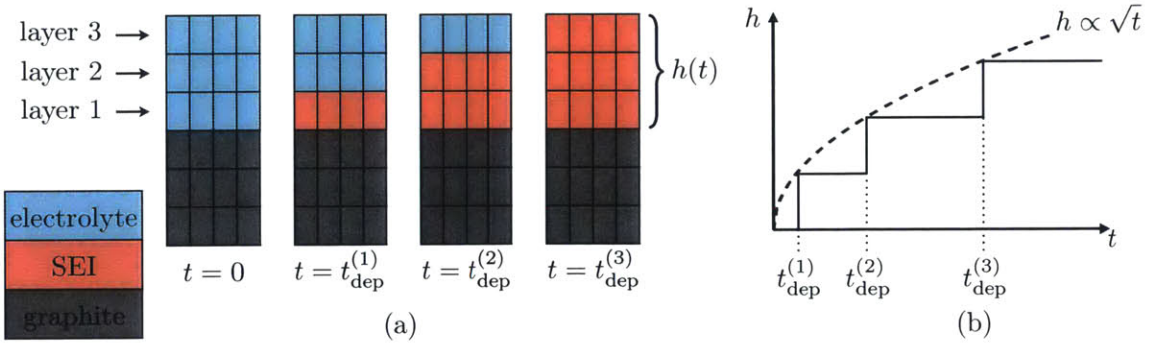

Figure 13-2: Schematic of the numerical simulation scheme for the deposition of an SEI layer.

Chapter 14

SEI formation on the surface of a flat anode undergoing cyclic lithiation and delithiation

The purpose of this chapter is to use the novel experimental results of Mukhopadyay et al. (2012) to calibrate the material parameters in our theory and to verify whether our theory is able to reproduce their experimental results with reasonable quantitative accuracy.

In their experiments Mukhopadyay et al. (2012) did not continuously monitor the thickness of the SEI layer as it grows, they only reported that the thickness of the SEI layer after 811 hours of cyclic lithiation was $h \approx 100$nm. Thus, guided by the experimental results of Smith et al. (2011a) who showed that the loss of Li in the battery (capacity fade) is proportional to the square root of time, we assume (as discussed previously in Section 13.1) that

$$h(t) = h(t_f)\sqrt{t/t_f}, \qquad \text{with} \quad t_f = 811\,\text{hours} \quad \text{and} \quad h(t_f) = 100\,\text{nm}. \tag{14.1}$$

In order to estimate the material parameters in our in-plane SEI growth model, we carried out a finite-element simulation of the experiments of Mukhopadyay et al. (2012), which we describe below. Their physical experiment was performed on a 1 in-diameter quartz substrate, as shown schematically in Fig. 14-1(a). In order to minimize the computational effort, we considered a small section of the axisymmetric plate immediately adjacent to the axis of radial symmetry as our simulation domain, and meshed it with a single column of elements, as shown schematically in Fig. 14-1(b). The electrolyte/SEI layer was meshed with 150 elements whose constituve behavior is described by the deposition and expansion model developed in Sects. 13.1 and 13.2. The graphite layer was meshed with 40 elements whose constitutive behavior is described by the coupled deformation-diffusion theory summarized

in Sect. 13.3. Finally, the quartz layer was meshed with 30 elements which are prescribed a simple linear isotropic elastic constitutive behavior.

In our simulations *we neglect the diffusion of Li-ions through the SEI*, which effectively means that we neglect any resistance offered by the SEI to the diffusion of Li in the graphite. Henceforth, for brevity, we will use the terms "fully delithiated" and "fully lithiated" to describe the graphite layer when it has an average normalized Li concentration of $\bar{c} = 0.05$ and $\bar{c} = 0.95$, respectively.

The boundary/initial conditions that we used in our simulations are as follows:

- **Mechanical boundary conditions**: Consistent with the radial symmetry of the problem, the nodes along the edge AD in Fig. 14-1(b) are constrained to have zero radial displacement. All nodes on the edge EH are constrained to remain on a straight line as defined by the nodes at points E and H. The line formed by the nodes along edge EH is free to move and rotate, *and it is from the rotation of this line with respect to its initial vertical position that we computed the curvature of the plate.*

- **Initial concentration of Li in the graphite**: The initial concentration of lithium in the graphite layer is taken as a low value of $\bar{c}_0 = 0.05$. In order to model the experimentally-observed stress generated during the chemical vapor deposition of the graphite, we use an alternative form of (13.57), viz.,

$$J^c = 1 + \Omega(c_{\mathrm{R}} - c_0) + J_0^c, \tag{14.2}$$

  where J_0^c accounts for the initial strain mismatch in the graphite. This is used purely as a numerically-expedient tool for achieving a residual stress mimicking the stress developed during the chemical vapor deposition of the graphite layer on the quartz substrate in the experiments.

- **Chemical boundary conditions for the graphite**: The nodes on the edges BC, CF, and GF in Fig. 14-1 are prescribed to have zero outwards flux, i.e. $\breve{j} = 0$ (cf. eq. $(13.66)_2$). As mentioned above, we neglect the diffusion of Li-ions through the SEI and directly prescribe a constant flux of Li on the edge BG. Further, in order to study the effect of the lithiation/delithiation of the graphite on the process of SEI deposition and growth, in this particular geometry, we consider two separate cases:

  (a) **Simulation with lithiation/delithiation of the graphite**: In their experiments, Mukhopadyay et al. used a charge rate (C-rate) of C/10, which in the absence of capacity fade would yield a lithiation/delithiation cycle with a duration of 10 hours. Due to the capacity fade, the duration was shorter and changed from cycle to cycle. Since we do not model capacity fade in the graphite, we adjusted the C-rate to C/8.1, which corresponds to 50 cycles over the entire 811 hours of their experiment. The magnitude of the flux was then computed accordingly to get from the fully delithiated state to the fully lithiated state in a time $t_{\mathrm{hc}} = 8.1$

hours. That is,

$$\breve{j} = \begin{cases} -1.8 \cdot 10^{-7}\,\mathrm{mol/(m^2 sec)} & 2n-2 \le t/t_{\mathrm{hc}} < 2n-1, \\ 1.8 \cdot 10^{-7}\,\mathrm{mol/(m^2 sec)} & 2n-1 \le t/t_{\mathrm{hc}} < 2n, \end{cases} \tag{14.3}$$

where $n \in [1, \ldots, \mathbb{N}]$ is the cycle number. Such an idealized square-cyclic value for the boundary flux is schematcally shown in Fig. 14-2.

(b) **Simulation without lithiation/delithiation of the graphite**: In this case we ignored the lithiation and delithiation of the graphite and simply prescribed

$$\breve{j} = 0 \tag{14.4}$$

along the edge BG. Without any changes in Li concentration, the graphite responds as a purely elastic solid.

14.1 Material parameters

Using (13.54) in (13.55) we recall next the evolution equation for the area ratio Θ^g:

$$\dot{\Theta}^g = \begin{cases} k \left(1 - \dfrac{\Theta^g}{\Theta^g_{\max}}\right) \underbrace{\left(H + \mathbf{M}^e : \mathbb{S} - \tfrac{1}{2}\mathbf{E}^e : \mathbb{C}\mathbf{E}^e\right)}_{\mathcal{F}} & \text{if } \mathcal{F} > 0, \\ 0 & \text{otherwise.} \end{cases} \tag{14.5}$$

At this stage of research in the field, not enough is known to fully characterize the material parameters appearing in such an evolution equation. In our simulations, for pragmatic reasons, we choose a sufficiently large value of the chemical modulus H so that $H \gg (\mathbf{M}^e : \mathbb{S} - \frac{1}{2}\mathbf{E}^e : \mathbb{C}\mathbf{E}^e)$, and the steady state at which the evolution of Θ^g stops, occurs when $\Theta^g = \Theta^g_{\max}$. Thus, the rate at which the evolution of area growth strains occurs within the SEI is then primarily controlled by $1/(kH)$, which represents a characteristic time for the evolution of Θ^g. Specifically, we choose values of

$$H = 8 \times 10^6\,\mathrm{MJ/m^3} \quad \text{and} \quad k = 10^{-7}\,\mathrm{m^3/(MJ \cdot sec)}, \tag{14.6}$$

so that the characteristic time is

$$1/(kH) = 1.25\,\mathrm{sec}. \tag{14.7}$$

With this choice for the parameter pair (k, H), the area swelling ratio Θ^g in a particular layer of SEI elements reaches its maximum value $\Theta^g_{\max}$, before the next layer of SEI elements is deposited according to the deposition scheme described by (14.1).

With k and H fixed at the values in (14.6) above, the rest of the material parameters for the SEI, as well as the parameters for the graphite and the quartz that we have used to fit the experiments of Mukhopadyay et al. (2012), are summarized in Table 14.1.

Table 14.1: Material parameters for SEI, graphite, and quartz used to fit the experiments of Mukhopadyay et al. (2012)

Layer	Parameter	Value	Source
SEI	E_S	25 GPa	Fitted
	ν_S	0.3	
	$\Theta^g_{\max}$	1.088	
Graphite	E_G	100 GPa	Qi et al. (2010)
	ν_G	0.3	
	Ω	$1.249 \cdot 10^{-7}\,\mathrm{m}^3/\mathrm{mol}$	
	$c_{R,\max}$	$2.914 \cdot 10^4\,\mathrm{mol}/\mathrm{m}^3$	Christensen and Newman (2006)
	D_0	$10^{-13}\,\mathrm{m}^2/\mathrm{s}$	
Quartz	E_Q	72 GPa	De Jong et al. (2000)
	ν_Q	0.165	

Remark. The values for E_G and Ω for graphite used here are an adaptation of the results from a density functional theory (DFT) calculations by Qi et al. (2010). In their density functional theory analysis, Qi et al. (2010) predicted a 1.2% stretch of all material fibers in the basal plane. A corresponding value for isotropic swelling which yields 1.2% stretch of *all* material fibers is $\Omega c_{R,\max} = 3.63 \cdot 10^{-2}$. Further, they found the stiffness in the basal-plane to vary with respect to composition, with an average of $C_{11} \sim 1047$ GPa. However, we find these DFT-based calculated values to be too high, and inconsistent with the experimental results of Mukhopadyay et al. (2012). Accordingly, in our simulations we have chosen substantially reduced values for the stiffness E_G and the total swelling $\Omega c_{R,\max}$ — values which, when compared to those based on Qi et al. (2010), are lower by a factor of ten. □

14.2 Simulation results

As summarized in Section 12.2, Mukhopadyay et al. (2012) interpreted their experimentally-measured curvatures in terms of a nominal stress which was calculated using Stoney's formula (12.1); cf. Fig. 12-3. Since our numerical simulations directly give us the results for the curvature changes, we have converted their reported stress values back to curvature values by using (12.1), the material parameters for the quartz in Table 14.1, and the thicknesses of the quartz and graphite layers presented in Fig. 14-1. Their experimental curvature versus

time results are shown as a blue line in Fig. 14-3 (a). The corresponding curvature versus time from our finite element simulation results are also plotted in this figure as a red line. The two important experimentally-observed phenomena are clearly captured by our numerical simulations:

(i) First, there as an overall decrease of the curvature κ as a function of time — this is due to the growth of the SEI layer.

(ii) Second, overlaid on the overall decrease in curvature, there is a cyclic oscillation of the curvature — this is due to the lithiation/delithiation cycles of the graphite layer.

Highlighted in Fig. 14-3 (a) by blue dots are the experimental curvature measurements after a complete lithiation/delithiation cycle. These points correspond to instances when the graphite layer is essentially free of Li. These experimental curvature measurments after full lithiation/delithiation cycles are replotted in Fig. 14-3(b) as blue dots. In this figure we also show the results of our numerical simulations **without** the lithiation/delithiation of the graphite, that is, the case corresponding to the boundary condition (14.4); this result is shown as a red line. The drop in curvature with time in the numerical results in Fig. 14-3 (b) is due entirely to the growth of the SEI layer. This numerically-predicted curvature history agrees well with the experimental curvature measurements taken after full lithiation/delithiation cycles.

In in Fig. 14-3 (a) the experimental results show an increase in the amplitude of the cyclic oscillations of the curvature which, as noted by Mukhopadyay et al. (2012), are consistent with an increase in the capacity of the graphite. In our simulations, we have not considered any variation in the capacity of the graphite during cycling. Thus, the amplitude of the oscillations in the stress in our simulations remain constant during cycling.

The results in Fig. 14-3 are extremely encouraging, they show that our theory and numerical simulation capability — with suitable choices for the material parameters — can reproduce the sophisticated experimental results of Mukhopadyay et al. (2012) with reasonable *quantitative* accuracy.

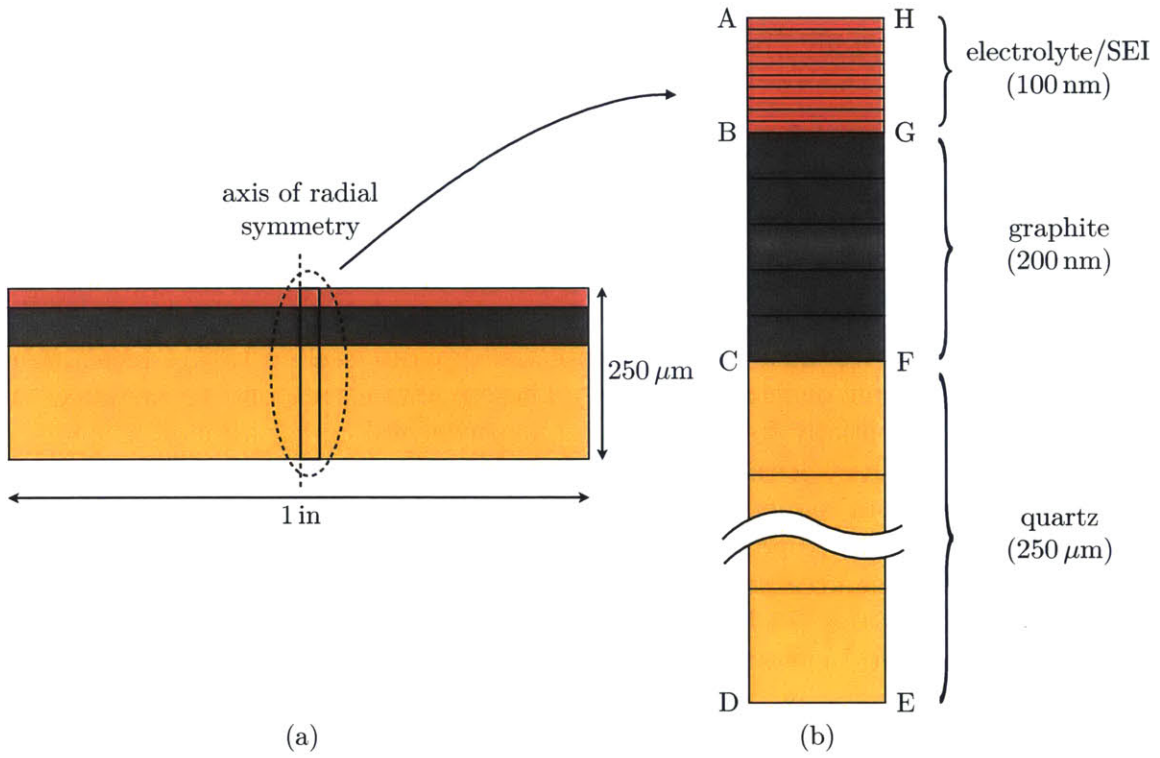

Figure 14-1: Plate geometry and a schematic of the single-column finite element mesh used in the simulations.

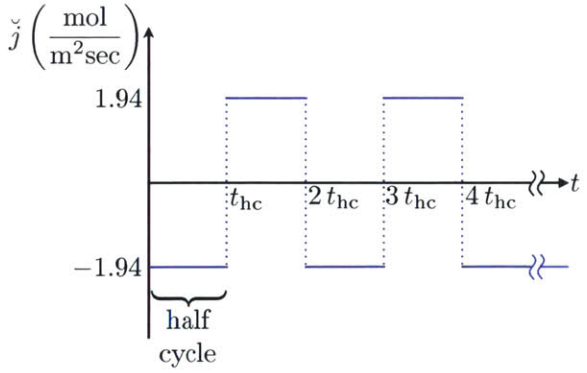

Figure 14-2: Schematic of the prescribed flux used in simulating galvanostatic charging/discharging. Here t_{hc} denotes the time for a half cycle of charging/discharging.

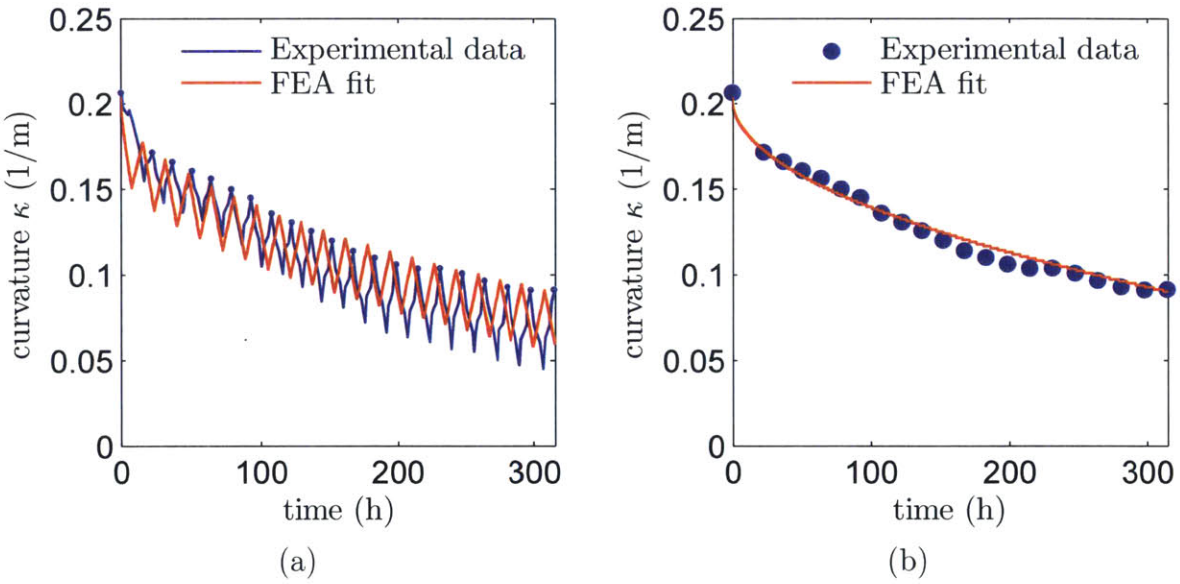

Figure 14-3: Experimental curvature versus time data of Mukhopadyay et al. (2012) compared with corresponding results from finite element simulation: (a) Experimental data and simulations including lithiation/delithiation of the graphite layer. (b) Experimental data for curvatures measured only at the end of a complete lithiation/delithiation cycle compared against a numerical simulation without lithiation of the graphite.

Chapter 15

SEI formation on the surface of spherical and spheroidal graphite particles undergoing cyclic lithiation and delithiation

In this section we numerically simulate SEI growth on a spherical-shaped anode particle during cyclic lithiation/delithiation, and compare the results obtained for a spherical particle against those for a particle geometry which is spheroidal rather than perfectly spherical.

Andersson et al. (2008) have reported on their measurements of SEI growth on graphite particles with an average diameter of $\approx 3\,\mu$m. In their experiments they performed two full lithiation/delithiation cycles at a C-rate of C/7. After cycling and washing of the anode, they measured an SEI thickness of $\approx 45\,$nm. Guided by the experiments of these authors, in our simulations we choose the dimensions of the graphite particles to have a diameter of $\approx 3\,\mu$m. Specifically, we consider the spherical- and spheroidal-shaped particles schematically shown in Fig. 15-1: the spherical particle is taken to have a radius of $1.5\,\mu$m, and the spheroidal particle to have a major axis of $2\,\mu$m and a minor axis of $1\,\mu$m. Due to the symmetries in the geometry, we mesh only one-half of the axisymmetric profile of each particle. Both particles are meshed using 7500 elements, together with an electrolyte/SEI layer which is meshed using 5000 elements — with 50 elements in the direction normal to the anode surface and 100 elements along the surface of the anode particle. The properties for the SEI are taken as those calibrated in Chapter 14 and listed in Table 14.1. However, following Christensen and Newman (2006), for an "isotropic" graphite anode we use,

$$\begin{gathered} E_G = 15\text{GPa}, \quad \nu_G = 0.3, \\ \Omega = 2.745 \cdot 10^{-6}\,\text{m}^3/\text{mol}, \quad c_{\text{R,max}} = 2.914 \cdot 10^4 \text{mol}/\text{m}^3, \quad D_0 = 10^{-13}\,\text{m}^2/\text{s}. \end{gathered} \tag{15.1}$$

Further, based on the work of Andersson et al. (2008), we prescribe the thickness of the SEI to evolve according to (cf., eq. (14.1))

$$h(t) = h(t_f)\sqrt{t/t_f}, \quad \text{with} \quad t_f = 28\,h \quad \text{and} \quad h(t_f) = 45\,\text{nm}, \tag{15.2}$$

With reference to Fig. 15-1, the boundary and initial conditions that we used in our simulations are as follows:

- **Mechanical boundary conditions**: Symmetry conditions are prescribed on edges BE and BD, where the nodes along BE are constrained to have zero radial displacement while the nodes along BD are constrained to have zero vertical displacement. The exterior boundary DE is taken to be traction-free.

- **Chemical initial conditions**: The initial concentration of Li in the graphite particles is taken to have a low value of $\bar{c}_0 = 0.05$.

- **Chemical boundary conditions**: In accordance with the symmetry conditions on edges BA and BC, the nodes along these edges are prescribed to have zero outwards flux, i.e. $\breve{j} = 0$. As in Chapter 14, we neglect diffusion of Li-ions through the electrolyte/SEI layer, and prescribe a constant flux of Li ions on the edge AC. We consider the following two cases:

  (a) **Simulations with lithiation/delithiation of the graphite particle**: First, we account for the lithiation and delithiation of the graphite anode particle, concurrently with SEI growth, by considering a non-zero value of the flux prescribed on the anode edge AC. Specifically, consistent with the experiments of Andersson et al. (2008) we prescribe a flux according to a C-rate of C/7; viz., a flux which takes the particle from a fully delithiated state into a fully lithiated state in 7 hours and vice verse:

  $$\breve{j} = \begin{cases} -5.20 \cdot 10^{-7}\,\text{mol}/(\text{m}^2\text{sec}) & 2n-2 \le t/t_{\text{hc}} < 2n-1 \\ 5.20 \cdot 10^{-7}\,\text{mol}/(\text{m}^2\text{sec}) & 2n-1 \le t/t_{\text{hc}} < 2n \end{cases} \tag{15.3}$$

  for the spherical particle, and

  $$\breve{j} = \begin{cases} -4.26 \cdot 10^{-7}\,\text{mol}/(\text{m}^2\text{sec}) & 2n-2 \le t/t_{\text{hc}} < 2n-1 \\ 4.26 \cdot 10^{-7}\,\text{mol}/(\text{m}^2\text{sec}) & 2n-1 \le t/t_{\text{hc}} < 2n \end{cases} \tag{15.4}$$

  for the spheroidal particle, with $t_{\text{hc}} = 7$ hours. The difference in the prescribed fluxes for the spherical and spheroidal particles is due to their different surface-area-to-volume ratios. As in the experiments of Andersson et al., in our simulations we carry out two full lithiation/delithiation cycles.

  (b) **Simulations without lithiation/delithiation of the graphite particle**: In order to study the effect of graphite swelling on the stresses in the SEI layer

we have also performed simulations with no lithiation of the graphite by simply prescribing a zero normal flux along the edge AC,

$$\breve{j} = 0.$$

We have applied the same SEI growth rates in order to have results comparable to the simulations with lithiation/delithiation.

The results from the numerical simulations for the spherical and spheroidal-shaped particles are discussed in the next two subsections.

15.1 Simulation results for SEI growth on a spherical anode particle

As described above, the simulations were run for two complete cycles of lithiation and delithiation of the anode particle, with simultaneous deposition and expansion of the SEI. The two full cycles of lithiation/delithiation are of course equivalent to four half-cycles — each half-cycle consisting of either fully lithiating or fully delithiating the anode particle. Figs. 15-2(a) and (b) show plots of the variation of the hoop stress $T_{\theta\theta} = \mathbf{e}_\theta \cdot \mathbf{T}\mathbf{e}_\theta$ (in a cylindrical coordinate system, cf. Fig. 15-2) within the SEI layer *at the north-pole of the particle*, as a function of the outward distance from the surface of the anode; cf. the schematic on the left of Fig. 15-2(a). These figures thus show the variation of the "hoop-stress" in the SEI as a function of the outward distance from the surface of the anode.

Fig. 15-2(a) compares the result for the hoop stress variation in the SEI for a simulation with two complete (or four half-cycles) of lithiation/delithiation of the graphite (solid line), against the result for a simulation in which the graphite is not lithiated (dashed line). At the end of the two full-cycles the graphite is delithiated, as it is in the case when the graphite is never lithiated. In the case of no lithiation of the graphite the hoop stress in the SEI layer is almost uniform at a value of approximately $-1.5\,\text{GPa}$, whereas with cyclic lithiation the hoop stress varies in the approximate range $-2.3\,\text{GPa}$ to $-1.5\,\text{GPa}$ across the thickness of the SEI layer.

The variation in hoop stress within the SEI thickness for the case of cyclic lithiation arises due to the fact that as the SEI deposition and growth is occurring, the underlying graphite is also undergoing relatively large volumetric changes due to the intercalation of Li. This result is easily understood using the schematic shown in Fig. 15-3. Consider a fully lithiated particle shown in Fig. 15-3(a) onto which an SEI layer forms, Fig. 15-3(b). The SEI layer which forms will be in compression due to the inherent growth hoop stress which arises during the process of SEI expansion. Once the particle delithiates, see Fig. 15-3(c), the SEI layer will develop *higher* compressive stresses due to volumetric shrinking of the graphite particle onto which the SEI layer is attached. The regions of the SEI in Fig. 15-2(a) which have the largest compressive stresses of $\sim -2.3\,\text{GPa}$ thus correspond to layers of SEI which were formed when the particle was fully lithiated.

To further illustrate the importance of accounting for stress generation due to both the SEI growth and the lithiation/delithiation of the underlying graphite particle, Fig. 15-2(b) shows the results of the simulation with cyclic lithiation of the graphite at two different times: (i) at the end of 4 half-cycles when the anode is delithiated (solid line), and (ii) at the end of 3 half-cycles when the anode is fully lithiated (dashed line). As expected, when the graphite is fully lithiated, the overall hoop stress profile through the thickness of the SEI exhibits lower levels of compressive hoop stress than at the state when it is fully delithiated, since some of the compressive stress is relieved by the volumetric swelling of the graphite anode when it is lithiated.

Of significant interest for judging the tendency for the SEI layer to delaminate from the anode particle is the normal component of the traction, $T_n = \mathbf{n} \cdot \mathbf{Tn}$, where $\mathbf{n}$ is the outward unit normal to the anode/SEI interface; cf. schematic on the left of Fig. 15-2(c). Figs. 15-2(c) and (d) show the variation of T_n at the anode/SEI interface as a function of the normalized distance along the circumference of the particle, starting from the north-pole of the particle. As before, Fig. 15-2(c) shows the result from a simulation with cyclic lithiation/delithiation of the graphite (solid line) versus the result from a simulation in which the graphite is not lithiated (dashed line). The normal stress profiles in this figure are computed at the end of four half-cycles when the graphite is equally devoid of Li in both simulations. Note that the addition of cyclic lithiation/delithiation of the graphite leads to the development of larger tensile normal stress T_n at the anode/SEI interface. The larger value of T_n in the simulation with cyclic lithiation of the graphite is consistent with the observation of the larger compressive hoop stress in the SEI layer for the same simulation, cf. Fig. 15-2(a).

Finally, Fig. 15-2(d) shows the results for T_n for the simulation with cyclic lithiation of the graphite at two different times: (i) at the end of 4 half-cycles when the anode is delithiatated (solid line), and (ii) at the end of 3 half-cycle when the anode is fully lithiated (dashed line). When the particle is lithiated (dashed line) the normal interface stress is $\sim$ 55 MPa, whereas at when the particle is delithiated (solid line) the normal stress is $\sim$ 115 MPa. This illustrates the contribution of the delithiation of graphite anode to the formation of additional normal stress along the anode/SEI interface.

15.2 Simulation results for SEI growth on a spheroidal anode particle

In this section we present the results of our simulations for a spheroidal graphite particle and compare (i) the hoop stress distribution in the SEI layer, as well as (ii) the normal stress distribution at the anode/SEI interface, against the corresponding results for a spherical particle. The results in this section are presented in the same fashion as was done in Sect. 15.1 for the case of a spherical particle.

Figs. 15-4(a) and (b) show plots of the variation of the hoop stress at the north-pole of the spheroidal particle in the SEI layer as a function of the distance from the surface of the anode. These results are similar to those in Figs. 15-2(a) and (b) for a spherical particle.

Figs. 15-4(c) and (d) show the normal traction T_n at the anode/SEI interface as a function of the normalized distance along the circumference of the particle. These results *differ significantly* from those obtained using a spherical particle; compare with Figs. 15-2(c) and (d). In the spheroidal particle the normal traction along the anode/SEI interface in the vicinity of the north-pole of the particle, is substantially higher than the normal traction in a spherical particle. Focusing on the normal traction after 4 half-cycles — when the particle is fully delithiated — we see that the normal traction for the spheroidal particle, Fig. 15-4(d) (solid line), reaches a maximum value of $\sim$ 320 MPa at the north-pole. In contrast, the normal traction in the sphere, Fig. 15-2(d) (solid line), reaches a maximum value of $\sim$ 120 MPa, which is constant along the circumference of the particle.

The substantial increase in normal tensile traction at the anode/SEI interface for a spheroidal (non-spherical) particle — as compared to a spherical particle — is important in developing a more complete understanding of the role of particle shape in increasing (or decreasing) the potential for delamination of a SEI layer from an anode particle.

Remark. In order to determine whether the SEI delaminates from the anode, the maximum calculated value of T_n must be compared with the cohesive strength of the interface. However, to the best of our knowledge, measurements of cohesive strengths of SEI/anode interfaces have not been reported in the literature. Still, examining the evolution of the normal stress T_n at the interface provides some insight as to when the SEI might delaminate. Fig. 15-5 shows the evolution of T_n near the north pole of the spheroidal particle for two full lithiation/delithiation cycles. In the first half-cycle of lithiation the normal stress T_n increases, while in the second half-cycle of lithiation T_n decreases. However T_n increases during both delithiation half-cycles — which is to be expected because the graphite shrinks away from the SEI layer during delithiation. Thus, once an SEI layer has been formed, delamination of this layer from the anode is most likeley to occur during *delithiation.* □

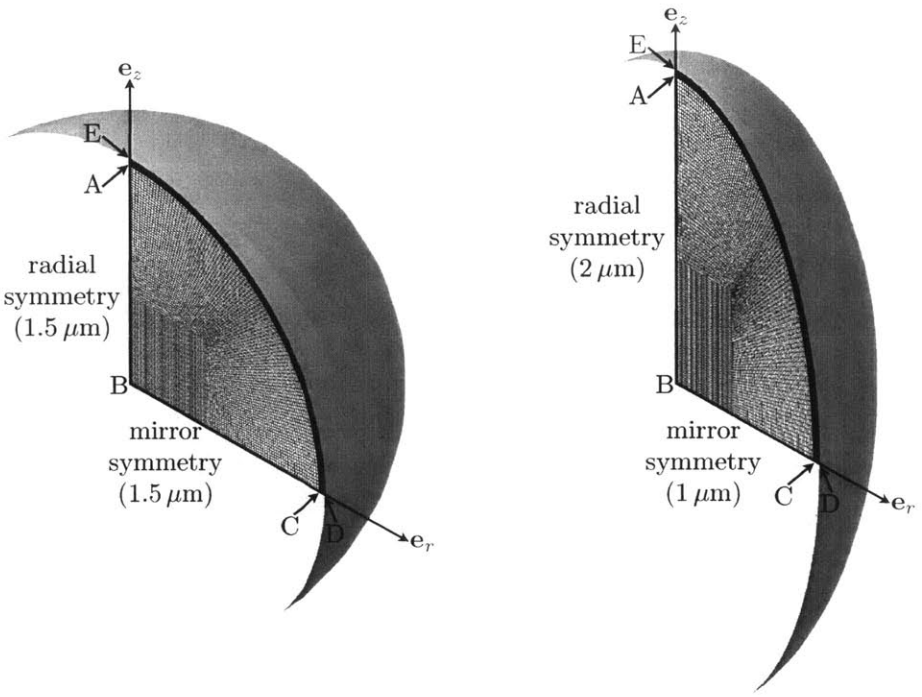

Figure 15-1: Geometry and finite-element mesh of the spherical and spheroidal particles used in the simulations. Due to the symmetry of the problem, only a quarter of the cross-section is meshed with axisymmetric elements.

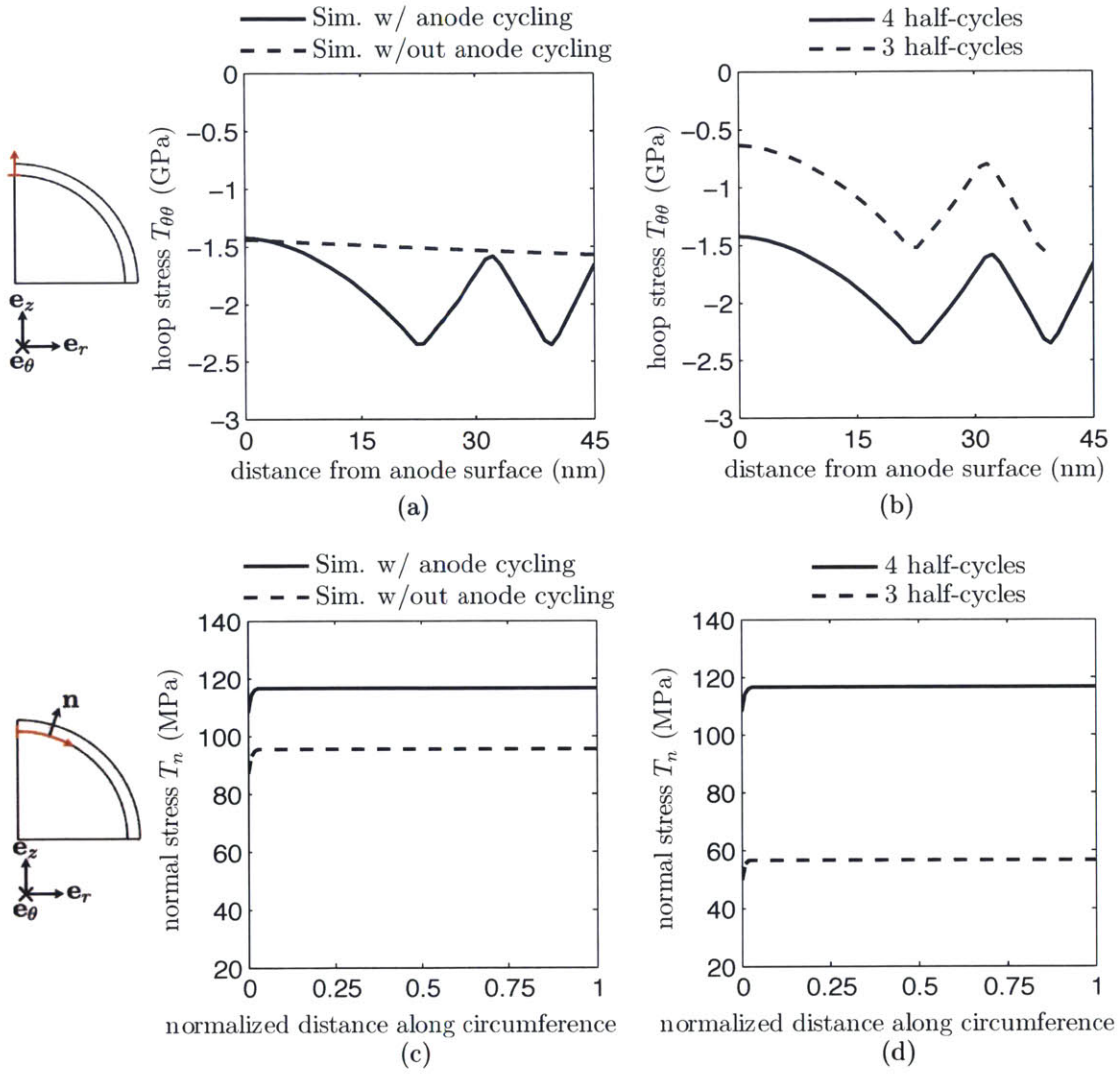

Figure 15-2: Simulation results for a spherical anode particle: (a) and (b) show the hoop stress $T_{\theta\theta}$ in the SEI layer as a function of the distance from the anode surface. (c) and (d) show the normal stress T_n at the anode/SEI interface as a function of the normalized distance along the circumference of the interface. (a) and (c) show results after 4 half-cycles (two full-cycles) for simulations including the cyclic lithiation/delithiation of the anode (solid lines) and for simulations without lithiation of the graphite anode (dashed lines). (b) and (d) show simulations with cycling of the anode after 3 half-cycles (dashed lines) when the graphite is lithiated and after 4 half-cycles (solid lines) when the graphite is delithiated.

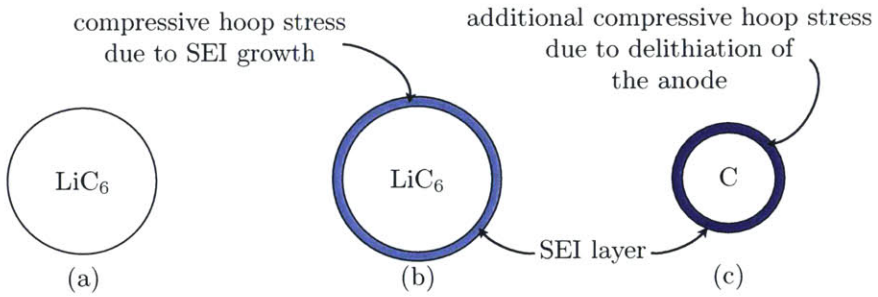

Figure 15-3: Schematic of SEI growth on a lithiated graphite anode followed by delithiation of the anode. The development of a compressive growth hoop stress, (a) to (b), is followed by further compression of the SEI layer due to delithiation of the graphite, (b) to (c).

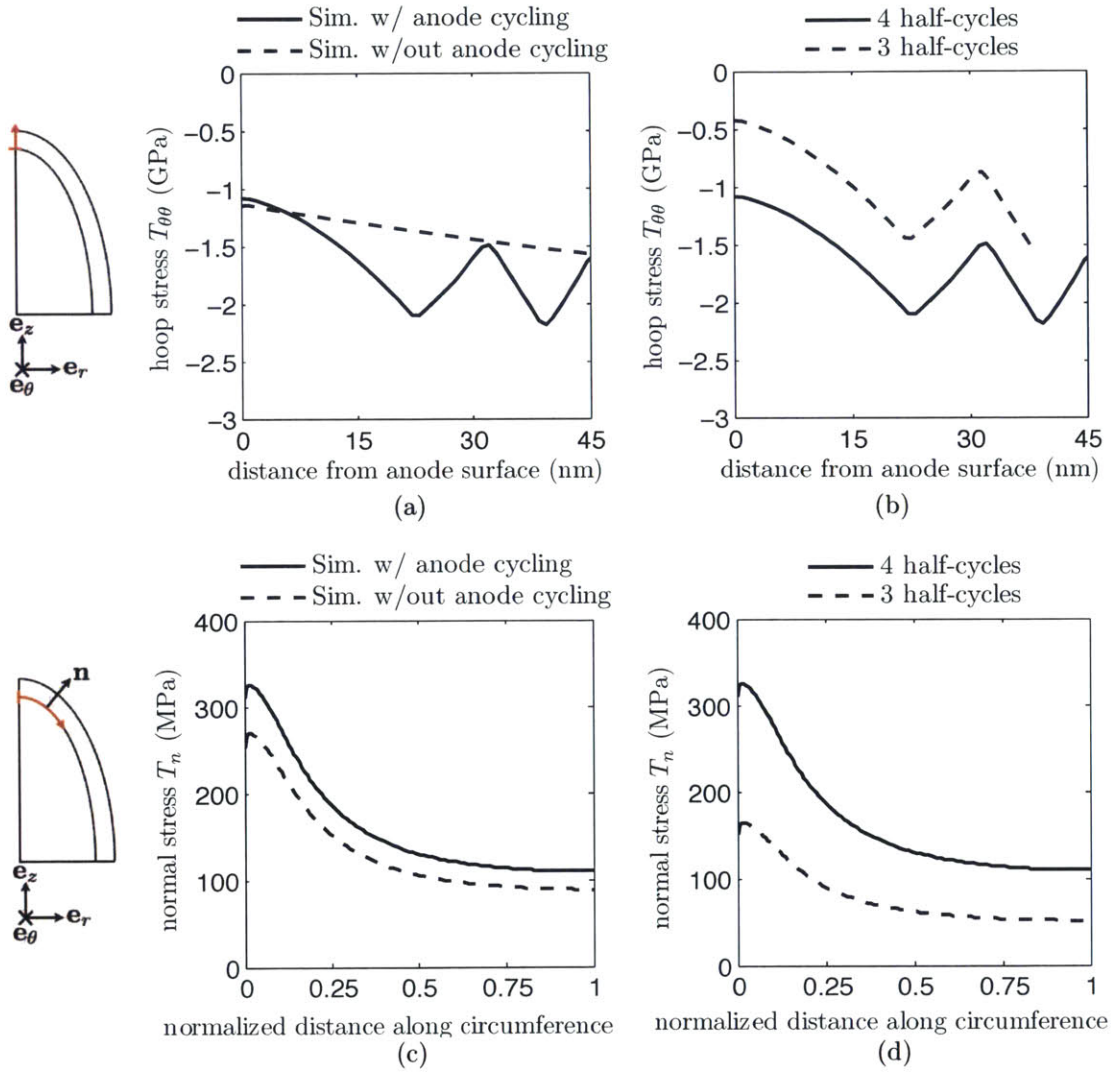

Figure 15-4: Simulation results for a spheroidal anode particle: (a) and (b) show the hoop stress $T_{\theta\theta}$ in the SEI layer as a function of the distance from the anode surface. (c) and (d) show the normal stress T_n at the anode/SEI interface as a function of the normalized distance along the circumference of the interface. (a) and (c) show results after 4 half-cycles for simulations including the cyclic lithiation/delithiation of the anode (solid lines) and for simulations without lithiation of the graphite anode (dashed lines). (b) and (d) show simulations with cycling of the anode after 3 half-cycles (dashed lines) when the graphite is lithiated and after 4 half-cycles (solid lines) when the graphite is delithiated.

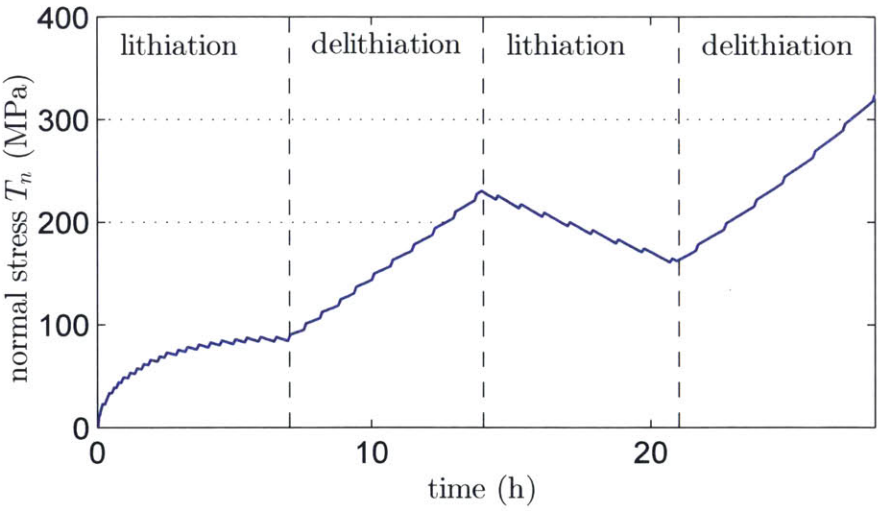

Figure 15-5: Variation of the normal interface traction T_n near the north pole of the spheroidal particle versus time.

Chapter 16

Concluding remarks

We have formulated a new continuum-mechanical theory and a finite-element-based capability for the simulation of growth of a solid electrolyte interphase layer at an anode particle in a Li-ion battery. Our simulation capability accounts for the stress-generation due to the growth of a SEI layer, as well as the cyclic stresses that are generated due to the lithiation and delithiation of the anode particle.

We have calibrated the material parameters in our theory by using available data from the literature, and by using results from the substrate curvature experiments of Mukhopadyay et al. (2012). The results that we have presented in Section 14 are extremely encouraging; they show that our theory and numerical simulation capability — with suitable choices for the material parameters — can reproduce the novel experimental results of Mukhopadyay et al. (2012) with reasonable *quantitative* accuracy.

The calibrated theory has been used to simulate SEI growth on a spherical and a spheroidal graphite anode particle. Our simulations show that large non-uniform compressive hoop stresses are generated within the SEI due to both the growth of the SEI and the lithiation/delithiation of the anode particle. Our study shows that SEI layers which are formed on the anode while it is in an expanded/lithiated state will develop higher compressive hoop stresses once the anode is subsequently delithiated. These findings are especially important since they in turn affect the large normal tensile tractions which develop along the anode/SEI interface — tractions which can lead to the delamination-type failure of the SEI and thus to accelerated capacity fade. Our study of spheroidal versus spherical particles shows that spheroidal particles develop much larger (order 3 times larger) normal tractions at certain points at the anode/SEI interface than spherical particles do. As such, spheroidal particles are at a higher risk for potential delamination failure of the SEI.

Our work presents a first step in the modeling of SEI growth at active anode particles, and carrying out a detailed stress analysis of the process. Much remains to be done; some important items that need attention in the future include:

- The square-root of time growth for the thickening of the SEI in our model is something that has been prescribed a-priori. In a more complete future theory the square-root of time growth might be the outcome of more completely modeled diffusion-limited chemical reaction processes which involve the electrolyte, electrons, and the resulting SEI (cf., e.g., Pinson and Bazant, 2013).
- Diffusion of Li through the SEI needs to be accounted for.
- Effects of anisotropic elasticity and anisotropic diffusion in the anode particles need to be accounted for.
- Arbitrary three-dimensional particle shapes need to be studied.
- SEI growth on other types of anode particles, such as those made from silicon — which exhibits significantly larger volume changes — needs to be studied.

Finally, there is a pressing need for the direct experimental measurement of the material properies of the anode particles, the SEI layers, and the SEI/anode interfaces. This statement regarding experimental measurement of material properies is true also for all other microscopic (and macrscopic) components of Li-ion batteries.

Chapter 17

Conclusion

17.1 Summary

The development of simulation-based tools for the design, life-prediction, and optimization of Lithium-Ion batteries (LIBs) is of crucial importance to the advancement of clean energy storage, and largely remains an open issue of research. In this thesis, we have developed such simulation-based tools with a focus on the the interaction between mechanical deformation and diffusion in single active particles of LIB electrodes.

This thesis has addressed the theoretical formulation, numerical implementation, and application of diffusion-deformation theories aimed at two different classes of electrode materials: (i) phase-separating electrodes, and (ii) elastic-plastic deforming electrodes. Further, we have developed a theory and simulation capability for modeling growth of a solid electrolyte interphase at the surface of an electrode. To conclude, we briefly summarize the main contributions of each part of this thesis:

Part I: Modeling phase-separating electrode materials

- We formulated a thermodynamically-consistent theory which couples Cahn-Hilliard species diffusion with large elastic deformations of a body. The theory was formulated using the principle of virtual power, which yields two coupled second-order partial differential equations which are amenable to being solved with a standard finite element implementation.

- The theory has been implemented in the finite-element program Abaqus (2010) by writing custom user-element subroutines.

- Using our simulation capability, we studied the chemo-mechanically-coupled problem of lithiation of isotropic spheroidal phase-separating electrode particles. We showed

that the coupling of mechanical deformation with diffusion is crucial in determining the lithiation morphology, and hence the Li distribution, within these particles.

Part II: Modeling amorphous Silicon electrodes

- We have formulated and numerically implemented a fully-coupled diffusion-deformation theory which accounts for transient diffusion of lithium and accompanying large elastic-plastic deformation of amorphous Silicon.
- The theory was calibrated to results from electrochemical cycling experiments of a-Si thin films deposited on quartz substrates performed by Pharr et al. (2014) and Bucci et al. (2014). By choosing appropriate material parameters, our simulations reproduce the experimentally measured voltage vs. state-of-charge and substrate curvature vs. state-of-charge curves.
- We have applied our numerical simulation capability to model galvanostatic charging of hollow a-Si nanotubes whose exterior walls have been oxidized to prevent outward expansion. We have shown that the results from our numerical simulations, without any parameter adjustments, are in reasonable agreement with the experimentally-measured voltage versus SOC behavior at various charging rates (C-rates).
- Using our numerical simulation capability we identify, and quantify, two major effects of plasticity on the performance of a-Si-based anodes of the type under consideration here:
  - First, plasticity enables lithiation of the anode to a higher SOC for a given voltage cut-off. This is because plastic flow reduces the stresses generated in the material, and thus reduces the potential required to lithiate the material.
  - Second, plastic deformation accounts for a significant amount of the energy dissipated during the cycling of the anode at low C-rates.
- We have demonstrated the applicability and importance of continuum-level models in making meaningful predictions of the electrochemical response of a-Si based nanostructured anodes.

Part III: Modeling growth of a solid electrolyte interphase

- We have formulated a new continuum-mechanical theory and a finite-element-based capability for the simulation of growth of a solid electrolyte interphase layer at an anode particle in a Li-ion battery.
- We have calibrated the theory to results from electrochemical cycling experiments of graphite thin films deposited on quartz substrates performed by Mukhopadyay et al. (2012). By choosing appropriate material parameters, our simulations reproduce the experimentally measured cyclic stresses, due to graphite lithiation/delithiation as well as the experimentally measured growth stresses.

- We have shown that SEI growth on spherical and spheroidal particles, as they are being charged/discharged, can lead to large non-uniform compressive hoop stresses within the SEI. Our finding that hoop stresses within the SEI remain compressive throughout the cycling of the anode, have important consequences for predicting failure of SEI. They suggest that SEI is not likely to fail through radial cracking but is prone to failure through delamination from the anode surface.

17.2 Outlook

While progress has been made in this thesis towards modeling deformation-diffusion processes in LIBs, much remains to be done. We list below, for the main parts of this thesis, as well as for the broader topic of modeling batteries as a whole, some directions for future work which have not been addresses in this thesis:

Outlook on modeling phase-separating electrode materials:

- Many cathode and anode materials currently used in Li-ion batteries are highly anisotropic. The general chemo-mechanically-coupled phase-field theory derived in this thesis is amenable to be specialized to account for such necessary anisotropies, however such work has not yet been performed.

- Boundary conditions are of major importance in modeling battery electrodes and need to be carefully considered. For nanometer-sized particles, there might also be a need to properly formulate and account for possible surface energy effects (i.e. surface-wetting), as recently studied by Cogswell and Bazant (2013). This is a non-trivial extension of the work in this thesis which requires careful theoretical as well as numerical considerations.

Outlook on modeling amorphous Silicon electrodes:

- The simulations considered in this thesis for hollow double-walled nanotubes include only *a single* nanotube, while the experimental results of Wu et al. (2012) were obtained from an anode which was made up of an *ensemble* of nanotubes of various dimensions. One extension of this work that is important, is the ability to model a variety of nanotubes with a statistical distribution of geometrical and material properties. Such an extension is non-trivial, from a computational implementation perspective, since it requires a highly non-linear multi-point constraine between the displacement and chemical potential degrees of freedom on the exterior surfaces of all of the tubes (cf. the Remark leading to (8.175)).

- In the modeling of the Si/SiO_2 double-walled nanotubes, the SiO_2 film is treated as a linear-elastic film through which diffusion of Li is neglected. This model needs to be extended to account for the fact that the SiO_2 film will react with Li to form a silicon-oxygen-lithium compound, which will consume some of the available Li, and which will affect Li diffusion to the a-Si anode.

- Recently, McDowell et al. (2013) and Wang et al. (2013) have experimentally observed that the first lithiation half-cycle of a-Si nanoparticle appears to proceed by a quasi-two-phase mechanism and not by single-phase diffusional insertion of Li. Such a mechanism has been neglected in this thesis with respect to modeling a-Si, however including such a mechanism would be a natural extension of this work, since two-phase mechanisms have been considered in detail when modeling phase-separating electrodes in Part I of this thesis.

- Finally, the simulation-based tool developed here for modeling nanostructured a-Si-based anodes should be further tested against other anode geometries. Some specific anodes of interest would be the "yolk-shell" structure of Liu et al. (2012a), and the Silicon-Copper nanolattices being developed by Xia and Greer (2015).

Outlook on modeling growth of a solid electrolyte interphase:

- In our model, the square-root of time growth for the thickening of the SEI is something that has been prescribed a-priori. In a more complete theory, the square-root of time growth might be the outcome of a diffusion-limited chemical reaction process which involves the electrolyte, electrons, and the resulting SEI (cf., e.g., Pinson and Bazant, 2013).

- Diffusion of Li through the SEI needs to be accounted for.

- Effects of anisotropic elasticity and anisotropic diffusion in the anode particles need to be accounted for.

- SEI growth on other types of anode particles, such as those made from silicon — which exhibits significantly larger volume changes — needs to be studied, both from a numerical as well as from an experimental perspective.

Overall outlook:

- A broader extension of this work, equally applicable to all parts discussed above, involves the up-scaling of our single active particle models to the porous electrode scale. One potential realization of such an up-scaling would be to fully discretize a portion of the porous-electrode scale including detailed discretizations of the active particles, binder, and conductivity enhancing particles. Further, to properly account for the chemical and mechanical connection between these various materials, we suggest the development of fully-coupled chemo-mechanical cohesive zone elements. Such "zero-thickness" elements could account for the electrochemical reaction kinetics at these interfaces (i.e. Butler-Volmer-type reaction kinetics), as well as account for possible failure of the mechanical interfaces through appropriate traction-separation relations. Finally, these fully-coupled elements could account for how mechanical damage affects loss of chemical connectivity as manifested through a loss of the flux of Li through the interface.

There are other approaches to modeling the porous-electrode scale. Notably, porous electrode theory (cf., e.g., Ferguson and Bazant, 2012), which introduces notions of porosity and tortuosity to effectively average across the porous-electrode scale, can be used as a predictive, and computationally efficient tool for modeling LIBs. However, it is unclear at this time how porous electrode theory might be extend to introduce notions of mechanical damage, such as fracture, within the active particles, and at the particle binder interfaces. The aforementioned approach, involving a full discretization of a portion of the porous-electrode scale, might help elucidate how damage mechanisms can be incorporated in regular porous electrode theory.

- Mechanical damage, for example through fracture of the active particles or through fracture or delamination of the SEI layer, is also of critical importance to understanding degradation in LIBs. Theoretical models and numerical tools need to be developed to extend the work in this thesis to include fracture mechanisms. Cohesive zone models, as detailed in the bullet point above, could also provide useful in the development of such fracture models.

- There is a pressing need for the experimental measurement of the material properties of the electrode particles, the SEI layers, and the SEI/electrode interfaces. This statement regarding experimental measurement of material properties is true also for all other microscopic (and macrscopic) components of Li-ion batteries.

- Other components of a LIB, such as the polymer membrane separating the anode and cathode materials, are also critical in the stability of the battery over its lifetime. Future work should also focus on understanding and modeling the mechanical behavior of the polymer membrane separator in order to better understand how such a component might fail under regular operation or due to mechanical abuse of the cell.

- Finally, we would like to note that the theoretical formulations, and numerical tools, developed in this thesis are broadly applicable to a large number of problems in energy production, transportation, and storage. For example, similar ideas to to the ones developed in this thesis have been applied to modeling hydrogen diffusion in metals (Di Leo and Anand, 2013), oxide growth in thermal barrier coatings (Loeffel and Anand, 2011), and dielectric elastomers (Henann et al., 2013) amongst others. Some example future applications might include developing deformation-diffusion models for: (i) high-temperature ceramic ion-transport membranes for fuel cells and air purification, (ii) hydrogen storage in metal-hydride systems, and (iii) catalysis.

Bibliography

A., T., Sheldon, B., Ku, P., Xiao, X., 2014. The origin of stress in the solid electrolyte interphase on carbon electrodes for li ion batteries. Journal of the Electrochemical Society 161, A58–A65.

Abaqus, 2010. Abaqus reference manuals.

Anand, L., 1979. Hencky's approximate strain-energy function for moderate deformations. ASME Journal of Applied Mechanics 46, 78–82.

Anand, L., 1986. Moderate deformations in extension-torsion of incompressible isotropic elastic materials. Journal of the Mechanics and Physics of Solids 34, 293–304.

Anand, L., 2012. A cahn-hilliard-type theory for species diffusion coupled with large elastic-plastic deformations. Journal of the Mechanics and Physics of Solids 60, 1983–2002.

Anand, L., Aslan, O., Chester, S., 2011. A large-deformation gradient theory for elasticplastic materials: Strain softening and regularization of shear bands. International Journal of Plasticity 30, 116–143.

Anand, L., Su, C., 2005. A theory for amorphous viscoplastic materials undergoing finite deformations, with application to metallic glasses. Journal of the Mechanics and Physics of Solids 53, 1362–1396.

Andersson, A., Henningson, A., Siegbahn, H., Jansoon, U., Edström, K., 2008. Electrochemically lithiated graphite characterized by photoelectron spectroscopy. Journal of Power Sources 119, 522–527.

Bai, P., Cogswell, D., Bazant, M., 2011. Suppression of phase separation in lifepo$_4$ nanoparticles during battery discharge. Nano Letters 11, 4890–4896.

Barré, A., Deguilhem, B., Grolleau, S., Geŕare, M., 2013. A review on lithium-ion battery aging mechanisms and estimations for automotive applications. Journal of Power Sources 241, 680–689.

Bazant, M., 2013. Theory of chemical kinetics and charge transfer based on nonequilibrium thermodynamics. Accounts of Chemical Research 46(5), 1144–1160.

Berla, L., Lee, S., Cui, Y., Nix, W., 2014. Robustness of amorphous silicon during the initial lithiation/delithiation cycle. Journal of Power Sources 258, 253–259.

Bower, A., Guduru, P., 2012. A simple finite element model of diffusion, finite deformation, plasticity and fracture in lithium ion insertion electrode materials. Modeling and Simulation in Materials Science and Engineering 20, 045004.

Bower, A., Guduru, P., Sethuraman, V., 2011. A finite strain model of stress, diffusion, plastic flow, and electrochemical reactions in a lithium-ion half-cell. Journal of the Mechanics and Physics of Solids 59, 804–828.

Bruce, P., Scrosati, B., J-M, T., 2008. Nanomaterials for rechargeable lithium batteries. Angewandte Chemie International 47, 2930–2946.

Bucci, G., Nadimpalli, S., Sethuraman, V., Bower, A., Guduru, P., 2014. Measurement and modeling of the mechanical and electrochemical response of amorphous si thin film electrodes during cyclic lithiation. Journal of the Mechanics and Physics of Solids 62, 276–294.

Cahn, J., 1961. On spinodal decomposition. Acta Metallurgica 9, 795–801.

Cahn, J., 1977. Critical point wetting. Journal of Chemical Physics 66, 3667–3672.

Cahn, J., Hilliard, J., 1958. Free energy of a nonuniform system-i: Interfacial free energy. The Journal of Chemical Physics 28, 258–267.

Cahn, J., Hilliard, J., 1959. Free energy of a nonuniform system-iii:nucleation in a two component incompressible fluid. The Journal of Chemical Physics 31, 688–699.

Chester, S., 2011. Mechanics of amorphous polymers and polymer gels. Ph.D. thesis. Massachusetts Institute of Technology.

Chester, S., Di Leo, C., Anand, L., 2015. A finite element implementation of a coupled diffusion-deformation theory for elastomeric gels. International Journal of Solids and Structures 52, 1–18.

Christensen, J., Newman, J., 2006. Stress generation and fracture in lithium insertion materials. Journal of Solid State Electrochemistry 10, 293–319.

Cogswell, D., Bazant, M., 2013. Theory of coherent nucleation in phase-separating nanoparticles. Nano Letters 13, 3036–3041.

De Jong, B., Beerkens, R., van Nijnatten, P., Le Bourhis, E., 2000. Glass, 1. Fundamentals. Ullmann's Encyclopedia of Industrial Chemistry. John Wiley & Sons, Ltd.

de Souza Neto, E., Peric, D., Dutko, M., Owen, D., 1996. Design of simple low order finite element for large strain analysis of nearly incompressible solids. International Journal of Solids and Structures 33, 3277–3296.

DeHoff, R., 2006. Thermodynamics in Materials Science. CRC Press, Boca Raton.

Di Leo, C., 2012. A coupled theory for diffusion of hydrogen and large elastic-plastic deformations of metals. Master's thesis. Massachusetts Institute of Technology. Cambridge, MA.

Di Leo, C., Anand, L., 2013. Hydrogen in metals: A coupled theory for species diffusion and large elasticplastic deformations. International Journal of Plasticity 43, 42–69.

Di Leo, C., Rejovitzky, E., Anand, L., 2014. A cahn-hilliard-type phase-field theory for species diffusion coupled with large elastic deformations: Application to phase-segragating li-ion electrode materials. Journal of the Mechanics and Physics of Solids 70, 1–29.

Ding, N., Xu, J., Yao, Y., Wegner, G., Fang, X., Chen, C., Lieberwirth, I., 2009. Determination of the diffusion coefficient of lithium ions in nano-si. Solid State Ionics 180(2), 222–225.

Ferguson, T., Bazant, M., 2012. Nonequilibrium thermodynamics of porous electrodes. Journal of the Electrochemical Society 159(12), A1967–A1985.

Forest, S., 2009. Micromorphic approach for gradient elasticity, viscoplasticity, and damage. Journal of Engineering Mechanics 135, 117–131.

Germain, P., 1973. The method of virtual power in continuum mechanics. part 2: microstructure. SIAM Journal of Applied Mathematics 25, 556–575.

Gomez, H., Calo, V., Bazilevs, Y., Hughes, T., 2008. Isogeoemetric analysis of the cahn-hilliard phase-field model. Computer Methods in Applied Mechanics and Engineering 197, 4333–4352.

Gomez, H., Hughes, T., 2011. Provably unconditionally stable, second-order time-accurate, mixed variational methods for phase-field models. Journal of Computational Physics 230, 5310–5327.

Gurtin, M., 1996. Generalized ginzburg-landau and cahn-hilliard equations based on a microforce balance. Physica D 92, 178–192.

Gurtin, M., 2002. A gradient theory of single-crystal viscoplasticity that accounts for geometrically necessary dislocations. Journal of the Mechanics and Physics of Solids 50, 5–32.

Gurtin, M., Fried, E., Anand, L., 2010. The Mechanics and Thermodynamics of Continua. Cambridge University Press, Cambridge.

He, Y., Xu, X., Wang, Y., Ki, H., Huang, X., 2011. Alumina-coated patterned amorphous silicon as the anode for a lithium-ion battery with high coulombic efficiency. Advanced Mater 23, 4938–4941.

Henann, D., Chester, S., Bertoldi, K., 2013. Modeling of dielectric elastomers: Design of actuators and energy harvesting devices. Journal of the Mechanics and Physics of Solids 61(10), 2047–2066.

Kröner, E., 1960. Allgemeine kontinuumstheorie der versetzungen und eigenspannungen. Archive for Rational Mechanics and Analysis 4, 273–334.

Kuhl, E., 2014. Growing matter: a review of growth in living systems. Journal of the Mechanical Behavior of Biomedical Materials 29, 529–543.

Kuhl, E., Schmidt, D., 2007. Computational modeling of mineral unmixing and growth. Computational Mechanics 39, 439–451.

Lee, E., 1969. Elastic plastic deformation at finite strain. ASME Journal of Applied Mechanics 36, 1–6.

Lee, M., Lee, J., Shim, H., Lee, J., Park, J., 2007. Sei layer formation on amorphous si thin electrode during precycling. Journal of The Electrochemical Society 154, A515–A519.

Li, H., Huang, X., Chen, L., Wu, Z., Liang, Y., 1999. A high capacity nano-si composite anode material for lithium rechargeable batteries. Electrochemical and Solid-State Letters 2(11), 547–549.

Liu, N., Wu, H., H., M., M.T., Y., Wang, C., Cui, Y., 2012a. A yolk-shell design for stabilized and scalable li-ion battery alloy anodes. Nano Letters 12(6), 3315–3321.

Liu, X., Zhong, L., Huang, S., Mao, S., Zhu, T., Huang, J., 2012b. Size-dependent fracture of silicon nanoparticles during lithiation. Acs Nano 6(2), 1522–1531.

Loeffel, K., Anand, L., 2011. A chemo-thermo-mechanically coupled theory for elastic-viscoplastic deformation, diffusion, and volumetric swelling due to a chemical reaction. International Journal of Plasticity 27, 1409–1431.

Malik, R., Burch, D., Bazant, M., Ceder, G., 2010. Particle size dependence of the ionic diffusivity. Nano Letters 10, 4123–4127.

Maxisch, T., Ceder, G., 2006. Elastic properties of olivine li_xfepo_4 from first principles. Physical Review B 73, 174112–1 - 174112–4.

McDowell, M., Lee, S., Harris, J., Korgel, B., Wang, C., Cui, Y., 2013. In situ tem of two-phase lithiation of amorphous silicon nanospheres. Nano Letters 13, 758–764.

McDowell, M., Ryu, I., Lee, S., Wang, C., Nix, W., Cui, Y., 2012. Studying the kinetics of crystalline silicon nanoparticle lithiation with in situ transmission electron microscopy. Advanced Mater 24, 6034–6041.

Mohr, P., Taylor, B., Newell, D., 2008. Codata recommended values of the fundamental physical constant. Rev. Mod. Phys. 90, 633–730.

Mukhopadyay, A., Tokranov, A., Xiao, X., Sheldon, B., 2012. Stress development due to surface processes in graphite electrodes for li-ion batteries: A first report. Electrochimica Acta 66, 28–37.

Newman, J., Thomas-Alyea, E., 2010. Electrochemical systems. John Wiley & Sons.

Obrovac, M., Krause, K., 2007. Reversible cycling of crystalline silicon powder. Journal of the Electrochemical Society 154, A103–A108.

Pharr, M., Suo, Z., Vlassak, J., 2014. Variation of stress with charging rate due to strain-rate sensitivity of silicon electrodes of li-ion batteries. Journal of Power Sources 270, 569–575.

Pinson, M., Bazant, M., 2013. Theory of sei formation in rechargeable batteries: capacity fade, accelerated aging and lifetime prediction. Journal of The Electrochemical Society 160(2), A243–A250.

Qi, Y., Guo, H., Hector, L., Timmons, A., 2010. Threefold increase in the young's modulus of graphite negative electrode during lithium intercalation. Journal of The Electrochemical Society 157, A558–A566.

Rejovitzky, E., Di Leo, C., Anand, L., 2014. A theory and simulation capability for growth of a solid electrolyte interphase layer at an anode particle in a li-ion battery. Journal of the Mechanics and Physics of Solids 78, 210–230.

Ros, A., 2005. The isoperimetric problem. chapter in global theory of minimal surfaces. Amer. Math. Soc 2, 175–209.

Rousse, G., Rodriguez-Carvajal, J., Patoux, S., C.Masquelier, 2003. Magnetic structures of the triphylite $lifepo_4$ and of its delithiated form $fepo_4$. Chemistry of Materials 15, 4082–4090.

Ryu, I., Choi, J., Cui, Y., Nix, W., 2011. Size-dependent fracture of si nanowire battery anodes. Journal of the Mechanics and Physics of Solids 59, 1717–1730.

Scrosati, B., Garche, J., 2010. Lithium batteries; status, prospects and future. Journal of Power Sources 195, 2419–2430.

Sethuraman, V., Chon, M., Shimshak, M., Winkle, N.V., Guduru, P., 2012. *In situ* measurement of biaxial modulus of si anode for li-ion batteries. Electrochemistry Communications 12(11), 1614–1617.

Sethuraman, V., Srinivasan, V., Bower, A., Guduru, P., 2010a. In situ measurements of stress-potential coupling in lithiated silicon. Journal of the Electrochemical Society 157, A1253–A1261.

Sethuraman, V., Srinivasan, V., Bower, A., Guduru, P., 2010b. In situ measurements of stress-potential coupling in lithiated silicon. Journal of the Electrochemical Society 11, A1253–A1261.

Shenoy, V., Johari, P., Qi, Y., 2010. Elastic softening of amorphous and crystalline lisi phases with increasing li concentration: a first-principles study. Journal of Power Sources 195, 6825–6830.

Smith, A., Burns, J., Xiong, D., Dahn, J., 2011a. Interpreting high precision coulometry results on li-ion cells. Journal of The Electrochemical Society 158, A1136–A1142.

Smith, A., Burns, J., Zhao, X., Xiong, D., Dahn, J., 2011b. A high precision coulometry study of the sei growth in li/graphite cells. Journal of The Electrochemical Society 158(5), A447–A452.

Stoney, G., 1909. The tension of metallic films deposited by electrolysis. Proceeding of the Royal Society A 82, 172–175.

Tang, M., Carter, W., Chiang, Y.M., 2010. Electrochemically driven phase transitions in insertion electrodes for lithium-ion batteries: examples in lithium metal phosphate olivines. Annual Reviews of Materials Research 40, 501–529.

Tarascon, J., Armand, M., 2001a. Issues and challenges facing rechargeable batteries. Nature 414, 359–367.

Tarascon, J., Armand, M., 2001b. Issues and challenges facing rechargeable lithium batteries. Nature 414, 359–367.

Ubachs, R., Schreurs, P., Geers, M., 2004. A nonlocal diffuse interface model for microstructure evolution of tin-lead solder. Journal of the Mechanics and Physics of Solids 52, 1763–1792.

Verma, P., Maire, P., Novák, P., 2010. A review of the features and analyses of the solid electrolyte interphase in li-ion batteries. Electrochemica Acta 55, 6332–6341.

Wang, J., H.Yu, Feifei, F., Liu, X., Xia, S., Liu, Y., Harris, C., Li, H., Huang, J., Mao, S., Zhu, T., 2013. Two-phase electrochemical lithiation in amorphous silicon. Nano Letters 13, 709–715.

Weber, G., Anand, L., 1990. Finite deformation constitutive equations and a time integration procedure for isotropic, hyperelastic viscoplastic solids. Computer Methods in Applied Mechanics and Engineering 79, 173–202.

Wells, G., Kuhl, E., Garikapati, K., 2006. A discontinuous galerkin method for the cahn-hilliard equation. Journal of Computational Physics 218, 860–877.

Wodo, O., Ganapathysubramanian, B., 2011. Computationally efficient solution to the cahn-hilliard equation: Adaptive implicit time schemes, mesh sensitivity analysis and the 3d isoperimetric problem. Journal of Computational Physics 230, 6037–6060.

Wu, H., Chan, G., Choi, J., Yao, Y., McDowell, M., Lee, S., Jackson, A., Yang, Y., Hu, L., Cui, Y., 2012. Stable cycling of double-walled silicon nanotube battery anodes through solid-electrolyte interphase control. Nature Nanotechnology 7(5), 31–315.

Xia, X., Greer, J., 2015. Personal communication.

Zeng, Y., Bazant, M., 2014. Phase separation dynamics in isotropic ion-intercalation particles. SAIm Journal on Applied Mathematics 74, 980–1004.

Zhang, Y., Li, Y., Wang, Z., Zhao, K., 2014. Lithiation of sio_2 in li-ion batteries: In situ transmission electron microscopy experiments and theoretical studies. Nano Letters 14(12), 7161–7170.

Zhao, K., Pharr, M., Cai, S., Vlassak, J., Suo, Z., 2011. Large plastic deformation in high-capacity lithium-ion batteries caused by charge and discharge. Journal of American Ceramic Society 94, S226–S235.

Zhao, K., Pharr, M., Hartle, L., Vlassak, J., Suo, Z., 2012. Fracture and debonding in lithium-ion batteries with electrodes of hollow core-shell nanostructures. Journal of Power Sources 218, 6–14.

Appendix A

Numerical methodology for Part I: Modeling phase-separating electrode materials.

A.1 Introduction

Following the framework developed by Chester et al. (2015), in this Appendix we present the details of our numerical implementation of the constitutive model developed in Part I for the coupled diffusion-deformation behavior of phase-separating electrode materials. In particular, we present here the "Residual" vector and "Tangent" matrix which must be implemented in order to solve the coupled set of equations in the finite element program Abaqus/Standard through the use of the user element (UEL) subroutine. Details on how to implement the residuals and tangents developed here within the UEL fortran subroutines can be found in Chester et al. (2015), and are thus omitted from this Appendix.

In Sect. A.2 we begin by recalling the governing partial differential equations and boundary conditions, and then formulate the variational statements which will serve to develop the residual necessary in the finite element implementation. In Sect. A.3 we derive the tangents. We summarize our results in Sect. A.4.

A.2 Variational formulation. Residuals

We begin by recalling the governing partial differential equations (3.106), (3.107), and (3.108), along with the equation for the stress potential (3.117), and their boundary condi-

tions:

$$\left.\begin{aligned}
&\text{Macroforce balance}\left\{\begin{array}{rll} \operatorname{div}\mathbf{T}+\mathbf{b}=\mathbf{0} & \text{in} & \mathcal{B},\\ \mathbf{u}=\breve{\mathbf{u}} & \text{on} & \mathcal{S}_u,\\ \mathbf{T}\mathbf{n}=\breve{\mathbf{t}} & \text{on} & \mathcal{S}_t,\end{array}\right.\\
&\text{Mass balance}\left\{\begin{array}{rll} \dot{\bar{c}}=\operatorname{Div}\left(\bar{m}\nabla\mu\right) & \text{in} & \mathrm{B},\\ \bar{c}=\breve{\bar{c}} & \text{on} & \mathcal{S}_c,\\ -\bar{m}\nabla\mu\cdot\mathbf{n}_{\mathrm{R}}=\breve{j} & \text{on} & \mathcal{S}_j.\end{array}\right.\\
&\text{Microforce balance}\left\{\begin{array}{rll} \lambda\Delta\bar{\mathbb{c}}+\beta(\bar{c}-\bar{\mathbb{c}})=0 & \text{in} & \mathrm{B},\\ \bar{\mathbb{c}}=\breve{\bar{\mathbb{c}}} & \text{on} & \mathcal{S}_{\mathbb{c}},\\ \lambda(\nabla\bar{\mathbb{c}})\cdot\mathbf{n}_{\mathrm{R}}=\breve{\xi} & \text{on} & \mathcal{S}_{\xi}.\end{array}\right.\\
&\text{Equation for the stress potential}\left\{\begin{array}{rll} \mu_\sigma=-\Omega\dfrac{1}{3}\operatorname{tr}\mathbf{M}^e & \text{in} & \mathrm{B},\\ \mu_\sigma=\breve{\mu}_\sigma & \text{on} & \mathcal{S}_{\mu_\sigma}.\end{array}\right.
\end{aligned}\right\} \tag{A.1}$$

Note that in writing (A.1) we have made the following choices:

- The macroforce balance in (3.106) is stated in the reference configuration, whereas here we have stated it in the *deformed configuration* and will also numerically implement it in the deformed configuration. Such a choice is made following the finite element developments of Chester (2011), on which this development is based. We note that this choice will not affect the accuracy of our results.

- The mass balance is written in terms of the normalized concentration $\bar{c}=c_{\mathrm{R}}/c_{\mathrm{R,max}}$, and the degree of freedom (dof) used in the numerical implementation is also the normalized concentration $\bar{c}$. In doing so, using (3.107) we have defined

$$\bar{m}\overset{\text{def}}{=}m_0\bar{c}(1-\bar{c}). \tag{A.2}$$

  Similarly, the microforce balance is written in terms of the normalized micromorphic concentration $\bar{\mathbb{c}}$ which is also the dof for this pde.

With

$$\mathbf{w}_1,\quad w_2,\quad w_3,\quad w_4, \tag{A.3}$$

denoting weighting (or test) fields which vanish on $\mathcal{S}_u$, $\mathcal{S}_c$, $\mathcal{S}_{\mathfrak{c}}$, and $\mathcal{S}_{\mu_\sigma}$ respectively, the weak forms corresponding to (A.1) are given by

$$\left.\begin{aligned}
&\int_{\mathcal{B}} (\mathbf{T}\colon \mathrm{grad}\mathbf{w}_1 - \mathbf{w}_1 \cdot \mathbf{b})\, dv - \int_{\mathcal{S}_t} \mathbf{w}_1 \cdot \breve{\mathbf{t}}\, da = 0,\\
&\int_{\mathrm{B}} (w_2 \dot{\bar{c}} + \nabla w_2 \cdot (\bar{m}\nabla\mu))\, dv_{\mathrm{R}} + \int_{\mathcal{S}_j} w_2 \breve{j}\, da_{\mathrm{R}} = 0,\\
&\int_{\mathrm{B}} (w_3\beta(\bar{\mathfrak{c}} - \bar{c}) + \lambda\nabla w_3 \cdot \nabla\bar{\mathfrak{c}})\, dv_{\mathrm{R}} - \int_{\mathcal{S}_\xi} w_3 \breve{\xi}\, da_{\mathrm{R}} = 0,\\
&\int_{\mathrm{B}} w_4 \left(\mu_\sigma + \Omega\frac{1}{3}\mathrm{tr}\mathbf{M}^e\right) dv_{\mathrm{R}} = 0.
\end{aligned}\right\} \tag{A.4}$$

The body is approximated using finite elements, $\mathrm{B} = \cup\mathrm{B}^e$, and the trial solutions for the displacement, the concentration, the micromorphic concentration, and the stress potential are interpolated inside each element by

$$\mathbf{u} = \sum_A \mathbf{u}^A N^A, \quad \bar{c} = \sum_A \bar{c}^A N^A, \quad \bar{\mathfrak{c}} = \sum_A \bar{\mathfrak{c}}^A N^A, \quad \mu_\sigma = \sum_A \mu_\sigma^A N^A, \tag{A.5}$$

with the index $A = \{1, 2, ..., M\}$ denoting the nodes of the element, $\mathbf{u}^A$ denoting the nodal displacements, $\bar{c}^A$ denoting the nodal concentrations, $\bar{\mathfrak{c}}^A$ denoting the nodal micromorphic concentrations, μ_σ denoting the nodal stress potentials, and N^A the shape functions. Using a standard Galerkin approach, the weighting fields are interpolated by the same functions, that is

$$\mathbf{w}_1 = \sum_A \mathbf{w}_1^A N^A, \quad w_2 = \sum_A w_2^A N^A, \quad w_3 = \sum_A w_3^A N^A, \quad w_4 = \sum_A w_4^A N^A. \tag{A.6}$$

Using (A.5) and (A.6) in (A.4), yields the following element-level system equations.

$$\left.\begin{aligned}
&\int_{\mathcal{B}^e} \left(\mathbf{T}\mathrm{grad}N^A - N^A\mathbf{b}\right) dv - \int_{\mathcal{S}_t^e} N^A \breve{\mathbf{t}}\, da = \mathbf{0},\\
&\int_{\mathrm{B}^e} \left(N^A \dot{\bar{c}} + \nabla N^A \cdot (\bar{m}\nabla\mu)\right) dv_{\mathrm{R}} + \int_{\mathcal{S}_j^e} N^A \breve{j}\, da_{\mathrm{R}} = 0,\\
&\int_{\mathrm{B}^e} \left(N^A\beta(\bar{\mathfrak{c}} - \bar{c}) + \lambda\nabla N^A \cdot \nabla\bar{\mathfrak{c}}\right) dv_{\mathrm{R}} - \int_{\mathcal{S}_\xi^e} N^A \breve{\xi}\, da_{\mathrm{R}} = 0,\\
&\int_{\mathrm{B}^e} N^A \left(\mu_\sigma + \Omega\frac{1}{3}\mathrm{tr}\mathbf{M}^e\right) dv_{\mathrm{R}} = 0.
\end{aligned}\right\} \tag{A.7}$$

This system of coupled equations is solved using a Newton procedure in Abaqus by defining element-level residuals and tangents. Using (A.7), the element-level residuals for the displacements, the concentration, the micromorphic concentration, and the stress potential are given by

$$\left.\begin{aligned} \mathbf{R}^A_{\mathbf{u}} &= \int_{\mathcal{B}^e} \left(\mathbf{T}\mathrm{grad}N^A - N^A\mathbf{b}\right)\, dv - \int_{\mathcal{S}^e_t} N^A \check{\mathbf{t}}\, da, \\ R^A_{\bar{c}} &= \int_{\mathrm{B}^e} \left(N^A\dot{\bar{c}} + \nabla N^A \cdot (\bar{m}\nabla\mu)\right)\, dv_{\mathrm{R}} + \int_{\mathcal{S}^e_j} N^A \check{j}\, da_{\mathrm{R}}, \\ R^A_{\bar{\mathbb{c}}} &= \int_{\mathrm{B}^e} \left(N^A\beta(\bar{\mathbb{c}} - \bar{c}) + \lambda\nabla N^A \cdot \nabla\bar{\mathbb{c}}\right)\, dv_{\mathrm{R}} - \int_{\mathcal{S}^e_\xi} N^A \check{\xi}\, da_{\mathrm{R}}, \\ R^A_{\mu_\sigma} &= \int_{\mathrm{B}^e} N^A \left(\mu_\sigma + \Omega\frac{1}{3}\mathrm{tr}\mathbf{M}^e\right)\, dv_{\mathrm{R}}. \end{aligned}\right\} \tag{A.8}$$

Next, recall equation (3.96) for the chemical potential μ which may be written as

$$\mu = \hat{f}(\bar{c}) - \beta\bar{\mathbb{c}} + \mu_\sigma, \quad \text{with} \quad \hat{f}(\bar{c}) = R\vartheta \ln\left(\frac{\bar{c}}{1-\bar{c}}\right) + \chi(1-2\bar{c}) + \beta\bar{c}. \tag{A.9}$$

Using (A.9), we may write the residual $R^A_{\bar{c}}$ for the concentration in terms of all other degrees of freedom as

$$\begin{aligned} R^A_{\bar{c}} = \int_{B^e} \left(N^A\dot{\bar{c}} + \bar{m}\left(\nabla N^A \cdot \frac{\partial f}{\partial\bar{c}}\nabla\bar{c} - \nabla N^A \cdot \beta\nabla\bar{\mathbb{c}} + \nabla N^A \cdot \nabla\mu_\sigma\right)\right)\, dv_{\mathrm{R}} \\ + \int_{\mathcal{S}_j} N^A \check{j}\, da_{\mathrm{R}}, \end{aligned} \tag{A.10}$$

with

$$\frac{\partial f}{\partial\bar{c}} = \frac{R\vartheta}{\bar{c}(1-\bar{c})} - 2\chi + \beta, \quad \text{and} \quad \bar{m} = \frac{D_0}{R\vartheta}\bar{c}(1-\bar{c}). \tag{A.11}$$

A.3 Tangents

In addition to the residuals, the following tangents are also required:

$$\begin{aligned} K^{AB}_{\mathbf{uu}} &= -\frac{\partial\mathbf{R}^A_{\mathbf{u}}}{\partial\mathbf{u}^B}, & K^{AB}_{\bar{c}\bar{c}} &= -\frac{\partial R^A_{\bar{c}}}{\partial\bar{c}^B}, & K^{AB}_{\bar{\mathbb{c}}\bar{\mathbb{c}}} &= -\frac{\partial R^A_{\bar{\mathbb{c}}}}{\partial\bar{\mathbb{c}}^B}, \\ K^{AB}_{\mathbf{u}\bar{c}} &= -\frac{\partial\mathbf{R}^A_{\mathbf{u}}}{\partial\bar{c}^B}, & K^{AB}_{\bar{c}\bar{\mathbb{c}}} &= -\frac{\partial R^A_{\bar{c}}}{\partial\bar{\mathbb{c}}^B}, & K^{AB}_{\bar{\mathbb{c}}\bar{c}} &= -\frac{\partial R^A_{\bar{\mathbb{c}}}}{\partial\bar{c}^B}, \\ & & K^{AB}_{\bar{c}\mu_\sigma} &= -\frac{\partial R^A_{\bar{c}}}{\partial\mu^B_\sigma}, & K^{AB}_{\bar{\mathbb{c}}\mu_\sigma} &= -\frac{\partial R^A_{\bar{\mathbb{c}}}}{\partial\mu^B_\sigma}, \end{aligned} \tag{A.12}$$

and

$$
\begin{aligned}
K^{AB}_{\mu_\sigma \mu_\sigma} &= -\frac{\partial R^A_{\mu_\sigma}}{\partial \mu^B_\sigma}, \\
K^{AB}_{\mu_\sigma \bar{c}} &= -\frac{\partial R^A_{\mu_\sigma}}{\partial \bar{c}^B}, \\
K^{AB}_{\mu_\sigma \mathbf{u}} &= -\frac{\partial R^A_{\mu_\sigma}}{\partial \mathbf{u}^B}.
\end{aligned}
\tag{A.13}
$$

First, the tangent of the displacement residual with respect to the displacement dof, in indicial notation, is given by (cf. Chester et al. (2015))

$$
K^{AB}_{u_i u_k} = -\int_{\mathrm{B}^e} \frac{\partial N^A}{\partial x_j} \mathbb{A}_{ijkl} \frac{\partial N^B}{\partial x_l}\, dv + \int_{\mathcal{S}^e_t} N^A N^B \frac{\partial \breve{t}_i}{\partial u_k}\, da, \tag{A.14}
$$

with

$$
\mathbb{A}_{ijkl} = J^- 1 F_{jm} F_{ln} \frac{\partial T_{\mathrm{R},im}}{\partial F_{kn}}. \tag{A.15}
$$

In our numerical implementation we make the simplifying *approximation* that the spatial tangent modulus (A.15) is equal to the elasticity tensor (3.90), that is

$$
\mathbb{A} \approx \mathbb{C} = 2G\mathbb{I} + \left(K - \frac{2}{3}G\right) \mathbf{1} \otimes \mathbf{1}, \tag{A.16}
$$

where G and K are the shear and bulk moduli respectively, and $\mathbb{I}$ and $\mathbf{1}$ are fourth- and second-order identity tensors.

Remark. As detailed in Chester et al. (2015), to accommodate compressible and nearly incompressible material behavior and mitigate volumetric locking behavior, we use the so called *F-bar* method (de Souza Neto et al., 1996). In such a method, the deformation gradient is suitably replaced such that the incompressibility constrained is enforced as an approximate average throughout the element, rather than point wise at each integration point. The use of the F-bar method does not change the integration point residuals, simply the modified deformation is used. However, the tangent (A.14), and all tangents which involve residuals being derived with respect to the displacement degrees of freedom, must be modified. The necessary modifications are discussed in detail in Chester et al. (2015), □

The tangent of the displacement residual with respect to the concentration dof is given by

$$
K^{AB}_{\mathbf{u}\bar{c}} = -\int_{\mathrm{B}^e} N^B \frac{\partial \mathbf{T}}{\partial \bar{c}} \operatorname{grad} N^A\, dv + \int_{\mathcal{S}^e_t} N^A N^B \frac{\partial \breve{\mathbf{t}}}{\partial \bar{c}}\, da. \tag{A.17}
$$

We make the *approximation* that

$$\frac{\partial \mathbf{T}}{\partial \bar{c}} \approx \frac{\partial \mathbf{M}^e}{\partial \bar{c}}. \tag{A.18}$$

Recalling (3.93) and (3.82), and using the fact that $\operatorname{tr}\mathbf{E}^e = \ln(J/J^c)$, we may write

$$\mathbf{M}^e = 2G\mathbf{E}_0^e + K \ln\left(\frac{J}{J^c}\right)\mathbf{1}, \quad J^c = 1 + \Omega \bar{c} c_{\mathrm{R,max}}, \tag{A.19}$$

which yields

$$\frac{\partial \mathbf{M}^e}{\partial \bar{c}} = -\frac{K\Omega c_{\mathrm{R,max}}}{J^c}\mathbf{1}. \tag{A.20}$$

Next, the tangent of the concentration residual (A.10) with respect to the concentration dof is given by

$$\begin{aligned} K^{AB}_{\bar{c}\bar{c}} = -\int_{\mathrm{B}^e} \Bigg(& N^A N^B \frac{\partial \dot{\bar{c}}}{\partial \bar{c}} + \frac{\partial \bar{m}}{\partial \bar{c}} N^B \left(\nabla N^A \cdot \frac{\partial f}{\partial \bar{c}} \nabla \bar{c} - \nabla N^A \cdot \beta \nabla \bar{\mathbb{c}} + \nabla N^A \cdot \nabla \mu_\sigma \right) \\ & + \bar{m} N^B \nabla N^A \cdot \frac{\partial^2 f}{\partial \bar{c}^2} \nabla \bar{c} + \bar{m} \nabla N^A \cdot \frac{\partial f}{\partial \bar{c}} \nabla N^B \Bigg) \, dv_{\mathrm{R}} - \int_{\mathcal{S}^e_j} N^A N^B \frac{\partial \breve{j}}{\partial \bar{c}} \, da_{\mathrm{R}}, \end{aligned} \tag{A.21}$$

with

$$\frac{\partial \bar{m}}{\partial \bar{c}} = \frac{D_0}{R\vartheta}(1 - 2\bar{c}), \quad \text{and} \quad \frac{\partial^2 f}{\partial \bar{c}^2} = \frac{R\vartheta(2\bar{c} - 1)}{\bar{c}^2(1 - \bar{c})^2}. \tag{A.22}$$

The tangent of the concentration residual (A.10) with respect to the micromorphic concentration is given by

$$K^{AB}_{\bar{c}\bar{\mathbb{c}}} = -\int_{\mathrm{B}^e} -\bar{m} \nabla N^A \cdot \beta \nabla N^B \, dv_{\mathrm{R}} - \int_{\mathcal{S}^e_j} N^A N^B \frac{\partial \breve{j}}{\partial \bar{\mathbb{c}}} \, da_{\mathrm{R}}. \tag{A.23}$$

The tangent of the concentration residual (A.10) with respect to the stress potential dof is given by

$$K^{AB}_{\bar{c}\mu_\sigma} = -\int_{\mathrm{B}^e} \bar{m} \nabla N^A \cdot \nabla N^B \, dv_{\mathrm{R}} - \int_{\mathcal{S}^e_j} N^A N^B \frac{\partial \breve{j}}{\partial \mu_\sigma} \, da_{\mathrm{R}}. \tag{A.24}$$

The tangent of the micromorphic concentration residual with respect to the micromorphic concentration dof is given by

$$K^{AB}_{\bar{\mathbb{c}}\bar{\mathbb{c}}} = -\int_{\mathrm{B}^e} \left(\beta N^A N^B + \lambda \nabla N^A \cdot \nabla N^B \right) dv_{\mathrm{R}} + \int_{\mathcal{S}^e_\xi} N^A N^B \frac{\partial \breve{\xi}}{\partial \bar{\mathbb{c}}} \, da_{\mathrm{R}}. \tag{A.25}$$

The tangent of the micromorphic concentration residual with respect to the concentration dof is given by

$$K^{AB}_{\breve{c}\bar{c}} = -\int_{\mathrm{B}^e} -\beta N^A N^B \, dv_{\mathrm{R}} + \int_{\mathcal{S}^e_\xi} N^A N^B \frac{\partial \breve{\xi}}{\partial \bar{c}} \, da_{\mathrm{R}}. \tag{A.26}$$

The tangent of the stress potential residual with respect to the stress potential dof is given by

$$K^{AB}_{\mu_\sigma \mu_\sigma} = -\int_{\mathrm{B}^e} N^A N^B \, dv_{\mathrm{R}}. \tag{A.27}$$

The tangent of the stress potential residual with respect to the concentration dof is given by

$$K^{AB}_{\mu_\sigma \bar{c}} = -\int_{\mathrm{B}^e} N^A N^B \Omega \frac{1}{3} \frac{\partial \mathrm{tr}\,\mathbf{M}^e}{\partial \bar{c}} \, dv_{\mathrm{R}}, \tag{A.28}$$

where, using (A.19), we have that

$$\frac{\partial \mathrm{tr}\,\mathbf{M}^e}{\partial \bar{c}} = -\frac{3K\Omega c_{\mathrm{R,max}}}{J^c}. \tag{A.29}$$

The tangent of the stress potential residual with respect to the displacement dof in indicial notation is given by

$$K^{AB}_{\mu_\sigma u_i} = -\int_{\mathrm{B}^e} N^A \Omega \frac{1}{3} \frac{\partial \mathrm{tr}\,\mathbf{M}^e}{F_{jk}} \frac{\partial F_{jk}}{\partial u^B_i} \, dv_{\mathrm{R}}. \tag{A.30}$$

which using the identity

$$F_{ij} = \delta_{ij} + \sum u^B_i \frac{\partial N^B}{\partial X_j}, \quad \rightarrow \quad \frac{\partial F_{ij}}{\partial u^B_k} = \delta_{ik} \frac{\partial N^B}{\partial X_j}, \tag{A.31}$$

may be written as

$$K^{AB}_{\mu_\sigma u_i} = -\int_{\mathrm{B}^e} N^A \Omega \frac{1}{3} \frac{\partial \mathrm{tr}\,\mathbf{M}^e}{F_{ik}} \frac{\partial N^B}{\partial X_k} \, dv_{\mathrm{R}}. \tag{A.32}$$

From (A.19) we have that

$$\frac{\partial \mathrm{tr}\,\mathbf{M}^e}{\partial \mathbf{F}} = \frac{3K}{J} \frac{\partial J}{\partial \mathbf{F}} = \frac{3K}{J} J \mathbf{F}^{-\mathsf{T}} = 3K \mathbf{F}^{-\mathsf{T}}. \tag{A.33}$$

A.4 Summary

We may summarize the element-level residuals and tangents for the displacements $\mathbf{u}$, normalized concentration $\bar{c}$, normalized micromorphic concentration $\bar{\mathbb{c}}$, and stress potential μ_σ

degrees of freedom as

$$\mathbf{R}^A_{\mathbf{u}} = \int_{\mathcal{B}^e} \left(\mathbf{T}\mathrm{grad}N^A - N^A\mathbf{b}\right)\, dv - \int_{\mathcal{S}^e_t} N^A \breve{\mathbf{t}}\, da,$$

$$R^A_{\bar{c}} = \int_{B^e} \left(N^A \dot{\bar{c}} + \bar{m}\left(\nabla N^A \cdot \frac{\partial f}{\partial \bar{c}} \nabla \bar{c} - \nabla N^A \cdot \beta \nabla \bar{\mathfrak{c}} + \nabla N^A \cdot \nabla \mu_\sigma \right)\right) dv_{\mathrm{R}} + \int_{\mathcal{S}_j} N^A \breve{j}\, da_{\mathrm{R}}, \tag{A.34}$$

$$R^A_{\bar{\mathfrak{c}}} = \int_{\mathrm{B}^e} \left(N^A \beta(\bar{\mathfrak{c}} - \bar{c}) + \lambda \nabla N^A \cdot \nabla \bar{\mathfrak{c}}\right)\, dv_{\mathrm{R}} - \int_{\mathcal{S}^e_\xi} N^A \breve{\xi}\, da_{\mathrm{R}},$$

$$R^A_{\mu_\sigma} = \int_{\mathrm{B}^e} N^A \left(\mu_\sigma + \Omega \frac{1}{3}\mathrm{tr}\,\mathbf{M}^e\right)\, dv_{\mathrm{R}},$$

and

$$
\begin{aligned}
K^{AB}_{u_i u_k} &= -\int_{\mathrm{B}^e} \frac{\partial N^A}{\partial x_j}\mathbb{A}_{ijkl}\frac{\partial N^B}{\partial x_l}\,dv + \int_{\mathcal{S}^e_t} N^A N^B \frac{\partial \breve{t}_i}{\partial u_k}\,da,\\
K^{AB}_{u_i \bar{c}} &= -\int_{\mathrm{B}^e} N^B \frac{\partial T_{ij}}{\partial \bar{c}}\frac{\partial N^A}{\partial x_j}\,dv + \int_{\mathcal{S}^e_t} N^A N^B \frac{\partial \breve{t}_i}{\partial \bar{c}}.\,da,\\
K^{AB}_{\bar{c}\bar{c}} &= -\int_{\mathrm{B}^e} \left(N^A N^B \frac{\partial \dot{\bar{c}}}{\partial \bar{c}} + \frac{\partial \bar{m}}{\partial \bar{c}} N^B \left(\nabla N^A \cdot \frac{\partial f}{\partial \bar{c}}\nabla \bar{c} - \nabla N^A \cdot \beta \nabla \bar{\mathbb{c}} + \nabla N^A \cdot \nabla \mu_\sigma \right) \right.\\
&\qquad \left. + \bar{m} N^B \nabla N^A \cdot \frac{\partial^2 f}{\partial \bar{c}^2}\nabla \bar{c} + \bar{m}\nabla N^A \cdot \frac{\partial f}{\partial \bar{c}}\nabla N^B \right) dv_{\mathrm{R}} - \int_{\mathcal{S}^e_j} N^A N^B \frac{\partial \breve{j}}{\partial \bar{c}}\,da_{\mathrm{R}},\\
K^{AB}_{\bar{c}\bar{\mathbb{c}}} &= -\int_{\mathrm{B}^e} -\bar{m}\nabla N^A \cdot \beta \nabla N^B\,dv_{\mathrm{R}} - \int_{\mathcal{S}^e_j} N^A N^B \frac{\partial \breve{j}}{\partial \bar{\mathbb{c}}}\,da_{\mathrm{R}},\\
K^{AB}_{\bar{c}\mu_\sigma} &= -\int_{\mathrm{B}^e} \bar{m}\nabla N^A \cdot \nabla N^B\,dv_{\mathrm{R}} - \int_{\mathcal{S}^e_j} N^A N^B \frac{\partial \breve{j}}{\partial \mu_\sigma}\,da_{\mathrm{R}},\\
K^{AB}_{\bar{\mathbb{c}}\bar{\mathbb{c}}} &= -\int_{\mathrm{B}^e} \left(\beta N^A N^B + \lambda \nabla N^A \cdot \nabla N^B \right) dv_{\mathrm{R}} + \int_{\mathcal{S}^e_\xi} N^A N^B \frac{\partial \breve{\xi}}{\partial \bar{\mathbb{c}}}\,da_{\mathrm{R}},\\
K^{AB}_{\bar{\mathbb{c}}\bar{c}} &= -\int_{\mathrm{B}^e} -\beta N^A N^B\,dv_{\mathrm{R}} + \int_{\mathcal{S}^e_\xi} N^A N^B \frac{\partial \breve{\xi}}{\partial \bar{c}}\,da_{\mathrm{R}},\\
K^{AB}_{\mu_\sigma \mu_\sigma} &= -\int_{\mathrm{B}^e} N^A N^B\,dv_{\mathrm{R}},\\
K^{AB}_{\mu_\sigma \bar{c}} &= -\int_{\mathrm{B}^e} N^A N^B \Omega \frac{1}{3}\frac{\partial \mathrm{tr}\,\mathbf{M}^e}{\partial \bar{c}}\,dv_{\mathrm{R}},\\
K^{AB}_{\mu_\sigma u_i} &= -\int_{\mathrm{B}^e} N^A \Omega \frac{1}{3}\frac{\partial \mathrm{tr}\,\mathbf{M}^e}{F_{ik}}\frac{\partial N^B}{\partial X_k}\,dv_{\mathrm{R}},
\end{aligned}
\tag{A.35}
$$

with

$$
\begin{aligned}
&\bar{m} = \frac{D_0}{R\vartheta}\bar{c}(1-\bar{c}),\\
&\frac{\partial \bar{m}}{\partial \bar{c}} = \frac{D_0}{R\vartheta}(1-2\bar{c}),\\
&\frac{\partial f}{\partial \bar{c}} = \frac{R\vartheta}{\bar{c}(1-\bar{c})} - 2\chi + \beta,\\
&\frac{\partial^2 f}{\partial \bar{c}^2} = \frac{R\vartheta(2\bar{c}-1)}{\bar{c}^2(1-\bar{c})^2},\\
&\mathbb{A} \approx \mathbb{C} = 2G\mathbb{I} + \left(K - \frac{2}{3}G\right)\mathbf{1}\otimes\mathbf{1},\\
&\frac{\partial \mathbf{T}}{\partial \bar{c}} \approx \frac{\partial \mathbf{M}^e}{\partial \bar{c}} = -\frac{K\Omega c_{\mathrm{R,max}}}{J^c}\mathbf{1},\\
&\frac{\partial \mathrm{tr}\,\mathbf{M}^e}{\partial \bar{c}} = -\frac{3K\Omega c_{\mathrm{R,max}}}{J^c},\\
&\frac{\partial \mathrm{tr}\,\mathbf{M}^e}{\partial \mathbf{F}} = 3K\mathbf{F}^{-\top}.
\end{aligned}
\tag{A.36}
$$

Appendix B

Split methods for solving the Cahn-Hilliard equation

As mentioned in Chapter 2, the Cahn-Hilliard equation for the diffusion of a species involves solving a partial differential equation (pde) which contains fourth-order spatial derivatives. From a practical engineering application, the use of the finite-element method to solve such equations is often preferable since it allows for modeling in arbitrary geometries. However, if solved using the finite-element procedure, such fourth-order equations necessitate basis functions which are piecewise smooth and globally C^1-continuos. In order to use standard C^0-continuos finite-elements, one often employs a split method formulation to reduce the fourth-order equation into two second-order partial differential equations. In reducing the fourth-order equation of interest into two second-order equations, two distinct split method formulations may be used:

- The first method involves introducing an additional pde which governs an internal variable of the model, usually one whose gradients are necessary for computation of the original equation. As we shall see in Sect. B.1, when the two second-order pdes in this method are combined they recover the classical Cahn-Hilliard equation. We thus refer to this method as the **classical formulation**.

- The second method, involves the introduction of an additional variable, not present in the original model, to serve as an additional kinematical degree of freedom (DOF) on which to formulate the split method. We refer to this method as the **micromorphic formulation** since we will refer to the additional variable as the micromorphic variable.

The classical formulation has the clear advantage that it does not introduce any additional variables or material/simulation properties. However, in some applications the classical formulation can lead to stiff and numerically difficult to solve equations. Thus, in certain cases, it may then be useful and numerically convenient to use the micromorphic formulation to

reformulate the fourth-order equation as two coupled second-order pdes. However, the micromorphic formulation does not directly solve the physical problem of interest, and introduces an additional parameter which must be appropriately determined.

The Cahn-Hilliard equation is ideal for studying the aforementioned split method formulations since it is amenable to being formulated with both classical and micromorphic split methods and has been studied extensively in the literature. Wodo and Ganapathysubramanian (2011) and Gomez and Hughes (2011) both solve the Cahn-Hilliard equation using a classical split method formulation approach with a focus on new and novel time-stepping algorithms. Gomez et al. (2008) solve the fourth-order Cahn-Hilliard equation using the novel and non-standard isogeometric analysis which, although it does not require a split method, involves complicated numerics which are difficult to implement in commercially available FEA codes. Wells et al. (2006) solve the problem using a classical split method formulation as a reference for their development of a discontinuous Galerkin method. Ubachs et al. (2004), in the context of modeling the microstructural evolution of tin-lead solder, solve the Cahn-Hilliard equation using a micromorphic split method formulation similar to previous formulations of micromorphic theories (cf. e.g. Forest, 2009).

The Cahn-Hilliard theory for diffusion of a species within a body may be summarized by

$$\dot{\bar{c}} = \text{Div}\left(\hat{m}(\bar{c})\nabla\left(\frac{\partial\hat{\psi}^{\text{c}}(\bar{c})}{\partial\bar{c}} - \lambda\Delta\bar{c}\right)\right), \tag{B.1}$$

which is a nonlinear partial differential equation for the normalized concentration of the diffusing species $\bar{c} \in [0,1]$, and involves fourth-order derivatives of $\bar{c}$. In (B.1), $\hat{\psi}^{\text{c}}$ is the chemical free energy of mixing and the term $(-\lambda\Delta\bar{c})$ is the contribution of the the interfacial free energy to the chemical potential, with λ a gradient energy parameter and $\Delta\bar{c}$ the Laplacian of the normalized concentration. Further, $\hat{m}(\bar{c}) > 0$ is the mobility of the diffusing species.

In the **classical formulation** the fourth-order equation (B.1) is described by the following two second-order equations

$$\left.\begin{aligned} \dot{\bar{c}} &= \text{Div}\left(\hat{m}(\bar{c})\nabla\mu\right), \\ \mu &= \frac{\partial\hat{\psi}^{\text{c}}(\bar{c})}{\partial\bar{c}} - \lambda\Delta\bar{c}, \end{aligned}\right\} \quad \text{classical formulation} \tag{B.2}$$

where the two solution variables are the concentration $\bar{c}$ and the chemical potential μ.

In the **micromorphic formulation** an additional variable $\bar{\text{c}}$ is introduced, which we refer to as the *micromorphic variable*. Using a microforce balance, and suitable constitutive equations, we may show that formulating the diffusion theory with this additional kinematical degree of freedom yields a split method formulation with the following governing partial

differential equations

$$\left.\begin{aligned} \dot{\bar{c}} &= \mathrm{Div}\left(\hat{m}(\bar{c})\nabla\left(\frac{\partial\hat{\psi}^{\mathrm{c}}(\bar{c})}{\partial\bar{c}} + \beta(\bar{c}-\bar{\mathfrak{c}})\right)\right), \\ \lambda\Delta\bar{\mathfrak{c}} &+ \beta(\bar{c}-\bar{\mathfrak{c}}) = 0, \end{aligned}\right\} \quad \text{micromorphic formulation} \qquad \text{(B.3)}$$

where the additional second-order pde is a Hemholtz-type equation governing the micromorphic variable $\bar{\mathfrak{c}}$. We note that:

- The micromorphic formulation introduces an additional parameter, β, which we refer to as the **penalty modulus**.

As briefly introduced here, and further elaborated on in Sect. B.2, it is not immediately clear when the micromorphic formulation produces suitable results when compared to the classical formulation; specifically how the parameter $\bar{\beta}$ should be chosen. In Chapter 4 we performed a limited set of simulations aimed at illustrating how the micromorphic formulation of the Cahn-Hilliard equation should converge as the penalty modulus β is increased. However, no comparison was performed between the micromorphic (B.3) and classical (B.2) split methods for soliving the Cahn-Hilliard equation. Such a comparison, along with some theoretical details for completeness, is presented in this Appendix.

The purpose of this Appendix is thus as follows:

- First, we derive the classical split method formulations (B.2) in a thermodynamically consistent fashion by using the principle of virtual power. Unlike derivations based on the variational derivative, the formulation shown here clearly distinguishes between balance laws and constitutive equations. Further, from the formulation it is clear what the appropriate boundary conditions for the resulting pdes are.

- Second, we investigate through numerical simulations the two different split method formulations aimed at solving the Cahn-Hilliard equation using finite-elements. Specifically, we show that the micromorphic formulation converges to the classical formulation for appropriately chosen simulation parameters.

- Finally, we present in detail the numerical procedures used to implement the aforementioned split methods in the commercial FEA package Abaqus (2010).

Finally, we remark that in this Appendix we consider *only the diffusion problem* and do not account for the deformation of the body. Hence, we do not distinguish between spatial and referential quantities (i.e. vectors, operators, etc.), and all quantities should be considered to be defined with respect to the reference body.

B.1 Cahn-Hilliard diffusion theory derived using the principle of virtual power

In contrast to a standard derivation of the Cahn-Hilliard equation based on a variational derivative of the total energy, see eqs. (2.1) through (2.7), following Gurtin (1996) and Anand (2012), this derivation is based on using the principle of virtual power. The derivation is similar to that presented in Chapter 3, however here we do not introduce an additional kinematical variable. Further, here we will consider only diffusion of a species, without any consideration for mechanical deformation.

B.1.1 Mass balance

With $\bar{c}(\mathbf{X}, t) \in [0, 1]$ denoting a normalized concentration, the local mass balance law for the concentration is given by (cf. Sect. 3.1)

$$\dot{\bar{c}} = -\mathrm{Div}(\mathbf{j}), \tag{B.4}$$

where $\mathbf{j}$ is the species flux.

B.1.2 Microforce balance derived via the principle of virtual power

Consider a part P of the body B within which the species is diffusing. The virtual power principle is based on a fundamental power balance between the *internal power* $\mathcal{W}_{\mathrm{int}}(\mathrm{P})$ expended within the part P, and the *external power* $\mathcal{W}_{\mathrm{ext}}(\mathrm{P})$ expended on P. Specifically, we allow for power expended internally by

(i) a scalar microscopic force π power-conjugate to $\dot{\bar{c}}$;

(ii) a vector microscopic force $\boldsymbol{\xi}$ power-conjugate to the gradient $\nabla\dot{\bar{c}}$;

and take $\mathcal{W}_{\mathrm{int}}(\mathrm{P})$ to be given by

$$\mathcal{W}_{\mathrm{int}}(\mathrm{P}) = \int_{\mathrm{P}} \left(\pi\dot{\bar{c}} + \boldsymbol{\xi}\cdot\nabla\dot{\bar{c}}\right) dV, \tag{B.5}$$

where π and $\boldsymbol{\xi}$ are defined over the body for all time. We also allow for power to be expended externally by

(i) a scalar microscopic traction ζ that expends power over $\dot{\bar{c}}$ on the boundary of the part;

and take $\mathcal{W}_{\mathrm{ext}}(\mathrm{P})$ to be given by

$$\mathcal{W}_{\mathrm{ext}}(\mathrm{P}) = \int_{\partial\mathrm{P}} \zeta\dot{\bar{c}}\, dA. \tag{B.6}$$

Assume that at some arbitrarily-chosen but fixed time, the field $\bar{c}$ is known, and consider $\dot{\tilde{c}}$ as a virtual velocity. Then, denoting the virtual field by $\tilde{c}$ to differentiate it from the field associated with the actual evolution of the body, we may use (B.5) and (B.6) to write the internal and external expenditures of virtual power as

$$\begin{aligned} \mathcal{W}_{\text{int}}(\mathrm{P}, \tilde{c}) &= \int_{\mathrm{P}} \left(\pi\tilde{c} + \boldsymbol{\xi} \cdot \nabla\tilde{c}\right) dV, \\ \mathcal{W}_{\text{ext}}(\mathrm{P}, \tilde{c}) &= \int_{\partial\mathrm{P}} \zeta\tilde{c}\, dA. \end{aligned} \tag{B.7}$$

The principle of virtual power then consist of the requirement that

$$\mathcal{W}_{\text{int}}(P, \tilde{c}) = \mathcal{W}_{\text{ext}}(P, \tilde{c}) \quad \text{for all virtual velocities } \tilde{c}. \tag{B.8}$$

which using (B.5) and (B.6) yields

$$\int_{\mathrm{P}} \left(\pi\tilde{c} + \boldsymbol{\xi} \cdot \nabla\tilde{c}\right) dV = \int_{\partial\mathrm{P}} \zeta\tilde{c}\, dA. \tag{B.9}$$

Next, using the identity $\mathrm{Div}\,(\mathbf{a}\alpha) = \mathrm{Div}\,(\mathbf{a})\alpha + \mathbf{a} \cdot \nabla\alpha$ and the divergence theorem, we may write (B.9) as

$$\int_{\partial\mathrm{P}} \left(\zeta - \boldsymbol{\xi} \cdot \mathbf{n}\right)\tilde{c}\, dA - \int_{P} \left(\pi - \mathrm{Div}\,(\boldsymbol{\xi})\right)\tilde{c}\, dV = 0, \tag{B.10}$$

where $\mathbf{n}$ is the outward unit normal on the boundary $\partial\mathrm{P}$. Since this relation must hold for all P and for all $\tilde{c}$, standard variational arguments yield the traction condition

$$\zeta(\mathbf{n}) = \boldsymbol{\xi} \cdot \mathbf{n}, \tag{B.11}$$

and the microforce balance

$$\pi - \mathrm{Div}\boldsymbol{\xi} = 0. \tag{B.12}$$

B.1.3 Free energy imbalance

Let ψ denote the Helmholtz free energy per unit volume, and consider a material region P. Then, under *isothermal conditions*, the first and second laws of thermodynamics may be combined to form the *free energy imbalance* as

$$\dot{\int_{P}} \psi\, dV \leq \mathcal{W}_{\text{ext}}(P) - \int_{\partial\mathrm{P}} \mu\mathbf{j} \cdot \mathbf{n}\, dA, \tag{B.13}$$

where μ represents the chemical potential of the diffusing species, and $\mathbf{j}$ is the species flux. Thus, since $\mathcal{W}_{\text{ext}}(\mathrm{P}) = \mathcal{W}_{\text{int}}(\mathrm{P})$, recalling (B.5) and applying the divergence theorem to the term involving an integral over the boundary $\partial\mathrm{P}$ of P, we may write the free energy imbalance

(B.13) as

$$\int_P \left(\dot{\psi} - \pi\dot{\bar{c}} - \boldsymbol{\xi}\cdot\nabla\dot{\bar{c}} + \mu\mathrm{Div}(\mathbf{j}) + \mathbf{j}\cdot\nabla\mu\right) dV \leq 0. \tag{B.14}$$

Finally, using mass balance (B.4), and the fact that (B.14) must hold for all parts P, the local form of the free energy imbalance is

$$\dot{\psi} - \pi_{\mathrm{net}}\dot{\bar{c}} - \boldsymbol{\xi}\cdot\nabla\dot{\bar{c}} + \mathbf{j}\cdot\nabla\mu \leq 0, \tag{B.15}$$

where we have defined

$$\pi_{\mathrm{net}} \stackrel{\mathrm{def}}{=} \mu + \pi \tag{B.16}$$

for a net microforce. Finally, for later use, using (B.6) and (B.11) we may also write the free-energy imbalance (B.13) as

$$\overline{\int_P \psi\, dV} \leq \int_{\partial\mathrm{P}} \dot{\bar{c}}\,(\boldsymbol{\xi}\cdot\mathbf{n})\, dA - \int_{\partial\mathrm{P}} \mu\,(\mathbf{j}\cdot\mathbf{n})\, dA. \tag{B.17}$$

B.1.4 Constitutive theory

Guided by the free energy imbalance (B.15) we consider energetic constitutive equations for the free energy ψ, the net microforce π_{net}, and the vector microforce $\boldsymbol{\xi}$ of the form

$$\begin{aligned} \psi &= \hat{\psi}(\bar{c}, \nabla\bar{c}), \\ \pi_{\mathrm{net}} &= \hat{\pi}_{\mathrm{net}}(\bar{c}, \nabla\bar{c}), \\ \boldsymbol{\xi} &= \hat{\boldsymbol{\xi}}(\bar{c}, \nabla\bar{c}). \end{aligned} \tag{B.18}$$

Substituting the constitutive equation $(\mathrm{B.18})_1$ into the free energy imbalance (B.15), we find that it may be written as

$$\left(\frac{\partial\hat{\psi}}{\partial\bar{c}} - \pi_{\mathrm{net}}\right)\dot{\bar{c}} + \left(\frac{\partial\hat{\psi}}{\partial\nabla\bar{c}} - \boldsymbol{\xi}\right)\cdot\nabla\dot{\bar{c}} + \mathbf{j}\cdot\nabla\mu \leq 0. \tag{B.19}$$

This inequality must hold for all values of $\bar{c}$ and $\nabla\bar{c}$. Since $\dot{\bar{c}}$ and $\nabla\dot{\bar{c}}$ appear linearly, their "coefficients" must vanish, for otherwise they may be chosen to violate (B.19). We are therefor led to the thermodynamic restriction that the free energy determine the net microforce π_{net}, and the vector microscopic force $\boldsymbol{\xi}$ through the "state relations"

$$\left.\begin{aligned} \pi_{\mathrm{net}} &= \frac{\partial\hat{\psi}(\bar{c}, \nabla\bar{c})}{\partial\bar{c}}, \\ \boldsymbol{\xi} &= \frac{\partial\hat{\psi}(\bar{c}, \nabla\bar{c})}{\partial\nabla\bar{c}}, \end{aligned}\right\} \tag{B.20}$$

and we are left with the following dissipation inequality

$$\mathcal{D} = -\mathbf{j} \cdot \nabla\mu \geq 0. \tag{B.21}$$

Based on the dissipation inequality (B.21), the flux is constitutively prescribed to obey

$$\mathbf{j} = -\hat{m}(\bar{c})\nabla\mu, \tag{B.22}$$

and the dissipation inequality is given as

$$\mathcal{D} = \hat{m}(\bar{c})|\nabla\mu| \geq 0, \tag{B.23}$$

which imposes the restriction that the mobility $\hat{m}(\bar{c}) \geq 0$.

Then, using (B.20) and (B.16) in the microforce balance (B.12), we arrive at the following partial differential equation for the chemical potential

$$\mu = \frac{\partial\psi}{\partial\bar{c}} - \text{Div}\left(\frac{\partial\psi}{\partial\nabla\bar{c}}\right). \tag{B.24}$$

Finally, recalling mass balance (B.4), using (B.22), and the governing pde for the chemical potential (B.24) we may, without specifying the specific form of the free energy ψ, summarize the gradient diffusion theory through the equations

$$\left.\begin{aligned} \dot{\bar{c}} &= \text{Div}\left(\hat{m}(\bar{c})\nabla\left(\mu\right)\right), \\ \mu &= \frac{\partial\hat{\psi}(\bar{c},\nabla\bar{c})}{\partial\bar{c}} - \text{Div}\left(\frac{\partial\hat{\psi}(\bar{c},\nabla\bar{c})}{\partial\nabla\bar{c}}\right), \end{aligned}\right\} \tag{B.25}$$

and to complete the theory we are left only with specifying the form of the free energy function $\hat{\psi}(\bar{c},\nabla\bar{c})$, and the form of the concentration dependent mobility $\hat{m}(\bar{c})$.

B.1.5 Boundary Conditions

Eqs. (B.25) must also be accompanied by appropriate boundary and initial conditions. The boundary conditions are based on the external mechanisms which may result in changes to the free-energy. Recall the free-energy imbalance, viz. (B.17)

$$\dot{\int_P \psi\, dV} \leq \int_{\partial\text{P}} \dot{\bar{c}}\,(\boldsymbol{\xi}\cdot\mathbf{n})\, dA - \int_{\partial\text{P}} \mu\,(\mathbf{j}\cdot\mathbf{n})\, dA, \tag{B.26}$$

then, based on this imbalance, we define the following boundary conditions for a time interval $t \in [0,T]$:

- With $\mathcal{S}_{\bar{c}}$ and $\mathcal{S}_j$ denoting complementary subsurfaces of the boundary ∂B of the body B, we consider first a pair of boundary conditions in which the normalized species

concentration is specified on $\mathcal{S}_{\bar{c}}$ and the species flux on $\mathcal{S}_j$:

$$\left.\begin{aligned} \bar{c} &= \breve{\bar{c}} \quad \text{on} \quad \mathcal{S}_{\bar{c}} \times [0,T], \\ \mathbf{j}\cdot\mathbf{n} = -\hat{m}(\bar{c})\nabla\mu\cdot\mathbf{n} &= \breve{j} \quad \text{on} \quad \mathcal{S}_j \times [0,T]. \end{aligned}\right\} \tag{B.27}$$

- With $\mathcal{S}_\mu$ and $\mathcal{S}_\zeta$ denoting complementary subsurfaces of the boundary ∂B of the body B, we consider a pair of boundary conditions in which the chemical potential is specified on $\mathcal{S}_\mu$ and the scalar microscopic traction is specified on $\mathcal{S}_\zeta$:

$$\left.\begin{aligned} \mu &= \breve{\mu} \quad \text{on} \quad \mathcal{S}_\mu \times [0,T], \\ \boldsymbol{\xi}\cdot\mathbf{n} = \frac{\partial\hat{\psi}}{\partial\nabla\bar{c}}\cdot\mathbf{n} &= \breve{\zeta} \quad \text{on} \quad \mathcal{S}_\zeta \times [0,T], \end{aligned}\right\} \tag{B.28}$$

where in writing $(\text{B.28})_2$ we have used the state relation $(\text{B.20})_2$. Note that the specified quantities $\breve{j}$ and $\breve{\zeta}$ may be functions of time as well as functions of the variables $\bar{c}$ and μ at the point where the boundary condition is specified.

Finally, the initial conditions are taken as

$$\bar{c}(\mathbf{X},0) = \bar{c}_0(\mathbf{X}), \quad \text{and} \quad \mu(\mathbf{X},0) = \mu_0(\mathbf{X}), \quad \text{in} \quad \text{B}. \tag{B.29}$$

Together, the coupled set of equations (B.25), with boundary conditions (B.27) and (B.28), and initial conditions (B.29), yield a boundary-value problem for the normalized concentration $\bar{c}(\mathbf{X},t)$ and the chemical potential $\mu(\mathbf{X},t)$, and form the basis of the classical formulation split method discussed in this work.

Remark. In writing (B.27) and (B.28) we made an implicit assumption that mass balance $(\text{B.25})_1$ will be the pde governing the normalized concentration $\bar{c}$ dof, hence allowing us to prescribe $(\text{B.27})_1$, and that the microforce balance $(\text{B.25})_2$ will be the pde governing the chemical potential μ dof, allowing us to prescribe $(\text{B.28})_1$. This choice is reflected in Section B.7, where we detail our numerical methodology.

This choice is not unique. In fact, the first term on the right-hand-side of (B.26) suggests that $\bar{c}$ and $\boldsymbol{\xi}\cdot\mathbf{n}$ should be conjugate, while the second term suggests that μ and $\mathbf{j}\cdot\mathbf{n}$ should be conjugate. This could easily be achieved by choosing mass balance $(\text{B.25})_1$ as the governing pde for the chemical potential μ dof, and choosing the microforce balance $(\text{B.25})_2$ as the governing pde for the normalized concentration $\bar{c}$ dof. In such an implementation, the boundary conditions would be as follows

$$\left.\begin{aligned} \mu &= \breve{\mu} \quad \text{on} \quad \mathcal{S}_\mu \times [0,T], \\ \mathbf{j}\cdot\mathbf{n} = -\hat{m}(\bar{c})\nabla\mu\cdot\mathbf{n} &= \breve{j} \quad \text{on} \quad \mathcal{S}_j \times [0,T]. \end{aligned}\right\} \tag{B.30}$$

and

$$\left.\begin{aligned} \bar{c} &= \breve{\bar{c}} \quad \text{on} \quad \mathcal{S}_{\bar{c}} \times [0,T], \\ \boldsymbol{\xi}\cdot\mathbf{n} = \frac{\partial\hat{\psi}}{\partial\nabla\bar{c}}\cdot\mathbf{n} &= \breve{\zeta} \quad \text{on} \quad \mathcal{S}_{\zeta} \times [0,T], \end{aligned}\right\} \tag{B.31}$$

where $\mathcal{S}_{\mu} \cup \mathcal{S}_{\mathrm{j}} = \partial\mathrm{B}$, $\mathcal{S}_{\mu} \cap \mathcal{S}_{\mathrm{j}} = \emptyset$, $\mathcal{S}_{\bar{c}} \cup \mathcal{S}_{\zeta} = \partial\mathrm{B}$, and $\mathcal{S}_{\bar{c}} \cap \mathcal{S}_{\zeta} = \emptyset$.

In the numerical results presented in this appendix, we will only consider periodic boundary conditions which are implemented as constrains on the concentration $\bar{c}$ and the chemical potential μ, and hence either of the two aforementiond implementation choices is equivalent.

However, from a physical point of view, based on (B.26), the second choice, whereby mass balance $(\mathrm{B}.25)_1$ is the pde governing the chemical potential μ dof, and the microforce balance $(\mathrm{B}.25)_2$ is the pde governing the normalized concentration $\bar{c}$ dof, is more appealing. □

B.2 Micromorphic Cahn-Hilliard diffusion theory derived using the principle of virtual power

In addition to the classical split method formulation developed in Sect. B.1, one may use a similar procedure, to derive another set of two coupled second-order PDEs describing the Cahn-Hilliard equation. In this formulation however we introduce an additional variable, which we define through the symbol $\bar{\mathbb{c}}$ and refer to as the **micromorphic concentration**. The variable $\bar{\mathbb{c}}$ serves as an additional kinematical degree of freedom in developing a gradient theory for species diffusion. Specifically, in contrast to the a formulation based on $\bar{c}$ and $\nabla\bar{c}$, see Sect. B.1, this formulations is based on $\bar{c}$, $\bar{\mathbb{c}}$, and the gradient $\nabla\bar{\mathbb{c}}$.

Since the theoretical derivation using the additional variable $\bar{\mathbb{c}}$ has been developed in Chapter 3 in the context of a coupled diffusion-deformation framework, and since it is similar to the derivation detailed in Sect. B.1, we present here only a summary of the resulting pdes and their boundary and initial conditions.

A diffusion theory based on the additional kinematical variable $\bar{\mathbb{c}}$, and derived using the principle of virtual power, yields the following two coupled second-order differential equations:

$$\left.\begin{aligned} \dot{\bar{c}} &= \mathrm{Div}\left(\hat{m}(\bar{c})\nabla\mu\right), \quad \mu = \frac{\partial\hat{\psi}(\bar{c},\bar{\mathbb{c}},\nabla\bar{\mathbb{c}})}{\partial\bar{c}}, \\ 0 &= \frac{\partial\hat{\psi}(\bar{c},\bar{\mathbb{c}},\nabla\bar{\mathbb{c}})}{\partial\bar{\mathbb{c}}} - \mathrm{Div}\left(\frac{\partial\hat{\psi}(\bar{c},\bar{\mathbb{c}},\nabla\bar{\mathbb{c}})}{\partial\nabla\bar{\mathbb{c}}}\right), \end{aligned}\right\} \tag{B.32}$$

where we note that that the free energy $\hat{\psi}(\bar{c},\bar{\mathbb{c}},\nabla\bar{c})$ is now a function of the concentration $\bar{c}$, the micromorphic concentration $\bar{\mathbb{c}}$ and the gradient of the micromorphic concentration $\nabla\bar{\mathbb{c}}$. The additional pde $(\mathrm{B}.32)_2$ is a hemholtz-type equation governing the micromorphic variable $\bar{\mathbb{c}}$.

For the mass balance pde $(B.32)_1$, we have the boundary conditions

$$\left.\begin{aligned} \bar{c} &= \breve{\bar{c}} \quad \text{on} \quad \mathcal{S}_{\bar{c}} \times [0,T], \\ -m\nabla\mu \cdot \mathbf{n} &= \breve{j} \quad \text{on} \quad \mathcal{S}_{\mathrm{j}} \times [0,T], \end{aligned}\right\} \tag{B.33}$$

and for the microforce balance pde $(B.32)_2$ we have the boundary conditions

$$\left.\begin{aligned} \bar{\mathbb{c}} &= \breve{\bar{\mathbb{c}}} \quad \text{on} \quad \mathcal{S}_{\bar{\mathbb{c}}} \times [0,T], \\ \frac{\partial\psi}{\partial\nabla\bar{\mathbb{c}}} \cdot \mathbf{n} &= \breve{\zeta} \quad \text{on} \quad \mathcal{S}_{\zeta} \times [0,T]. \end{aligned}\right\} \tag{B.34}$$

In (B.33) $\mathcal{S}_{\bar{c}}$ and $\mathcal{S}_{\mathrm{j}}$ are complementary subsurfaces of the boundary ∂B of the body B, while similarly in (B.34) $\mathcal{S}_{\bar{\mathbb{c}}}$ and $\mathcal{S}_{\zeta}$ are complementary subsurfaces of the boundary ∂B of the body B. Finally, the initial conditions are taken as

$$\bar{c}(\mathbf{X},0) = \bar{c}_0(\mathbf{X}), \quad \text{and} \quad \bar{\mathbb{c}}(\mathbf{X},0) = \bar{\mathbb{c}}_0(\mathbf{X}), \quad \text{in} \quad \mathrm{B}. \tag{B.35}$$

Together, the coupled set of equations (B.32), with boundary conditions (B.33), (B.34), and initial conditions (B.35), yield a boundary-value problem for the normalized concentration $\bar{c}$ and the micromorphic variable $\bar{\mathbb{c}}$, and form the basis of the micromorphic formulation split method discussed in this work.

We must now specify the free energy functions required to complete the diffusion theories derived in Sects. B.1 and B.2. Recall that the free energy function in the classical diffusion theory depends on $\bar{c}$ and its gradient $\nabla\bar{c}$ while the free energy function in the micromorphic diffusion theory depends on $\bar{c}$, $\bar{\mathbb{c}}$ and the gradient $\nabla\bar{\mathbb{c}}$.

B.2.1 Free energy for the classical formulation

In the classical diffusion theory we employ the standard free energy proposed by Cahn and Hilliard. The free energy is of the form

$$\hat{\psi}(\bar{c},\nabla\bar{c}) = \hat{\psi}^{\text{chemical}}(\bar{c}) + \hat{\psi}^{\text{interface}}(\nabla\bar{c}). \tag{B.36}$$

Here

(i) ψ^{chemical} is the free energy of mixing for the species in the body (also known as the coarse-grain or configurational energy), and it is taken to be given by

$$\psi^{\text{chemical}} = \mu^0\bar{c} + R\vartheta\Big(\bar{c}\ln\bar{c} + (1-\bar{c})\ln(1-\bar{c})\Big) + \chi\bar{c}(1-\bar{c}), \tag{B.37}$$

which represents a regular solid solution model. The second term in (B.37), involving the gas constant R and the absolute temperature ϑ, represent the entropy of mixing; while the last term in (B.37), involving χ, is an energetic interaction between the

diffusing species and the host material which accounts for the mixing being non-ideal. For a two-phase material, as is of interest in this work, the free energy ψ^{chemical} is a double-well potential whose wells (known as the "binodal points") define the two phases of the material.

(ii) $\psi^{\text{interface}}$ is an interfacial free energy which depends on the gradient of the concentration $\nabla\bar{c}$. It is taken to be given by

$$\psi^{\text{interface}} = (1/2)\lambda|\nabla\bar{c}|^2, \tag{B.38}$$

with $\lambda > 0$ a gradient energy coefficient.

Thus, using (B.37) and (B.38) in (B.36), the total free energy in the classical formulation is given by

$$\psi = \mu^0\bar{c} + R\vartheta\Big(\bar{c}\ln\bar{c} + (1-\bar{c})\ln(1-\bar{c})\Big) + \chi\bar{c}(1-\bar{c}) + (1/2)\lambda|\nabla\bar{c}|^2. \tag{B.39}$$

Finally, for a regular solid solution model as described through (B.37), the appropriate mobility is given by

$$m = m_0\bar{c}(1-\bar{c}), \quad m_0 = \frac{D_0}{R\vartheta} > 0, \tag{B.40}$$

which represents the physical requirement that the mobility vanish for the pure phases $\bar{c} = 0$ and $\bar{c} = 1$.

Using the free energy (B.39) and the mobility (B.40) in (B.25), we have the following specialized governing pdes for the classical formulation

$$\left.\begin{aligned} \dot{\bar{c}} &= \text{Div}\,(m_0\bar{c}(1-\bar{c})\nabla\mu)\,, \\ \mu &= \mu^0 + R\vartheta\ln\left(\frac{\bar{c}}{1-\bar{c}}\right) + \chi(1-2\bar{c}) - \lambda\Delta\bar{c}, \end{aligned}\right\} \quad \begin{array}{c}\text{classical}\\ \text{split formulation.}\end{array} \tag{B.41}$$

Further, using (B.39) in (B.27) and (B.28), the boundary conditions are

$$\left.\begin{aligned} \bar{c} &= \breve{\bar{c}} \quad \text{on} \quad \mathcal{S}_{\bar{c}} \times [0,T], \\ -m\nabla\mu\cdot\mathbf{n} &= \breve{j} \quad \text{on} \quad \mathcal{S}_{\text{j}} \times [0,T], \\ \mu &= \breve{\mu} \quad \text{on} \quad \mathcal{S}_{\mu} \times [0,T], \\ \lambda\nabla\bar{c}\cdot\mathbf{n} &= \breve{\zeta} \quad \text{on} \quad \mathcal{S}_{\zeta} \times [0,T], \end{aligned}\right\} \quad \text{with} \quad \begin{array}{l} \mathcal{S}_{\bar{c}} \cup \mathcal{S}_{\text{j}} = \partial\text{B}, \quad \mathcal{S}_{\bar{c}} \cap \mathcal{S}_{\text{j}} = \emptyset, \\ \mathcal{S}_{\mu} \cup \mathcal{S}_{\zeta} = \partial\text{B}, \quad \mathcal{S}_{\mu} \cap \mathcal{S}_{\zeta} = \emptyset. \end{array} \tag{B.42}$$

B.2.2 Free energy for the micromorphic diffusion theory

In the micromorphic diffusion theory we consider a separable free energy of the form

$$\hat{\psi}(\bar{c}, \bar{\mathbb{c}}, \nabla\bar{\mathbb{c}}) = \hat{\psi}^{\text{chemical}}(\bar{c}) + \hat{\psi}^{\text{penalty}}(\bar{c}, \bar{\mathbb{c}}) + \hat{\psi}^{\text{interface}}(\nabla\bar{\mathbb{c}}). \tag{B.43}$$

Here

(i) ψ^{chemical} is the free energy of mixing and is identical to that used in the classical formulation (B.37), viz.

$$\psi^{\text{chemical}} = \mu^0 \bar{c} + R\vartheta\Big(\bar{c}\ln\bar{c} + (1-\bar{c})\ln(1-\bar{c})\Big) + \chi\bar{c}(1-\bar{c}). \tag{B.44}$$

(ii) ψ^{penalty} accounts for an energetic penalty incurred by the micromorphic variable $\bar{\mathfrak{c}}$ being different from the concentration field $\bar{c}$. We take this energetic penalty to be given by the following simple quadratic form

$$\psi^{\text{penalty}} = (1/2)\beta(\bar{c}-\bar{\mathfrak{c}})^2, \tag{B.45}$$

with $\beta > 0$ a penalty modulus.

(iii) $\psi^{\text{interface}}$ is an interfacial free energy, similar to (B.38) in the classical formulation, however here taken to depend on the gradient of the micromorphic concentration $\nabla\bar{\mathfrak{c}}$. It is thus taken to be given by

$$\psi^{\text{interface}} = (1/2)\lambda|\nabla\bar{\mathfrak{c}}|^2, \tag{B.46}$$

with $\lambda > 0$ a gradient energy coefficient.

Thus, using (B.44), (B.45), and (B.46) in (B.43), the total free energy in the micromorphic-formulation is given by

$$\psi = \mu^0\bar{c} + R\vartheta\Big(\bar{c}\ln\bar{c} + (1-\bar{c})\ln(1-\bar{c})\Big) + \chi\bar{c}(1-\bar{c}) + (1/2)\beta(\bar{c}-\bar{\mathfrak{c}})^2 + (1/2)\lambda|\nabla\bar{\mathfrak{c}}|^2. \tag{B.47}$$

Finally, the mobility in the micromorphic formulation is identical to that used for the classical formulation (B.40) since the chemical free energies of the two formulations are also the same.

Using the free energy (B.47) and the mobility (B.40) in (B.32), we have the following specialized governing pdes for the micromorphic diffusion theory

$$\left.\begin{aligned} &\dot{\bar{c}} = \text{Div}\,(m_0\bar{c}(1-\bar{c})\nabla\mu)\,,\ \mu = \mu^0 + R\vartheta\left(\frac{\bar{c}}{1-\bar{c}}\right) + \chi(1-2\bar{c}) + \beta(\bar{c}-\bar{\mathfrak{c}}),\\ &0 = \lambda\Delta\bar{\mathfrak{c}} + \beta(\bar{c}-\bar{\mathfrak{c}}). \end{aligned}\right\} \begin{array}{c}\text{micromorphic}\\ \text{split}\\ \text{formulation}\end{array} \tag{B.48}$$

Using (B.47) in (B.33) and (B.34), the boundary conditions are

$$\left.\begin{aligned} \bar{c} &= \breve{\bar{c}} \quad \text{on} \quad \mathcal{S}_{\bar{c}} \times [0,T], \\ -m\nabla\mu \cdot \mathbf{n} &= \breve{j} \quad \text{on} \quad \mathcal{S}_{\mathrm{j}} \times [0,T], \\ \bar{\mathfrak{c}} &= \breve{\bar{\mathfrak{c}}} \quad \text{on} \quad \mathcal{S}_{\bar{\mathfrak{c}}} \times [0,T], \\ \lambda\nabla\bar{\mathfrak{c}} \cdot \mathbf{n} &= \breve{\zeta} \quad \text{on} \quad \mathcal{S}_{\zeta} \times [0,T], \end{aligned}\right\} \quad \text{with} \quad \begin{aligned} \mathcal{S}_{\bar{c}} \cup \mathcal{S}_{\mathrm{j}} &= \partial\mathrm{B}, \quad \mathcal{S}_{\bar{c}} \cap \mathcal{S}_{\mathrm{j}} = \emptyset, \\ \mathcal{S}_{\bar{\mathfrak{c}}} \cup \mathcal{S}_{\zeta} &= \partial\mathrm{B}, \quad \mathcal{S}_{\bar{\mathfrak{c}}} \cap \mathcal{S}_{\zeta} = \emptyset. \end{aligned} \tag{B.49}$$

Remark. The free energy used in the micromorphic diffusion theory (B.47), is similar to the classical free energy proposed by Cahn and Hilliard used in the classical formulation (B.39), however there are two important differences:

- First, the interfacial energy in the micromorphic theory depends on the gradient of the micromorphic concentration $\nabla\bar{\mathfrak{c}}$ and not on the gradient of the concentration $\nabla\bar{c}$.
- Second, the micromorphic theory includes a penalty free energy ψ^{penalty} (B.45), which effectively enforces that the micromorphic $\bar{\mathfrak{c}}$ mimic the behavior of the real concentration $\bar{c}$.

It is this penalty energy which introduces an additional parameter into the model, the penalty modulus β. It is clear from (B.47) that larger values of β will result in a greater energetic penalty being paid for by $\bar{\mathfrak{c}}$ being different from $\bar{c}$. Thus, one aim of this work is determining what an appropriate value of the penalty modulus β is such that we obtain solutions using the micromorphic formulation which are in some sense close to those obtained with the classical formulation which does not have any additional parameters. □

B.3 Summary of the theoretical framework

The two formulations presented in Sects. B.1 and B.32, and specialized in B.2 may be succinctly summarized as follows:

$$
\left.\begin{array}{ll}
\text{free energy} & \left\{\begin{array}{l}
\hat{\psi}(\bar{c},\nabla\bar{c}) = \hat{\psi}^{\text{chem}}(\bar{c}) + \hat{\psi}^{\text{inter}}(\nabla\bar{c}),\\
\psi^{\text{chem}} = \mu^0\bar{c} + R\vartheta\Big(\bar{c}\ln\bar{c} + (1-\bar{c})\ln(1-\bar{c})\Big) + \chi\bar{c}(1-\bar{c}),\\
\psi^{\text{inter}} = (1/2)\lambda|\nabla\bar{c}|^2, \quad \lambda > 0,
\end{array}\right.\\
\text{governing equations} & \left\{\begin{array}{l}
\dot{\bar{c}} = \text{Div}\,(m_0\bar{c}(1-\bar{c})\nabla\mu)\,,\\
\mu = \mu^0 + R\vartheta\ln\left(\dfrac{\bar{c}}{1-\bar{c}}\right) + \chi(1-2\bar{c}) - \lambda\Delta\bar{c},
\end{array}\right.\\
\text{boundary conditions} & \left\{\begin{array}{rcll}
\bar{c} = \breve{\bar{c}} & \text{on} & \mathcal{S}_{\bar{c}}\times[0,T], & \mathcal{S}_{\bar{c}}\cup\mathcal{S}_{\mathbf{j}} = \partial\mathrm{B},\\
-m\nabla\mu\cdot\mathbf{n} = \breve{j} & \text{on} & \mathcal{S}_{\mathbf{j}}\times[0,T], & \mathcal{S}_{\bar{c}}\cap\mathcal{S}_{\mathbf{j}} = \emptyset,\\
\mu = \breve{\mu} & \text{on} & \mathcal{S}_{\mu}\times[0,T], & \mathcal{S}_{\mu}\cup\mathcal{S}_{\zeta} = \partial\mathrm{B},\\
\lambda\nabla\bar{c}\cdot\mathbf{n} = \breve{\zeta} & \text{on} & \mathcal{S}_{\zeta}\times[0,T], & \mathcal{S}_{\mu}\cap\mathcal{S}_{\zeta} = \emptyset.
\end{array}\right.
\end{array}\right\}
\begin{array}{l}\text{classical}\\ \text{split}\\ \text{formulation}\end{array}
\tag{B.50}
$$

$$
\left.\begin{array}{ll}
\text{free energy} & \left\{\begin{array}{l}
\hat{\psi}(\bar{c},\bar{\mathfrak{c}},\nabla\bar{\mathfrak{c}}) = \hat{\psi}^{\text{chem}}(\bar{c}) + \hat{\psi}^{\text{pen}}(\bar{c},\bar{\mathfrak{c}}) + \hat{\psi}^{\text{inter}}(\nabla\bar{\mathfrak{c}}),\\
\psi^{\text{chem}} = \mu^0\bar{c} + R\vartheta(\bar{c}\ln\bar{c} + (1-\bar{c})\ln(1-\bar{c})) + \chi\bar{c}(1-\bar{c}),\\
\psi^{\text{pen}} = (1/2)\beta(\bar{c}-\bar{\mathfrak{c}})^2, \quad \beta > 0,\\
\psi^{\text{inter}} = (1/2)\lambda|\nabla\bar{\mathfrak{c}}|^2, \quad \lambda > 0,
\end{array}\right.\\
\text{governing equations} & \left\{\begin{array}{l}
\dot{\bar{c}} = \text{Div}\,(m_0\bar{c}(1-\bar{c})\nabla\mu)\,, \quad \mu = \mu^0 + R\vartheta\left(\dfrac{\bar{c}}{1-\bar{c}}\right) + \chi(1-2\bar{c}) + \beta(\bar{c}-\bar{\mathfrak{c}}),\\
0 = \lambda\Delta\bar{\mathfrak{c}} + \beta(\bar{c}-\bar{\mathfrak{c}}),
\end{array}\right.\\
\text{boundary conditions} & \left\{\begin{array}{rcll}
\bar{c} = \breve{\bar{c}} & \text{on} & \mathcal{S}_{\bar{c}}\times[0,T], & \mathcal{S}_{\bar{c}}\cup\mathcal{S}_{\mathbf{j}} = \partial\mathrm{B},\\
-m\nabla\mu\cdot\mathbf{n} = \breve{j} & \text{on} & \mathcal{S}_{\mathbf{j}}\times[0,T], & \mathcal{S}_{\bar{c}}\cap\mathcal{S}_{\mathbf{j}} = \emptyset,\\
\bar{\mathfrak{c}} = \breve{\bar{\mathfrak{c}}} & \text{on} & \mathcal{S}_{\bar{\mathfrak{c}}}\times[0,T], & \mathcal{S}_{\bar{\mathfrak{c}}}\cup\mathcal{S}_{\zeta} = \partial\mathrm{B},\\
\lambda\nabla\bar{\mathfrak{c}}\cdot\mathbf{n} = \breve{\zeta} & \text{on} & \mathcal{S}_{\zeta}\times[0,T], & \mathcal{S}_{\bar{\mathfrak{c}}}\cap\mathcal{S}_{\zeta} = \emptyset.
\end{array}\right.
\end{array}\right\}
\begin{array}{l}\text{micromorphic}\\ \text{split}\\ \text{formulation}\end{array}
\tag{B.51}
$$

B.4 Numerical implementation

The two theories summarized in Sect. B.3, have been numerically implemented in the commercially available implicit finite element program Abaqus (2010) through the writing of a set of user element subroutines (UEL). For each of the two theories, we have developed two different elements: (i) a 2D 4-node linear isoparametric quadrilateral which we refer to as U2D4; and (ii) a 3D 8-node linear isoparametric brick which we refer to as U3D8.

In the case of the classical split formulation, the degrees of freedom for these elements are the normalized concentration $\bar{c}$ and the chemical potential μ. In the case of the micromorphic split formulation, the degrees of freedom for these elements are the normalized concentration $\bar{c}$ and the normalized micromorphic concentration $\bar{\mathbb{c}}$. Details of our numerical methodology, and some specifics regarding its implementation in Abaqus, are provided in Sect. B.7.

B.5 Simulations of spinodal decomposition by diffusion

The aforementioned theoretical and numerical framework was applied to modeling spinodal decomposition by diffusion in a similar fashion as described in Sect. 4. Spinodal decomposition is a process in which an initially homogeneous binary mixture phase segregates into distinct regions which are characterized by being either rich or poor in their concentration of a particular component. This phase segregation results in the creation of interfaces with sharp concentration gradients which introduce additional energy into the system. The system then evolves by coarsening of the phases such that the interfacial energy is minimized until a steady-sate morphology is achieved.

The purpose of this section is two-fold.

1. First, we perform a brief mesh refinement study using one-dimensional simulations to compare steady-state concentration profiles in simulations with varying mesh densities. Such a study is not performed in Sect. 4.

2. Second, we investigate the effect of varying the penalty modulus β in the micromorphic split method implementation. Specifically, using the classical formulation as a basis for comparison, we aim to find appropriately high values of the penalty modulus β such that the micromorphic formulation converges to the classical formulation and thus recovers a solution of the original Cahn-Hilliard equation.

There are several criteria which one might use in order to compare the two split methods and determine if the penalty modulus β is appropriately large. In this work we consider the following methods:

(i) First, from simulations using the micromorphic formulation, we measure the maximum difference between the concentration $\bar{c}$ and the micromorphic concentration $\bar{\mathbb{c}}$ at steady-state as a function of β.

(ii) Second, we consider measurements of the interface width d at steady-state. Here, spinodal decomposition simulations of isolated periodic systems are performed until a steady-state morphology is reached at which point a phase interface width d can be measured. We then compare the interface widths computed using the micromorphic formulation with varying β to that computed using the classical formulation.

(ii) Third, we consider the free energy of the system as it evolves from an unstable configuration until steady-state is reached. This criteria is important since it compares the transient behavior of the two formulations. Comparison of this measure between the two formulations, demonstrates that the transient behavior of the micromorphic formulation is also suitably converged to that of the classic formulation.

We begin by writing the free energies of the two formulations in a normalized fashion. For the classical formulation, the free energy (B.39) may be written normalized as

$$\bar{\psi} = \frac{\psi}{R\vartheta} = \underbrace{\Big(\bar{c}\ln\bar{c} + (1-\bar{c})\ln(1-\bar{c}) + \bar{\chi}\,\bar{c}(1-\bar{c})\Big)}_{\text{chemical energy } \bar{\psi}^{\text{chem}}} + \underbrace{\bar{\lambda}(1/2)|\nabla\bar{c}|^2}_{\text{interfacial energy } \bar{\psi}^{\text{inter}}}, \tag{B.52}$$

and for the micromorphic formulation, the free energy (B.47) may be written normalized as

$$\bar{\psi} = \frac{\psi}{R\vartheta} = \underbrace{\Big(\bar{c}\ln\bar{c} + (1-\bar{c})\ln(1-\bar{c}) + \bar{\chi}\,\bar{c}(1-\bar{c})\Big)}_{\text{chemical energy } \bar{\psi}^{\text{chem}}} + \underbrace{\bar{\lambda}(1/2)|\nabla\bar{\mathbb{c}}|^2}_{\text{interfacial energy } \bar{\psi}^{\text{inter}}} + \underbrace{\bar{\beta}(1/2)(\bar{c}-\bar{\mathbb{c}})^2}_{\text{penalty energy } \bar{\psi}^{\text{pen}}}. \tag{B.53}$$

In writing the normalized free energies (B.52) and (B.53), we have set the reference chemical potential $\mu^0 = 0$, and have defined the following "normalized" material parameters

$$\bar{\chi} = \frac{\chi}{R\vartheta}, \quad \bar{\lambda} = \frac{\lambda}{R\vartheta}, \quad \text{and} \quad \bar{\beta} = \frac{\beta}{R\vartheta}. \tag{B.54}$$

The quantities $\bar{\chi}$ and $\bar{\beta}$ are dimensionless, while the normalized gradient energy coefficient $\bar{\lambda}$ has units of length squared.[1] Henceforth, we focus only on the normalized quantities $\bar{\chi}$, $\bar{\lambda}$, and $\bar{\beta}$.

Further, we are only interested in studying the effect of the normalized penalty modulus $\bar{\beta}$, we thus fix the value of all other relevant material parameters at

$$\bar{\chi} = 3, \quad \bar{\lambda} = 2.5 \times 10^{-4}\,\mu\text{m}^2. \tag{B.55}$$

The diffusivity is set to $D_0 = 2.5 \times 10{-}3\,\mu\text{m}^2/\text{sec}$ and acts only the set the time scale within which phase-segregation evolves — it has no effect on the actual morphology of of the phase segregation, and is thus arbitrarily set to its given value.

[1]When prescribing the normalized quantities $\bar{\chi}$, $\bar{\lambda}$, and $\bar{\beta}$, the thermal energy $R\vartheta$ is effectively removed as a material parameter and has no effect on the physical problem. That is, any variations of $R\vartheta$ — for fixed value of $\bar{\chi}$, $\bar{\lambda}$, and $\bar{\beta}$, have no effect on the simulations. We thus arbitrarily chose $\vartheta = 300\,\text{K}$ for this work.

Remark. In both (B.52) and (B.53), for values of $\bar{\chi} > 2$, the normalized chemical energy $\bar{\psi}^{\text{chem}}$ is a double-well potential which governs phase segregation. A plot of $\bar{\psi}^{\text{chem}}$ for $\bar{\chi} = 3$ is shown schematically in Fig. 4-1. When the initial concentration $\bar{c}$ is within the spinodal region $\bar{c} \in (\bar{c}_\gamma, \bar{c}_\delta)$ (i.e. regions where $\partial^2 \bar{\psi}^{\text{chem}}/\partial \bar{c}^2 < 0$), the system may spinodally decompose into multiple phases of equilibrium concentrations $\bar{c}_\alpha$ and $\bar{c}_\beta$, called the binodal concentrations. □

B.5.1 Consistent definition of an interface width

For completeness of this Appendix, we repeat our definition of an interface width which was previously presented in Sect. 4.

In order to consistently define the width of an interface between two phases, we consider the specific method shown schematically for a one-dimensional phase-separation situation in Fig. 4-2 (c.f. Wodo and Ganapathysubramanian, 2011). With respect to this figure, the interface width d is defined by the intersection of the tangent to the concentration profile at the mean concentration $\bar{c}_m = |\bar{c}_\alpha - \bar{c}_\beta|/2$ with the binodal concentrations. That is,

$$d \stackrel{\text{def}}{=} (\bar{c}_\alpha - \bar{c}_\beta) \left(\left. \frac{d\bar{c}}{dx} \right|_{\bar{c}_m} \right)^{-1}. \tag{B.56}$$

Further, in order to chose an appropriately fine finite-element mesh, it is important that we have an a-priori estimate of the interface width d. To this end, we recall from Cahn and Hilliard (1958) that an *estimate* of the concentration gradient at the mean concentration may be obtained through

$$\left. \frac{d\bar{c}}{dx} \right|_{\bar{c}_m} = \left(\frac{\delta \bar{\psi}^{\text{chem}}_{\text{max}}}{\bar{\lambda}} \right)^{1/2}, \tag{B.57}$$

where the quantity $\delta \bar{\psi}^{\text{chem}}_{\text{max}}$ is shown schematically in Fig. 4-2. Combining (B.57) with (B.56) we have the following important estimate for the width of the interface separating two phases

$$d_{\text{est}} = (\bar{c}_\alpha - \bar{c}_\beta) \left(\frac{\bar{\lambda}}{\delta \bar{\psi}^{\text{chem}}_{\text{max}}} \right)^{1/2}, \tag{B.58}$$

which we note also depends on $\bar{\chi}$ through the binodal concentrations $\bar{c}_\alpha$ and $\bar{c}_\beta$. Finally, for the values of the material parameters $\bar{\chi}$ and $\bar{\lambda}$ given in(B.55), we obtain a numerical estimate of the front width as

$$d_{\text{est}} = 40\,\text{nm}. \tag{B.59}$$

B.5.2 Mesh refinement

In simulations involving spinodal decomposition and phase-segregation, the interface width is an important physical parameter of the system. From a numerical perspective, this in-

terface width must be discretized with a sufficiently large number of elements in order to achieve accurate results. Here we briefly investigate the effect of mesh refinement using one-dimensional simulations and the classical formulation split method.

To quantify the resolution of our finite-element mesh, we define the normalized quantity

$$\bar{R} = \frac{d_{\text{est}}}{l_{\text{elem}}} \tag{B.60}$$

where d_{est} is the estimated interface width (B.58), and l_{elem} is the edge length of a single element in the simulation. The quantity $\bar{R}$ is thus simply the number of finite-elements across a potential phase interface of size d_{est}. Further:

- With respect to Fig. B-1(a), we performed one-dimensional simulations by using a single row of 2D elements in which all of the degrees of freedom on the nodes on face AB are constrained to equal those of the nodes on face CD.

- For all of the simulations in this section, regardless of mesh density, the initial concentration $\bar{c}$ is taken to vary linearly between $\bar{c}_0 = 0.4$ on the boundary AC and $\bar{c}_0 = 0.6$ on the boundary BD, see Fig. B-1(a).[2]

- The simulation domain size is kept constant at $0.2\,\mu$m, which is sufficiently large compared to the estimated front width $d_{\text{est}} = 40\,$nm computed in (B.59).

- Finally, we consider mesh resolutions in the range

  $$\bar{R} \in [5, 10, 20, 40, 80, 160].$$

  We note that we increase the mesh resolution $\bar{R}$ always by a factor of two such that when comparing two simulations with different mesh resolutions we can compare concentrations at the same physical locations.

In all simulations, we allow the system to equilibrate until a steady-state concentration profile is formed, see Fig. B-1(b) for an example of the steady-state profile with $\bar{R} = 10$.

In order to measure convergence of the numerical solution as we refine the mesh, we chose as an "exact" solution the numerical simulation with $\bar{R} = 160$. Fig. B-2 shows the maximum difference between the steady-state concentration profile and the "exact" concentration profile computed with $\bar{R} = 160$ as a function of varying mesh resolution $\bar{R}$ in a log-log scale. As shown in Fig. B-2, the quantity $\max|\bar{c} - \bar{c}_{\bar{R}=160}|$ converges with increasing resolution $\bar{R}$. Further, in accordance with other mesh refinement studies in the literature (cf. Wodo and Ganapathysubramanian, 2011), a resolution of $\bar{R} = 5$ or higher produces less than 1% error. Based on this brief analysis we may now chose appropriately fine finite-element meshes in our subsequent studies.

[2] The initial chemical potential μ_0 is computed using $(B.41)_2$ using the initial concentration $\bar{c}_0$ and assuming no gradients of concentration, i.e. $\Delta\bar{c} = 0$.

B.5.3 Convergence of the micromorphic formulation split method with increasing values of the penalty modulus β

We now focus on investigating the effect of the normalized penalty modulus $\bar{\beta}$ on the micromorphic formulation split method. For all of the simulations presented in this section we make the following specific choices:

- With respect to Fig. B-3, which shows simulation domains for one-, two-, and three-dimensional simulations of spinodal decomposition, we apply period boundary conditions on all exterior surfaces. One-dimensional simulations are achieved by using a single row of 2D elements and constraining all degrees of freedom on the nodes on face AB to equal those of the nodes on face CD.

- Unless otherwise specified, the initial normalized concentration in the domain $\bar{c}_0$ was given as a random uniform distribution with a mean of $\bar{c}_0 = 0.75$ and a maximum fluctuation of 0.05, see Fig. B-3. For simulations using the classical formulation, the initial chemical potential μ_0 was computed based on the initial normalized concentration according to

$$\mu_0 = R\vartheta \log\left(\frac{\bar{c}_0}{1-\bar{c}_0}\right) + \bar{\chi}(1-2\bar{c}_0).$$

  For simulations using the micromorphic formulation, the initial micromorphic concentration $\bar{\mathrm{c}}_0$ is set equal to the initial normalized concentration $\bar{c}_0$.

- To quantify the physical size of the simulation domain we define the dimensionless quantity

$$\bar{D} = \frac{D}{d_{\text{est}}},$$

  where d_{est} is the estimated interface width (B.58), and D is the physical edge length of the domain in either one, two, or three dimensions as defined in Fig. B-3.

In order to illustrate the spinodal decomposition process, Fig. B-4 shows three representative simulations of spinodal decomposition in one, two, and three dimensions using the classical formulation split method at different stages in the spinodal decomposition process. In these simulations, the normalized domain size is $\bar{D} = 20$, while the resolutions are $\bar{R} = 5$ for the one- and two-dimensional simulations and $\bar{R} = 2.5$ for the three-dimensional simulation.[3] For the one-dimensional simulation, Fig. B-4(a) shows both contours of normalized concentration $\bar{c}$ as well as the concentration profile as a function of the normalized distance $\bar{x} = x/D$ from from the left edge of the simulations domain. For the three-dimensional simulation, Fig. B-4(c) shows iso-surfaces of the normalized concentration $\bar{c}$.

Fig. B-4 illustrates the spinodal decomposition process — from the early stages of spinodal decomposition, when the components are well-mixed and the concentration is nearly

[3]We chose a lower resolution for the three-dimensional simulations in order to reduce the computational time. These simulations, using $\bar{R} = 2.5$, are purely for illustration and thus the accuracy is not of particular concern.

homogeneous, until a steady-state morphology is reached, at which time two distinct phases are observed. In the 2D simulation, Fig. B-4(b), the steady-state morphology consists of a circular concentration-poor region surrounded by a concentration-rich domain. Similarly, in the 3D simulation, Fig. B-4(c), the steady-state morphology consists of a spherical concentration-poor region surrounded by a concentration-rich domain.

Similar simulations were performed using the micromorphic formulation, keeping all parameters constant, and varying the normalized penalty modulus in the range

$$\bar{\beta} \in [5, 10, 25, 50, 100, 250, 500, 1000].$$

These simulations, in order to maximize their accuracy, were performed using a normalized domain size of $\bar{D} = 5$, and a resolution of $\bar{R} = 20$. Fig. B-5 shows the difference $\bar{c} - \bar{\mathfrak{c}}$ at steady-state for one- two- and three-dimensional simulations with varying $\bar{\beta}$. In all cases we see that as we increase the value of $\bar{\beta}$ towards 10^3, the difference $\bar{c} - \bar{\mathfrak{c}}$ decreases to a low value of $|\bar{c} - \bar{\mathfrak{c}}| \lessapprox 5 \times 10^{-4}$. Further, from the simulations shown in Fig. B-5, in Fig. B-6 we plot the maximum absolute value of the difference, $\max|\bar{c} - \bar{\mathfrak{c}}|$, for increasing values of $\bar{\beta}$ on a log-log scale. From this figure we observe that $\max|\bar{c} - \bar{\mathfrak{c}}|$ tends to zero as the normalized penalty modulus $\bar{\beta}$ is increased. Thus, as $\bar{\beta}$ is increased, the micromorphic concentration $\bar{\mathfrak{c}}$ approaches the real concentration $\bar{c}$ and we expect the solutions from the micromorphic formulation split method to converge to those that would be obtained using the classical formulation split method.

As an alternative measure of convergence, one which compares the micromorphic and classic formulations directly, we measure the interface widths d, defined in Sect. B.5.1, at steady-state using the same simulations shown in Fig. B-5. The results for the interface width measurements from the simulations using the micromorphic formulation are shown in Fig. B-7(a); note that the x-scale is logarithmic. In Fig. B-7(b) we plot the variation of $|d_{\text{micro}} - d_{\text{classic}}|/d_{\text{classic}}$ as a function $\bar{\beta}$ on a log-log scale. This plot clearly shows that for values of $\bar{\beta} > 100$ the difference $|d_{\text{micro}} - d_{\text{classic}}|/d_{\text{classic}}$ is approximately 2% and the micromorphic formulation is clearly converging to the classical formulation with regards to the interface width.

Remark. The second PDE in the micromorphic formulation $(\text{B.48})_2$, namely the microforce balance for the micromorphic concentration $\bar{\mathfrak{c}}$, may alternatively be written as

$$0 = \ell^2 \, \Delta\bar{\mathfrak{c}} + (\bar{c} - \bar{\mathfrak{c}}), \quad \ell = \sqrt{\lambda/\beta}, \tag{B.61}$$

where the quantity ℓ is a parameter with units of length. In Ubachs et al. (2004) this parameter is incorrectly determined as being critical in controlling the interface width d which forms in the process of spinodal decomposition. We have shown here, see Fig. B-7, that at a fixed temperature and for fixed values of the material parameters χ and λ, which are also properties in the original Cahn-Hilliard formulation, as we increase the modulus β we converge to a fixed interface width d. That is, for appropriately high values of β, *the interface width d is solely controlled by the material parameters χ and λ.* Further, we need

not concern ourselves with properly discretizing the length ℓ since it has no effect on the actual length scale of the solution. □

Our third measure of convergence for the micromorphic formulation is based on convergence of the system free energy as the process of spinodal decomposition takes place. For simplicity, in this convergence criteria we consider only two-dimensional simulations with a normalized domain size of $\bar{D} = 20$ and a resolution of $\bar{R} = 5$.

Fig. B-8(a) shows the average chemical $\bar{\psi}^{\text{chem}}$, interfacial $\bar{\psi}^{\text{inter}}$, and penalty $\bar{\psi}^{\text{pen}}$ normalized free energies[4], as a function of time for simulations using the micromorphic formulation with $\bar{\beta} = 5$ and $\bar{\beta} = 1000$; note that the x-scale is logarithmic. First we note the overall behavior of the free energies. When spinodal decomposition first occurs, at $t \approx 10\,\text{sec}$, the chemical free energy is significantly reduced as distinct phases of lower chemical free energy are formed. Simultaneously, the interfacial free energy increases since sharp gradients in concentration are present at the various interfaces which form between distinct phases. The system then evolves, reducing its total free energy, by coarsening of the morphology through the coalescence of the different phases. Finally, a steady-state is reached at $t \gtrsim 3 \times 10^3\,\text{sec}$ when the system energy reaches a steady minimum. We also note in Fig. B-8 that as $\bar{\beta}$ is increased from 5 to 10^3, the penalty free energy is reduced, and the chemical and interfacial energies also change.

Fig. B-8(b) compares average normalized chemical $\bar{\psi}^{\text{chem}}$ and interfacial $\bar{\psi}^{\text{inter}}$ free energies as a function of time for a simulation using the classical formulation (dashed red line) and simulations using the micromorphic formulation with $\bar{\beta} \in [5, 10, 10^3]$ (solid blue lines). We can clearly see that as $\bar{\beta}$ is increased to $\bar{\beta} = 10^3$, both the chemical and interfacial energies from the micromorphic formulation match those obtained using the classical formulation not just at steady-state but also throughout the transient response of the system. This figure serves to show that the solutions obtained using the micromorphic formulation converge to those obtained using the classical formulation not just at steady-state but also throughout the transient response.

Remark. As we have shown in this Section, it it essentially that one chose a sufficiently large value of the normalized penalty modulus $\bar{\beta}$, however one is not free to chose an arbitrarily large vale of $\bar{\beta}$. Large values of $\bar{\beta}$ result in ill conditioned matrices for the finite-element problem, see App. B.7. It has been our experience that increasing the value of $\bar{\beta}$ to arbitrarily high numbers (i.e. $\bar{\beta} = 10^5$) in fact results in non-convergence of the simulations under the same convergence criteria which result in converged simulations with $\bar{\beta} = 10^3$. Thus, one may not simply chose an arbitrarily high value of $\bar{\beta}$, rather one should chose the value of the penalty modulus only as large as necessary in order to achieve the desired accuracy. □

[4]The average free energy is computed as $\sum_{i=1}^{N} \bar{\psi}_i / N$ where $\bar{\psi}_i$ is the free energy of interest computed at the i-th integration point and N is the total number of integration points in the simulation domain.

B.6 Steady-state morphologies in three dimensions

As a demonstration of the robustness and efficiency of the numerical methodology developed in this work, similar to Wodo and Ganapathysubramanian (2011), in this section we present various three-dimensional steady-state solutions to the Cahn-Hilliard equation computed using our numerical implementation.

The three-dimensional simulations discussed in this Section are computed with the classical formulation split method with $\bar{D} = 10$, $\bar{R} = 5$, and with different initial concentrations having a uniform distribution with a mean of $\bar{c}_0$ and a maximum fluctuation of 0.05. Fig. B-9 shows steady-state morphologies for simulations with different initial mean concentrations $\bar{c}_0$; note that the simulations have been translated within their periodic simulation domains to provide the best visualization of the resulting morphology.

Fig. B-9(a) uses $\bar{c}_0 = 0.625$ and the resulting interface is representative of a Lawson surface (cf. Ros, 2005), while (b) uses $\bar{c}_0 = 0.75$ and the resulting interface is spherical. Figs. B-9(c) through (e) were all computed using a mean of $\bar{c}_0 = 0.5$ however each one with a different initial distribution. In (c) the interface is representative of a P-Schwarz surface (cf. Ros, 2005), while (d) and (e) are representative of Lamella and cylindrical surfaces respectively. As illustrated by Fig. B-9, with the use of the numerical method provided in this work we have been able to, with relative ease, compute the shown possible solutions to the Cahn-Hilliard equation in a periodic three-dimensional domain.

Further, as noted by Wodo and Ganapathysubramanian (2011), the process of simulating spinodal decomposition over long terms, including up steady-states, involves a large variation in temporal scales. The time scales associated with reaching a steady-state solution are orders of magnitude larger than the time scales associated with an event in which a rapid coarsening of the concentration morphology occurs through the merger of two distinct phases. As such, an adaptive time stepping algorithm is required in order to efficiently compute steady-state solutions of simulations involving spinodal decomposition. An additional benefit of solving within the Abaqus (2010) framework is that the built-in adaptive time-stepping algorithm has proven effective in transitioning between the multiple time scales associated with simulating spinodal decomposition, and has thus enabled efficient simulations of spinodal decomposition up to steady-sate.

To illustrate this feature, Fig. B-10 shows the evolution of the simulation time step Δt as a function of simulation time t in a log-log scale for the particular three-dimensional simulation shown in Fig. B-9(b). In Fig. B-10, the drastic reduction in time steps Δt observed at multiple times (i.e. at $t \approx 4 \times 10\,\text{sec}$), correspond to events during the simulation where two phases merge in order to coarsen the concentration morphology and lower the system energy. Following the coarsening event, the built-in adaptive time stepping in Abaqus is able to quickly increase the simulation time step until another coarsening event occurs, thus effectively switching between the different temporal scales — which from Fig. B-10 we note can span 3 orders of magnitude, involved in simulating spinodal decomposition. Finally, as

a benchmark for computational time required, the simulation shown in Fig. B-9(b) had a total (wall-clock) computation time of 21.4 h using 22 CPUs (CPU time of 10.6 h).[5]

B.7 Numerical methodology

Following Chester et al. (2015), for each of the two split methods summarized in Sect. B.3 we present here the numerical methodology employed in this work.

B.7.1 Numerical methodology for the classical formulation split method

We begin with the solution procedure for the classical formulation $(B.50)_1$., the strong form of which is given by

$$\begin{aligned}
&\text{mass balance} \quad \left\{ \begin{array}{lll} \dot{\bar{c}} - \operatorname{Div}(m\nabla\mu) = 0, \quad m = m_0\bar{c}(1-\bar{c}) & \text{in} & \mathrm{B}, \\ \bar{c} = \breve{\bar{c}} & \text{on} & \mathcal{S}_{\bar{c}}, \\ -m\nabla\mu\cdot\mathbf{n} = \breve{j} & \text{on} & \mathcal{S}_{\mathrm{j}}, \end{array} \right. \\
&\text{microforce balance} \quad \left\{ \begin{array}{lll} \mu - \mu^0 - R\vartheta\ln\left(\dfrac{\bar{c}}{1-\bar{c}}\right) - \chi(1-2\bar{c}) + \lambda\Delta\bar{c} = 0 \quad s & \text{in} & \mathrm{B}, \\ \mu = \breve{\mu} & \text{on} & \mathcal{S}_{\mu}, \\ \lambda\nabla\bar{c}\cdot\mathbf{n} = \breve{\zeta} & \text{on} & \mathcal{S}_{\zeta}. \end{array} \right.
\end{aligned} \tag{B.62}$$

Then with w_1 and w_2 denoting two test fields which vanish on $\mathcal{S}_{\bar{c}}$ and $\mathcal{S}_{\mu}$ respectively, the corresponding weak forms are

$$\begin{aligned}
&\int_{\mathrm{B}} \left(w_1\left(\dot{\bar{c}} - \operatorname{Div}(m\nabla\mu)\right)\right) dv = 0, \\
&\int_{\mathrm{B}} \left(w_2\left(\mu - \mu^0 - R\vartheta\ln\left(\frac{\bar{c}}{1-\bar{c}}\right) - \chi(1-2\bar{c}) + \lambda\Delta\bar{c}\right)\right) dv = 0.
\end{aligned} \tag{B.63}$$

[5]Significant computational time improvements can also be achieved by using the build-in iterative solver provided in Abaqus (2010)

Using the identity $\mathrm{Div}(\alpha\mathbf{a}) = \nabla\alpha \cdot \mathbf{a} + \alpha\mathrm{Div}(\mathbf{a})$, the divergence theorem, and the boundary conditions on $\mathcal{S}_\mathrm{j}$ and $\mathcal{S}_\zeta$ we may simplify the weak form (B.63) to

$$\begin{aligned}
&\int_\mathrm{B} \left(w_1\dot{\bar{c}} + \nabla w_1 \cdot (m\nabla\mu)\right)\, dv + \int_{\mathcal{S}_\mathrm{j}} w_1 \breve{j}\, da = 0,\\
&\int_\mathrm{B} \left(w_2\left(\mu - \mu^0 - R\vartheta \ln\left(\frac{\bar{c}}{1-\bar{c}}\right) - \chi(1-2\bar{c})\right) - \nabla w_2 \cdot (\lambda\nabla\bar{c})\right)\, dv + \int_{\mathcal{S}_\zeta} w_2 \breve{\zeta}\, da = 0.
\end{aligned} \tag{B.64}$$

The body is approximated using finite elements, $\mathrm{B} = \cup\mathbf{B}^e$, and the trial solutions for the concentration and the chemical potential are interpolated inside each element by

$$\bar{c} = \sum_A \bar{c}^A N^A, \quad \text{and} \quad \mu = \sum_A \mu^A N^A, \tag{B.65}$$

with the index $A = 1, 2, ..., M$ denoting the nodes of the element, $\bar{c}^A$ denoting the nodal normalized concentrations, μ^A denoting the nodal chemical potentials, and N^A the shape functions. We employ a standard Galerkin approach, in that the test fields are interpolated by the shame shape functions, that is

$$w_1 = \sum_A w_1^A N^A, \quad \text{and} \quad w_2 = \sum_A w_2^A N^A. \tag{B.66}$$

Using (B.65) and (B.66) in (B.64) yields the following element-level system of equations

$$\begin{aligned}
&\int_\mathbf{B}^e w_1^A \left(N^A\dot{\bar{c}} + \nabla N^A \cdot (m\nabla\mu)\right)\, dv + \int_{\mathcal{S}_\mathrm{j}^e} w_1^A N^A \breve{j}\, da = 0,\\
&\int_\mathbf{B}^e w_2^A \left(N^A\left(\mu - \mu^0 - R\vartheta \ln\left(\frac{\bar{c}}{1-\bar{c}}\right) - \chi(1-2\bar{c})\right) - \nabla N^A \cdot (\lambda\nabla\bar{c})\right)\, dv + \int_{\mathcal{S}_\zeta^e} w_2^A N^A \breve{\zeta}\, da = 0.
\end{aligned} \tag{B.67}$$

The system of equations (B.67) is solved using a Newton procedure. Thus, since w_1 and w_2 are arbitrary, we define the element-level residuals for the concentration and the chemical potential as

$$\begin{aligned}
R_{\bar{c}}^A &= \int_\mathbf{B}^e \left(N^A\dot{\bar{c}} + \nabla N^A \cdot (m\nabla\mu)\right)\, dv + \int_{\mathcal{S}_\mathrm{j}^e} N^A \breve{j}\, da,\\
R_\mu^A &= \int_\mathbf{B}^e \left(N^A\left(\mu - \mu^0 - R\vartheta \ln\left(\frac{\bar{c}}{1-\bar{c}}\right) - \chi(1-2\bar{c})\right) - \nabla N^A \cdot (\lambda\nabla\bar{c})\right)\, dv + \int_{\mathcal{S}_\zeta^e} N^A \breve{\zeta}\, da.
\end{aligned} \tag{B.68}$$

In addition to the residuals (B.68), the following tangents are also required for the Newton procedure

$$K^{AB}_{\bar{c}\bar{c}} = -\frac{\partial R^A_{\bar{c}}}{\partial \bar{c}^B}, \quad K^{AB}_{\bar{c}\mu} = -\frac{\partial R^A_{\bar{c}}}{\partial \mu^B}, \quad K^{AB}_{\mu\mu} = -\frac{\partial R^A_{\mu}}{\partial \mu^B}, \quad \text{and} \quad K^{AB}_{\mu\bar{c}} = -\frac{\partial R^A_{\mu}}{\partial \bar{c}^B}. \tag{B.69}$$

Using (B.68) the tangents (B.69) may be evaluated as

$$\begin{aligned}
K^{AB}_{\bar{c}\bar{c}} &= -\int_{\mathbf{B}}^{e} \left(N^A N^B \frac{\partial \dot{\bar{c}}}{\partial \bar{c}} + N^B \frac{\partial m}{\partial \bar{c}} \nabla N^A \cdot \nabla \mu \right) dv - \int_{\mathcal{S}^e_{\mathrm{j}}} N^A N^B \frac{\partial \breve{j}}{\partial \bar{c}}\, da, \\
K^{AB}_{\bar{c}\mu} &= -\int_{\mathbf{B}}^{e} \left(\nabla N^A \cdot (m \nabla N^B) \right) dv - \int_{\mathcal{S}^e_{\mathrm{j}}} N^A N^B \frac{\partial \breve{j}}{\partial \mu}\, da, \\
K^{AB}_{\mu\mu} &= -\int_{\mathbf{B}}^{e} N^A N^B\, dv - \int_{\mathcal{S}^e_{\zeta}} N^A N^B \frac{\partial \breve{\zeta}}{\partial \mu}\, da, \\
K^{AB}_{\mu\bar{c}} &= -\int_{\mathbf{B}}^{e} N^A N^B \left(-\frac{R\vartheta}{\bar{c}(1-\bar{c})} + 2\chi \right) dv - \int_{\mathcal{S}^e_{\zeta}} N^A N^b \frac{\partial \breve{\zeta}}{\partial \bar{c}}\, da.
\end{aligned} \tag{B.70}$$

Finally, the term $\dot{\bar{c}}$ in $(\mathrm{B.68})_1$ is computed using the approximation $\dot{\bar{c}} = (\bar{c}_{n+1} - \bar{c}_n)/\Delta t$, and to complete the evaluation of the tangents (B.70) we have

$$\frac{\partial \dot{\bar{c}}}{\partial \bar{c}} = \frac{1}{\Delta t}, \quad \text{and} \quad \frac{\partial m}{\partial \bar{c}} = m_0(1 - 2\bar{c}). \tag{B.71}$$

B.7.2 Numerical methodology for the micromorphic formulation split method

Below we present the solution procedure for the micromorphic formulation $(\mathrm{B.51})_2$, the strong form of which is given by

$$\left.\begin{aligned}
&\text{mass balance} \quad \begin{cases} \dot{\bar{c}} - \mathrm{Div}\,(m\nabla\mu) = 0 & \text{in} \quad \mathrm{B}, \\ \bar{c} = \breve{\bar{c}} & \text{on} \quad \mathcal{S}_{\bar{c}}, \\ -m\nabla\mu \cdot \mathbf{n} = \breve{j} & \text{on} \quad \mathcal{S}_{\mathrm{j}}, \end{cases} \\
&\text{microforce balance} \quad \begin{cases} \lambda \Delta \bar{\mathfrak{c}} + \beta(\bar{c} - \bar{\mathfrak{c}}) = 0 & \text{in} \quad \mathrm{B}, \\ \bar{\mathfrak{c}} = \breve{\bar{\mathfrak{c}}} & \text{on} \quad \mathcal{S}_{\bar{\mathfrak{c}}}, \\ \lambda \nabla \bar{\mathfrak{c}} \cdot \mathbf{n} = \breve{\zeta} & \text{on} \quad \mathcal{S}_{\zeta}, \end{cases}
\end{aligned}\right\} \tag{B.72}$$

where the chemical potential μ is given by

$$\mu^0 + R\vartheta\left(\frac{\bar{c}}{1-\bar{c}}\right) + \chi(1-2\bar{c}) + \beta(\bar{c}-\bar{\mathbb{c}}), \tag{B.73}$$

and the mobility is given by $m = m_0\bar{c}(1-\bar{c})$. Then with w_1 and w_2 denoting two test fields which vanish on $\mathcal{S}_{\bar{c}}$ and $\mathcal{S}_{\bar{\mathbb{c}}}$ respectively, the corresponding weak forms are

$$\begin{aligned} &\int_{\mathrm{B}} w_1\left(\dot{\bar{c}} - \mathrm{Div}\left(m\nabla\mu\right)\right) dv = 0, \\ &\int_{\mathrm{B}} w_2\left(\lambda\Delta\bar{\mathbb{c}} + \beta(\bar{c}-\bar{\mathbb{c}})\right) dv = 0. \end{aligned} \tag{B.74}$$

Using the identity $\mathrm{Div}(\alpha\mathbf{a}) = \nabla\alpha\cdot\mathbf{a} + \alpha\mathrm{Div}(\mathbf{a})$, the divergence theorem, and the boundary conditions on $\mathcal{S}_{\mathrm{j}}$ and $\mathcal{S}_{\zeta}$ we may simplify the weak form (B.74) to

$$\begin{aligned} &\int_{\mathrm{B}}\left(w_1\dot{\bar{c}} + \nabla w_1\cdot\left(m\frac{\partial\mu}{\partial\bar{c}}\nabla\bar{c}\right) + \nabla w_1\cdot\left(m\frac{\partial\mu}{\partial\bar{\mathbb{c}}}\nabla\bar{\mathbb{c}}\right)\right) dv + \int_{\mathcal{S}_{\mathrm{j}}} w_1\breve{j}\, da = 0, \\ &\int_{B}\left(w_2\beta(\bar{c}-\bar{\mathbb{c}}) - \nabla w_2\cdot(\lambda\nabla\bar{\mathbb{c}})\right) dv + \int_{\mathcal{S}_{\zeta}} w_2\breve{\zeta}\, da = 0, \end{aligned} \tag{B.75}$$

where we have used (B.73) to write $(\mathrm{B}.75)_2$ in terms of the gradients of the solution variables $\bar{c}$ and $\bar{\mathbb{c}}$. The body is approximated using finite elements, $\mathrm{B} = \cup\mathbf{B}^e$, and the trial solutions for the normalized concentration and the normalized micromorphic concentration are interpolated inside each element by

$$\bar{c} = \sum_A \bar{c}^A N^A, \quad \text{and} \quad \bar{\mathbb{c}} = \sum_A \bar{\mathbb{c}}^A N^A, \tag{B.76}$$

with the index $A = 1, 2, ..., M$ denoting the nodes of the element, $\bar{c}^A$ denoting the nodal normalized concentrations, $\bar{\mathbb{c}}^A$ denoting the nodal normalized micromorphic concentrations, and N^A the shape functions. We employ a standard Galerkin approach, in that the test fields are interpolated by the shame shape functions, that is

$$w_1 = \sum_A w_1^A N^A, \quad \text{and} \quad w_2 = \sum_A w_2^A N^A. \tag{B.77}$$

Using (B.76) and (B.77) in (B.75) yields the following element-level system of equations

$$\begin{aligned} &\int_{\mathbf{B}}^{e} w_1^A\left(N^A\dot{\bar{c}} + \nabla N^A\cdot\left(m\frac{\partial\mu}{\partial\bar{c}}\nabla\bar{c}\right) + \nabla N^A\cdot\left(m\frac{\partial\mu}{\partial\bar{\mathbb{c}}}\nabla\bar{\mathbb{c}}\right)\right) dv + \int_{\mathcal{S}_{\mathrm{j}}^{\mathrm{e}}} w_1^A N^A\breve{j}\, da = 0 \\ &\int_{\mathbf{B}}^{e} w_2^A\left(N^A\beta(\bar{c}-\bar{\mathbb{c}}) - \nabla N^A\cdot(\lambda\nabla\bar{\mathbb{c}})\right) dv + \int_{\mathcal{S}_{\zeta}^{\mathrm{e}}} w_2^A N^A\breve{\zeta}\, da = 0 \end{aligned} \tag{B.78}$$

The system of equations (B.78) is solved using a Newton procedure. Thus, since w_1 and w_2 are arbitrary, we define the element-level residuals for the normalized concentration and the normalized micromorphic concentration as

$$\begin{aligned} R^A_{\bar{c}} &= \int_{\mathbf{B}}^{e} \left(N^A \dot{\bar{c}} + \nabla N^A \cdot \left(m \frac{\partial \mu}{\partial \bar{c}} \nabla \bar{c} \right) + \nabla N^A \cdot \left(m \frac{\partial \mu}{\partial \bar{\mathfrak{c}}} \nabla \bar{\mathfrak{c}} \right) \right) dv + \int_{\mathcal{S}^e_{\mathrm{j}}} N^A \breve{j}\, da, \\ R^A_{\bar{\mathfrak{c}}} &= \int_{\mathbf{B}}^{e} \left(N^A \beta (\bar{c} - \bar{\mathfrak{c}}) - \nabla N^A \cdot (\lambda \nabla \bar{\mathfrak{c}}) \right) dv + \int_{\mathcal{S}^e_{\zeta}} N^A \breve{\zeta}\, da. \end{aligned} \tag{B.79}$$

The term $\dot{\bar{c}}$ in $(\text{B.79})_1$ is computed using the approximation $\dot{\bar{c}} = (\bar{c}_{n+1} - \bar{c}_n)/\Delta t$, and using (B.73), we have

$$\frac{\partial \mu}{\partial \bar{c}} = \frac{R\vartheta}{\bar{c}(1-\bar{c})} - 2\chi + \beta, \quad \text{and} \quad \frac{\partial \mu}{\partial \bar{\mathfrak{c}}} = -\beta, \tag{B.80}$$

which, along with the mobility $m = m_0 \bar{c}(1-\bar{c})$, are necessary to evaluate the residuals (B.79). In addition to the residuals (B.68), the following tangents are also required for the Newton procedure

$$K^{AB}_{\bar{c}\bar{c}} = -\frac{\partial R^A_{\bar{c}}}{\partial \bar{c}^B}, \quad K^{AB}_{\bar{c}\bar{\mathfrak{c}}} = -\frac{\partial R^A_{\bar{c}}}{\partial \bar{\mathfrak{c}}^B}, \quad K^{AB}_{\bar{\mathfrak{c}}\bar{\mathfrak{c}}} = -\frac{\partial R^A_{\bar{\mathfrak{c}}}}{\partial \bar{\mathfrak{c}}^B}, \quad \text{and} \quad K^{AB}_{\bar{\mathfrak{c}}\bar{c}} = -\frac{\partial R^A_{\bar{\mathfrak{c}}}}{\partial \bar{c}^B}. \tag{B.81}$$

Using (B.68) the tangents (B.81) may be evaluated as

$$\begin{aligned} K^{AB}_{\bar{c}\bar{c}} &= -\int_{\mathbf{B}}^{e} \left(N^A N^B \frac{\partial \dot{\bar{c}}}{\partial \bar{c}} + N^B \left(\frac{\partial m}{\partial \bar{c}} \frac{\partial \mu}{\partial \bar{c}} + m \frac{\partial^2 \mu}{\partial \bar{c}^2} \right) \nabla N^A \cdot \nabla \bar{c} \right. \\ &\qquad \left. + m \frac{\partial \mu}{\partial \bar{c}} \nabla N^A \cdot \nabla N^B + N^B \frac{\partial m}{\partial \bar{c}} \frac{\partial \mu}{\partial \bar{\mathfrak{c}}} \nabla N^A \cdot \nabla \bar{\mathfrak{c}} \right) dv - \int_{\mathcal{S}^e_{\mathrm{j}}} N^A N^B \frac{\partial \breve{j}}{\partial \bar{c}}\, da = 0, \\ K^{AB}_{\bar{c}\bar{\mathfrak{c}}} &= -\int_{\mathbf{B}}^{e} \left(m \frac{\partial \mu}{\partial \bar{\mathfrak{c}}} \nabla N^A \cdot \nabla N^B \right) dv - \int_{\mathcal{S}^e_{\mathrm{j}}} N^A N^B \frac{\partial \breve{j}}{\partial \bar{\mathfrak{c}}}\, da = 0, \\ K^{AB}_{\bar{\mathfrak{c}}\bar{\mathfrak{c}}} &= -\int_{\mathbf{B}}^{e} \left(-N^A N^B \beta - \lambda \nabla N^A \cdot \nabla N^B \right) dv - \int_{\mathcal{S}^e_{\zeta}} N^A N^B \frac{\partial \breve{\zeta}}{\partial \bar{\mathfrak{c}}}\, da = 0, \\ K^{AB}_{\bar{\mathfrak{c}}\bar{c}} &= -\int_{\mathbf{B}}^{e} \left(N^A N^B \beta \right) dv - \int_{\mathcal{S}^e_{\zeta}} N^A N^B \frac{\partial \breve{\zeta}}{\partial \bar{c}}\, da = 0. \end{aligned} \tag{B.82}$$

Finally, to complete the evaluation of the tangents (B.82) we require

$$\frac{\partial^2 \mu}{\partial \bar{c}^2} = \frac{R\vartheta(2\bar{c}-1)}{\bar{c}^2(1-\bar{c})^2}, \quad \text{and} \quad \frac{\partial m}{\partial \bar{c}} = m_0(1-2\bar{c}). \tag{B.83}$$

B.7.3 Implementation in Abaqus

We have implemented both the classical, Section B.7.1, and the micromorphic, Section B.7.2, formulations of the Cahn-Hilliard equation by writing user-element subroutines (UEL) in Abaqus (2010). During an analysis in Abaqus/Standard, the user subroutine UEL is called for each iteration. Passed into the subroutine are the current guesses for all nodal quantities,[6] and the user is required to evaluate and/or update two matrices denoted, in Abaqus' notation, `RHS` and `AMATRX`, which represent matrices of the nodal residuals and nodal tangents. Specifically:

- The matrix `RHS`, as defined by the Abaqus documentation, is "An array containing the contributions of this element to the right-hand side vectors of the overall system of equations." In the classical formulation, referring to (B.68), `RHS` is the overall elemental residual which in matrix form is given by

$$\mathsf{R} = \begin{bmatrix} R^1_{\bar{c}} & R^1_{\mu} & R^2_{\bar{c}} & R^2_{\mu} & \dots & R^M_{\bar{c}} & R^M_{\mu} \end{bmatrix}^{\mathsf{T}}. \tag{B.84}$$

  where M is the total number of nodes per element. Similarly, for the micromorphic formulation, referring to (B.79), `RHS` is the overall elemental residual which in matrix form is given by

$$\mathsf{R} = \begin{bmatrix} R^1_{\bar{c}} & R^1_{\bar{\mathfrak{c}}} & R^2_{\bar{c}} & R^2_{\bar{\mathfrak{c}}} & \dots & R^M_{\bar{c}} & R^M_{\bar{\mathfrak{c}}} \end{bmatrix}^{\mathsf{T}}. \tag{B.85}$$

- The matrix `AMATRX` as defined by the Abaqus documentation is "An array containing the contribution of this element to the Jacobian (stiffness) or other matrix of the overall system of equations." In the mixed formulation, referring to (B.70), `AMATRX` is the overall element tangent which is given by

$$\mathsf{K} = \begin{bmatrix} K^{11}_{\bar{c}\bar{c}} & K^{11}_{\bar{c}\mu} & K^{12}_{\bar{c}\bar{c}} & K^{12}_{\bar{c}\mu} & \cdots & K^{1M}_{\bar{c}\bar{c}} & K^{1M}_{\bar{c}\mu} \\ K^{11}_{\mu\bar{c}} & K^{11}_{\mu\mu} & K^{12}_{\mu\bar{c}} & K^{12}_{\mu\mu} & \cdots & K^{1M}_{\mu\bar{c}} & K^{1M}_{\mu\mu} \\ K^{21}_{\bar{c}\bar{c}} & K^{21}_{\bar{c}\mu} & K^{22}_{\bar{c}\bar{c}} & K^{22}_{\bar{c}\mu} & \cdots & K^{2M}_{\bar{c}\bar{c}} & K^{2M}_{\bar{c}\mu} \\ K^{21}_{\mu\bar{c}} & K^{21}_{\mu\mu} & K^{22}_{\mu\bar{c}} & K^{22}_{\mu\mu} & \cdots & K^{2M}_{\mu\bar{c}} & K^{2M}_{\mu\mu} \\ \vdots & \vdots & \vdots & \vdots & \ddots & \vdots & \vdots \\ K^{M1}_{\bar{c}\bar{c}} & K^{M1}_{\bar{c}\mu} & K^{M2}_{\bar{c}\bar{c}} & K^{M2}_{\bar{c}\mu} & \cdots & K^{MM}_{\bar{c}\bar{c}} & K^{MM}_{\bar{c}\mu} \\ K^{M1}_{\mu\bar{c}} & K^{M1}_{\mu\mu} & K^{M2}_{\mu\bar{c}} & K^{M2}_{\mu\mu} & \cdots & K^{MM}_{\mu\bar{c}} & K^{MM}_{\mu\mu} \end{bmatrix} \tag{B.86}$$

[6] In the case of the mixed formulation the nodal quantities are the normalized nodal concentrations $\bar{c}^A$ and nodal chemical potentials μ^A. In the case of the micromorphic formulation the nodal quantities are the normalized nodal concentrations $\bar{c}^A$ and the normalized nodal micromorphic concentrations $\bar{\mathfrak{c}}^A$.

Similarly, for the micromorphic formulation, referring to (B.82), **AMATRX** is the overall element tangent which is given by

$$\mathsf{K} = \begin{bmatrix} K^{11}_{\bar{c}\bar{c}} & K^{11}_{\bar{c}\bar{\mathfrak{c}}} & K^{12}_{\bar{c}\bar{c}} & K^{12}_{\bar{c}\bar{\mathfrak{c}}} & \cdots & K^{1M}_{\bar{c}\bar{c}} & K^{1M}_{\bar{c}\bar{\mathfrak{c}}} \\ K^{11}_{\bar{\mathfrak{c}}\bar{c}} & K^{11}_{\bar{\mathfrak{c}}\bar{\mathfrak{c}}} & K^{12}_{\bar{\mathfrak{c}}\bar{c}} & K^{12}_{\bar{\mathfrak{c}}\bar{\mathfrak{c}}} & \cdots & K^{1M}_{\bar{\mathfrak{c}}\bar{c}} & K^{1M}_{\bar{\mathfrak{c}}\bar{\mathfrak{c}}} \\ K^{21}_{\bar{c}\bar{c}} & K^{21}_{\bar{c}\bar{\mathfrak{c}}} & K^{22}_{\bar{c}\bar{c}} & K^{22}_{\bar{c}\bar{\mathfrak{c}}} & \cdots & K^{2M}_{\bar{c}\bar{c}} & K^{2M}_{\bar{c}\bar{\mathfrak{c}}} \\ K^{21}_{\bar{\mathfrak{c}}\bar{c}} & K^{21}_{\bar{\mathfrak{c}}\bar{\mathfrak{c}}} & K^{22}_{\bar{\mathfrak{c}}\bar{c}} & K^{22}_{\bar{\mathfrak{c}}\bar{\mathfrak{c}}} & \cdots & K^{2M}_{\bar{\mathfrak{c}}\bar{c}} & K^{2M}_{\bar{\mathfrak{c}}\bar{\mathfrak{c}}} \\ \vdots & \vdots & \vdots & \vdots & \ddots & \vdots & \vdots \\ K^{M1}_{\bar{c}\bar{c}} & K^{M1}_{\bar{c}\bar{\mathfrak{c}}} & K^{M2}_{\bar{c}\bar{c}} & K^{M2}_{\bar{c}\bar{\mathfrak{c}}} & \cdots & K^{MM}_{\bar{c}\bar{c}} & K^{MM}_{\bar{c}\bar{\mathfrak{c}}} \\ K^{M1}_{\bar{\mathfrak{c}}\bar{c}} & K^{M1}_{\bar{\mathfrak{c}}\bar{\mathfrak{c}}} & K^{M2}_{\bar{\mathfrak{c}}\bar{c}} & K^{M2}_{\bar{\mathfrak{c}}\bar{\mathfrak{c}}} & \cdots & K^{MM}_{\bar{\mathfrak{c}}\bar{c}} & K^{MM}_{\bar{\mathfrak{c}}\bar{\mathfrak{c}}} \end{bmatrix} \tag{B.87}$$

We have implemented the aforementioned theory and numerical procedure in Abaqus (2010) by writing user element subroutines (UEL) for two different elements:

- a 2D 4-node linear isoparametric quadrilateral, which we refer to as U2D4;
- a 3D 8-node linear isoparametric brick which we refer to as U3D8.

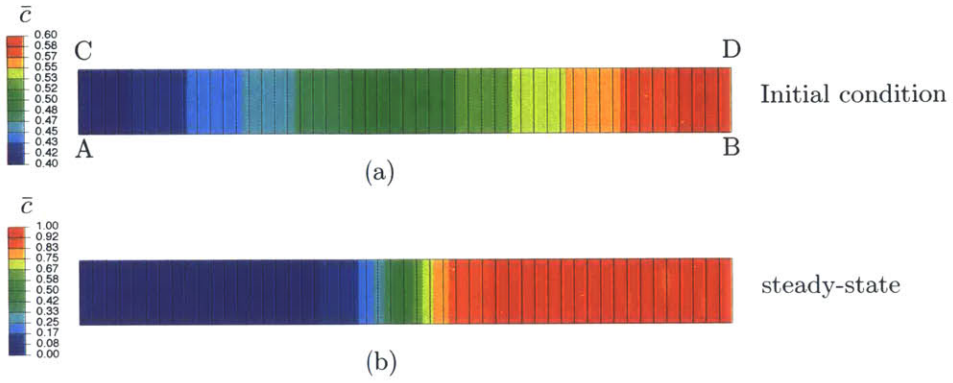

Figure B-1: One-dimensional simulation used in studying mesh refinement with $\bar{R} = 10$ elements across a potential phase interface width. (a) shows the initial concentration $\bar{c}_0$, while (b) shows contours of concentration at steady-state.

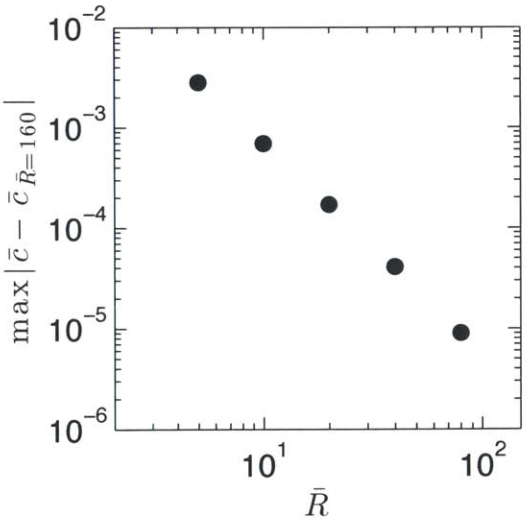

Figure B-2: Convergence of the maximum difference between the steady-state concentration profiles and the "exact" concentration profile computed with $\bar{R} = 160$ as a function of varying mesh resolution $\bar{R}$.

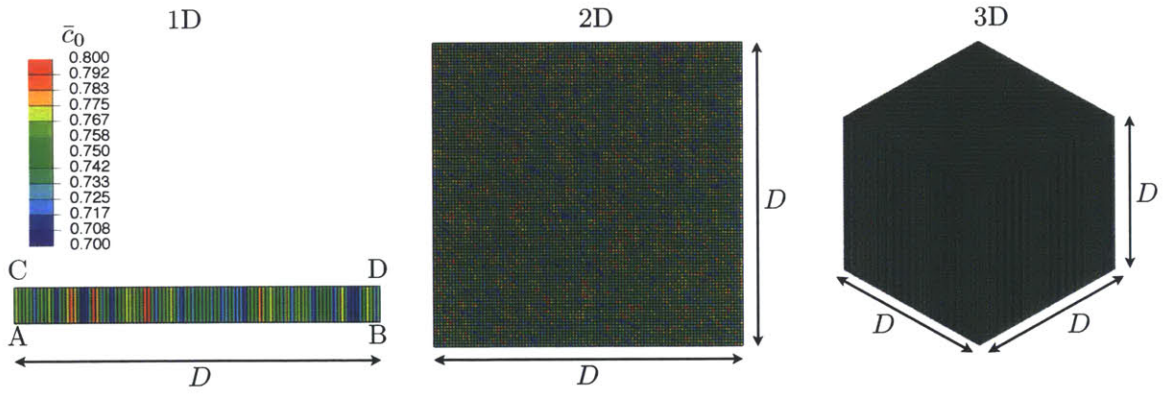

Figure B-3: Simulation domains for one- two- and three-dimensional simulations of spinodal decomposition. Contours show the initial concentration $\bar{c}_0$ which has a uniform random fluctuation of 0.05 about a mean of 0.75.

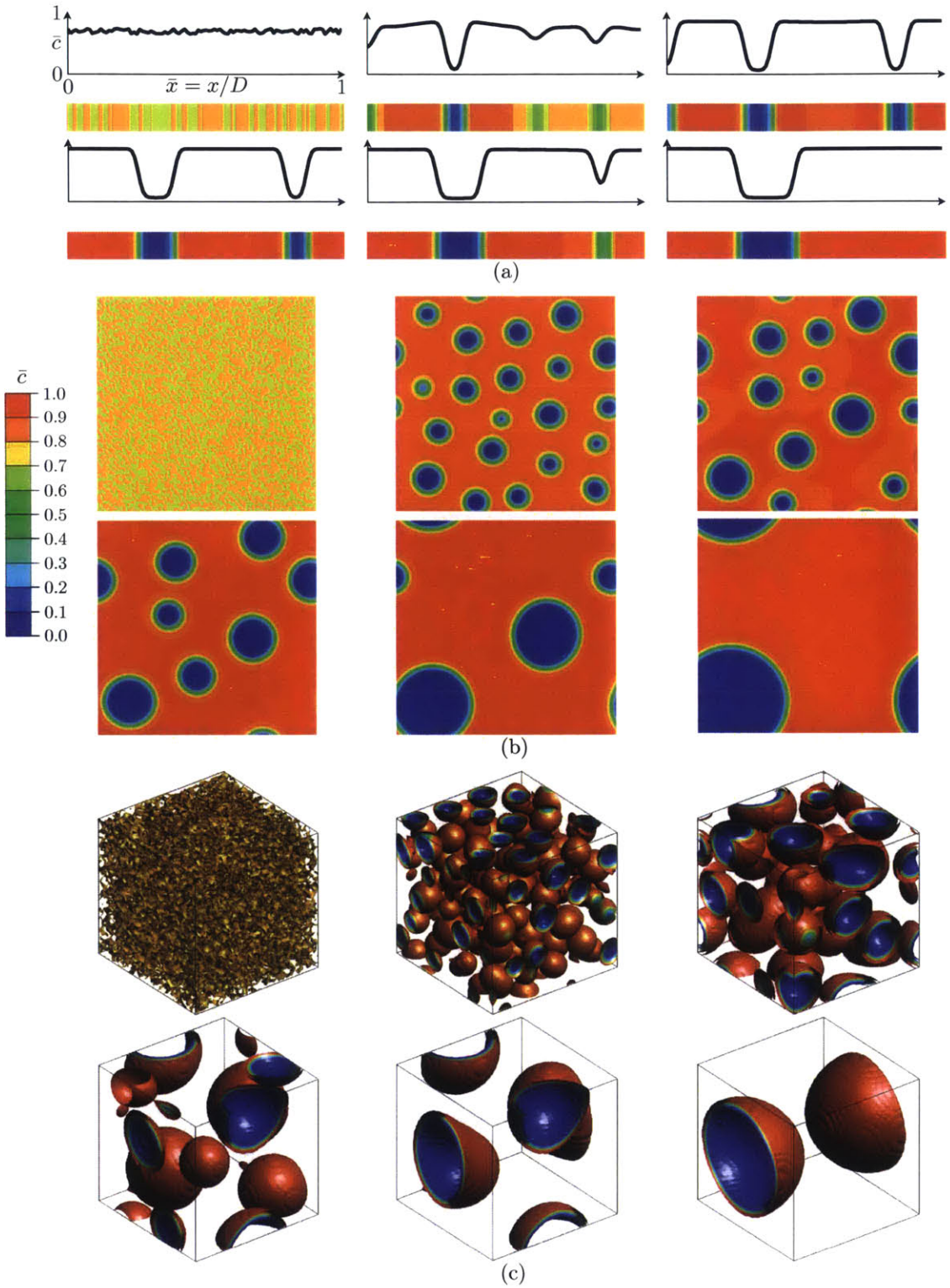

Figure B-4: Phase-separation and morphology evolution for (a) 1D simulations showing contours of concentration and concentration vs. normalized distance plots, (b) 2D simulations showing contours of normalized concentration, and (c) 3D simulations showing iso-surfaces of normalized concentration.

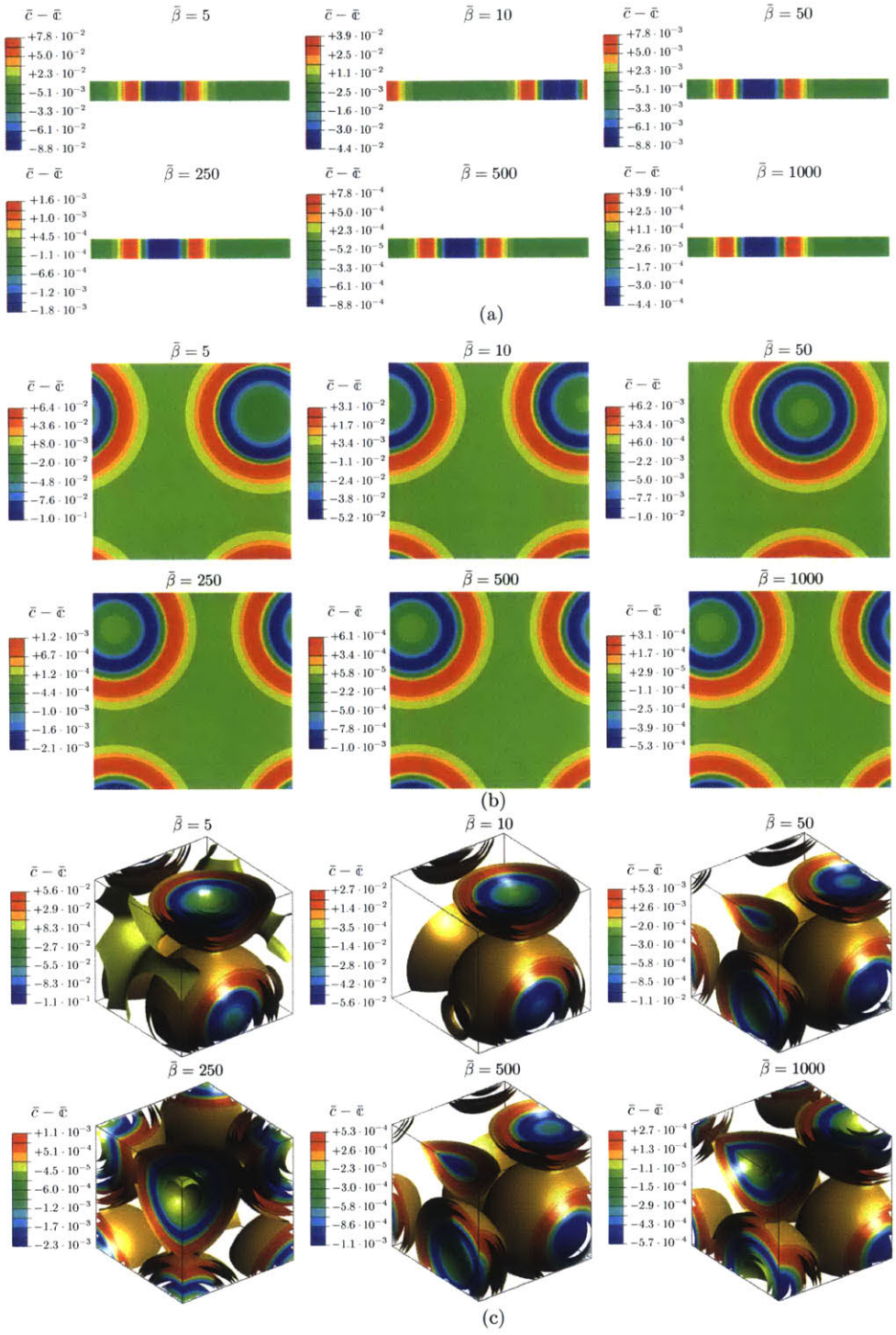

Figure B-5: The difference $\bar{c} - \bar{\mathfrak{c}}$ at steady-state for various values of $\bar{\beta}$ for (a) 1D simulations showing contours of the difference, (b) 2D simulations showing contours of the difference, and (c) 3D simulations showing iso-surfaces of the difference.

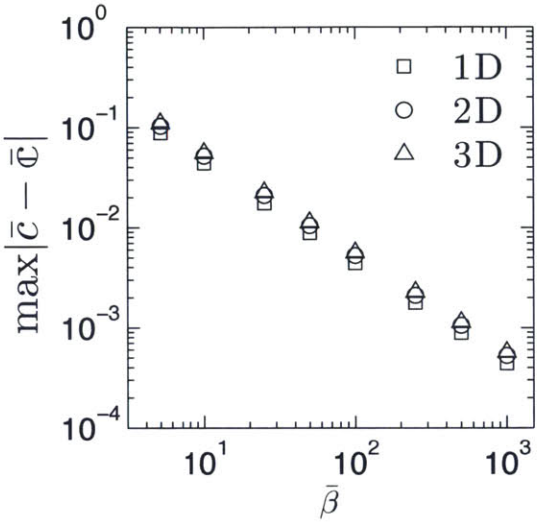

Figure B-6: Convergence of the maximum of the absolute difference of $\bar{c} - \bar{\mathfrak{c}}$ as a function of the normalized penalty modulus $\bar{\beta}$ in one, two, and three dimensions using the micromorphic formulation.

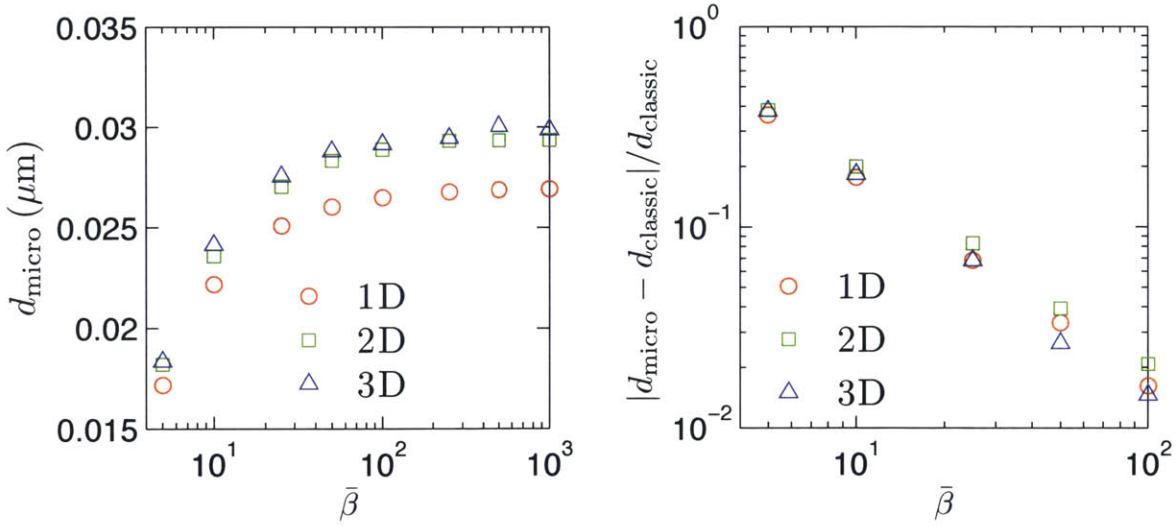

Figure B-7: (a) Interface width d_{micro} for simulations using the micromorphic formulation with varying normalized penalty modulus $\bar{\beta}$. Convergence of the front width d_{micro} computed from simulations using the micromorphic simulation to the front width d_{classic} computed from simulations using the classical formulation for increasing values of $\bar{\beta}$.

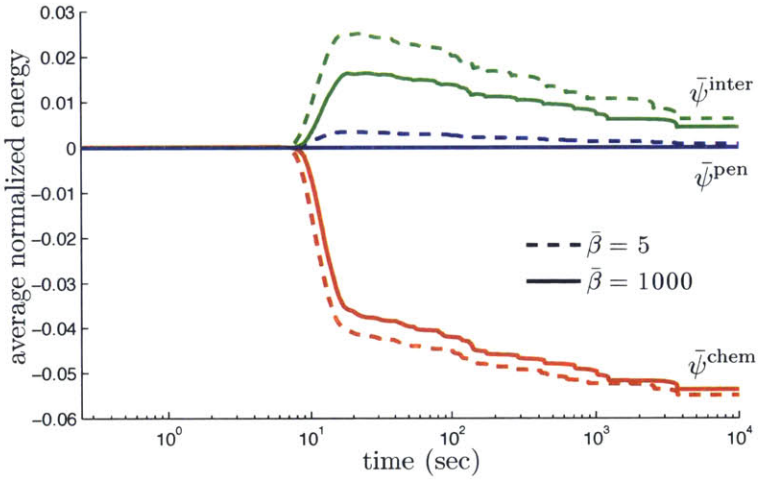

(a)

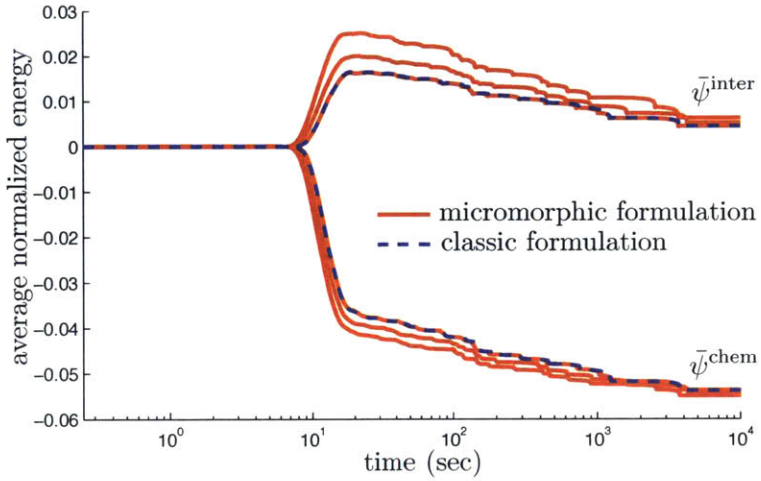

(b)

Figure B-8: (a) Evolution of the chemical $\bar{\psi}^{\text{chem}}$ (red), interfacial $\bar{\psi}^{\text{inter}}$ (green), and penalty $\bar{\psi}^{\text{pen}}$(blue) normalized energies (B.53) for a simulation with $\bar{\beta} = 5$ (dashed line) and a simulation with $\bar{\beta} = 1000$ (solid line). (b) Convergence of the micromorphic formulation (red solid lines) chemical $\bar{\psi}^{\text{chem}}$ and interfacial $\bar{\psi}^{\text{inter}}$ normalized energies to those computed using the classical formulation (blue dashed lines).

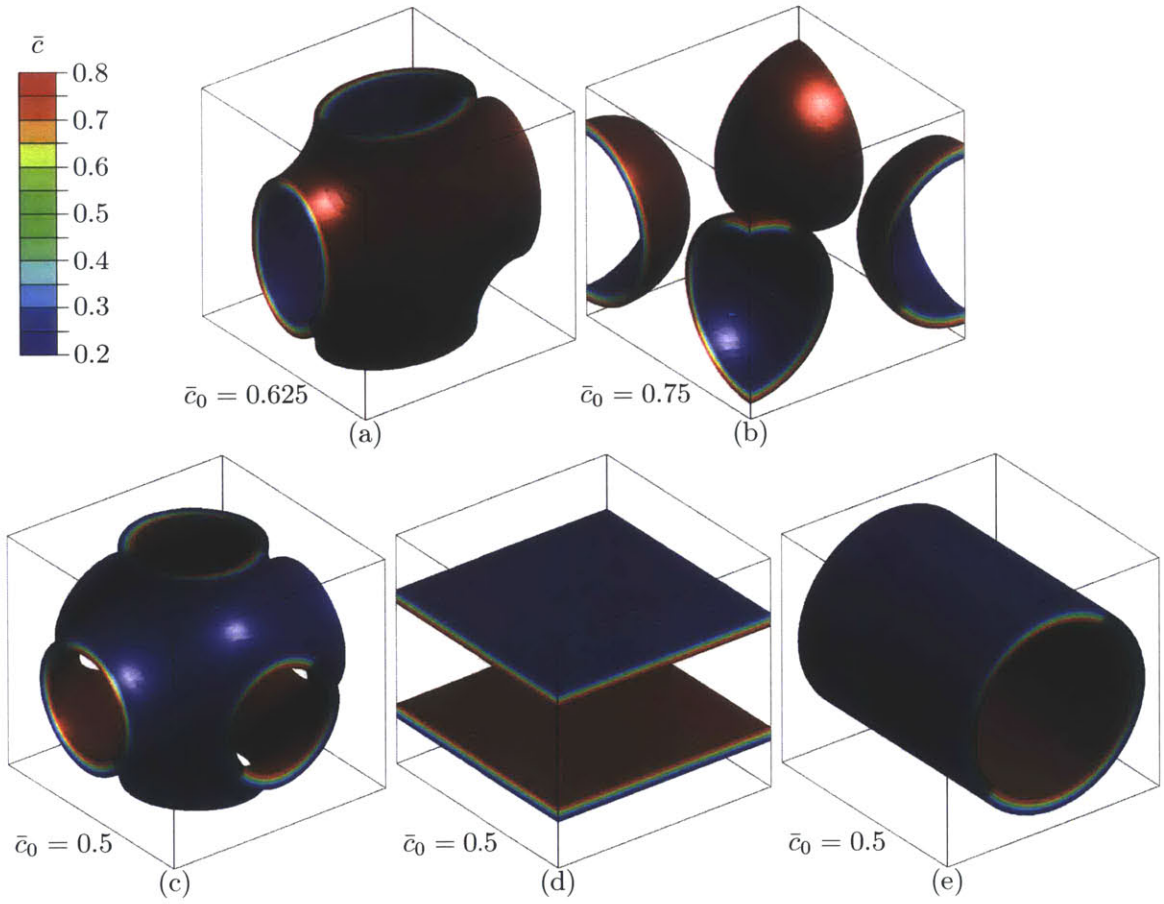

Figure B-9: Steady-state phase separation morphologies in three dimensions for simulations with $\bar{D} = 10$, $\bar{R} = 5$. The simulations have a uniformly distributed initial concentration with mean $\bar{c}_0$ and maximum fluctuation of 0.05. (a) with $\bar{c}_0 = 0.625$ results in a Lawson surface. (b) with $\bar{c}_0 = 0.75$ results in a spherical surface. (c) through (d) all have a $\bar{c}_0 = 0.5$ but have different initial random fluctuations, (c) results in a P-Schwarz surface, (d) results in Lamella, and (e) results in a cylindrical surface.

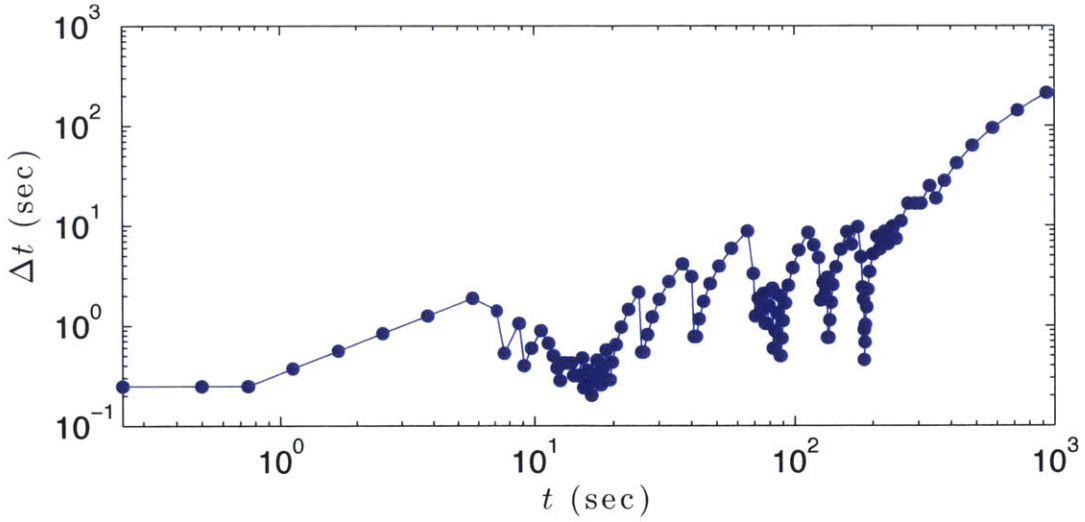

Figure B-10: Evolution of the simulation time steps Δt as a function of the simulation time t for the 3D simulation shown in Fig. B-9(b). The drastic reduction in time steps at certain points correspond to periods in the simulation where two phases merged to coarsen the morphology of the system.

Appendix C

Numerical methodology for Part II: Modeling amorphous Silicon electrodes

C.1 Introduction

Following the framework developed by Chester et al. (2015), in this Appendix we present the details of our numerical implementation of the constitutive model developed in Part II for the coupled diffusion-deformation behavior of amorphous Silicon (a-Si) electrodes. In particular, we present here the "residual" vector and "tangent" matrix which must be implemented in order to solve the coupled set of equations in the finite element program Abaqus/Standard through the use of the user element (UEL) subroutine. Details on how to implement the residuals and tangents developed here within the UEL fortran subroutines can be found in Chester et al. (2015), and are thus omitted from this Appendix.

In Sect. C.2 we begin by recalling the governing partial differential equations and boundary conditions, and then formulate the variational statements which will serve to develop the residuals necessary for the finite element implementation. In Sect. C.3 we derive the tangents. The residuals and tangents are summarized in Sect. C.4. In Sect. C.5 we summarize our constitutive time integration procedure, and in Sect. C.6 we derive an algorithmically consistent approximation for the spatial tangent modulus.

C.2 Variational formulation. Residuals

We begin by recalling the governing partial differential equations (8.151), and (8.152), and their boundary conditions:

$$\left.\begin{array}{lll} \text{Force balance} & \left\{\begin{array}{rll} \operatorname{div}\mathbf{T}+\mathbf{b}=\mathbf{0}, & \text{in} & \mathcal{B}, \\ \mathbf{u}=\breve{\mathbf{u}} & \text{on} & \mathcal{S}_u, \\ \mathbf{T}\mathbf{n}=\breve{\mathbf{t}} & \text{on} & \mathcal{S}_t, \end{array}\right. \\ \text{Mass balance} & \left\{\begin{array}{rll} \dot{c}_{\mathrm{R}}=-J\operatorname{div}\mathbf{j}, & \text{in} & \mathcal{B}, \\ \mu=\breve{\mu} & \text{on} & \mathcal{S}_\mu, \\ -m\operatorname{grad}\mu\cdot\mathbf{n}=\breve{j} & \text{on} & \mathcal{S}_j. \end{array}\right. \end{array}\right\} \tag{C.1}$$

Note that in this numerical implementation, the degrees of freedom are the displacements $\mathbf{u}$, governed by force balance, and the chemical potential μ, governed by mass balance. The choice of using the chemical potential as the degree of freedom for the mass balance equation, rather than the concentration c_{R}, is made for two reasons. First, it allows us to prescribe, if needed, chemical potential boundary conditions. Second, it negates the necessity of introducing an additional variable to capture the effect of stress on the chemical potential, as was necessary in our the numerical implementation for Part I, see Sect. 8.14.

With

$$\mathbf{w}_1, \quad \text{and} \quad w_2 \tag{C.2}$$

denoting weighting (or test) fields which vanish on $\mathcal{S}_u$, and $\mathcal{S}_\mu$ respectively, the weak forms corresponding to (C.1) are given by

$$\left.\begin{array}{l} \displaystyle\int_{\mathcal{B}} (\mathbf{T}:\operatorname{grad}\mathbf{w}_1-\mathbf{w}_1\cdot\mathbf{b})\,dv-\int_{\mathcal{S}_t}\mathbf{w}_1\cdot\breve{\mathbf{t}}\,da=0, \\ \displaystyle\int_{\mathcal{B}}\left(w_2\dot{c}_{\mathrm{R}}(J^{-1})+\operatorname{grad}w_2\cdot(m\operatorname{grad}\mu)\right)dv+\int_{\mathcal{S}_j}w_2\breve{j}\,da=0. \end{array}\right\} \tag{C.3}$$

The body is approximated using finite elements, $\mathrm{B}=\cup\mathrm{B}^e$, and the trial solutions for the displacement and the chemical potential are interpolated inside each element by

$$\mathbf{u}=\sum_A \mathbf{u}^A N^A, \quad \text{and} \quad \mu=\sum_A \mu^A N^A, \tag{C.4}$$

with the index $A=\{1,2,...,M\}$ denoting the nodes of the element, $\mathbf{u}^A$ denoting the nodal displacements, μ denoting the nodal chemical potentials, and N^A the shape functions. Using a standard Galerkin approach, the weighting fields are interpolated by the same functions,

that is

$$\mathbf{w}_1 = \sum_A \mathbf{w}_1^A N^A, \quad \text{and} \quad w_2 = \sum_A w_2^A N^A, \tag{C.5}$$

Using (C.4) and (C.5) in (C.3), yields the following element-level system equations.

$$\left.\begin{aligned} &\int_{\mathcal{B}^e} \left(\mathbf{T}\text{grad}N^A - N^A\mathbf{b}\right)\, dv - \int_{\mathcal{S}_t^e} N^A \check{\mathbf{t}}\, da = \mathbf{0}, \\ &\int_{\mathcal{B}^e} \left(N^A \dot{c}_{\mathrm{R}}(J^{-1}) + \text{grad}\, N^A \cdot (m\text{grad}\,\mu)\right)\, dv + \int_{\mathcal{S}_j^e} N^A \check{j}\, da = 0. \end{aligned}\right\} \tag{C.6}$$

This system of coupled equations is solved using a Newton procedure in Abaqus/Standard by defining element-level residuals and tangents. Using (C.7), the element-level residuals for the displacements and the chemical potential are given by

$$\left.\begin{aligned} \mathbf{R}_{\mathbf{u}}^A &= \int_{\mathcal{B}^e} \left(\mathbf{T}\text{grad}N^A - N^A\mathbf{b}\right)\, dv - \int_{\mathcal{S}_t^e} N^A \check{\mathbf{t}}\, da, \\ R_\mu^A &= \int_{\mathcal{B}^e} \left(N^A \dot{c}_{\mathrm{R}}(J^{-1}) + \text{grad}\, N^A \cdot (m\text{grad}\,\mu)\right)\, dv + \int_{\mathcal{S}_j^e} N^A \check{j}\, da. \end{aligned}\right\} \tag{C.7}$$

In the solution procedure, in order to compute the residuals above and the tangents that follow, one needs to compute the concentration c_{R} at every increment. Recall, the chemical potential (8.141), which may be written in the following dimensionless form

$$\frac{\mu^0 - \mu}{R\vartheta} + \ln\left(\gamma \frac{\bar{c}}{1-\bar{c}}\right) - \frac{\Omega}{3R\vartheta}\text{tr}\mathbf{M}^e = 0. \tag{C.8}$$

Further, using (8.140) and (8.137), we may write the $\text{tr}\mathbf{M}^e$ term in (C.8) as

$$\frac{\mu^0 - \mu}{R\vartheta} + \ln\left(\gamma \frac{\bar{c}}{1-\bar{c}}\right) - \frac{\Omega K}{R\vartheta} \ln\left(\frac{J}{1 + \Omega(\bar{c} - \bar{c}_0)c_{\mathrm{R,max}}}\right) = 0, \tag{C.9}$$

which serves as an implicit equation for $\bar{c} = c_{\mathrm{R}}/c_{\mathrm{R,max}}$ which may be solved given a value for J, which is computed from the displacement degrees of freedom, and a value for the chemical potential degree of freedom. The term $\dot{c}_{\mathrm{R}}$ in $(\text{C.7})_2$ is computed using the approximation,

$$\dot{c}_{\mathrm{R}} = \frac{c_{\mathrm{R},n+1} - c_{\mathrm{R},n}}{\Delta t}. \tag{C.10}$$

C.3 Tangents

In addition to the residuals, the following tangents are also required:

$$\begin{aligned} K^{AB}_{\mathbf{uu}} &= -\frac{\partial \mathbf{R}^A_{\mathbf{u}}}{\partial \mathbf{u}^B}, \quad K^{AB}_{\mu\mu} = -\frac{\partial R^A_{\mu}}{\partial \mu^B}, \\ K^{AB}_{\mathbf{u}\mu} &= -\frac{\partial \mathbf{R}^A_{\mathbf{u}}}{\partial \mu^B}, \quad K^{AB}_{\mu\mathbf{u}} = -\frac{\partial R^A_{\mu}}{\partial \mathbf{u}^B}. \end{aligned} \tag{C.11}$$

First, the tangent of the displacement residual with respect to the displacement dof, in indicial notation, is given by (cf. Chester et al., 2015)

$$K^{AB}_{u_i u_k} = -\int_{\mathcal{B}^e} \frac{\partial N^A}{\partial x_j} \mathbb{A}_{ijkl} \frac{\partial N^B}{\partial x_l}\, dv + \int_{\mathcal{S}^e_t} N^A N^B \frac{\partial \breve{t}_i}{\partial u_k}\, da, \tag{C.12}$$

with

$$\mathbb{A}_{ijkl} = J^{-1} F_{jm} F_{ln} \frac{\partial T_{\mathrm{R},im}}{\partial F_{kn}}. \tag{C.13}$$

The spatial tangent modulus $\mathbb{A}$, will depend on the elastic-plastic constitutive response of the material. An approximation for $\mathbb{A}$ is specified in Sect. C.5.

Remark. As detailed in Chester et al. (2015), to accommodate compressible and nearly incompressible material behavior and mitigate volumetric locking behavior, we use the so called *F-bar* method (de Souza Neto et al., 1996). In such a method, the deformation gradient is suitably replaced such that the incompressibility constrained is enforced as an approximate average throughout the element, rather than point wise at each integration point. The use of the F-bar method does not change the integration point residuals, simply the modified deformation is used. However, the tangent (A.14), and all tangents which involve residuals being derived with respect to the displacement degrees of freedom, must be modified. The necessary modifications are discussed in detail in Chester et al. (2015), □

The tangent of the displacement residual with respect to the chemical potential dof is given by

$$K^{AB}_{\mathbf{u}\mu} = -\int_{\mathcal{B}^e} N^B \frac{\partial \mathbf{T}}{\partial \mu} \operatorname{grad} N^A\, dv + \int_{\mathcal{S}^e_t} N^A N^B \frac{\partial \breve{\mathbf{t}}}{\partial \mu}\, da. \tag{C.14}$$

Based on $(8.140)_2$, we make the *approximation* that

$$\frac{\partial \mathbf{T}}{\partial \mu} \approx J^{e-1} \frac{\partial \mathbf{M}^e}{\partial \mu}. \tag{C.15}$$

Recalling $(8.140)_1$ and (8.136), and using the fact that $\operatorname{tr}\mathbf{E}^e = \ln(J/J^s)$, we may write

$$\mathbf{M}^e = 2G\mathbf{E}_0^e + K\ln\left(\frac{J}{J^s}\right)\mathbf{1}, \quad J^s = 1 + \Omega(c_{\mathrm{R}} - c_{\mathrm{R},0}), \tag{C.16}$$

which yields

$$\frac{\partial \mathbf{M}^e}{\partial \mu} = -\frac{K\Omega}{J^s}\frac{\partial c_{\mathrm{R}}}{\partial \mu}\mathbf{1}, \tag{C.17}$$

where the term $\partial c_{\mathrm{R}}/\partial\mu$ is computed numerically using a finite difference scheme as detailed in Sect. C.5.

Next, the tangent of the chemical potential residual with respect to the chemical potential dof is given by

$$K_{\mu\mu}^{AB} = -\int_{\mathcal{B}^e}\left(N^A N^B \frac{\partial \dot{c}_{\mathrm{R}}}{\partial \mu}\frac{1}{J} + \frac{\partial m}{\partial \mu}N^B \operatorname{grad} N^A \cdot \operatorname{grad}\mu + m\operatorname{grad} N^A \cdot \operatorname{grad} N^B\right) dv - \int_{\mathcal{S}_j^e} N^A N^B \frac{\partial \breve{j}}{\partial \mu}\, da \tag{C.18}$$

where the term $\partial \dot{c}_{\mathrm{R}}/\partial\mu$ is computed numerically using a finite difference scheme, and where, using (8.150), we may write

$$\frac{\partial m}{\partial \mu} = \frac{\partial m}{\partial c_{\mathrm{R}}}\frac{\partial c_{\mathrm{R}}}{\partial \mu} = \frac{D_0}{R\vartheta}(J^{-1})(1-2\bar{c})\frac{\partial c_{\mathrm{R}}}{\partial \mu}. \tag{C.19}$$

The tangent of the chemical potential residual with respect to the displacement dof is given by

$$K_{\mu u_i}^{AB} = -\int_{\mathcal{B}^e}\left(N^A \frac{\partial \dot{c}_{\mathrm{R}}}{\partial J}\frac{\partial N^B}{\partial x_i} - \frac{\partial N^A}{\partial x_i} m \frac{\partial N^B}{\partial x_0}\frac{\partial \mu}{\partial x_0} + \frac{\partial N^A}{\partial x_p}\frac{\partial m_{\mathrm{R}}}{\partial c_{\mathrm{R}}}\frac{\partial c_{\mathrm{R}}}{\partial J}\frac{\partial N^B}{\partial x_i}\frac{\partial \mu}{\partial x_p} - \frac{\partial N^A}{\partial x_q} m \frac{\partial N^B}{\partial x_q}\frac{\partial \mu}{\partial x_i}\right) dv - \int_{\mathcal{S}_j^e} N^A N^B \frac{\partial \breve{j}}{\partial u_i}\, da, \tag{C.20}$$

where

$$m_{\mathrm{R}} = Jm = \frac{D_0}{R\vartheta}c_{\mathrm{R}}(1-\bar{c}), \quad \frac{\partial m_{\mathrm{R}}}{\partial c_{\mathrm{R}}} = \frac{D_0}{R\vartheta}(1-2\bar{c}), \quad \frac{\partial c_{\mathrm{R}}}{\partial J} = \frac{\partial c_{\mathrm{R}}}{\partial \mu}\frac{\partial \mu}{\partial J}, \quad \frac{\partial \mu}{\partial J} = -\frac{\Omega K}{J} \tag{C.21}$$

Note that in deriving (C.20) we have assumed that the deformation gradient is computed from the displacements in the standard fashion. Additional terms will appear when using a modified deformation gradient as discussed in the Remark following (C.13).

In our particular numerical implementation we have simply taken the tangent (C.20) to be equal to zero, that is we use

$$K^{AB}_{\mu u_i} = 0. \tag{C.22}$$

Although this will affect our convergence rate, it does not affect the accuracy of our solutions. We also note that convergence, even with the tangent (C.20) set to zero, has been found to be sufficiently fast for the problems under consideration in this thesis.

C.4 Summary

We may summarize the element-level residuals and tangents for the displacements $\mathbf{u}$ and chemical potential μ degrees of freedom as

$$\begin{aligned}
\mathbf{R}^A_{\mathbf{u}} &= \int_{\mathcal{B}^e} \left(\mathbf{T}\text{grad}N^A - N^A\mathbf{b}\right)\, dv - \int_{\mathcal{S}^e_t} N^A \check{\mathbf{t}}\, da, \\
R^A_{\mu} &= \int_{\mathcal{B}^e} \left(N^A \dot{c}_{\mathrm{R}}(J^{-1}) + \text{grad}\, N^A \cdot (m\text{grad}\,\mu)\right)\, dv + \int_{\mathcal{S}^e_j} N^A \check{j}\, da,
\end{aligned} \tag{C.23}$$

and

$$\begin{aligned}
K^{AB}_{u_i u_k} &= -\int_{\mathcal{B}^e} \frac{\partial N^A}{\partial x_j} \mathbb{A}_{ijkl} \frac{\partial N^B}{\partial x_l}\, dv + \int_{\mathcal{S}^e_t} N^A N^B \frac{\partial \check{t}_i}{\partial u_k}\, da, \\
K^{AB}_{\mathbf{u}\mu} &= -\int_{\mathcal{B}^e} N^B \frac{\partial \mathbf{T}}{\partial \mu} \text{grad}N^A\, dv + \int_{\mathcal{S}^e_t} N^A N^B \frac{\partial \check{\mathbf{t}}}{\partial \mu}\, da, \\
K^{AB}_{\mu\mu} &= -\int_{\mathcal{B}^e} \Bigg(N^A N^B \frac{\partial \dot{c}_{\mathrm{R}}}{\partial \mu}\frac{1}{J} + \frac{\partial m}{\partial \mu} N^B \text{grad}\, N^A \cdot \text{grad}\,\mu \\
&\qquad + m\,\text{grad}\, N^A \cdot \text{grad}\, N^B \Bigg)\, dv - \int_{\mathcal{S}^e_j} N^A N^B \frac{\partial \check{j}}{\partial \mu}\, da, \\
K^{AB}_{\mu\mathbf{u}} &= 0.,
\end{aligned} \tag{C.24}$$

with

$$
\begin{aligned}
m &= \frac{D_0}{R\vartheta} c(1-\bar{c}), \\
\frac{\partial m}{\partial \mu} &= \frac{D_0}{R\vartheta}(J^{-1})(1-2\bar{c})\frac{\partial c_{\mathrm{R}}}{\partial \mu}, \\
\frac{\partial \mathbf{T}}{\partial \mu} &\approx -\frac{K\Omega}{J^e J^s}\frac{\partial c_{\mathrm{R}}}{\partial \mu}\mathbf{1},
\end{aligned}
\tag{C.25}
$$

and where at each increment, the concentration $c_{\mathrm{R}} = \bar{c}c_{\mathrm{R,max}}$ is computed through the implicit equation (viz. C.9),

$$
\frac{\mu^0 - \mu}{R\vartheta} + \ln\left(\gamma\frac{\bar{c}}{1-\bar{c}}\right) - \frac{\Omega K}{R\vartheta}\ln\left(\frac{J}{1+\Omega(\bar{c}-\bar{c}_0)c_{\mathrm{R,max}}}\right) = 0. \tag{C.26}
$$

Finally, the term $\dot{c}_{\mathrm{R}}$ is computed through (viz. C.10)

$$
\dot{c}_{\mathrm{R}} = \frac{c_{\mathrm{R},n+1} - c_{\mathrm{R},n}}{\Delta T}, \tag{C.27}
$$

and the terms

$$
\frac{\partial c_{\mathrm{R}}}{\partial \mu}, \quad \text{and} \quad \frac{\partial \dot{c}_{\mathrm{R}}}{\partial \mu}
$$

are computed numerically through a finite difference scheme as elaborated on in the next Section.

C.5 Time integration procedure

The time integration procedure may be phrased as follows:

- Given $\{\mu_{\mathrm{n+1}}, \mathbf{F}_{\mathrm{n+1}}\}$ and $\{\mathbf{F}^p_{\mathrm{n}}\}$,
- Solve for $\{\mathbf{T}_{\mathrm{n+1}}, \mathbf{F}^p_{\mathrm{n+1}}, c_{\mathrm{R},n+1}\}$.

This integration procedure has three steps:

1. Compute $c_{\mathrm{R},n+1}$;
2. Compute $\mathbf{F}^p_{\mathrm{n+1}}$ and $\mathbf{T}_{\mathrm{n+1}}$; and
3. Compute

$$
\frac{\partial c_{\mathrm{R}}}{\partial \mu}, \quad \text{and} \quad \frac{\partial \dot{c}_{\mathrm{R}}}{\partial \mu}, \tag{C.28}
$$

   using a finite difference scheme.

We begin by recalling the implicit equation (C.26), which on account of the fact that the swelling distortion is spherical and the fact that plastic deformation is incompressible, is a relationship only between the chemical potential μ_{n+1}, which is known, the volume ratio J_{n+1} which is known from $\mathbf{F}_{n+1}$, and the unknown concentration $c_{R,n+1} = \bar{c}_{n+1}\, c_{R,max}$. Hence we may solve

$$\frac{\mu^0 - \mu_{n+1}}{R\vartheta} + \ln\left(\gamma \frac{\bar{c}_{n+1}}{1-\bar{c}_{n+1}}\right) - \frac{\Omega K}{R\vartheta} \ln\left(\frac{J_{n+1}}{1+\Omega(\bar{c}_{n+1}-\bar{c}_0)c_{R,max}}\right) = 0, \tag{C.29}$$

for the unknown $c_{R,n+1} = \bar{c}_{n+1}\, c_{R,max}$. Note that with $c_{R,n+1}$ known, we may compute

$$\mathbf{F}^s_{n+1} = (J^s_{n+1})^{1/3}\mathbf{1}, \quad J^s_{n+1} = 1 + \Omega(c_{R,n+1} - c_{R,0}). \tag{C.30}$$

Next, the evolution equation $\dot{\mathbf{F}}^p = \mathbf{D}^p\mathbf{F}^p$, reiterated from (8.144), is integrated by means of the exponential map (cf. Weber and Anand, 1990), as

$$\mathbf{F}^p_{n+1} = \exp(\Delta t \mathbf{D}^p_{n+1})\mathbf{F}^p_n, \tag{C.31}$$

and the inverse $\mathbf{F}^{p-1}_{n+1}$ is given by

$$\mathbf{F}^{p-1}_{n+1} = \mathbf{F}^{p-1}_n \exp(-\Delta t \mathbf{D}^p_{n+1}). \tag{C.32}$$

Using $\mathbf{F} = \mathbf{F}^e\mathbf{F}^p\mathbf{F}^s$, the fact that $\mathbf{F}^s = (J^s)^{1/3}\mathbf{1}$, and (C.32), we may write

$$\mathbf{F}^e_{n+1} = \mathbf{F}^e_{tr} \exp(-\Delta \mathbf{D}^p_{n+1}). \tag{C.33}$$

where we have defined the trial elastic distortion $\mathbf{F}^e_{tr}$, a known quantity, through

$$\mathbf{F}^e_{tr} \overset{\text{def}}{=} \mathbf{F}_{n+1}\, \mathbf{F}^{p-1}_n\, (J^s)^{-1/3}. \tag{C.34}$$

The tensors $\mathbf{F}^e_{n+1}$ and $\mathbf{F}^e_{tr}$ admit the polar decomposition

$$\mathbf{F}^e_{n+1} = \mathbf{R}^e_{n+1}\, \mathbf{U}^e_{n+1}, \quad \text{and} \quad \mathbf{F}^e_{tr} = \mathbf{R}^e_{tr}\mathbf{U}^e_{tr}. \tag{C.35}$$

Using (C.35) in (C.34), and rearranging, we obtain

$$\mathbf{R}^e_{n+1}\, \mathbf{U}^e_{n+1} \exp(\Delta t \mathbf{D}^p_{n+1}) = \mathbf{R}^e_{tr}\mathbf{U}^e_{tr}. \tag{C.36}$$

Since the principal directions of $\mathbf{D}^p_{n+1}$ are the same as those of $\mathbf{U}^e_{n+1}$, and on account of the uniqueness of the polar decomposition, from (C.36) we may write

$$\begin{aligned} \mathbf{R}^e_{n+1} &= \mathbf{R}^e_{tr}, \\ \mathbf{U}^e_{n+1} \exp(\Delta t \mathbf{D}^p_{n+1}) &= \mathbf{U}^e_{tr}. \end{aligned} \tag{C.37}$$

Taking the natural logarithm of $(C.37)_2$ we obtain

$$\mathbf{E}^e_{n+1} = \mathbf{E}^e_{tr} - \Delta t \mathbf{D}^p_{n+1}, \quad \text{where} \quad \mathbf{E}^e_{tr} \stackrel{\text{def}}{=} \ln \mathbf{U}^e_{tr} \tag{C.38}$$

Using plastic incompressibility, (C.38) may be written as

$$\begin{aligned} \operatorname{tr} \mathbf{E}^e_{n+1} &= \operatorname{tr} \mathbf{E}^e_{tr}, \\ \mathbf{E}^e_{0,n+1} &= \mathbf{E}^e_{0,tr} - \Delta t \mathbf{D}^p_{n+1}. \end{aligned} \tag{C.39}$$

Recalling the stress-strain relation $(8.140)_2$, we may write (C.39) as

$$\begin{aligned} \operatorname{tr} \mathbf{M}^e_{n+1} &= \operatorname{tr} \mathbf{M}^e_{tr}, \\ \mathbf{M}^e_{0,n+1} &= \mathbf{M}^e_{0,tr} - 2G\Delta t \mathbf{D}^p_{n+1}, \end{aligned} \tag{C.40}$$

where we have used

$$\operatorname{tr} \mathbf{M}^e_{tr} = 3K \operatorname{tr} \mathbf{E}^e_{tr}, \quad \text{and} \quad \mathbf{M}^e_{0,tr} = 2G\mathbf{E}^e_{0,tr}. \tag{C.41}$$

Recall that the plastic stretching is given by

$$\mathbf{D}^p = \sqrt{\frac{3}{2}} \dot{\bar{\epsilon}}^p \mathbf{N}^p, \quad \mathbf{N}^p = \sqrt{\frac{3}{2}} \frac{\mathbf{M}^e_0}{\bar{\sigma}}. \tag{C.42}$$

Using $(C.42)_1$ in $(C.40)_2$ yields

$$\mathbf{M}^e_{0,n+1} = \mathbf{M}^e_{0,tr} - \sqrt{6} G \dot{\bar{\epsilon}}^p_{n+1} \Delta t \mathbf{N}^p_{n+1} \tag{C.43}$$

which using $(C.42)_2$ and rearranging yields

$$\left(\sqrt{2/3}\, \bar{\sigma}_{n+1} + \sqrt{6}\, \dot{\bar{\epsilon}}^p_{n+1} \Delta t \right) \mathbf{N}^p_{n+1} = \mathbf{M}^e_{0,tr}. \tag{C.44}$$

Defining

$$\bar{\sigma}_{tr} \stackrel{\text{def}}{=} \sqrt{\frac{3}{2}} |\mathbf{M}^e_{0,tr}|, \quad \text{and} \quad \mathbf{N}^p_{tr} = \frac{\mathbf{M}^e_{0,tr}}{|\mathbf{M}^e_{0,tr}|}, \tag{C.45}$$

we may write (C.44) as

$$\left(\sqrt{2/3}\, \bar{\sigma}_{n+1} + \sqrt{6}\, \dot{\bar{\epsilon}}^p_{n+1} \Delta t \right) \mathbf{N}^p_{n+1} = \sqrt{2/3}\, \bar{\sigma}_{tr} \mathbf{N}^p_{tr}, \tag{C.46}$$

which yields

$$\begin{aligned} \mathbf{N}^p_{n+1} &= \mathbf{N}^p_{tr}, \\ \bar{\sigma}_{n+1} &= \bar{\sigma}_{tr} - 3G(\dot{\bar{\epsilon}}^p_{n+1} \Delta t). \end{aligned} \tag{C.47}$$

Thus, the direction of plastic flow at the end of the increment is determined from the trial direction of plastic flow.

Next, during plastic flow $\dot{\bar{\epsilon}}^p > 0$, the equivalent tensile stress is given by the flow strength (viz. 8.146)

$$\bar{\sigma}_{\mathrm{n+1}} = \hat{Y}(\bar{c}_{\mathrm{n+1}}) + Y_* \left(\frac{\dot{\bar{\epsilon}}^p_{\mathrm{n+1}}}{\dot{\epsilon}_0} \right)^{1/m}. \tag{C.48}$$

Finally, using (C.48) in $(\mathrm{C.47})_2$, gives the following implicit equation for $\dot{\bar{\epsilon}}^p$

$$g = \bar{\sigma}_{\mathrm{tr}} - \hat{Y}(\bar{c}_{\mathrm{n+1}}) - Y_* \left(\frac{\dot{\bar{\epsilon}}^p_{\mathrm{n+1}}}{\dot{\epsilon}_0} \right)^{1/m} - 3G(\dot{\bar{\epsilon}}^p_{\mathrm{n+1}}\, \Delta t). \tag{C.49}$$

Once a solution for $\dot{\bar{\epsilon}}^p_{\mathrm{n+1}}$ has been found we can update all necessary quantities as follows. First the plastic stretching, plastic distortion, and elastic distortion may be updated as

$$\mathbf{D}^p_{\mathrm{n+1}} = \sqrt{3/2}\, \dot{\bar{\epsilon}}^p_{\mathrm{n+1}}\, \mathbf{N}^p_{\mathrm{tr}}, \quad \mathbf{F}^p_{\mathrm{n+1}} = \exp(\Delta t \mathbf{D}^p_{\mathrm{n+1}})\mathbf{F}^p_n, \quad \mathbf{F}^e_{\mathrm{n+1}} = \mathbf{F}^e_{\mathrm{tr}} \exp(-\Delta \mathbf{D}^p_{\mathrm{n+1}}), \tag{C.50}$$

from which $\mathbf{E}^e_{\mathrm{n+1}}$ may be computed. The Mandel stress is then computed as

$$\mathbf{M}^e_{\mathrm{n+1}} = 2G\mathbf{E}^e_{0,n+1} + K(\mathrm{tr}\,\mathbf{E}^e_{\mathrm{n+1}})\mathbf{1}, \tag{C.51}$$

and finally the Cauchy stress is given by

$$\mathbf{T}_{\mathrm{n+1}} = (J^{e-1}_{\mathrm{n+1}})\mathbf{R}^e_{\mathrm{tr}}\mathbf{M}^e_{\mathrm{n+1}}\mathbf{R}^{e\top}_{\mathrm{tr}}. \tag{C.52}$$

The only remaining part of this time integration procedure is to compute

$$\frac{\partial c_{\mathrm{R}}}{\partial \mu}, \quad \text{and} \quad \frac{\partial \dot{c}_{\mathrm{R}}}{\partial \mu}.$$

To do this we use a simple numerical perturbation and finite difference scheme. We define positively and negatively perturbed chemical potentials as

$$\mu^+ = \mu_{\mathrm{n+1}} + \delta\mu, \quad \text{and} \quad \mu^- = \mu_{\mathrm{n+1}} - \delta\mu, \tag{C.53}$$

where the perturbation $\delta\mu$ is given by

$$\delta\mu = \begin{cases} |\mu_{\mathrm{n+1}}| \cdot 10^{-8} & \text{if} \quad |\mu_{\mathrm{n+1}}| \geq 1, \\ 10^{-8} & \text{if} \quad |\mu_{\mathrm{n+1}}| < 1. \end{cases} \tag{C.54}$$

Using the perturbed values of the chemical potential in the implicit equation (C.29), we then solve for the positively perturbed concentration c^+_{R} and the negatively perturbed concentra-

tion c_{R}^{-}, and compute

$$\frac{\partial c_{\mathrm{R},n+1}}{\partial \mu_{\mathrm{n+1}}} = \frac{c_{\mathrm{R}}^{+} - c_{\mathrm{R}}^{-}}{2\delta\mu}. \tag{C.55}$$

Further, we compute positively and negatively perturbed time rate of changes of the concentration through

$$\dot{c}_{\mathrm{R}}^{+} = \frac{c_{\mathrm{R}}^{+} - c_{\mathrm{R},n}}{\Delta t}, \quad \text{and} \quad \dot{c}_{\mathrm{R}}^{-} = \frac{c_{\mathrm{R}}^{-} - c_{\mathrm{R},n}}{\Delta t}, \tag{C.56}$$

from which we then compute

$$\frac{\partial \dot{c}_{\mathrm{R},n+1}}{\partial \mu_{\mathrm{n+1}}} = \frac{\dot{c}_{\mathrm{R}}^{+} - \dot{c}_{\mathrm{R}}^{-}}{2\delta\mu}. \tag{C.57}$$

C.6 Spatial tangent modulus

In order to complete the tangents developed in Sect. C.3, we must compute the spatial tangent modulus (viz. C.13)

$$\mathbb{A}_{ijkl} = J^{-1} F_{jm} F_{ln} \frac{\partial T_{\mathrm{R},im}}{\partial F_{kn}}. \tag{C.58}$$

In this section we develop an *estimate* for this modulus. Specifically, we approximate (C.58) by a derivative of the elastic Mandel stress with respect to the trial elastic strain, that is

$$\mathbb{A}_{n+1} = \frac{\partial \mathbf{M}_{\mathrm{n+1}}^{e}}{\partial \mathbf{E}_{\mathrm{tr}}^{e}}. \tag{C.59}$$

We will make use of different spatial tangent moduli for steps in which the deformation is purely elastic, and steps in which there is plastic deformation, that is

$$\mathbb{A}_{\mathrm{n+1}} = \begin{cases} \mathcal{C}_{\mathrm{elastic}} & \text{if} \quad \bar{\sigma}_{\mathrm{tr}} \leq 0, \\ \mathcal{C}_{\mathrm{plastic}} & \text{if} \quad \bar{\sigma}_{\mathrm{tr}} > 0 \quad \text{and} \quad \dot{\bar{\epsilon}}^{p} > 0, \end{cases} \tag{C.60}$$

where the elastic $\mathcal{C}_{\mathrm{elastic}}$, and plastic $\mathcal{C}_{\mathrm{plastic}}$ moduli are defined next.

C.6.1 Elastic tangent

During a computational increment in which the deformation is purely elastic, $\mathbf{E}_{\mathrm{n+1}}^{e} = \mathbf{E}_{\mathrm{tr}}^{e}$, and we may write the stress strain relation (C.51) as

$$\mathbf{M}_{\mathrm{n+1}}^{e} = 2G\mathbf{E}_{\mathrm{tr}}^{e} + \left(K - \frac{2}{3}G\right) \mathrm{tr}\,\mathbf{E}^{e}. \tag{C.61}$$

The elastic tangent modulus is then simply equal to the standard elastic stiffness

$$\mathcal{C}_{\text{elastic}} = \frac{\partial \mathbf{M}^e_{\text{n+1}}}{\partial \mathbf{E}^e_{\text{tr}}} = 2G\mathbb{I} + \left(K - \frac{2}{3}G\right)\mathbf{1}\otimes\mathbf{1}, \tag{C.62}$$

where $\mathbb{I}$ and $\mathbf{1}$ are the fourth- and second-order identity tensors.

C.6.2 Plastic tangent

We begin by writing $\mathbf{M}^e_{\text{n+1}}$ in terms of its deviatoric and trace parts

$$\mathbf{M}^e_{\text{n+1}} = \mathbf{M}^e_{0,n+1} + \frac{1}{3}\text{tr}\,\mathbf{M}^e_{\text{n+1}}\,\mathbf{1}. \tag{C.63}$$

which, using

$$\mathbf{M}^e_{0,n+1} = |\mathbf{M}^e_{0,n+1}|\mathbf{N}^p_{\text{n+1}}, \quad \mathbf{N}^p_{\text{n+1}} = \mathbf{N}^p_{\text{tr}}, \quad \text{and} \quad \text{tr}\,\mathbf{M}^e_{\text{n+1}} = \text{tr}\,\mathbf{M}^e_{\text{tr}},$$

and the definitions (C.42) and (C.45), may be written as

$$\mathbf{M}^e_{\text{n+1}} = \left(\frac{\bar{\sigma}_{\text{n+1}}}{\bar{\sigma}_{\text{tr}}}\right)\mathbf{M}^e_{0,\text{tr}} + \frac{1}{3}\text{tr}\,\mathbf{M}^e_{\text{tr}}\mathbf{1}. \tag{C.64}$$

Taking the derivative with respect to the trial elastic strain yields

$$\begin{aligned}\mathcal{C}_{\text{plastic}} = \frac{\partial \mathbf{M}^e_{\text{n+1}}}{\partial \mathbf{E}^e_{\text{tr}}} &= \left(\frac{\bar{\sigma}_{\text{n+1}}}{\bar{\sigma}_{\text{tr}}}\right)\frac{\partial \mathbf{M}^e_{0,\text{tr}}}{\partial \mathbf{E}^e_{\text{tr}}} + \frac{1}{3}\frac{\partial \text{tr}\,\mathbf{M}^e_{\text{tr}}}{\mathbf{E}^e_{\text{tr}}}\mathbf{1} \\ &\quad + \frac{1}{\bar{\sigma}_{\text{tr}}}\mathbf{M}^e_{0,\text{tr}}\otimes\frac{\partial \bar{\sigma}_{\text{n+1}}}{\partial \mathbf{E}^e_{\text{tr}}} - \left(\frac{\bar{\sigma}_{\text{n+1}}}{\bar{\sigma}^2_{\text{tr}}}\right)\mathbf{M}^e_{0,\text{tr}}\otimes\frac{\partial \bar{\sigma}_{\text{tr}}}{\partial \mathbf{E}^e_{\text{tr}}}.\end{aligned} \tag{C.65}$$

Noting that $\mathbf{E}^e_{\text{tr}}$ enters the update equation through $\bar{\sigma}_{\text{tr}}$ we may write

$$\frac{\partial \bar{\sigma}_{\text{n+1}}}{\partial \mathbf{E}^e_{\text{tr}}} = \frac{\partial \bar{\sigma}_{\text{n+1}}}{\partial \bar{\sigma}_{\text{tr}}}\frac{\partial \bar{\sigma}_{\text{tr}}}{\partial \mathbf{E}^e_{\text{tr}}},$$

and (C.65) may thus be written as

$$\mathcal{C}_{\text{plastic}} = \left(\frac{\bar{\sigma}_{\text{n+1}}}{\bar{\sigma}_{\text{tr}}}\right)\frac{\partial \mathbf{M}^e_{0,\text{tr}}}{\partial \mathbf{E}^e_{\text{tr}}} + \frac{1}{3}\frac{\partial \text{tr}\,\mathbf{M}^e_{\text{tr}}}{\mathbf{E}^e_{\text{tr}}}\mathbf{1} + \left(\frac{\partial \bar{\sigma}_{\text{n+1}}}{\partial \bar{\sigma}_{\text{tr}}} - \frac{\bar{\sigma}_{\text{n+1}}}{\bar{\sigma}_{\text{tr}}}\right)\frac{\mathbf{M}^e_{0,\text{tr}}}{\bar{\sigma}_{\text{tr}}}\otimes\frac{\partial \bar{\sigma}_{\text{tr}}}{\partial \mathbf{E}^e_{\text{tr}}}. \tag{C.66}$$

Then using (C.41) we may write

$$\mathcal{C}_{\text{plastic}} = \tilde{\mathcal{C}}_{\text{elastic}} + \left(\frac{\partial \bar{\sigma}_{\text{n+1}}}{\partial \bar{\sigma}_{\text{tr}}} - \frac{\bar{\sigma}_{\text{n+1}}}{\bar{\sigma}_{\text{tr}}}\right)\frac{\mathbf{M}^e_{0,\text{tr}}}{\bar{\sigma}_{\text{tr}}}\otimes\frac{\partial \bar{\sigma}_{\text{tr}}}{\partial \mathbf{E}^e_{\text{tr}}}. \tag{C.67}$$

where for conciseness we have defined a modified elastic modulus as

$$\tilde{\mathcal{C}}_{\text{elastic}} = \left(\frac{\bar{\sigma}_{\text{n+1}}}{\bar{\sigma}_{\text{tr}}}\right) 2G\left(\mathbb{I} - \frac{1}{3}\mathbf{1}\otimes\mathbf{1}\right) + K\mathbf{1}\otimes\mathbf{1}. \tag{C.68}$$

Next, using the definition of $\bar{\sigma}_{\text{tr}}$, and the fact that $\mathbf{N}^p$ is deviatoric we may write

$$\begin{aligned}
\frac{\partial\bar{\sigma}_{\text{tr}}}{\partial\mathbf{E}^e_{\text{tr}}} &= \sqrt{\frac{3}{2}}\frac{\partial}{\partial\mathbf{E}^e_{\text{tr}}}\left(\sqrt{\mathbf{M}^e_{0,\text{tr}}:\mathbf{M}^e_{0,\text{tr}}}\right) \\
&= \sqrt{\frac{3}{2}}\frac{\partial\mathbf{M}^e_{0,\text{tr}}}{\partial\mathbf{E}^e_{\text{tr}}}\frac{\mathbf{M}^e_{0,\text{tr}}}{|\mathbf{M}^e_{0,\text{tr}}|} \\
&= \sqrt{\frac{3}{2}}2G\left(\mathbb{I} - \frac{1}{3}\mathbf{1}\otimes\mathbf{1}\right)\mathbf{N}^p_{\text{tr}} \\
&= \sqrt{\frac{3}{2}}2G\mathbf{N}^p_{\text{tr}}.
\end{aligned} \tag{C.69}$$

Using the result (C.69) and the fact that

$$\mathbf{N}^p_{\text{tr}} = \sqrt{\frac{3}{2}}\frac{\mathbf{M}^e_{0,\text{tr}}}{\bar{\sigma}_{\text{tr}}}, \tag{C.70}$$

we may write (C.67)

$$\mathcal{C}_{\text{plastic}} = \tilde{\mathcal{C}}_{\text{elastic}} + 2G\left(\frac{\partial\bar{\sigma}_{\text{n+1}}}{\partial\bar{\sigma}_{\text{tr}}} - \frac{\bar{\sigma}_{\text{n+1}}}{\bar{\sigma}_{\text{tr}}}\right)\mathbf{N}^p_{\text{tr}}\otimes\mathbf{N}^p_{\text{tr}}, \tag{C.71}$$

and all that remains is to determine $\partial\bar{\sigma}_{\text{n+1}}/\partial\bar{\sigma}_{\text{tr}}$.

Recall the flow strength (C.48) and the update equation $(C.47)_2$ which may be written as

$$\begin{aligned}
\bar{\sigma}_{\text{n+1}} &= \hat{Y}(\bar{c}_{\text{n+1}}) + \hat{S}(\dot{\bar{\epsilon}}^p_{\text{n+1}}), \\
\bar{\sigma}_{\text{n+1}} &= \bar{\sigma}_{\text{tr}} - 3G(\dot{\bar{\epsilon}}^p_{\text{n+1}}\,\Delta t),
\end{aligned} \tag{C.72}$$

where

$$\hat{S}(\dot{\bar{\epsilon}}^p_{\text{n+1}}) = Y_*\left(\frac{\dot{\bar{\epsilon}}^p_{\text{n+1}}}{\dot{\epsilon}_0}\right)^{1/m}, \tag{C.73}$$

is the portion of the flow strength which depends on the equivalent tensile plastic strain rate. Taking the derivative of (C.72) with respect to $\bar{\sigma}_{\text{tr}}$ yields

$$\begin{aligned} \frac{\partial \bar{\sigma}_{\text{n+1}}}{\partial \bar{\sigma}_{\text{tr}}} &= \hat{H}(\dot{\bar{\epsilon}}^p_{\text{n+1}}) \frac{\partial \dot{\bar{\epsilon}}^p_{\text{n+1}}}{\partial \bar{\sigma}_{\text{tr}}}, \\ \frac{\partial \bar{\sigma}_{\text{n+1}}}{\partial \bar{\sigma}_{\text{tr}}} &= 1 - 3G \frac{\partial \dot{\bar{\epsilon}}^p_{\text{n+1}}}{\partial \bar{\sigma}_{\text{tr}}} \Delta t, \end{aligned} \tag{C.74}$$

where we have defined

$$\hat{H}(\dot{\bar{\epsilon}}^p_{\text{n+1}}) \stackrel{\text{def}}{=} \frac{d\hat{S}(\dot{\bar{\epsilon}}^p_{\text{n+1}})}{d\dot{\bar{\epsilon}}^p_{\text{n+1}}} = \frac{Y_*}{\dot{\epsilon}_0} \frac{1}{m} \left(\frac{\dot{\bar{\epsilon}}^p_{\text{n+1}}}{\dot{\epsilon}_0} \right)^{\frac{1}{m}-1}. \tag{C.75}$$

Eliminating $\partial \dot{\bar{\epsilon}}^p_{\text{n+1}} / \partial \bar{\sigma}_{\text{tr}}$ from (C.74), we may solve for

$$\frac{\partial \bar{\sigma}_{\text{n+1}}}{\partial \bar{\sigma}_{\text{tr}}} = \frac{\hat{H}(\dot{\bar{\epsilon}}^p_{\text{n+1}})}{\hat{H}(\dot{\bar{\epsilon}}^p_{\text{n+1}}) + 3G\Delta t}. \tag{C.76}$$

Finally using (C.76) in (C.71) yields

$$\mathcal{C}_{\text{plastic}} = \tilde{\mathcal{C}}_{\text{elastic}} + 2G \left(\frac{\hat{H}(\dot{\bar{\epsilon}}^p_{\text{n+1}})}{\hat{H}(\dot{\bar{\epsilon}}^p_{\text{n+1}}) + 3G\Delta t} - \frac{\bar{\sigma}_{\text{n+1}}}{\bar{\sigma}_{\text{tr}}} \right) \mathbf{N}^p_{\text{tr}} \otimes \mathbf{N}^p_{\text{tr}}, \tag{C.77}$$

In summary, recalling (C.60), (C.62) and (C.77), the spatial tangent modulus is given by

$$\mathbb{A}_{\text{n+1}} = \begin{cases} \mathcal{C}_{\text{elastic}} & \text{if} \quad \bar{\sigma}_{\text{tr}} \leq 0, \\ \mathcal{C}_{\text{plastic}} & \text{if} \quad \bar{\sigma}_{\text{tr}} > 0 \quad \text{and} \quad \dot{\bar{\epsilon}}^p > 0, \end{cases}$$

with

$$\begin{aligned} \mathcal{C}_{\text{elastic}} &= 2G\mathbb{I} + \left(K - \frac{2}{3}G \right) \mathbf{1} \otimes \mathbf{1}; \quad \text{and} \\ \mathcal{C}_{\text{plastic}} &= \tilde{\mathcal{C}}_{\text{elastic}} + 2G \left(\frac{\hat{H}(\dot{\bar{\epsilon}}^p_{\text{n+1}})}{\hat{H}(\dot{\bar{\epsilon}}^p_{\text{n+1}}) + 3G\Delta t} - \frac{\bar{\sigma}_{\text{n+1}}}{\bar{\sigma}_{\text{tr}}} \right) \mathbf{N}^p_{\text{tr}} \otimes \mathbf{N}^p_{\text{tr}}, \end{aligned} \tag{C.78}$$

with $\tilde{\mathcal{C}}_{\text{elastic}}$ given by (C.68), and $\hat{H}(\dot{\bar{\epsilon}}^p_{\text{n+1}})$ given by (C.75).